UFMG

Universidade Federal de Minas Gerais

Instituto de Ciências Exatas

Departamento de Física

Laboratório de Estrutura Eletrônica

Lídia Carvalho Gomes

Two-Dimensional Materials: Electronic and Structural Properties of Defective Graphene and Boron Nitride from First Principles.

Tese de Doutorado

September 2014

Lídia Carvalho Gomes

Two-Dimensional Materials: Electronic and Structural Properties of Defective Graphene and Boron Nitride from First Principles.

Orientador:
Prof. Ricardo Wagner Nunes

Tese apresentada ao Programa de Pós-graduação do Departamento de Física da Universidade Federal de Minas Gerais como requisito parcial à obtenção do grau de Doutor em Física.

September 2014

Agradecimentos

Aos meus pais João e Cleusa, e à minha irmã Laís, pelo amor imenso e pelo apoio. Mais que minha família são mesmo anjos na minha vida, a quem sempre dedicarei cada passo novo que eu der. Amo vocês.

A todos os tios e tias, primos e primas, vovôs e vovós. Mais que família no nome ou no sangue, é família de coração, que torce e está presente a todo momento. Em especial à Tia Lê, que esteve em meus pensamentos a cada palavra colocada aqui.

Ao Ricardo, pelo exemplo profissional e humano. Muito obrigada pela orientação sempre paciente e presente. Obrigada pelos minutos rápidos de tirar dúvidas que sempre viraram verdadeiras aulas de física. Esses anos foram certamente de valor imenso na minha formação.

À Simone, ao Mário e ao Hélio Chacham, pela amizade, pelas colaborações, discussões, e por estarem sempre abertos a nos dar apoio quando preciso.

A todos os amigos desse lado do mundo: Aninha, Alana, Débora, Lígia, Vivi, Regi, Mangos, Medeirão, Matheus, Ananias, Emilson, Daniel, Davi, Ingrid, Campô, Jena ... Enfim, a todos aqueles (e foram muitos) que de alguma maneira contribuíram para que esses quatro anos tenham valido a pena.

Ao Antônio Hélio, pela oportunidade de crescimento profissional e pessoal. Muito obrigada pela confiança, pelo incentivo e pelas portas abertas. Isso terá sempre uma importância enorme para mim.

À minha família portuguesa/singapurense: Nádia, Manuel, Zé Carlos, Inês, Fábio, Miguel, Paula, Alan, Alexandra, Tânia e Vítor. Ao João Nuno, pelo carinho e apoio todo especiais. Sem vocês meu último ano não teria sido tão sorridente e acolhedor. Obrigada de todo o coração.

A todo o departamento de Física da UFMG: professores, secretaria, administração, moças da limpeza. O conjunto todo faz desse lugar um ambiente tão saudável de se trabalhar.

À FAPEMIG pelo apoio financeiro e ao LCC-CENAPAD-UFMG pelo suporte computacional.

À todos aqueles que por motivos diversos foram impedidos de realizar o sonho de estudar.

Abstract

We use first principles calculations based on the formalism of Density Functional Theory (DFT) to investigate electronic and structural properties of graphene and boron nitride two-dimensional materials. In the first work, we present a study of stability and electronic properties of nine different models for extended one-dimensional (1D) defects in monolayer BN. A low-energy stoichiometric model for an armchair-direction antiphase boundary (APB) in monolayer BN is introduced. The second work investigates four different grain boundaries in bilayer graphene, aiming an understanding of the degree of localization of the electronic states in the atoms that compose the line defects. Interesting results like magnetic instabilities and changes from metallic to semi-metallic character of these systems are discussed. In the third work we study the low-energy electronic transport across stacking boundaries in graphene. The electron scattering by interfaces formed between regions of monolayer and bilayer graphene is investigated by a continuum approach. The fourth work was developed in collaboration with the experimental group of the National University of Singapore (NUS) which synthesized coherent interfaces between graphene and h-BN. We use DFT calculations to investigate the introduction of a core dislocation in the h-BN lattice as a mechanism of strain release in order to keep the continuity of the film along the interface. In the fifth work we present a recently started study of two-dimensional semiconductors monochalcogenides, focus on the electronic and optical properties of these materials.

Resumo

Utilizamos cálculos de primeiros princípios, baseados na teoria do funcional da densidade (DFT) para investigar propriedades estruturais e eletrônicas de materiais bidimensionais. No primeiro trabalho apresentamos um estudo de estabilidade e propriedades eletrônicas de diferentes defeitos unidimensionais estendidos em monocamadas de BN. Introduzimos um modelo estequiométrico de baixa energia formado na direção armchair, e que define uma fronteira de antifase nesse material. O segundo trabalho aborda a introdução de defeitos lineares em bi-camadas de grafeno, focando no grau de localização dos estados eletrônicos nos átomos que formam os defeitos. Instabilidades magnéticas e transições de metal para um semi-metal são observadas e discutidas. No terceiro trabalho utilizamos um modelo contínuo de baixas energias para estudar o espalhamento eletrônico em interfaces formadas entre mono e bi-camadas de grafeno. O quarto trabalho foi desenvolvido em colaboração com o grupo experimental da Universidade Nacional de Singapura. Filmes hibridos de grafeno e BN foram sintetizados com interfaces coerentes entre esses materiais. Utilizamos cálculos DFT para investigar a introdução de discordâncias no BN como um mecanismo de relaxação de strain da rede, permitindo a formação de filmes coerentes ao longo da interface. O quinto trabalho apresenta resultados preliminares de semicondutores bi-dimensionais formados por átomos do grupo dos calcogênios. Esse trabalho está em seus passos iniciais, e será focado no estudo das propriedades estruturais, ópticas e eletrônicas desses materiais.

Contents

5 Electronic Properties of Grain Boundaries in Graphene Bilayers. 36

6 Electronic Transmission in Graphene: Monolayer−Bilayer interfaces. 59

7 Lattice Relaxation at the Interface of Two Two-Dimensional Crystals: Graphene and Hexagonal Boron-Nitride 89

List of Figures

List of Tables

Chapter 1

Introduction

Two-dimensional (2D) materials have been an extensively studied classes of materials since a single-layer graphene was obtained in a stable form by mechanical exfoliation[1]. From there, the interest in 2D crystals was promptly extended to matherials other than graphene, such as hexagonal boron nitride (h-BN) and layered metal dichalcogenides (LMDCs) to name a few[2–4].

The development of reliable synthesis methods of single and few-layer 2D materials combined with their unusual and very interesting properties, directly related to their lower dimensionality, has attracted a massive attention of the scientific and industrial community. Much progress has been made, but it is still a challenge to obtain a total control of the properties of any material at the nanoscale.

The synthesis process of materials in this scale results in polycristalline samples with abundant topological defects. A great improvement in the production of defect-free low dimensional materials has been made[5, 6], but defective samples are very commonly obtained. Introduction of defects strongly influence the electronic, chemical, and mechanical properties of materials, and a deep understanding on how these properties are altered in the presence of different defects is of essential importance to achieve the desired control of these properties.

In this thesis we use first principles calculations based on the formalism of Density Functional Theory (DFT) to investigate electronic and structural properties of two-dimensional materials. Defective graphene and hexagonal boron nitride are the main focus, while preliminary results of a work in progress are also presented, were we investigate two-dimensional monochalcogenide semiconductors.

The thesis is organized as follows:

- In the Chapter 2, we provide a brief overview of basic concepts on graphene and boron nitride.
- In the Chapter 3 we present the methodology used for the development of the work.
- In the Chapter 4, we present a study of stability and electronic properties of nine different models for extended one-dimensional (1D) defects in monolayer BN. A low-energy stoichiometric model for an armchair-direction antiphase boundary (APB) in monolayer BN is introduced.
- In the Chapter 5, grain boundaries in graphene bilayers are investigated, aiming at the understanding of the degree of localization of the electronic states in the atoms that compose the core of the line defects. Interesting results like magnetic instabilities and changes from metallic to semi-metallic character of these systems are discussed.
- In the third work, presented in Chapter 6, we study the low-energy electronic transport across stacking boundaries in graphene. The electron scattering by interfaces formed between regions of monolayer and bilayer graphene is investigated by a continuum approach.
- In the Chapter 7, we discuss a work that was developed in collaboration with an experimental group of the Graphene Research Centre (GRC) of the National University of Singapore (NUS) and with Prof. Antônio Hélio Castro Neto. Results obtained from synthesis of coherent interfaces between graphene and h-BN motivated DFT calculations to investigate the introduction of a core dislocation in the h-BN lattice as a mechanism of strain relief, in order to keep the continuity of the film along the interface. Electronic properties of this system are also discussed.
- In the Chaper 8, preliminary results of a study of two-dimensional semiconductors monochacogenides is presented. It focuses on the electronic and optical properties of these materials. This work will be further developed in collaboration with the theoretical group of the GRC/NUS.

Chapter 2

Two-Dimensional Materials: A brief introduction to Graphene and hexagonal-Boron Nitride.

2.1 Graphene structure and electronic dispersion.

2.1.1 Single layer graphene.

The hexagonal structure of graphene, with two carbon atoms per unit cell, can be seen as made out of two interpenetrating triangular lattices as presented in Fig. 2.1-a. With the value of the carbon-carbon distance $a = 1.42$ Å obtained experimentally[7], the lattice vectors can be written:

$$\mathbf{a_1} = \frac{a}{2}(3, \sqrt{3}), \quad \mathbf{a_2} = \frac{a}{2}(3, -\sqrt{3}), \tag{2.1}$$

with the three nearest-neighbor vectors $\vec{\delta}_1$, $\vec{\delta}_2$ and $\vec{\delta}_3$ given by:

$$\delta_{\mathbf{1}} = \frac{a}{2}(1, \sqrt{3}), \quad \delta_{\mathbf{2}} = \frac{a}{2}(1, -\sqrt{3}), \quad \delta_{\mathbf{3}} = -a(1, 0) \tag{2.2}$$

as shown in Fig. 2.2.

In addition to the aforementioned lattice vectors $\mathbf{a_1}$ and $\mathbf{a_2}$ usually adopted to describe the structure of graphene, we define the vector $\mathbf{a_{ac}}$ as shown in Fig. 2.2, which define the lattice period along the armchair direction of graphene.

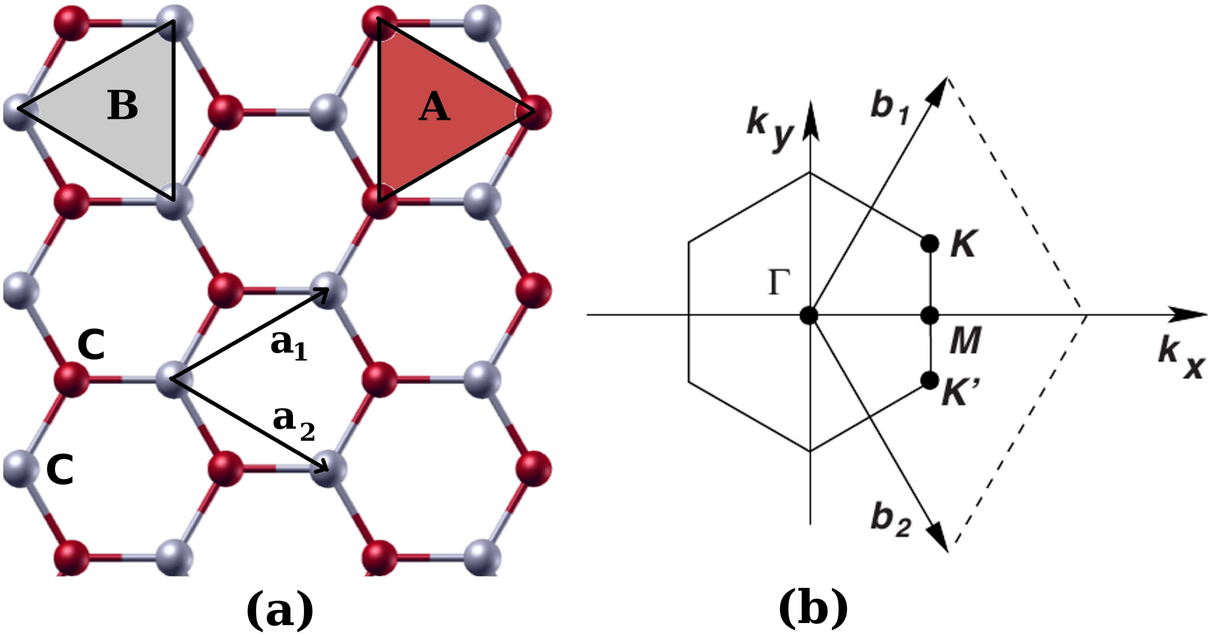

FIGURE 2.1: (a) Honeycomb lattice of graphene formed by two interpenetrating triangular lattices named A (atoms in red) and B (atoms in gray) lattices. The lattice vectors $\vec{a}_1$ and $\vec{a}_2$ are also shown. (b) Brillouin Zone defined by the reciprocal lattice vectors $\vec{b}_1$ and $\vec{b}_2$ and the position of the special Dirac points K and K', around which the electronic dispersion is linear for low energies.

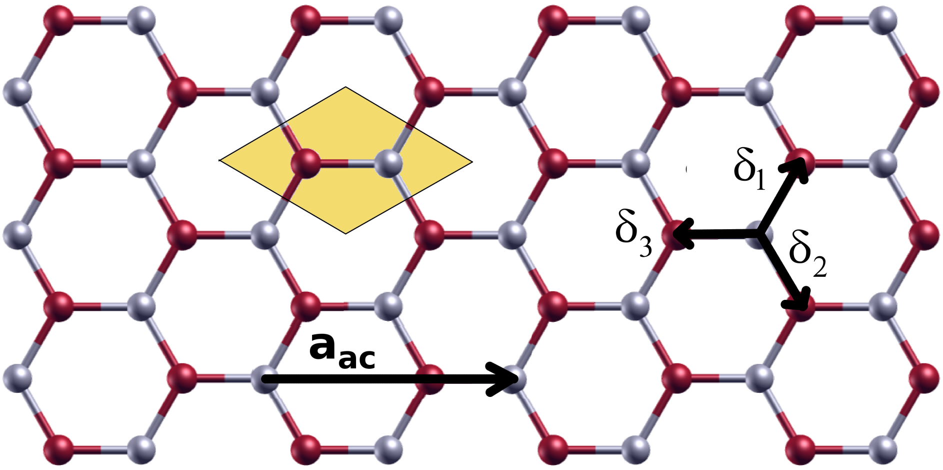

FIGURE 2.2: The unitcell of graphene highlighted by the yellow box and the translational vector $\mathbf{a_{ac}}$ that defines the period along the armchair directions of the hexagonal structure. The three nearest-neighbor vectors $\vec{\delta}_1$, $\vec{\delta}_2$ and $\vec{\delta}_3$ are also shown.

By the definition of reciprocal space vectors, $\mathbf{b_i} = 2\pi \frac{\vec{a}_j \times \vec{a}_k}{\vec{a}_i \cdot (\vec{a}_j \times \vec{a}_k)}$, the reciprocal vectors for this triangular lattice are given by:

$$\mathbf{b_1} = \frac{2\pi}{3a}(1, \sqrt{3}), \quad \mathbf{b_2} = \frac{2\pi}{3a}(1, -\sqrt{3}). \tag{2.3}$$

The two-dimensional Brillouin Zone (BZ) of graphene, defined by $\mathbf{b_1}$ and $\mathbf{b_2}$, has also a hexagonal form, but rotated by 30° in relation to the lattice in the real space, as seen in Fig. 2.1-b.

The main electronic properties of graphene are well documented in the literature, with a massive number of works on this topic, since it became the "material of the future". The tight-binding approach has been largely used to describe its electronic dispersion, as an analytic expression for the energy bands can be obtained in a reasonable accordance with more accurate results.

The energy bands derived from a tight-binding Hamiltonian were first derived by P. R. Wallace [8], and have the form:

$$E_{\pm}(\mathbf{k}) = \pm t\sqrt{3 + f(\mathbf{k})} - t' f(\mathbf{k}), \tag{2.4}$$

with

$$f(\mathbf{k}) = 2cos\left(\sqrt{3}k_y a\right) + 4cos\left(\frac{\sqrt{3}}{2}k_y a\right) cos\left(\frac{3}{2}k_x a\right). \tag{2.5}$$

Here, $t \approx 2.8$ eV is the nearest-neighbor hopping energy (hopping between different sublattices), and t', the next nearest-neighbor hopping energy.

By expanding the full band structure in Eq.2.4 around to the $\vec{K}$ ($\vec{K}'$) vectors, which define the K (K') points in the BZ, as $\mathbf{k} = \vec{K} + \mathbf{q}$, with $|\mathbf{q}| \ll |\vec{K}|$, we have, for the π bands:

$$E_{\pm}(\mathbf{q}) = \pm\hbar\nu_F|\mathbf{q}| + O[(q/K)^2], \tag{2.6}$$

where ν_F is the Fermi velocity, given by $\nu_F = 3ta/(2\hbar) \simeq 1 \times 10^6$m/s. The linear energy dispersion close to the **K** (**K'**) points, is characteristic of massless Dirac fermions.

It is this unusual two-dimensional Dirac-like behavior of electrons that makes this material so interesting and different from others.

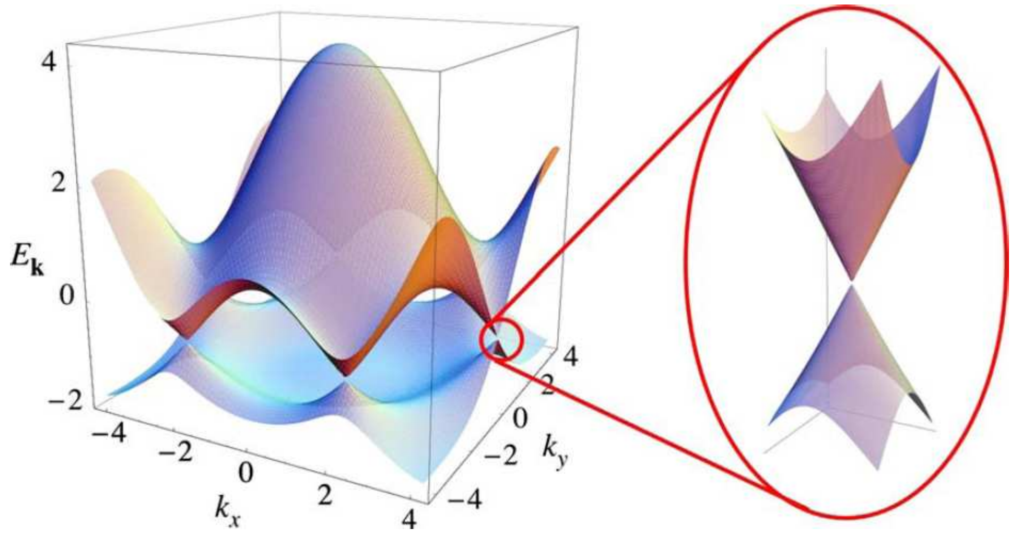

Figure 2.3: Electronic dispersion for the honeycomb lattice of graphene. The Dirac points localized at the six corners of the hexagon that define the BZ show linear dispersion at low energies.

2.1.2 Bilayer graphene: AB' and AA' stackings.

The simplest realization of a multilayer graphene system is that formed by two layers pilling up together in the known Bernal or AB' stacking. As shown in Fig. 2.4, the Bernal stacking is defined when different sublattices of the two graphene layers are positioned directly above each other. So, if a sublattice A of a 'top' graphene layer is positioned above the sublattice B' of a 'bottom' graphene layer, where we use the prime to distinguish the two layers, this stacking is of the AB' type, as shown in Fig. 2.4. In the same way, if the same sublattices from both layers are positioned directly above each other, we have an AA' stacking. Such definitions will be used throughout this work.

The two layers in a graphene bilayer system are weakly coupled by van der Waals forces[7], and the measured interlayer distance is ~ 3.4Å.

The tight-binding model developed for graphene and briefly presented here, can be extended to stacks with a finite number of graphene layers. The first approximation for this problem is to consider the inclusion of the hopping energy between nearest-atoms belonging to different layers, γ. For AB' stacking, γ is the hopping energy between the atoms of sublattices A and B' of the two layers.

For free electrons in a bilayer graphene with AB' stacking, the solution of the eigenvalue problem gives a parabolic relation between low energy states and total momentum $q = \sqrt{{q_x}^2 + {q_y}^2}$, as

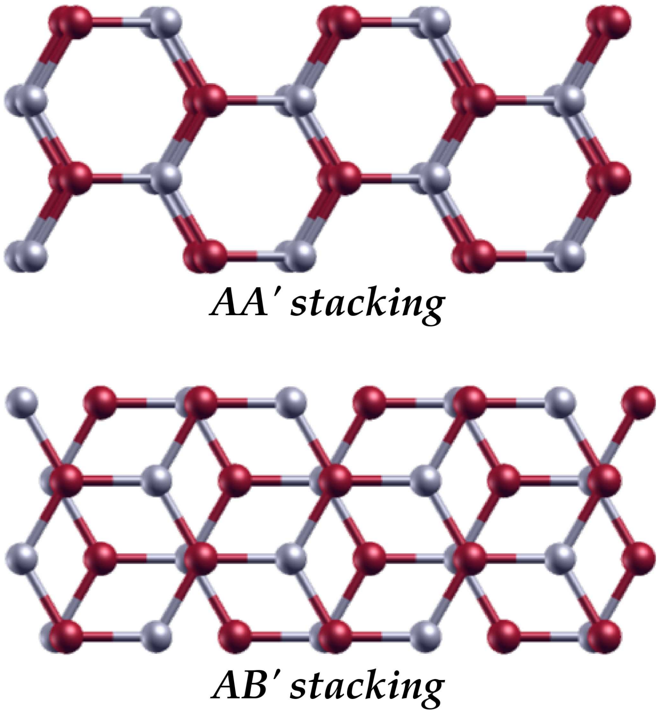

FIGURE 2.4: (a) AA' and AB' stackings in bilayer graphene. The AB' stacking is defined whit the A sub-lattice (in red) of the top layer positioned directly above the B' sub-lattice (in gray) of the bottom layer. In a similar way, a AA' stacking is defined when the top A(B) sub-lattice is directly above the bottom A'(B') sub-lattice.

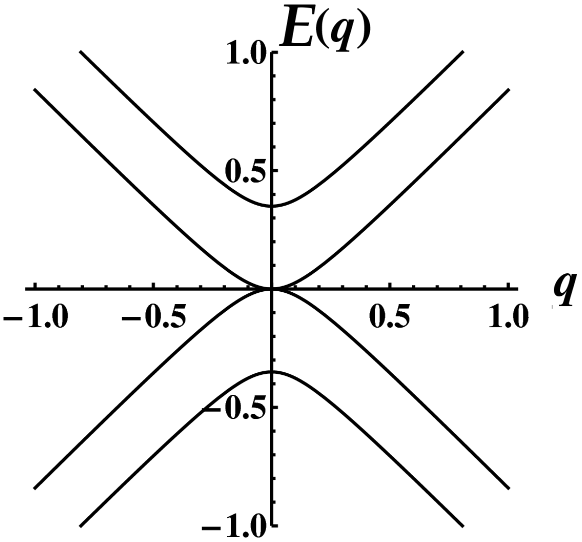

FIGURE 2.5: Parabolic electronic dispersion for bilayer graphene in the AB' stacking.

$$E(\mathbf{q}) = \pm\frac{\gamma \pm \sqrt{4q^2+\gamma^2}}{2} \tag{2.7}$$

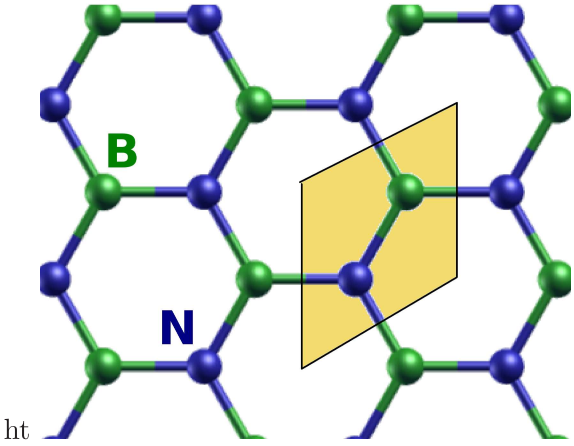

FIGURE 2.6: h-BN lattice adopts the same structure as in graphene but is formed by different atomic species: B and N. The unit cell is shown by the yellow box.

2.2 Hexagonal Boron Nitride.

Despite adopting exactly the same hexagonal structure as graphene, hexagonal boron nitride (h-BN) shows a completely different electronic behavior, due to the asymmetry between the two sublattices, that are now occupied by different atomic species. By considering a minimal tight-binding model for a single layer h-BN, that takes into account the hopping t among nearest neighbor atoms and on-site energies for boron (E_B) and nitrogen (E_N) atoms, it can be shown[9] that the energy relation dispersion assumes the form:

$$E(\mathbf{k}) = E_0 \pm \frac{1}{2}\sqrt{E_g^2 + 4|\phi|^2} \tag{2.8}$$

where it can be identified the insulating behavior of this material, with energy gap $E_g = E_B - E_N > 5$ eV[9, 10]. We also have in Eq. 2.8 $E_0 = (E_B + E_N)/2$ the energy in the middle of the gap and

$$\phi/t = 1 + e^{ia(-k_x/2+\sqrt{3}k_y/2)} + e^{ia(k_x/2+\sqrt{3}k_y/2)}. \tag{2.9}$$

In this way the Dirac cones observed in graphene do not appear in h-BN due to the symmetry breaking induced in the lattice by the different atomic species B and N. Instead, an insulating behavior is observed.

Chapter 3

Methodology

3.1 Density Functional Theory

In quantum mechanics, all information about a given system is contained on its wave function, that can be obtained by solving the Schrödinger equation (SE). So, in principle, if we know the wave function of a given system we can extract from it all other information of interest.

In this way, the starting point to solve a quantum system is the resolution of its Schrödinger equation, that for a generic electronic system with N electrons can be written:

$$H\Psi(\vec{r}_1, \vec{r}_2, ..., \vec{r}_N) = E\Psi(\vec{r}_1, \vec{r}_2, ..., \vec{r}_N). \tag{3.1}$$

However, resolution of such equation presents a great challenge. The exact solution of 3.1 can be obtained analytically just for the hydrogen atom (N=1); for a system with 2 electrons, it is already required the use of approximations to describe electron- electron interactions. For a simple system with about 10 electrons (a CH_4 molecule, for example), we are already facing a huge problem, which solution is quite difficult even with more sophisticated computational methods [11].

DFT is an alternative to solve the electronic Hamiltonian of many-body systems. The idea is to promote the particle density $\rho(\vec{r})$ to the status of key variable, on which the calculation of all other observables can be based.

The advantage of this choice is that now we are dealing with a function of just three variables, the three spacial coordinates of $\rho(\vec{r})$, that is more practical than the wave function, with $3N$ variables.

3.1.1 Hohenberg-Kohn Theorems

The Hohenberg-Kohn theorems [12] states that $\rho(\vec{r})$ can be used in a many-body electronic system as the key variable, of which all observables are functionals. The first Hohenberg-Kohn theorem states that:

> *The external potential $\nu(\vec{r})$, and hence the total energy, is a unique functional of the electron density.*

So, $\rho(\vec{r})$ would be sufficient to know $\Psi(\vec{r_1}, ..., \vec{r_N})$ from which we could obtain all relevant informations in our problem. From this, we conclude that the wave function $\Psi(\vec{r_1}, ..., \vec{r_N})$ is a functional of the density $\rho(\vec{r})$, and as all observables can be obtained from $\Psi(\vec{r_1}, ..., \vec{r_N})$, they can also be written as functionals of $\rho(\vec{r})$. In special, the ground state energy E_0 can be expressed in terms of the ground-state density $\rho_0(\vec{r})$:

$$E_0 = minE[\rho] = \langle \Psi[\rho_0] | H | \Psi[\rho_0] \rangle. \tag{3.2}$$

The energy functional presents the variational property

$$E[\rho_0] \leq E[\rho] \tag{3.3}$$

where ρ_0 is the ground-state density, and ρ is some other density. Equation (3.3) tell us that the calculation of the energy by a different density than the ground-state density, give us an energy higher than the ground-state energy. This important information is known as the second Hohenberg-Kohn theorem:

> *The ground state energy can be obtained variationally: the density that minimizes the total energy is the exact ground state density.*

Despite the great importance of the Hohenberg-Kohn theorems, which allow us to express any physical observable as unique functionals of the electronic density, effectively to solve the many-body problem requires a more practical scheme than the earlier attempts of minimizing E as a functional of ρ directly.

The Kohn-Sham approach, presented by Kohn and Sham [13] in the form of the called Kohn-Sham equations, is nowadays the most common and efficient way of minimizing the DFT functional. This formulation, used in our work, will be briefly discussed in the following.

3.1.2 Kohn-Sham equations

In the Kohn-Sham formulation, it is possible to solve the total energy functional almost exactly, remaining only a small part to be solved approximately.

The total energy functional of a generic system can be decomposed as:

$$E[\rho] = \underbrace{T_s[\rho] + T_c[\rho]}_{T_e[\rho]} + \underbrace{U_H[\rho] + U_{xc}[\rho]}_{V_{ee}[\rho]} + U_{ext}[\rho]. \tag{3.4}$$

Here, $T_s[\rho]$ is the single particle kinetic energy, that represents the kinetic energy of a non-interacting electron system with density ρ; $T_c[\rho]$ is the kinetic energy correlation term, due to the electron interactions effects. The electron- electron interaction potential $V_{ee}[\rho]$, is dismembered in a classical contribution, the Hartree energy $U_H[\rho]$, and in a part of quantum nature $U_{xc}[\rho]$, which includes exchange and correlation effects. The remaining term $U_{ext}[\rho]$, represents the potential due to the external sources.

The explicit form of $T_s[\rho]$, $U_{ext}[\rho]$ and $U_H[\rho]$ can be written:

$$T_s = -\frac{1}{2}\sum_{i=1}^{N}\int \phi_i^*(\vec{r})\nabla^2\phi_i(\vec{r})d\vec{r} \tag{3.5}$$

$$U_H[\rho] = \frac{1}{2}\int\int \frac{\rho(\vec{r})\rho(\vec{r}')}{|\vec{r}-\vec{r}'|}d\vec{r}d\vec{r}' \tag{3.6}$$

$$U_{ext}[\rho] = \int \rho(\vec{r})\nu_{ext}[\rho]d\vec{r} \tag{3.7}$$

with ϕ_i the single particle orbital, and ν_{ext} the external potential per particle, which depends on the interaction of the electronic system with external sources.

Despite of the fact that the explicit form of the remaining terms is not known, the Hohenberg-Kohn theorems ensure that they can be written as a density functional. It is usual to join these unknown terms in one, the so-called exchange-correlation energy E_{xc}=$E_{xc}[\rho]$.

With these informations, we can rewrite Eq. 3.4 as:

$$E[\rho] = T_s[\rho] + \frac{1}{2}\int\int \frac{\rho(\vec{r})\rho(\vec{r}')}{|\vec{r}-\vec{r}'|}d\vec{r}d\vec{r}' + \int \rho(\vec{r})\nu_{ext}[\rho]d\vec{r} + E_{xc}[\rho] \tag{3.8}$$

In order to find expressions that allow us to obtain the total energy of the system, as well as another relevant properties, we proceed by minimizing the energy functional relative to the electronic density $\rho(\vec{r})$. In their formulation, Kohn and Sham assume that the ground state density of the original interacting system $\rho_0(\vec{r})$ is equal to that of some chosen non-interacting system $\rho_o^s(\vec{r})$:

$$\rho_0(\vec{r}) \equiv \rho_0^s(\vec{r}) = \sum_i^N \phi_i^*(\vec{r})\phi_i(\vec{r}). \tag{3.9}$$

From this derivation considerations, we get the expressions:

$$\left[-\frac{1}{2}\nabla^2 + \left(\frac{1}{2}\int \frac{\rho(\vec{r})}{|\vec{r}-\vec{r'}|}d\vec{r} + U_{ext}[\rho] + \frac{\delta E_{xc}[\rho]}{\delta\rho}\right)\right]\phi_i(\vec{r}) = \varepsilon_i\phi_i(\vec{r}) \tag{3.10}$$

or

$$\left[-\frac{1}{2}\nabla^2 + \nu_{eff}(\vec{r})\right]\phi_i(\vec{r}) = \varepsilon_i\phi_i(\vec{r}) \tag{3.11}$$

where we consider the terms in parentheses as a unique effective potential ν_{eff}

$$\nu_{eff} = \frac{1}{2}\int \frac{\rho(\vec{r})}{|\vec{r}-\vec{r'}|}d\vec{r} + \nu_{ext}[\rho] + \frac{\delta E_{xc}[\rho]}{\delta\rho}. \tag{3.12}$$

Equation 3.11 has the form of a single-particle Schröedinger equation , and the single-particle orbitals $\phi_i(\vec{r})$ provide the electronic ground state density of the non-interacting system $\rho_0^s(\vec{r})$, that is the same as the one for the interacting system $\rho_0(\vec{r})$.

The Kohn-Sham ansatz for the density (Eq. 3.9) make it possible to replace the many-body interacting problem by an auxiliary single-body system, which can be solved more easily.

In Kohn-Sham formulation, DFT looks formally like a single-particle theory, thought many-body effects are still included via the so called exchange-correlation functional.

3.2 Exchange-Correlation functional approximations

There are several different approaches used for the exchange-correlation potential, being the local density approximation (LDA) and the generalized-gradient approximation (GGA), the most used of them.

In the LDA approximation, the real inhomogeneous system is decomposed in small cells on which the density $\rho(\vec{r})$ is approximately constant. If we consider, for each cell (i.e., locally), the per-volume energy (e_{xc}^{hom}) of a homogeneous system to be approximately the contribution of each cell to the real inhomogeneous system, we can make these cells infinitesimally small and sum over all cells to obtain:

$$E_{xc}[\rho] \approx E_{xc}^{LDA}[\rho] = \int e_{xc}^{hom}[\rho(\vec{r})]d^3r. \tag{3.13}$$

The functional e_{xc}^{hom} is decomposed in a contribution of the exchange and correlation energies so that $e_{xc}^{hom} = e_x^{hom} + e_c^{hom}$. For the exchange energy, the per-volume energy is considered as that of the homogeneous electron liquid [14, 15]. On the other hand, the correlation part e_c^{hom} is not known exactly, and approximations for this term are based on parametrization of results obtained from Quantum Monte Carlo (QMC) calculations for the electron liquid[16].

Although the local approximation has proved quite successful, the real systems, such as atoms, molecules and solids, are all inhomogeneous, that is, their density $\rho(\vec{r})$ varies spatially. An improvement of the LDA approximation is to consider the spatial variation of the density in terms of the gradient $\nabla\rho(\vec{r})$ in writing the exchange-correlation functional $E_{xc}[\rho]$. In this way, $E_{xc}[\rho]$ has the general form:

$$E_{xc}^{GGA}[\rho] = \int f(\rho(\vec{r}), \nabla\rho(\vec{r}))d\vec{r} \tag{3.14}$$

and have become known as the generalized-gradient approximations (GGAs)[17].

Many different GGAs can be obtained, depending on the method of construction employed for obtaining $f(\rho(\vec{r}), \nabla\rho(\vec{r}))$. In physics, the most popular GGAs functionals are that proposed by Perdew, Burke and Ernzerhof (PBE)[18]. The BLYP, which denotes a combination of Becke's exchange functional[19] and the correction functional of Lee, Yang and Parr[20] are mainly used in chemistry.

Both GGA and LDA functional are very useful and have shown to produce reliable results for a vast number of different systems with the main types of chemical bonds. However, such functional fail for interactions of the van der Waals type (vdW)[21]. These very week interactions are nowadays described by more specialized approaches.

3.3 The SIESTA and Quantum Espresso codes and the main parameters considered in the calculations.

Except for Chapter 6, where continuum approach for the Dirac Hamiltonian was used to study interfaces between graphene layers, in all other works we employ a first principles approach based on the Kohn-Sham density functional theory (KS-DFT), [13], as implemented in the SIESTA [22] (Chapters 4, 5.10 and 7) and Quantum Espresso [23] (Chapter 8) codes.

For works developed with SIESTA code, the generalized-gradient approximation (GGA) is used for the exchange-correlation term. [18] Interactions between valence electrons and ionic cores are described by Troullier-Martins pseudopotentials. [24] and a double-ζ pseudoatomic basis set augmented with polarization orbitals is employed, with an energy cutoff of 0.01 Ry. From previous work by ours and other groups, it is established that this is a carefully-tested calculation setup for problems involving BN and carbon systems. Careful convergence tests of all our results were performed with respect to the numerical parameters of these methodology. Structural optimization has been performed initially with residual forces of less than 0.04 eV/Å on each atom, and further relaxation of the geometries has been carried out with a more stringent tolerance of 0.005 eV/Å. Values of 200 Ry and 250 Ry for the equivalent plane-wave cutoff for the real-space integration mesh have been used for total energy calculations and geometry relaxations.

In Chapter 8 the DFT calculations are performed using the plane-wave pseudopotential method[25, 26] as implemented within the QUANTUM-ESPRESSO package. Norm-conserving pseudopotentials for Sn, Ge, Se and S are generated with the APE pseudopotential generator. For all calculations the wave functions are expanded in plane waves with a kinetic energy cutoff of 70 Ry. This value has been shown enough for energy convergence, as some earlier works[27] used for very similar systems a cutoff of 50 Ry, that already reproduces well converged results. Structural optimization was performed with residual forces af less than 0.01 eV/Å.

Chapter 4

Stability of edges and extended defects on boron nitride and graphene monolayers: the role of chemical environment

4.1 Introduction

Many proposed applications of nanomaterials require the ability to control their electronic properties. In particular, graphene and boron nitride (BN) in the two-dimensional (2D) monolayer form have become an important subject of research, owing to their mechanical strength and a rich variety of physical phenomena connected to their electronic structure. [7] The introduction of structural defects presents an alternative for manipulating the electronic and magnetic properties in these materials. [7, 28–33] In graphene grown on Ni(111) substrates, a translational grain boundary (GB) with a core structure consisting of topological defects (TD) in the form of non-hexagonal rings (pentagons and octagons) has been theoretically proposed [29] and recently observed in STM experiments by Lahiri *et. all* [30]. One of the images obtained in this experimental work is shown in Fig. 4.1, where we can easily identify the GB formed by two pentagons followed by one octagon.

The occurrence of magnetism for the quasi-one-dimensional electronic states introduced by this defect has also been suggested by *ab initio* calculations. [31] This graphene GB lies on the zigzag direction and arises due to the presence of two possible stackings of the graphene monolayer with respect to the Ni(111) substrate, which leads to the possibility

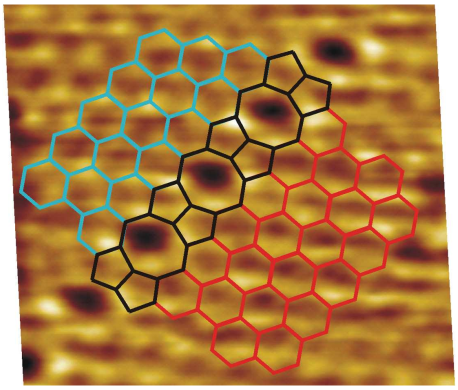

Figure 4.1: Scanning tunneling microscopy image of graphene on Ni(111) and the superimposed defect model obtained in the experimental work in Ref. [30].

of domains related by a relative translation, with the GB emerging as the boundary between two such domains. [30] In the case of monolayer BN grown on Ni(111), the same stacking mechanism holds, [34] and the possibility of engineering smaller band gaps in this large-band-gap material by the introduction of this zigzag-direction boundary has been recently considered. [32]

In this work, we introduce a low-energy stoichiometric model for an armchair-direction antiphase boundary (APB) in monolayer BN, [35] based on a structural pattern observed experimentally in irradiated graphene in the form of finite segments of squares and octagons. [36] A very recent experimental work [37], published after we finish our work presented in this chapter, also shows that extended one-dimensional lines formed by a sequence of square-octagon polygons can form in the hexagonal lattice of BN monolayers. The origin of this defect occurs by a reconstruction process after electron bean irradiation, and the obtained structure can be identified by transmission electron microscopy and computational simulations, as shown in Fig.4.2-b and c.

Furthermore, we investigate the electronic properties and compare the stability of the aforementioned zigzag and armchair boundaries in graphene, as well as of nine different models for extended one-dimensional (1D) defects in monolayer BN, including five variations of the zigzag boundary with TDs in the core. The two graphene boundaries are shown in Fig. 4.3, and the nine BN boundaries are shown in Fig. 4.4.

This work was published in The Journal of Physical Chemistry C. Reference: L. C. Gomes, S. S. Alexandre, H. Chacham, and R. W. Nunes. *J. Phys. Chem. C*, **2013**, 117 (22), pp 11770-11779.

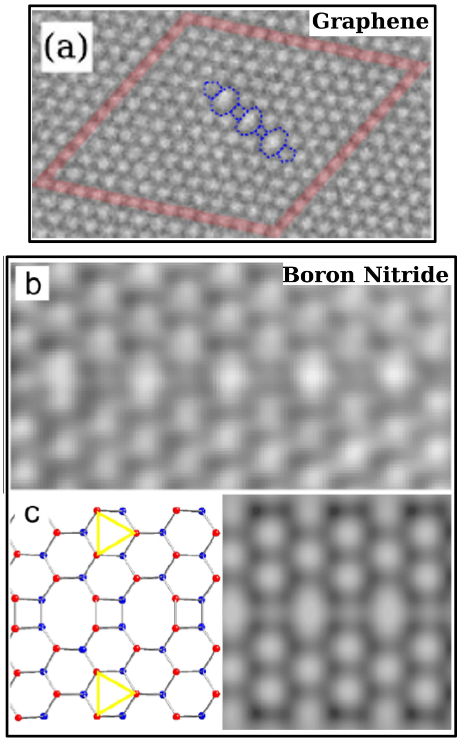

FIGURE 4.2: Transmission electron microscopy image for the finite segment of squares and octagons obtained by electron bean irradiation in graphene in Ref.[36] in shown in (a). By the same process, this defect configuration was also obtained in the form of extended defect lines in BN [37]. In this case, TEM image is shown in (b), with the atomic theoretical model (left panel) and corresponding simulated image in (c).

4.2 GB Models

The translational GB observed in graphene in Ref.[30] is obtained by cutting a graphene sheet along the zigzag direction, displacing the two halves by one-third of the lattice period in the direction perpendicular to the cut, and inserting carbon dimers with their common bond oriented along the cut, generating a line of pentagon-pentagon-octagon units, as shown in the right panel in Fig. 4.3. Being oriented along the zigzag direction, this boundary is labeled Z558 in our discussion. We also examine the armchair-direction counterpart of the Z558 in graphene. This armchair grain boundary, which we label A48, can be obtained by cutting a graphene sheet in the armchair direction and translating one side of the sheet with respect to the other side by half the lattice period along the armchair direction, generating a line defect that contains squares and octagons alternately arranged in its core, as shown in the left panel in Fig. 4.3. Small finite segments of this core structure have already been observed in graphene as result of reconstruction after electronic-beam irradiation. [36] Chiral GB geometries may also be built by combining these two basic structures.

In a binary system like monolayer BN, inversion symmetry is absent and an APB is

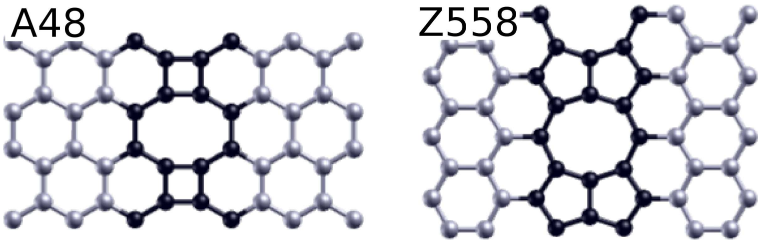

Figure 4.3: Structures of grain boundaries (GB) in monolayer graphene. Left - A48: an armchair-chirality graphene GB with fourfold and eightfold rings in the defect core. Right - Z558: a zigzag-chirality graphene GB with fivefold and eightfold rings in the defect core. Core atoms are drawn as darker circles.

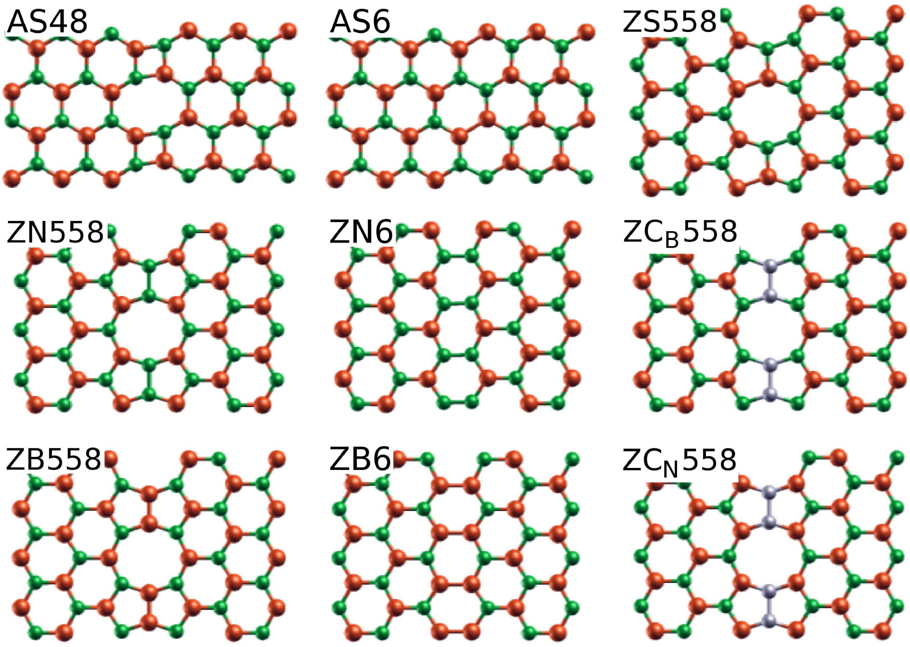

Figure 4.4: Structures of antiphase boundaries (APB) in monolayer boron nitride. Boron, nitrogen, and carbon atoms are shown by orange, green, and grey circles, respectively. Labeling is explained in the text. Top row shows stoichiometric boundaries. Left panel - AS48: armchair chirality with a fourfold and an eightfold ring in the periodic unit of the defect core; [38] middle panel - AS6: armchair chirality with a hexagon in the core; right panel - ZS558 (a GB, not an APB): zigzag chirality with two pentagons and an octagon in the core. Middle row shows nitrogen-rich boundaries. Left panel - ZN558: zigzag chirality with two pentagons and an octagon in the core; middle panel - ZN6: zigzag chirality with a hexagon in the core; right panel - ZC$_B$558: zigzag chirality with two pentagons and an octagon in the carbon-doped core. Bottom row shows boron-rich boundaries. Left panel - ZB558: zigzag chirality with two pentagons and an octagon in the core; middle panel - ZB6: zigzag chirality with a hexagon in the core; right panel - ZC$_N$558: zigzag chirality with two pentagons and an octagon in the carbon-doped core.

formed at the interface of two domains with opposite assignments of the B and N atoms to the two triangular sublattices of the BN honeycomb lattice. In this material, the geometries of the graphene Z558 and A48 translate naturally into APBs. In the present study, we consider a total of eight APB models and one translational GB model in BN. [32] The labeling we adopt for the line defects in BN is based on three features: (i) the chirality of the defect, with armchair(zigzag)-oriented defects denoted by the letter A(Z); (ii) the stoichiometry (i.e., the number of B and N atoms) of the defect core, with stoichiometric cores indicated by the letter S, and boron(nitrogen)-rich cores indicated by the letter B(N); (iii) the types and multiplicities of the polygons present in the periodic unit of the defect core, with each core polygon denoted by the number of its sides.

Hence, the two armchair-oriented stoichiometric APBs, shown in the left and middle panels in the top row in Fig. 4.4 are labeled AS48 and AS6, respectively, while the zigzag-oriented stoichiometric grain boundary (not an APB in this case) in the right panel is labeled ZS558. Generally, the core of zigzag APBs containing odd-membered TDs is either N-rich or B-rich, if one adopts the criterion of minimizing the number of homopolar (N-N or B-B) bonds. We consider two N-rich versions of zigzag boundaries, shown in the middle row on the left and middle panels, labeled ZN558 and ZN6, respectively, with the B-rich ZB558 and ZB6 counterparts shown in the bottom panel. Note that the ZN6 and ZB6 boundaries contain only hexagons in their core. [32] By replacing the B_2 and N_2 dimers with substitutional C_2 dimers in the cores of the ZB558 and ZN558, we obtain the carbon-doped ZC_B558 (N-rich) and ZC_N558 (B-rich) boundaries shown in the right panels of the middle and bottom rows, respectively.

To address all these models, we use supercells that are periodic in the monolayer plane. Very large vacuum regions (∼30-40 Å) are included to impose periodic boundary conditions in the perpendicular direction. We have tested convergence of the structural and electronic properties, as well as of the energetics of the defects, by performing calculations with supercells where distances between the defects and their nearest periodic images in the monolayer plane vary between 10 Å and 19 Å.

4.3 Energetics

4.3.1 Defective Graphene

We seek to compare the relative stability of the above 1D defects in graphene and BN. In the case of graphene, the formation energy of the GBs per unit length E_f^{GB} is given by

$$E_f^{GB} = \frac{E_{tot}^{GB}(N) - N\mu_{graph}^{bulk}}{\ell} \tag{4.1}$$

where $E_{tot}^{def}(N)$ is the total energy of the N-atom supercell containing a GB, μ_{graph}^{bulk} =-154.867 eV is the bulk chemical potential of graphene, obtained as the total energy per atom in a pristine graphene calculation, and ℓ is the length of the supercell along the defect direction.

Our calculated values for E_f^{Z558} and E_f^{A48} in graphene are included in Tab. 1. In this material, the Z558 is more stable than the A48 by 0.25 eV/Å due to the smaller bond-length and bond-angle distortions from the ideal bulk values (d_{bulk} = 1.442 Å and $\theta_{bulk} = 120°$ in our calculations) incurred in the pentagon-pentagon-octagon core of the Z558, when compared with the tetragon-octagon core of the A48. Average bond lengths and bond angles, as well as maximum and minimum values and standard deviations for these quantities are included in Tab. 1 for the Z558 and the A48. While average values are similar for both bond lengths and bond angles, deviations from the bulk reference values are larger in the A48 core.

This indicates that the nature of the energy difference between the A48 and the Z558 in graphene is essentially elastic. Indeed, a Keating-model calculation with a Keating potential fitted for diamond carbon [39] predicts the elastic energy of the A48 to be about twice that of the Z558, in qualitative agreement with our *ab initio* results. A more quantitative agreement would require fitting the Keating potential to the graphene bonding environment.

	E_f	$\bar{d}$	d_{max}	d_{min}	σ_d	$\bar{\theta}$	θ_{max}	θ_{min}	σ_θ
Z558	0.48	1.45	1.48	1.41	0.02	120°	141.7°	104.6°	11.1°
A48	0.73	1.44	1.52	1.40	0.04	120°	147.9°	90°	16.8°

TABLE 4.1: Formation energies (E_f in eV/Å), and average, maximum, minimum, and dispersion values for bond lengths (d in Å) and bond angles (θ) for zigzag and armchair grain boundaries in graphene.

4.3.2 Defective BN.

In BN, the lack of inversion symmetry means that in a periodic supercell calculation for non-stoichiometric boundaries, such as the ZN558 and its ZB558 partner [and the (ZN6,ZB6) and (ZC_B558,ZC_N558) pairs as well, both boundaries are included in the periodic cell, hence only the sum of the formation energies of the two 1D defects can be extracted from such calculation. Formation energies of individual boundaries can be obtained by using BN ribbons, containing a single boundary in the middle and hydrogen-saturated edges. The ribbons are finite in the direction perpendicular to the 1D boundary and periodic in the parallel direction. Fig. 4.5(a) shows the BN ribbons employed for the ZN558 calculations, and Fig. 4.5(b) shows the ribbon employed in the AS48 calculations. Similar ribbons are employed for the other line defects in Fig. 4.4, with the corresponding defect in the middle. For all these ribbon geometries, the distance between the line defect in the middle of the ribbon and the ribbon edges varies between 13 Å and 20 Å. With these sets of parameters, we achieve convergence of energy differences between the defects within ~2 meV/Å.

Stoichiometry is determinant for the stability of the various APBs in BN, since the chemical potentials of the B and N species will depend on the growth conditions, i.e., on the sources of B and N atoms in the synthesis process. In our calculations, supercells are stoichiometric, but the formation energies of the BN ribbons depend on the ribbon stoichiometry and is thus a function of the chemical potentials for B, N, and H. Hence, we must adopt a procedure to extract meaningful APB formation energies from the ribbon calculations, as follows.

Assuming that defect formation occurs in equilibrium with a bulk BN monolayer, we impose that $\mu_B + \mu_N = \mu_{BN}$, where μ_{BN} is the total energy per BN pair for a pristine BN monolayer, and explore the APB formation energy E_f^{APB} as a function of μ_B and μ_N, by considering two limiting chemical potential environments: in a B-rich scenario a gas-phase source of B atoms is available, thus the value of μ_B is obtained from the total energy of this B-rich molecular gas, and we consider BN bulk as the source of N atoms in the synthesis process. Conversely, in the N-rich case an N-rich gas source is employed for the calculation of μ_N, and BN bulk provides the chemical potential for B atoms. In the following, we discuss the stability of the 1D defects for an interval of chemical potentials defined by these limiting values that includes the chemical potentials associated with other molecular sources, and also solid-state sources of B and N atoms.

Thus, we define the following limiting values for the chemical potentials: in the N-rich limit we consider the obvious choice, the gas-phase N_2 molecule as the source of N atoms, and in the B-rich limit we consider the BH_3 gas as the source of B atoms. The latter choice is justified since reaction of ammonia (NH_3) with borane (BH_3) yields ammonia-borane (H_3NBH_3), a molecule that is commonly used in the synthesis of BN nanostructures. [6, 20, 40–42] Choosing μ_N as the independent variable, we write:

$$\begin{aligned}
&\mu_N + \mu_B = \mu_{BN} = -350.190 \text{ eV} \; ; \\
&\mu_N^{max} = \frac{E_{tot}^{N_2}}{2} = -270.159 \text{ eV} \quad (\mathrm{N-rich}) \; ; \qquad (4.2)\\
&\mu_N^{min} = \mu_{BN} - E_{tot}^{BH_3} + \frac{3E_{tot}^{H_2}}{2} = -274.177 \text{ eV} \quad (\mathrm{B-rich}) \; ;
\end{aligned}$$

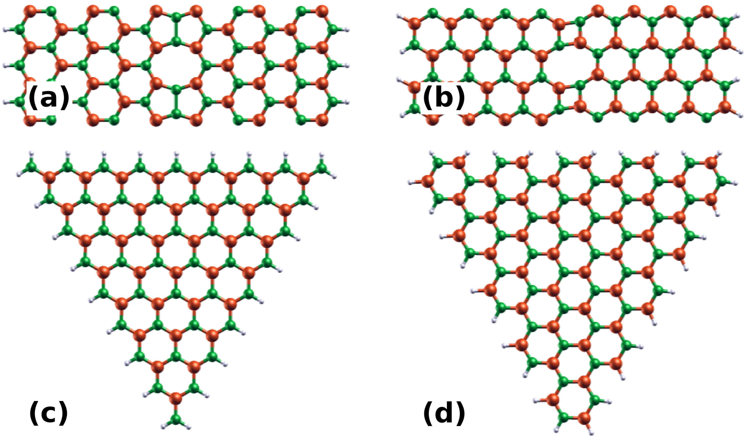

FIGURE 4.5: Ribbon and triangle geometries for computation of line-defect energies in monolayer boron nitride. (a) Ribbon with nitrogen-rich zigzag antiphase boundary in the middle and nitrogen-terminated zigzag edges. (b) Ribbon with stoichiometric armchair boundary in the middle and armchair edges. (c) Triangle with the same nitrogen-terminated zigzag edges as ribbon in (a). (d) Triangle with the same stoichiometric armchair edges as ribbon in (b).

where E_{tot} is the total energy of the molecule indicated, and the H_2 gas is used for the computation of μ_H.

In the following discussion, we show that the interval of μ_N values defined above includes the chemical potentials for two other B-rich environments, the solid-state α-B crystal and the gas-phase diborane molecule (B_2H_6), as well as the N-rich environments associated with the gas-phase ammonia molecule (NH_3) and the N_2 crystalline phase of nitrogen. Diborane is chosen since it reacts with ammonia to yield borazine ($B_3N_3H_6$), a molecular source that is also commonly employed in the synthesis of BN nanostructures. [34, 40]

We emphasize that the range of values for μ_B and μ_N we consider in Eq. 2 is determined for a condition of equilibrium with the monolayer phase of BN and with gas-phase or solid-state sources of N (in the N-rich case) or B (in the B-rich case). Since chemical potentials from liquid sources of these atoms should fall between these limits, we believe that our chemical potentials are representative of realistic sources of B and N in the synthesis of BN nanostructures. These physical constraints, previously considered in calculations of defects in bulk BN, [43] BCN monolayers, [44] BN fullerenes, [45, 46] and BN nanocones, [47] have not been considered in a recent calculation of the energetics of the edges of BN triangular islands. [48] As shown in the following, the determination of physically acceptable ranges for μ_N and μ_B is crucial to determine which extended-defect or edge structure is the most stable under N-rich, intrinsic, or B-rich conditions. Hence, comparison of our results for edge energies with those in ref 27 is fruitless, since no naturally available sources of B and N atoms would provide chemical potentials in the range considered in that work.

Given the limiting chemical potentials in Eq. 2, we define the formation energy of the BN ribbons E_f^{rib}, which includes the formation energies of the APB and of the edges, as follows:

$$E_f^{rib} = \frac{E_{tot}^{rib} - N_B\mu_B - N_N\mu_N - N_H\mu_H}{\ell} \tag{4.3}$$

$$E_f^{rib} = E_f^{APB} + 2E_f^{edge}. \tag{4.4}$$

where E_{tot}^{rib} is the calculated total energy of the ribbon, ℓ is the length of the ribbon along the APB direction, N_B, N_N, and N_H are the numbers of boron, nitrogen, and hydrogen atoms in the ribbon, and μ_B, μ_N, and μ_H are the respective chemical potentials.

In order to obtain E_f^{APB} from Eq. 4.4 above, we follow the procedure from ref 27 and consider BN triangles in which the three hydrogen-saturated edges are the same as those in the corresponding ribbons, as shown in Fig. 4.5. The formation energy of an N-atom triangle $E_f^{\triangle}$ is defined similarly to Eq. 4.3, and can be decomposed into three components: a bulk one that scales with the area of the triangle ($\propto N$), an edge one that scales with the edge length ($\propto N^{1/2}$), and a vertex component that does not scale with the size of the triangle. Since the bulk of the triangles is composed of BN units, and BN bulk is our reference chemical potential (c.f. Eq. 2 and 4.3), the bulk component of $E_f^{\triangle}$ vanishes by definition. It is then possible to obtain the edge energy per edge unit, by considering triangles of different sizes, and fitting $E_f^{\triangle}$ to a linear form:

$$E_f^{\triangle} = \lambda_f^{edge} n_{edge} + E_f^{vtx} \ ; \tag{4.5}$$

where λ_f^{edge} is the edge energy per edge unit, n_{edge} is the number of edge units in the triangle, which for zigzag-edge triangles and ribbons is the number of N (B) atoms saturated with one hydrogen in Fig. 4.5, and for armchair-edge triangles and ribbons is the number of boat-like BN units at the edges. With these definions we have $E_f^{edge} = \lambda_f^{edge} n_{edge}$. E_f^{vtx} is the contribution from the three vertices of the triangles.

The fittings we obtain for the energies of the triangles shown in Fig. 4.5(c), with B-rich zigzag edges (ZB-edge), and for the triangles with N-rich zigzag edges (ZN-edge), under the limiting B-rich and N-rich environments, are shown in the left and middle panels of Fig. 4.6, respectively. From the slope of the curves in Fig. 4.6 we obtain the ZN-edge and ZB-edge energies included in Tab. 4.2. In order to check the consistency of our approach, we also compute the edge energy for triangles shown in Fig. 4.5(d) with stoichiometric armchair edges (AS-edge), and E_f^{AS48} from Eq. 4.4, for the ribbon containing an AS48 and armchair edges, shown in Fig. 4.5(b). The fitting of the energies of the armchair-edge triangles is shown in the right panel in Fig. 4.6. The AS-edge is stoichiometric,

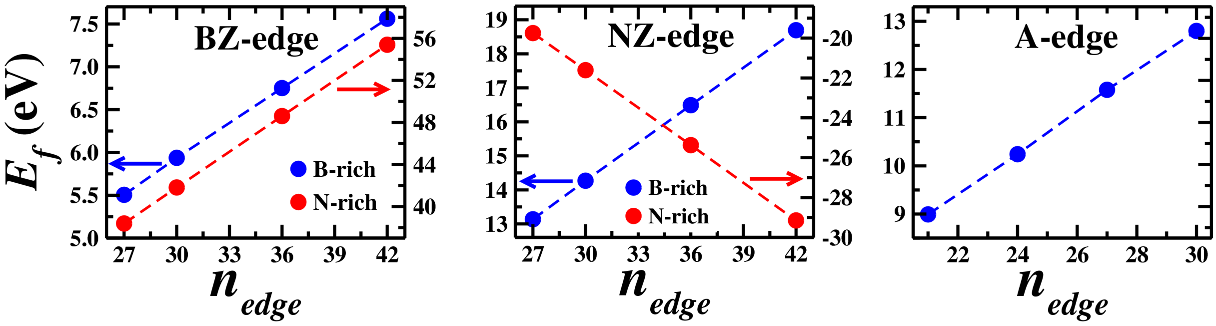

FIGURE 4.6: Formation energy of BN triangles as a function of the number of edge units. The left (middle) panel shows the energies of the triangles with boron-terminated (nitrogen-terminated) zigzag edges [ZB-edge (ZN-edge)], under the limiting N-rich and B-rich environments. The right panel shows the energy of the stoichiometric armchair AS-edge.

hence its energy (0.45 eV/edge-unit) is independent of the B and N chemical potentials.

	λ_f^{edge}(eV)					
	B-rich			N-rich		
	BH_3	B-bulk	B_2H_6	NH_3	N-bulk	N_2-gas
ZB-edge	-0.18	0.16	0.18	0.67	1.11	1.15
ZN-edge	0.73	0.36	0.36	-0.13	-0.59	-0.63

TABLE 4.2: Edge energy per edge unit λ_f^{edge} from fitting of triangle energies to Eq. 5, for the N-rich zigzag edge (ZN-edge), and the B-rich zigzag edge (ZB-edge), for different values of N-rich and B-rich chemical potentials.

It is worth commenting on the negative slope of E_f which implies a negative value of λ_f^{edge} for the ZN-edge, under the limiting N-rich environment. It indicates that the reaction by which hydrogen saturates the edge is exothermic and is consistent with experimental observations of a very high stability for N-terminated zigzag edges in BN islands. [40, 49, 50] In Tab. 4.2, we also include the values of the edge energies for different environments, obtained from different N-rich and B-rich sources. Note that $\lambda_f^{ZN-edge}$ is negative under N-rich conditions, regardless of the source of N atoms. Indeed, the strong tendency of BN patches to display a triangular shape with ZN-edges, observed experimentally, must be connected with this "across-the board" robust stability of the ZN-edges for a wide range of N-rich chemical potentials. On the other hand, our calculations also suggest that stable B-terminated zigzag edges may also form, although under a much more restrictive control of a B-rich environment. More specifically, should the synthesis of BN islands take place in a B-rich environment, with BH_3 as the source of B atoms, the relatively low stability of B atoms in this molecular system could lead to stabilization of ZB-edges, as indicated by the negative slope of the energy curve for ZB-edge triangles under a BH_3-rich environment, in our calculations. Hence, stabilization of a ZB-edge,

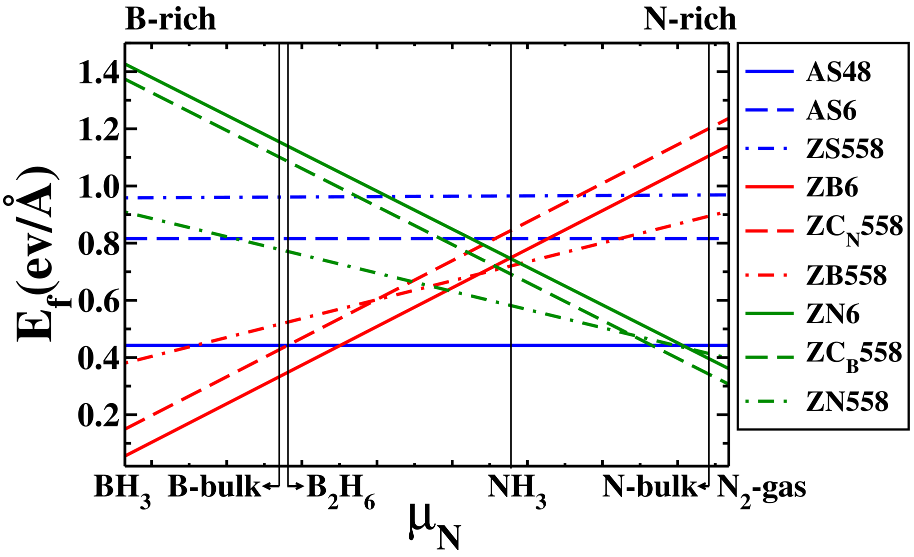

FIGURE 4.7: Formation energy E_f of grain boundaries and antiphase boundaries in boron nitride as a function of the nitrogen chemical potential μ_N. The maximum and minimum values of μ_N are given in the text (see Eq. 2). Vertical lines indicate the values of μ_N for different molecular and solid-state sources of N-rich and B-rich environments.

although less robust than the ZN-edge case, is possible by a proper choice of a B-rich environment.

Having obtained E_f^{edge} from the above procedure, we can obtain E_f^{APB} from Eq. 4.4. The results for the eight APB models, as well as E_f^{ZS558} for the ZS558 GB in BN, as functions of μ_N, are shown in Fig. 4.7. For the stoichiometric models E_f^{APB} is independent of μ_N. The consistency of the procedure outlined above is attested by the fact that E_f^{APB} values obtained using supercells and the H-terminated ribbons agree to within 0.6% in all cases, as included in Tab. 4.3. Note that for the non-stoichiometric defects we compare the sum of the energies of individual defects, obtained with the ribbons, with the summed energies of two partner defects, obtained with the supercells.

In Fig. 4.7, the vertical lines indicate three different values of μ_N corresponding to B-rich environments, and three corresponding to N-rich ones. This figure shows that, at zero temperature, the AS48 is the most stable boundary in the intrinsic range of chemical potentials we consider (the central portion of the interval of chemical potentials), while the ZN6 becomes the most stable defect in the N-rich limit of μ_N, and the ZB6 is the most stable in the B-rich end of the chemical potential interval. Furthermore, in the presence of a carbon source, the ZC_B558 becomes the most stable boundary in the N-rich limit of μ_N.

From a thermodynamical point of view, Fig. 4.7 indicates that several different boundaries may coexist in the temperature range of ~900-1500 K, where synthesis of BN and carbon nanostructures is usually performed. [6, 34, 40] Thermal fluctuation energies at these temperatures are in the range of ~120-190 meV/atom. Let us look first at the N-rich region in Fig. 4.7, where four boundaries are close in energy: the $\mathrm{ZC_B}558$, the ZN6, the ZN558, and the AS48 are within 70-80 meV/atom of each other, after we convert the energies in Tab. 4.3 to energies per atom at the core, [38] which indicates that the four boundaries (three in the absence of carbon sources) should coexist in thermal equilibrium. For the B-rich region in Fig. 4.7, we have two scenarios: (i) in the B-rich limit of the μ_N interval, the $\mathrm{ZC_N}558$ is only 44 meV/atom higher in energy than the ZB6, and the two boundaries should coexist, provided that a source of carbon dopants is present in the synthesis process; (ii) for an interval around the values of μ_N corresponding to the α-B and B_2H_6 environments, the ZB6, the $\mathrm{ZC_N}558$, the AS48, and the ZB558 have formation energies within 41 meV/atom of each other, indicating coexistence of the four boundaries when either of these systems is used as a source of B atoms.

We can gain a qualitative understanding of the energetics of the BN boundaries. From the geometries, we expect that the elastic-energy cost of the AS48 should be even higher than that for the A48 in graphene, because in BN the bond angles at the core of the defect depart even more strongly from the ideal bulk value of 120° than in graphene, as can be seen in Figs. 4.3 (left panel) and 4.4(top-left panel). Unlike the case in graphene, however, BN strongly prefers even-membered topological defects in order to avoid the energetically expensive homopolar bonds, except under the limiting chemical potential environments, where N-N or B-B bonds become more favorable. [45]

We can use a combination of two models to understand qualitatively the ordering of E_f values in Fig. 4.7. The idea is to divide the contributions to the formation energies of the boundaries in two components, an elastic one E_{el}, which we estimate by employing a Keating potential fitted for cubic BN, [51] and a chemical energy E_Q that is computed using the bond-energy model developed in Ref. [44] to account for the energetics of CBN sheets of various stoichiometries. In this latter model, two-atom bonds are assigned bond-energy values, which reflect the average energy of each type of bond across the various BCN sheets included in the fitting procedure.

The bond-energy values derived in Ref. [44] are $\varepsilon_{CC} = -103.24$ eV, $\varepsilon_{BN} = -116.73$ eV, $\varepsilon_{CN} = -141.67$ eV, $\varepsilon_{BB} = -50.40$ eV, and $\varepsilon_{NN} = -178.49$ eV, for carbon-carbon, boron-nitrogen, carbon-nitrogen, boron-boron, and nitrogen-nitrogen bonds, respectively. Within the model, the values of E_Q for one period of either the AS6 or the ZS558, the sum of E_Q values for one period of the ZN558 and the ZB558, as well as the sum for one period of the ZN6 and ZB6 should all be ~4.57 eV higher than the value for the AS48, i.e., $E_Q^{AS6} = E_Q^{ZS558} = E_Q^{(ZN558+ZB558)} = E_Q^{(ZN6+ZB6)} = E_Q^{AS48} + 4.57$ eV. Using the BN Keating potential from Ref. [51], we compute the values of E_{el} for the seven boundaries. Results for E_{el}, E_Q, and $E_f = E_Q + E_{el}$ for the AS48, AS6, ZS558,

Boundary	supercell	ribbon
AS48	0.44	0.44
AS6	0.82	0.82
ZS558	0.96	0.97
ZN558 + ZB558	1.29	1.29
ZN6 + ZB6	1.48	1.48
$ZC_B558 + ZC_N558$	1.53	1.52
Ribbon results for individual boundaries		
Boundary	B-rich (BH_3)	N-rich (N_2-gas)
ZB558	0.38	0.89
ZN558	0.91	0.40
ZB6	0.05	1.12
ZN6	1.43	0.36
ZC_N558	0.15	1.21
ZC_B558	1.37	0.31

TABLE 4.3: Comparison of formation energy values E_f of grain boundaries and antiphase boundaries in monolayer BN computed with supercells and ribbon geometries. Supercells are stoichiometric and corresponding E_f values do not depend on chemical potentials of B and N. Supercells for non-stoichiometric boundaries contain the pair of partner boundaries indicated. In the top part of the Table, the sum of the E_f values obtained for the two boundaries using the ribbons is given for comparison with supercell results. Values for the individual non-stoichiometric boundaries, computed with the ribbons, are given in the bottom part of the Table, for the limiting N-rich and B-rich environments.

and the sum of the values for the ZN558 and ZB558, and for the ZN6 and ZB6, computed using this scheme, are included in Tab. 4.4.

Boundary	E_Q(eV/Å)	E_{el} (eV/Å)	E_f(eV/Å)
AS48	0.00	1.02	1.02
AS6	1.05	0.18	1.23
ZS558	0.91	0.70	1.61
ZN558 + ZB558	0.91	1.08	1.99
ZN6 + ZB6	1.82	0.57	2.39

TABLE 4.4: Formation energy of grain boundaries and antiphase boundaries in monolayer BN from combination of elastic energy and chemical-bond energy models.

As shown in Tab. 4.4, this simplified partition of E_f appears to overestimate the elastic-energy cost of the AS48 boundary, but it correctly predicts, at a qualitative level, the ordering of the energies of the other six BN defects in Tab. 4.4 (the energies of the stoichiometric boundaries must be multiplied by two, for a proper comparison). This modeling is useful because it allows us to establish that E_Q is the predominant factor in determining the relative stability of the various boundary models in our study. Note the very low value of E_{el} for the AS6 and the (ZN6,ZB6) pair, with cores consisting of hexagons only, which is offset by the high energy cost of two “wrong” bonds per defect unit in the core. On the other hand, the highest value of E_{el} is found for the AS48, being associated with the strong departure from the bulk bond lengths and bond angles in the fourfold and eightfold rings at the core of this boundary. However, this is compensated by the fact that the chemical energy cost for the AS48 is very low ($E_Q^{AS48} = 0$, within the simplified bond-energy model above).

Again, a quantitative agreement between the above modeling and the *ab initio* results would require fitting both the Keating potential and the bond-energy model to bonding environments that are more similar to those in the boundary geometries in our study. This analysis also provides a qualitative explanation for one of the ingredients that determines the stability of the carbon-doped ZC_B558 boundary: because this structure is obtained from the ZB558 by replacing the B_2 dimer in the center of the defect core with a C_2 dimer, the elastic energy is reduced because the length of the C-C bonds is similar to the length of the BN bulk matrix, unlike the longer B_2-dimer bond. The other ingredient is electronic, and is determined by stoichiometry (i.e., the chemical potentials) and the fact that in low coordination bonding environments a B-B bond is generally less favorable than a C-C bond, except in very B-rich environments.

4.4 Electronic Properties: Band Structure and Density of States of defective graphene and h-BN.

4.4.1 Defective Graphene: A48 and Z558 boundaries.

Let us now examine the electronic structure of the graphene boundaries. The electronic structure of the Z558 in graphene has been discussed in Ref. [31], where the appearance of a highly-localized quasi-1D state, introduced by this boundary in the density of states (DOS) of graphene, has been shown to lead to a magnetic instability. [The Z558 is labeled $\mathrm{GB}(2,0)|(2,0)$ in the notation employed in Ref. [31].] Figs. 4.8(b) and (d) show the electronic band structure and the DOS for the A48 in graphene, and the DOS for the Z558 is shown in Fig. 4.8(c) for comparison. The Brillouin zone corresponding to all defect supercells in this work is shown in Fig. 4.8 (a). The Γ-X and Y-L lines are parallel to the defect direction (the x-axis of the supercell) in all cases. In order to identify the boundary-related electronic bands, and also to examine the degree of localization of the corresponding states on the core of the boundaries, we project the DOS onto the orbitals centered on the core atoms in each case. The core atoms for each defect geometry are shown by darker circles in Fig. 4.3, and we use the same definition of defect core for the graphene and BN boundaries.

From the A48 band structure, we can see that this boundary introduces only small electron and hole pockets near the Fermi level (FL), that show as two weak resonances

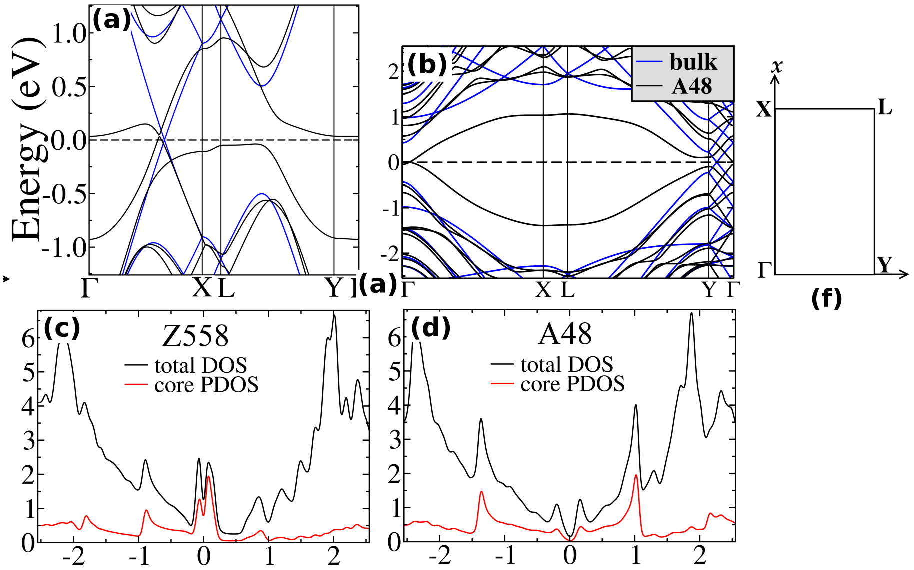

FIGURE 4.8: Band structure and density of states (DOS) for the A48 and Z558 in graphene. Black curves show the (a) Z558 and (b) A48 supercell band structure while the blue curves show bulk bands folded onto defect supercell. (c) and (d) show total DOS and the projected DOS (PDOS) for the core atoms for the Z558 and A48, respectively. (f) The Brillouin zone corresponding to the supercell calculations in the present study.

within ±0.2 eV from the FL in the DOS. The degree of localization of these electronic states on the eight atoms located at the A48 core is much weaker than what is found for the magnetic resonance in the Z558 case. [31] In the latter case, nearly 90% of the DOS derives from the ten core atoms. This is shown by the partial DOS (PDOS) for the core atoms as red curves in Fig. 4.8(b) and (d). In the A48 case, these resonances are much more spread out into the bulk of the cell, and the contribution from the core atoms is much smaller than in the Z558. The A48 also gives rise to stronger resonances at ±1.0 eV from the FL, connected to the flat portion of the defect bands seen in the band structure in Fig. 4.8(b)].

4.4.2 Defective h-BN: AS48, ZN558, ZB558, ZN6, ZB6, ZC_B558, and ZC_N558 boundaries.

In the case of BN, we concentrate on the AS48, ZN558, ZB558, ZN6, ZB6, ZC_B558, and ZC_N558 boundaries. In Fig. 4.9(a) and (b) we show the band structure and the density of states (DOS) for a pristine bulk BN monolayer. For ease of comparison, the bulk calculation was performed for a supercell of nearly the same dimensions as those employed for the BN boundaries. For our discussion, the important features of the bulk electronic structure are the size of the gap (∼4.7 eV within the GGA-DFT scheme) and the composition of the electronic states at the band edges: the top of the valence band

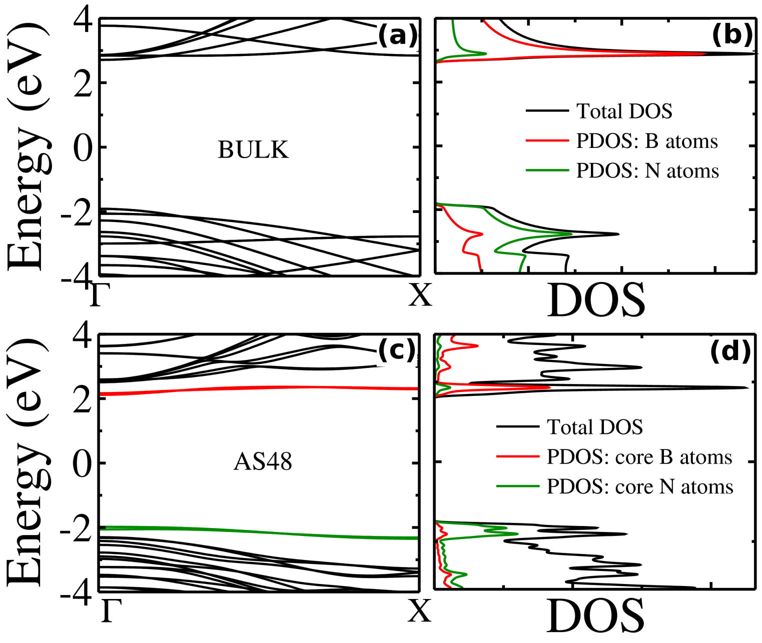

FIGURE 4.9: Band structure and DOS for bulk BN and the AS48 boundary. The contribution of the core-atom orbitals to the total DOS is shown by green (N orbitals) and red (B orbitals) PDOS curves. Defect-related bands are colored according to the dominant orbital contribution. (a) Band structure and (b) DOS for bulk BN. (c) Band structure and (d) DOS for the AS48 in BN.

is mainly composed of nitrogen p_z orbitals while the bottom of the conduction band derives from the boron p_z orbitals.

AS48: The electronic bands and the corresponding DOS for the AS48 are shown in Fig. 4.9(c) and (d). The AS48 introduces one set of two bands near each of the band edges, that show little dispersion and retain the character of the corresponding parent bulk bands. The acceptor bands near the valence-band maximum (VBM) are composed primarily of nitrogen p_z orbitals, while the donor bands near the conduction-band minimum (CBM) consist of boron p_z orbitals, with ~40% of the DOS concentrated on the core atoms in both cases, as shown by the core-projected PDOS curve in Fig. 4.9. Both sets of bands are shallow (~0.2 eV split from the corresponding band edges), and the lack of sizeable dispersion indicates very large effective masses and low mobilities of carriers, should doping of A48 defect bands become feasible.

The ZN558, ZB558, ZN6, ZB6, $\mathrm{ZC_B}$558, and $\mathrm{ZC_N}$558 defects display much richer electronic structures. Generally, we can see in Figs. 4.10, 4.11, and 4.12 that these boundaries introduce much deeper defect bands into the gap of the BN bulk, resulting in a much larger reduction of the electronic band gap in the spatial region surrounding either the ZN558 or the ZB558 [32] than in the case of the AS48. Moreover, the dispersions for these bands in the direction of the defect are much larger, indicating carrier with potentially larger mobilities than in the AS48 states. Furthermore, the defect-related bands for these boundaries are strongly localized on the core of the defects, and enhanced correlation effects (beyond the scope of this work) related to quasi 1D states are to be expected for these electronic states.

ZN558 and ZB558: The bands and DOS curves for the ZN558 and ZB558 boundaries are shown in Fig. 4.10. In the band-structure plots, defect bands are colored by their dominant atomic contribution, with the same color coding indicated in the PDOS plots. In this case, because supercell calculations include the two boundaries, we identify the bands associated with each defect by projecting the DOS curves onto the atoms at the core of each defect individually. The consistency of this procedure for the present systems can be checked by comparison with the electronic structures of the ribbons, that contain only one of the defects. In Fig. 4.10, the electronic states for both the supercell and ribbons are shown for comparison, with the ZB558 states shown of the two plots on the top and the ZN558 states on the bottom. For the ribbons, the electronic states characteristic of the edges are indicated by an orange-curve in the PDOS plots. An observation from the ribbon plots is that the electronic states associated with the edges of the ribbon are either shallow or resonant with the bulk bands, and do not mix with the defect bands in the gap, as can be observed in the PDOS plots. Thus, we can directly verify that the electronic structure we obtain from the supercell calculation is very consistent with a superposition of the corresponding states from the ribbons for each boundary, in the range of energies of the defect gap states shown in Fig. 4.10. The same is true for the (ZN6,ZB6) and (ZC_B558,ZC_N558) supercells, but for conciseness, below we only show the electronic structure obtained from the supercell calculations.

ZB558: The electronic structure of the ZB558 is shown in the top panels in Fig. 4.10. Because boron-boron bonds tend to be much longer than the other bonds in these BN systems, the ZB558 introduces a large compressive strain in its neighborhood, and we observe three defect bands connected with this boundary. Starting from the lower part of the gap, we observe a shallower band with an extended van Hove singularity connected to a large flat portion of this band, starting at the Γ point and extending up to the k-point at ∼0.6 of the Γ-X line, after which it disperses down and mixes with the bulk states, when reaching the X point at the edge of the one-dimensional BZ. This band derives primarily from the orbitals of the N atoms located on the BN zigzag chains in the core of the ZB558 (∼58% of the total DOS), with smaller contributions from the zigzag B atoms (∼8%), and from the two atoms forming the B_2 dimer at the geometric center of the defect (∼3%).

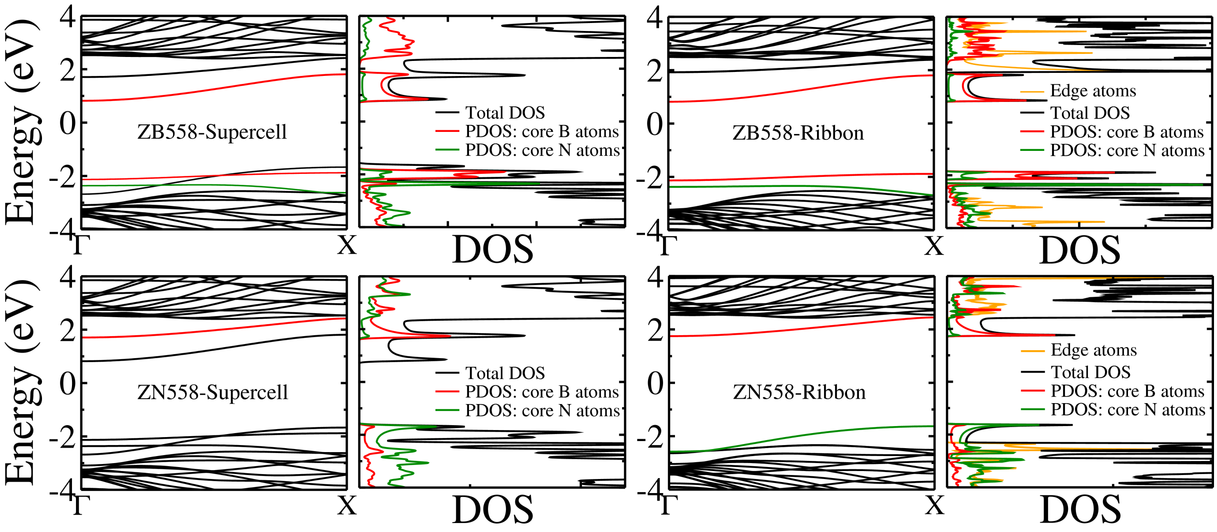

FIGURE 4.10: DOS, PDOS, and band structures along the Γ-X line (parallel to the APB direction) for the ZB558 (top row) and ZN558 (bottom row). Supercell calculations are shown in the left panels and ribbon calculations in the right panels. The contribution of the core-atom orbitals to the total DOS is shown by green (N orbitals) and red (B orbitals) PDOS curves. Defect bands in the gap are shown by green and red curves, according to the dominant atomic-orbital contribution in each case. The DOS features associated to the ribbon-edge states are shown by orange curves in the right panels.

The ZB558 also introduces a deeper flat band lying ∼0.5 eV above the VBM, with a total dispersion of ∼0.2 eV. This band is very strongly localized on the B_2 dimer at the center, with ∼75% of the total DOS deriving from the orbitals of the dimer atoms, with smaller contributions of ∼12% and ∼4% from the N and B atoms on the BN zigzag chains in the core, respectively. The characteristic 1D van Hove singularities associated with the minimum and maximum of this band can be observed in the DOS plot in top right panel in Fig. 4.10.

In the upper part of the gap, the ZB558 introduces a deep dispersive band that lies ∼1.7 eV below the CBM, at the Γ point, and at the X point it reaches its maximum of ∼0.7 below the CBM, for a total dispersion of 1 eV. This band is composed mostly of orbitals of the B atoms at the ZB558 core, with 53% of the DOS coming from the B_2 dimer at the center and 25% from the B atoms on the BN zigzag chains shouldering the B_2 dimer. A smaller contribution of 8% derives from the N core atoms on the zigzag chains.

ZN558: Electronic bands, DOS, and PDOS for the ZN558 are shown in the bottom panels in Fig. 4.10. In the lower part of the gap this boundary introduces a band with a maximum energy of ∼0.7 eV above the VBM, near the edge of the BZ at the X point, that shows a dispersion of ∼1.0 eV. Its minimum is at the Γ point where it becomes resonant and mixed with the bulk states in the VBM region. For most of the Γ-X line of the 1D BZ this band is deep in the gap and strongly localized, with ∼88% of the DOS

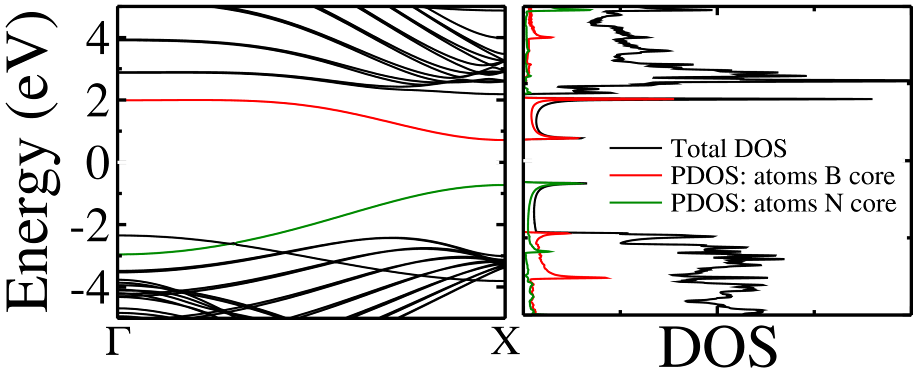

FIGURE 4.11: DOS, PDOS, and band structure along the Γ-X line (parallel to the APB direction) for the ZN6 and ZB6 boundaries, from a supercell calculation. Defect bands in the gap and PDOS curves are shown by green (ZN6 states) and red (ZB6 states) curves, according to the dominant atomic-orbital contribution in each case.

concentrated on the ZN558 core atoms (∼73% on the N core atoms). In the DOS plot, this bands shows a 1D van Hove singularity above the peak corresponding to the VBM.

In the upper part of gap, the ZN558 also introduces a band near the CBM that shows similar characteristics to the above one, being deep in the gap near Γ and becoming shallow and mixed with the bulk states when it reaches the edge of the BZ at the X point. This band is very strongly localized on the B and N atoms along the zigzag chain in the core of the ZN558, with ∼84% of the DOS concentrated on the orbitals of the B atoms and ∼7% on the orbitals of the N atoms. The corresponding 1D van Hove singularity is seen in the DOS plot the bottom right panel in Fig. 4.10.

ZN6, ZB6, ZC$_B$558, and ZC$_N$558: The electronic states of the ZN6, ZB6, ZC$_B$558, and ZC$_N$558 show similar patterns. The ZN6 and ZB6 states are shown in a single plot in Fig. 4.11. The ZN6 (ZB6) introduces a band of deep states in the gap, which is strongly localized on the two N (B) atoms that bond to each other across the boundary, as shown by the PDOS plots. As found in Ref. [32] introduction of such defects leads to large reductions of the gap for the electronic states in the region of the defects. Besides the deep band in the gap, the ZB6 also introduces a localized band that is resonant with the bulk bands at the top of the valence bands.

For the ZC$_B$558, and ZC$_N$558, we show the supercell states projected onto the B, N, and C atoms at the core of the ZC$_B$558 (ZC$_N$558) in the top (bottom) panel. In the ZC$_B$558 case, we observe the appearance of two bands that are reminiscent of those of a one-dimensional dimerized chain of carbon atoms, with a gap of ∼2.6 eV at the Brillouin zone edge, and dispersions of ∼1.0 eV (0.6 eV) for the lower (higher) band. The higher band is derived equally from C and B orbitals, while the lower band is dominated by the C orbitals, but with sizeable contributions from B and N orbitals. Both bands are

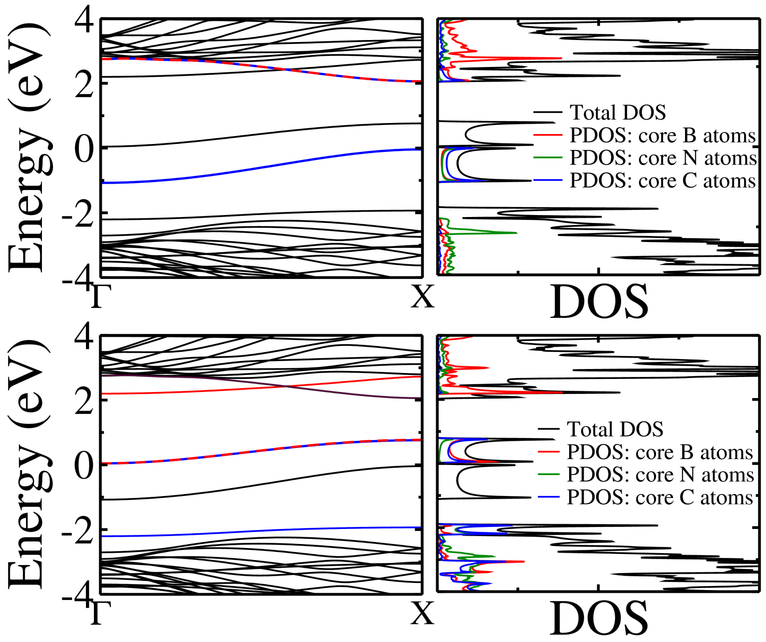

FIGURE 4.12: DOS, PDOS, and band structures along the Γ-X line (parallel to the APB direction) the ZC_B558 (top row) and ZC_N558 (bottom row) boundaries, from a supercell calculation. Contributions of the core-atom orbitals to the total DOS are shown by blue (N orbitals), green (B orbitals), and red (C orbitals) PDOS curves. Defect bands in the gap are shown by green, red, and blue curves, according to the dominant atomic-orbital contribution in each case.

strongly localized on the defect core, with 78% and 88% of the total DOS deriving from the core-atom orbitals.

For the ZC_N558, we identify three defect-related bands: (i) a shallow band near the top of the bulk valence bands with 80% of its DOS concentrated of the core atoms (mostly on the N and C atoms); (ii) a very strongly-localized band deep in the band gap, with a dispersion of 0.75 eV, that derives 95% of its DOS from the C and B atoms a the core; (iii) and a band near the bottom of the bulk conduction bands, localized on the B atoms at the core.

4.5 Conclusions

In conclusion, our calculations indicate that the relative stability of antiphase boundaries (APB) with armchair and zigzag chiralities in monolayer boron nitride (BN) is strongly dependent on the B and N chemical potential conditions (emulating the corresponding synthesis conditions). An interval of realistic boron and nitrogen chemical potentials values is considered, ranging from gas-phase to solid-state sources of B and N. At zero temperature, a stoichiometric armchair APB with a tetragon and an octagon in its core unit, and no “wrong” (B-B or N-N) bonds, is found to be the most stable boundary in the intrinsic region (the central part) of the chemical-potential range considered, while in the nitrogen-rich (boron-rich) end of the chemical potential interval, a zigzag-oriented boundary with a core consisting of hexagons only, containing N-N (B-B) bonds across the boundary line is found to be the most stable. Zigzag boundaries with a core structure consisting of two pentagons and an octagon, containing N-N or B-B bonds, are also considered, both in undoped and carbon-doped forms. Our *ab initio* results indicate that at the typical range of temperatures of BN-nanostructure synthesis experiments, several of these boundaries with zigzag chiralities should coexist with the stoichiometric armchair one under N-rich and B-rich conditions. Such stability transition as a function of B and N chemical potentials is shown to arise from a competition between "wrong-bond" (homopolar B-B and N-N bonds) and elastic-energy costs at the core of the APBs. This is contrasted with analogous cases of extended defects in graphene, where the geometry with pentagonal and octagonal rings is the most stable.

Regarding the electronic properties of the defects, we find that in monolayer BN the armchair APB introduces shallow flat bands near the bulk band edges which are weakly confined to the defect core, while the B-rich, the N-rich, and the C-doped zigzag APBs lead to the formation of electronic bands that are deep in the bulk band gap and strongly localized on the atoms at the defect core. In the case of graphene, the armchair GB introduces weaker resonances near the Fermi level (FL), associated to defect states that are only partially confined to the defect core, in contrast with the strongly localized states characteristic of the zigzag GB. [31]

Finally, we also report first principles results for the energies of nitrogen- and boron-terminated edges of triangular-shaped islands of BN. One one hand, our results indicating a robust stability for nitrogen-terminated edges, across a wide range of values for the chemical potentials of boron and nitrogen, are consistent with the experimentally-observed tendency of BN islands to display nitrogen-terminated zigzag edges. On the other hand, we predict that fine tuning the chemical potentials with a boron-rich source where boron is in a bonding environment of relatively low stability may lead to the formation of boron-terminated zigzag edges.

Chapter 5

Electronic Properties of Grain Boundaries in Graphene Bilayers.

5.1 Introduction

Achieving control of the transport properties in of is one of the great challenges in nanoscale engineering. The influence of the number of layers of this material on its electronic properties has been a subject of intense study in the recent years. It is well known that the electronic structure of an isolated graphene layer is characterized by linear electronic bands near the **K** points of the Brillouin zone (BZ). This linear character is lost when we introduce a second layer in the so-called Bernal or AB' stacked bilayer graphene (BLG): even though the gap is still null, the dispersion is no longer linear and we observe the emergence of two additional bands in the region of the Fermi level (FL). The BLG is also known to present a gap at the FL when an external electric field is applied perpendicular to the layers plane [52, 53].

By going beyond the Bernal bilayer graphene, a very interesting physics is also observed when two or more graphene layers are stacked with a relative angle between them. In a graphite surface, for example, it is very common the occurrence of a rotation of the top surface layers with respect to the bulk, giving rise to Moiré patterns [54–57]. The interlayer registry, defined by the type of stacking or by the relative angle of twist, can have a dramatic influence on the electronic properties of this material. As an example, for BLG with a small twist angle between layers, it has been observed[54] that, contrary to what happens in an AB' stacked bilayer, the low energy dispersion is linear, as in a single layer, but the Fermi velocity can be significantly reduced in comparison to the single-layer. It is also observed that an external electric field, perpendicular to the layers, does not open an electronic gap in this case.

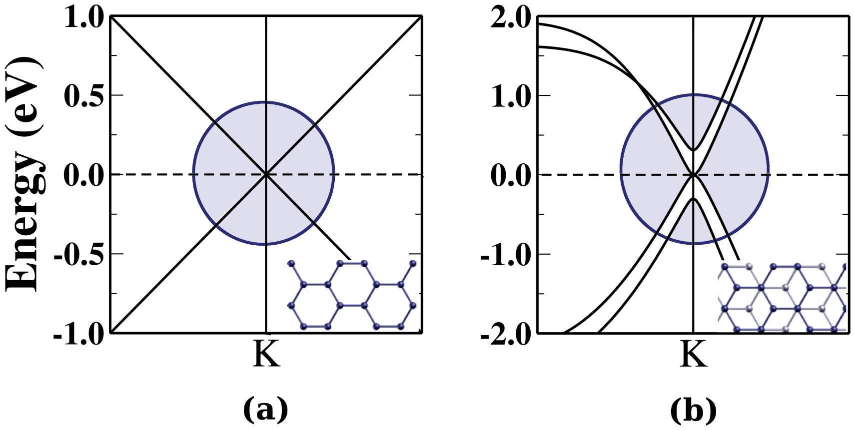

FIGURE 5.1: Electronic bands at the **K** point in the BZ for (a) graphene monolayer and (b) AB' stacked graphene bilayer: the linear character of the bands in monolayer is lost with the introduction of the second layer, giving rise to doubled bands with parabolic dispersion around the Fermi level.

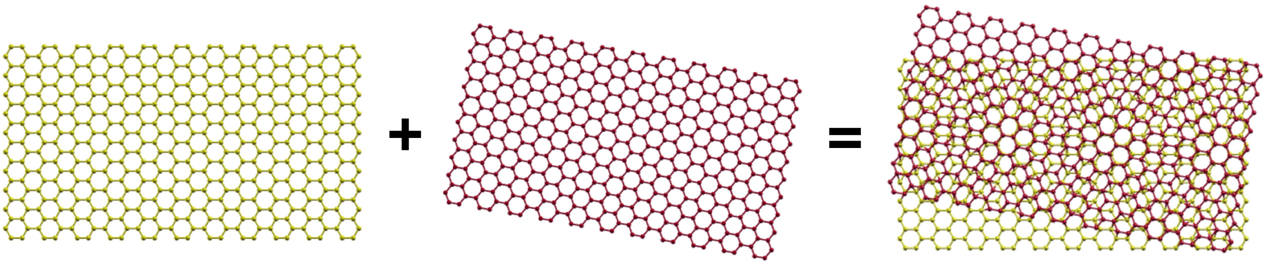

FIGURE 5.2: Moire pattern formed by relative rotations between graphene layers. For different angles of rotation θ, a characteristic physics is observed in the electronic properties of this material.

The attempt to control the electronic properties at the nanoscale has also been considered with the introduction of defects. As discussed in Chapter 4, extended line defects in graphene and Boron Nitride have been investigated in many different works, with interesting results.

In a recent theoretical work[31], Simone et. al, employ *ab initio* calculations to address the confinement of electronic states due to the introduction of a particular extended line defect formed by a translational grain boundary (GB). It is shown that such defect introduces a sharp resonance just above the FL in the density of states of graphene, indicating a strong confinement of such states on the core of the defect.

In the same work, the introduction of different tilt GBs is also considered in graphene, and the corresponding modifications on the electronic structure due to these defect lines are also discussed. While the translational GB introduces strongly confined states in the DOS, the electronic states due to tilt grain boundaries hybridize with the bulk states and are only partially confined to the defect core.

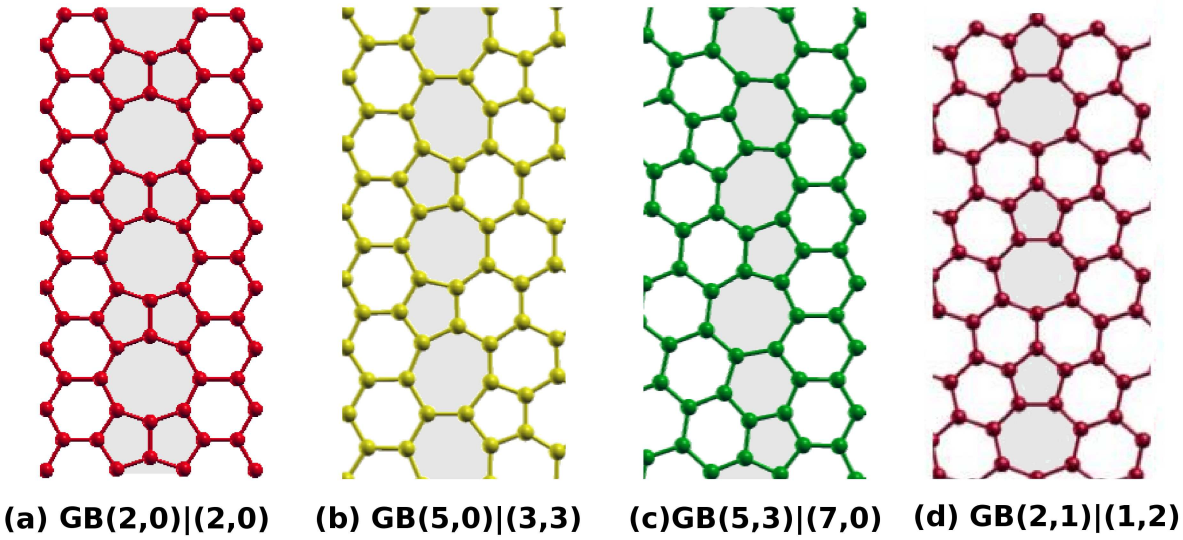

FIGURE 5.3: Geometries of extended one-dimensional periodic defects in graphene, investigated in Ref.[31]; Introduction of GB(2,0)|(2,0) gives rise to magnetic states in graphene. Grain boundaries GB(5,0)|(3,3), GB(5,3)|(7,0) and GB(2,1)|(1,2), introduces electronic states which hybridize with the bulk states and are only partially confined to the defect core.

In this chapter, we review some results and extend the study in Ref. [31] by considering a graphene bilayer with and extended line defect on one layer a top a pristine bottom layer. By *ab initio* calculations, electronic properties of the resulting graphene bilayers, are discussed.

5.2 Double-Layer Graphene: the AB' stacking.

It is well known that graphite is made out of stacked graphene layers that are weakly coupled by van der Walls forces. The simplest and best known use of graphite is in a pencil, possible because when we press it on a sheet of paper, we can easily detach the graphene layers from each other. There are many ways that graphene layers could be stacked up in order to form graphite. However, many theoretical and experimental works indicate that AB' or Bernal stacking have lower energy, being predominant in the formation of the bulk of this material[58–60].

The AB' stacking is defined when a carbon atom of sublattice A in the top layer is positioned directly above a carbon atom of sublattice B' at the bottom layer. Such configuration can be obtained if we consider two graphene layers in the so called AA' stacking, where atoms of the same sublattice are positioned directly above each other at the top and bottom layers, and translate one of the layers by 1/3 of the lattice parameter $\mathbf{a_{ac}}$, along an armchair direction. One alternative way to obtain the Bernal stacking, is by rotating one of the layers in a double layer system initially in an AA stacking, by an angle $\theta = 60°$.

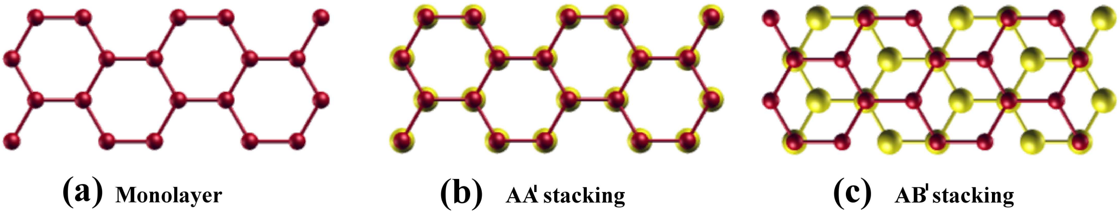

Figure 5.4: (a) The honeycomb structure of graphene monolayer in (a) and the two simplest stackings between two layers: The AA' stacking, in (b), where atoms of the same sublattice in the top and bottom layers are positioned directly above each other. The AB' stacking, in (c), is formed when sublattice A in the top layer is placed directly above sublattice B' in the bottom layer.

Despite the fact that the AB' stacking type is the most energetically favorable in bilayer graphene, it is quite common the occurrence of many different stackings, caused by rotation of one of the layers in relation to the other, giving rise to Moiré patterns. The commensurate angles of rotation, and the consequent modifications in the electronic structure of graphene, have been discussed in a vast number of theoretical and experimental [54, 55, 58, 61] works.

Besides the rotation of an entire graphene layer, which determines an uniform configuration throughout the sample, introduction of grain boundaries, in the form of linear topological defects, can define different domains in the hexagonal graphene lattice. Each domain is defined by a spacial orientation of the lattice vectors, which, in some cases, are different when we pass from one to another side of the GB.

5.3 Extended line defects in graphene monolayer.

We consider here four different GB introduced in a graphene layer. Three of these defects are of the tilt GB type, where the introduction of the one-dimensional periodic defect induces a rotation of a portion of the layer in relation to the other. We follow the same index notation as in [31], and denote these defects by the indices with which we write the translation vector of the GB ($\mathbf{T_{GB}}$) with respect to the lattice vectors on each side of the GB, as shown in Fig. 5.5. In this picture, we show in red the atoms that form the core defect.

The tilt grain boundary shown in Fig. 5.5-b, named GB(1,2)|(2,1), has a defect-core formed by a sequence of pentagon-heptagon pairs. This structural model is based on that proposed by Simonis et. al [62] who observed tilt grain boundaries in graphite from scanning tunneling microscopy (STM) (Fig. 5.6) experiments and proposed that,

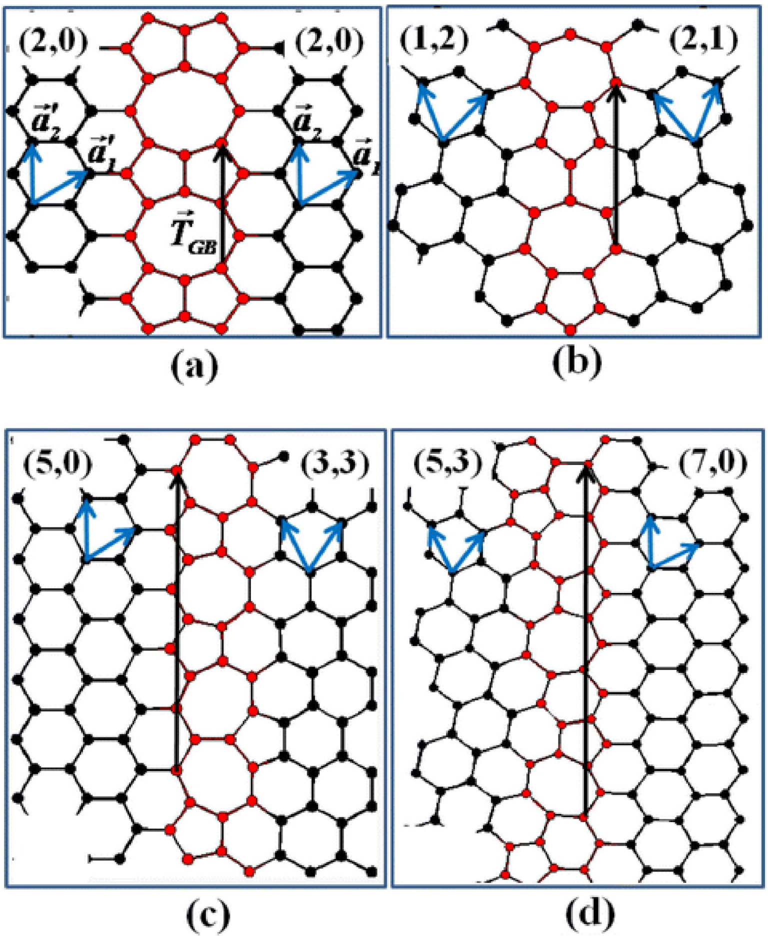

(a) (b)

(c) (d)

FIGURE 5.5: Geometries of one-dimensional periodic defects in graphene. In (a) the translational GB named GB(2,0)|(2,0) and the tilt GBs in (b) GB(1,2)|(2,1), (c) GB(5,0)|(3,3) and (d) GB(5,3)|(7,0). The translation vectors of the defect core $\mathbf{T_{GB}}$, shown as a black arrow, can be written as a sum of the lattice vectors in graphene bulk, in both sides of the grain boundary, and define the labels for the for different models considered.

in the absence of stress, the observed GB consists of a periodic structure described by a succession of pentagons and heptagons. In Ref. [63], this model is theoretically investigated for GBs of three different periodicities along the boundary, each introducing different relative tilt angles between the grains. In this work, we focus on a model that is formed by a periodicity as shown in Fig. 5.5-(b), that introduces a tilt angle of $\theta = 21.8°$ in the graphene layer.

In Fig. 5.5-c, we show the GB(5,0)|(3,3) defect. It is also formed by a periodic arrangement of pentagons and heptagons in the hexagonal graphene lattice, but with a different sequence and orientation. In this case, the introduction of the defect line makes the armchair orientation of the lattice in one side to be rotated by a tilt angle $\theta = 30°$ and assume a zigzag orientation. In the last tilt GB model considered, the GB(5,3)|(7,0), we have $\theta = 21.8°$ and the periodic defect core is formed by hexagons, pentagons and heptagons, as illustrated in Fig. 5.5-d.

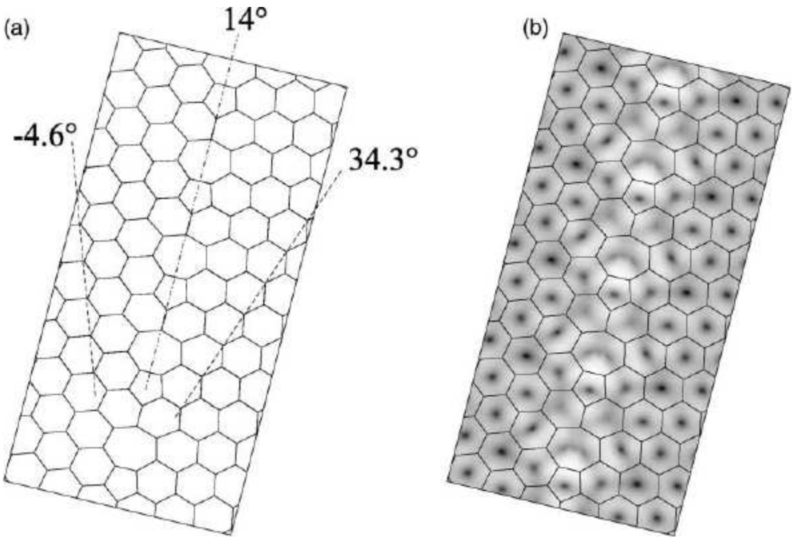

Figure 5.6: Optimized atomic model of the grain boundary with a linear chain of pentagons-heptagons separated by one row of hexagons (left panel), and simulated STM image superimposed on the atomic model (right panel). Figure taken from Ref. [62]

The translational grain boundary GB(2,0)|(2,0) differs from the others defects in the sense that it does not introduce a rotation of the graphene lattice, which has the same orientation on the left and right sides of the boundary. From this, $\theta = 0°$, and the effect of the linear defect, formed by two pentagons followed by an octagon as shown in Fig. 5.5-a, is just to translate the lattice in one of the sides by one-third of the periodicity of the bulk lattice in the direction perpendicular to the boundary line. This is the same structure discussed in Chapter 4 for graphene monolayer and h-BN.

The theoretical work in [31], discusses the modifications induced in the electronic structure of graphene layers when these one-dimensional periodic defects are introduced. The electronic structure of GB(1,2)|(2,1) had already been discussed in a previous theoretical work[63] . The results for this model show that the electronic states due to the defect near the Fermi level (FL), hybridizate with bulk states, as indicated by the very dispersive bands and the projected density of states (PDOS) on the core atoms, in Fig. 5.8-a and b. The calculations also indicate that an anisotropic Dirac cone can occur on the BZ line corresponding to the defect direction. The BZ for all models studied in this chapter is shown in Fig. 5.7.

For a graphene layer with GB(5,3)|(7,0) defect, the distance between adjacent line defects, which defines different supper-cell sizes, is shown to affect the energy gap of this model. The presence of a small gap for one cell size, indicates that this grain boundary introduces a strong electronic antiresonance in the system. In the limit of sufficiently large supercells, a vanishing gap at the FL is expected, as the characteristic result for pristine graphene layers.

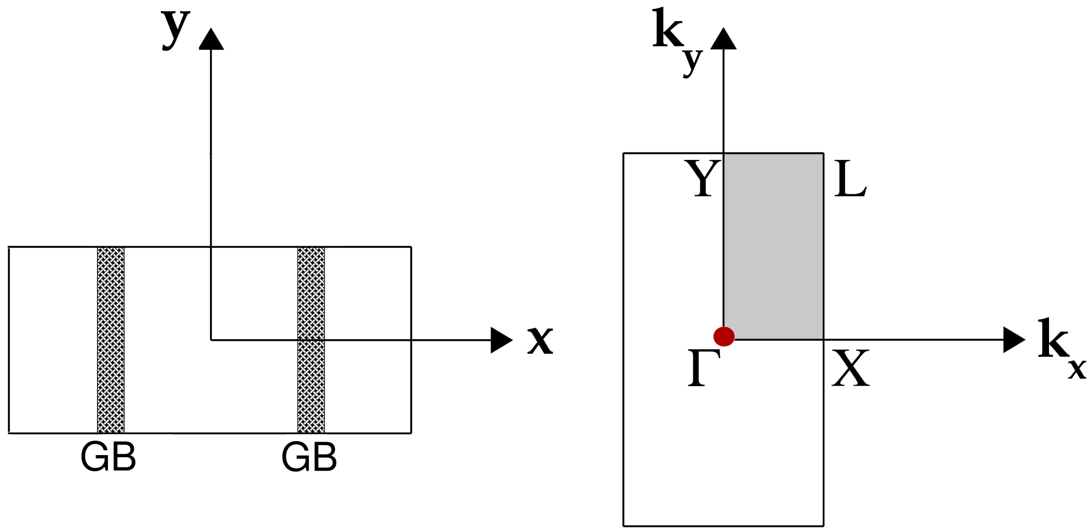

FIGURE 5.7: Schematic suppercell for the defective bilayer graphene (left) and the corresponding Brillouin zone (BZ) (right). The high-symmetry lines are defined by the special points Γ, X, L and Y. Γ-Y and X-L lines are in the same direction of the GB for all models.

To conclude some of the main results for tilt grain boundaries obtained in Ref. [31], we comment about the degree of hybridization of electronic states of the carbon atoms forming the line defects and those of the graphene "bulk". Analysis of total and partial DOS for these models clearly indicates a high degree of hybridization between defect and bulk electronic states for the three tilt GB models. In Fig. 5.8-b, d and f, the partial DOS projected onto the states of the carbon atoms at the defect core, are shown in red. The contribution of the core atoms to the total DOS near the FL ranges from 37% to 55%, which demonstrates a low degree of localization of these states onto the core atoms, for the three tilt GB models.

The results for a graphene layer with a GB(2,0)|(2,0) contrasts in many aspects with that summarized here for the tilt GB. A high degree of localization of defect states on the core atoms is observed in the calculated total and partial DOS represented in Fig. 5.9. The peak just above the FL, at $\sim$ 0.1 eV, shows a high concentration on the atoms of the defect core, which contribute with $\sim$ 85% of the total DOS, and a contribution of $\sim$ 96% is obtained when the orbitals from the carbon atoms that form the two zigzag lines closest to the core atoms is also included.

No spin polarization is induced in this case since, for this neutral system, these strongly confined states are empty. By doping the system with introduction of extra charge, the FL is raised by a few meV, and a ferromagnet state, lower in energy, is stabilized. The calculated formation energy for this state it is $\sim$ 40 meV (per defect unit) lower than that of the spin-unpolarized system, and a magnetic moment per defect unit of 0.52 μ_B is established.

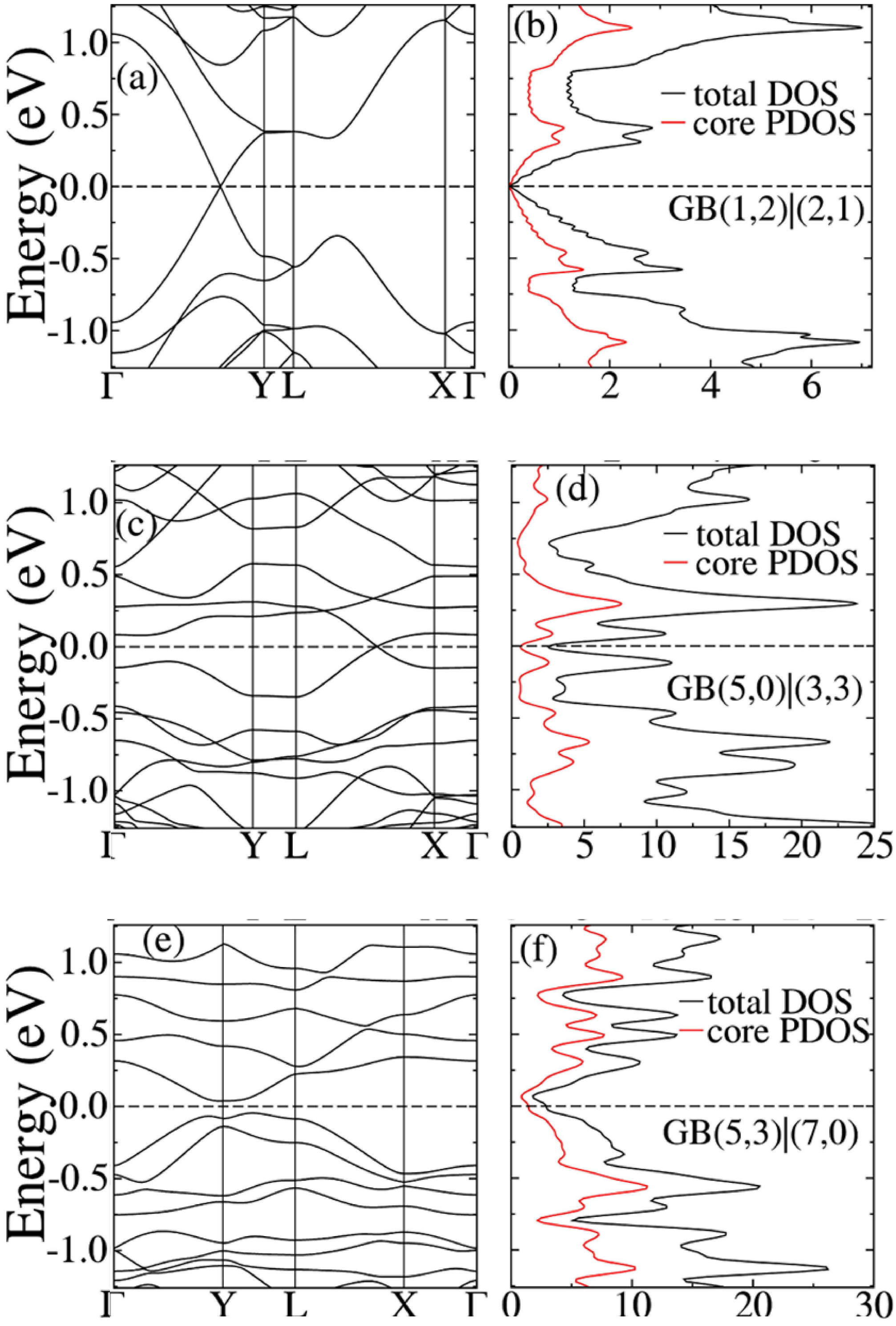

Figure 5.8: Electronic structure of the graphene monolayers with the tilt grain boundaries GB(1,2)|(2,1), GB(5,0)|(3,3) and GB(5,3)|(7,0). The total DOS is represented by the black curves, while the red curves represent the partial DOS, projected onto the carbon atoms that form the defect core.

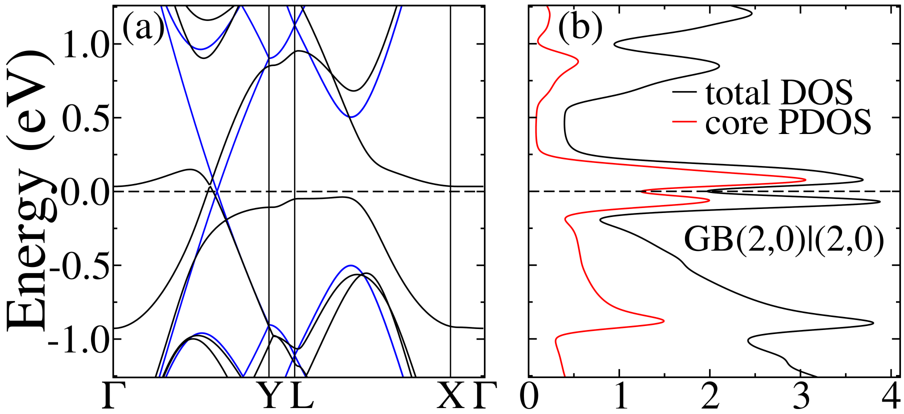

FIGURE 5.9: (a) Electronic bands and (b) DOS of the translational grain boundary GB(2,0)|(2,0) in the graphene monolayer. The total DOS is shown by the black curve and the PDOS, projected onto the core atoms, by the red curve. In (a) is also included (in blue color) the band structure of a bulk suppercel obtained by removing the two atoms forming the dimer at the center of the defect core .

5.4 Defective Graphene Bilayers

The very different and rich physics of mono and multilayer pristine graphene encourages us to extended this theoretical work on graphene layers with such periodic defect lines to the investigation of the electronic states of these systems in the form of double-layer structures. We proceed by including a pristine graphene "bottom" layer to the previous systems, forming the structures shown in Fig. 5.10. The main goal of this study is to identify the electronic properties of such defective graphene bilayers.

From all previous considerations, we study two basic types of extended one-dimensional defects in graphene bilayers: (i) tilt grain boundaries, which introduce a relative orientation angle between the regions of graphene in both sides of the defective line (structures in Fig. 5.10-b, c, and d) and (ii) a translational grain boundary, that just translates a portion of the layer, without changing its orientation (structure in Fig. 5.10-a).

The introduction of the second layer, chosen here as a pristine graphene layer, requires a choice of some reasonable stacking, in order to find low energy structures. To make such choice, we first emphasize that, as we perform periodic super-cell calculations, we have to introduce two or more defect lines in each unit cell of the defective bilayers, in order to obtain a periodic repetition of the structures. From this, we identify regions limited by two defect lines and their respective orientations, as show in Fig. 5.11 for the GB(5,3)|(7,0), and in Fig. 5.12 for the translational GB(2,0)|(2,0). For each of the four structures investigated, we choose one of these regions to have an AB'-stacking registry with the additional second layer. As a consequence, the neighboring region is rotated with respect to the pristine bottom layer giving rise to a Moiré pattern with the bottom pristine layer. This pattern can be observed in the bilayers GB(5,3)|(7,0), GB(5,0)|(3,3)

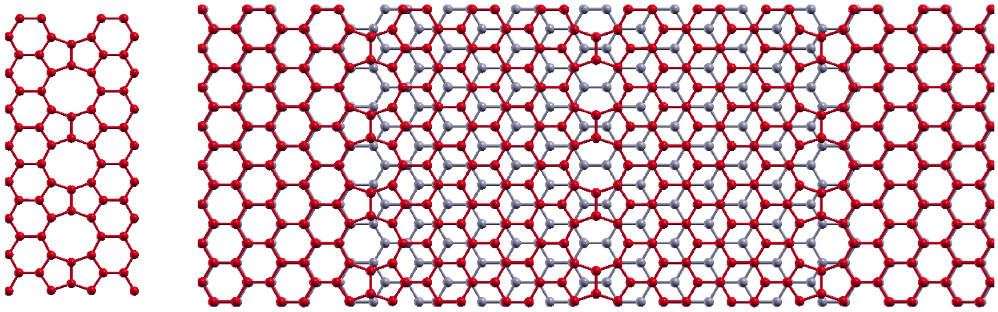

(a) GB(2,0)|(2,0)

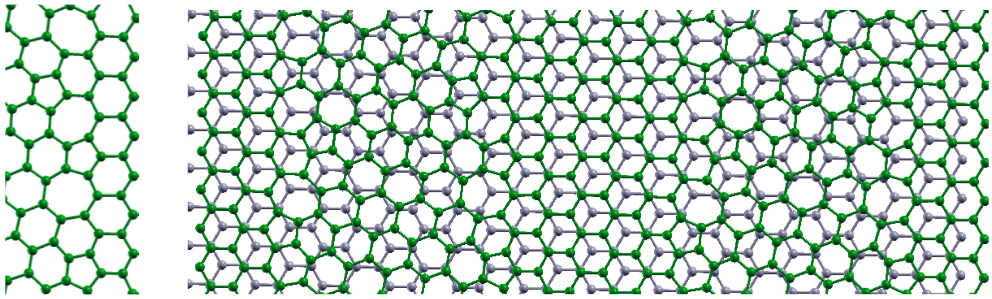

(b) GB(5,3)|(7,0)

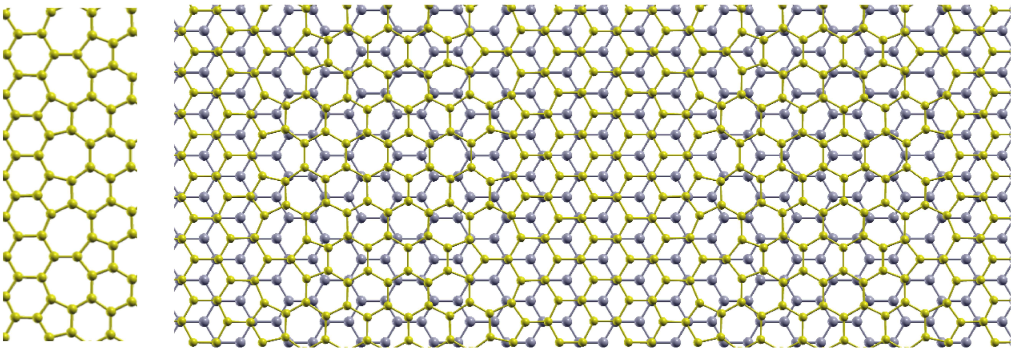

(c) GB (5,0)|(3,3)

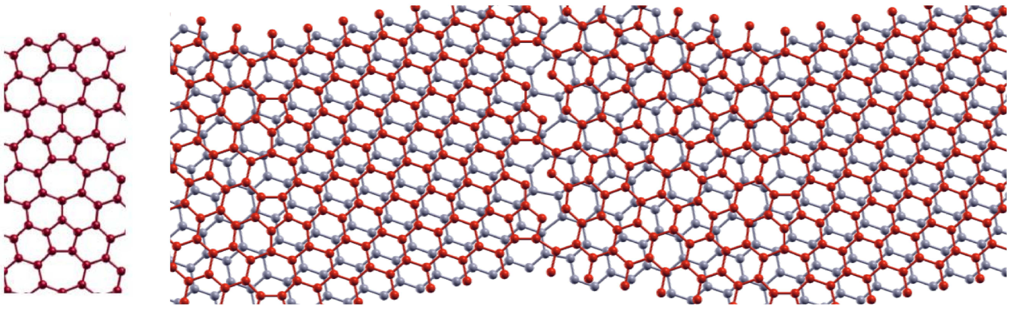

(d) GB (1,2)|(2,1)

Figure 5.10: Graphene Bilayers constructed from the monolayers with grain boundaries investigated in Ref. [31]. A reasonable choice of initial structures is to define an AB' stacking in some region, which consequently lead to the formation of Moire patterns in the region that presents a rotation due to the introduction of the GBs.

and GB(2,1)|(1,2). For the translational grain boundary GB(2,0)|(2,0), with the same orientation of the graphene lattice in both sides of the defective line, regions with AB' and AA' stacking are established.

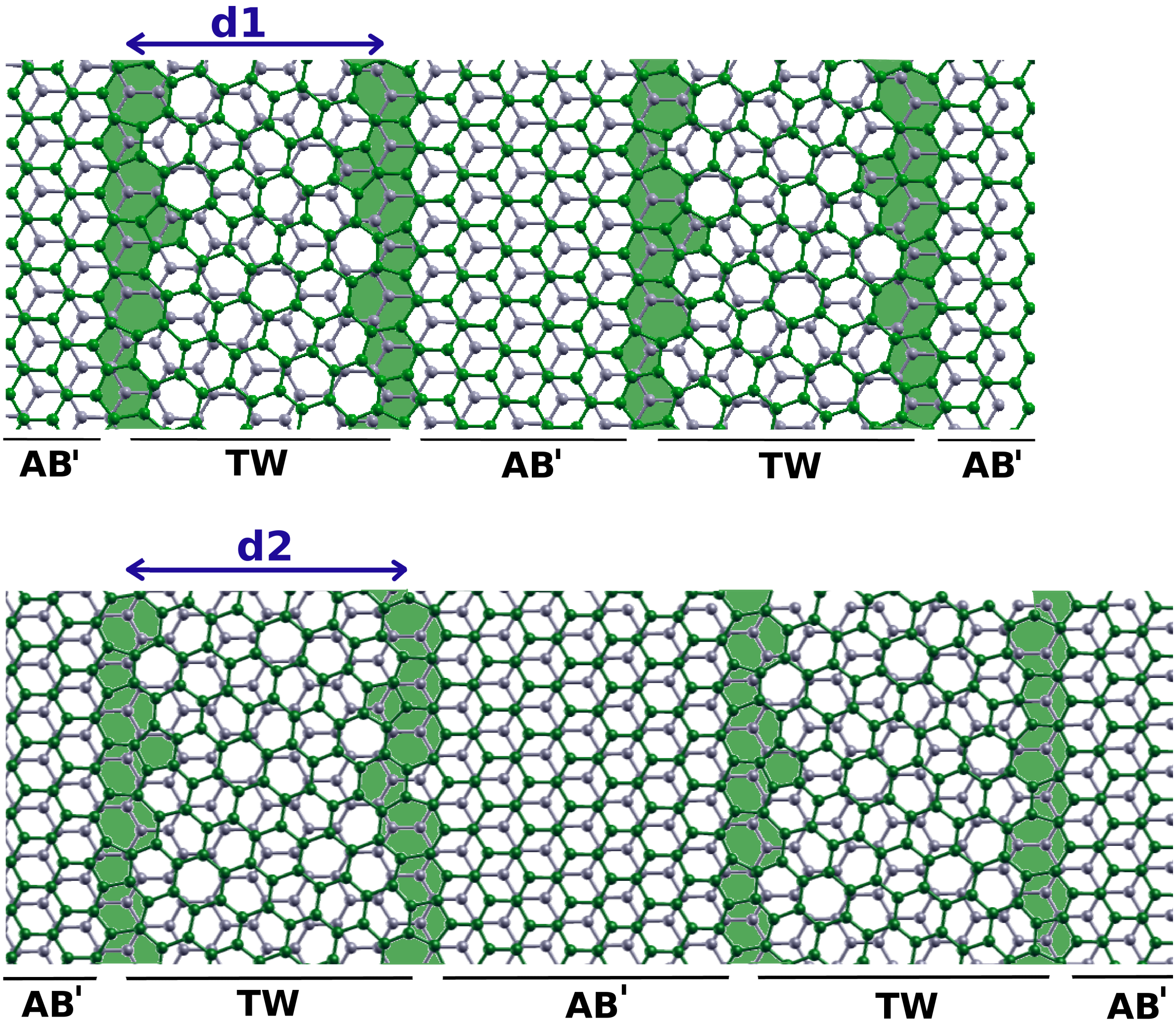

FIGURE 5.11: Unit cells for bilayer graphene with GB(5,3)|(7,0) defects with 336 and 422 atoms, with distance between GB $d = 10.2$ Å and 14.3 Å. The bottom pristine graphene layer is represented in gray, while the atoms in green represent the top layer, with two defect lines. The portion of the graphene lattice with armchair orientation along the GB direction is chosen to have an AB' stacking registry with the additional second layer.

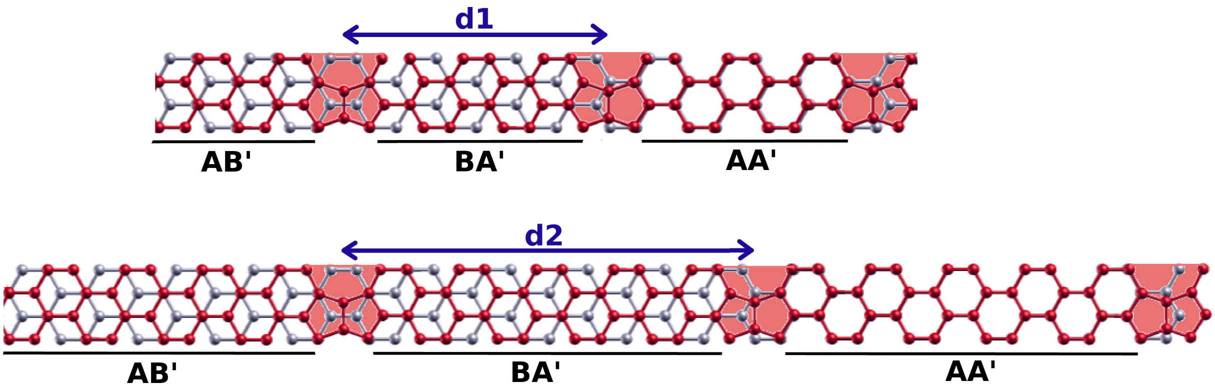

FIGURE 5.12: Unit cells for bilayer graphene with GB(2,0)|(2,0) formed by 168 and 254 carbon atoms with distances between adjacent GB of $d = 14.4$ Å and 23 Å, respectively. In this case, the introduction of three line defects is necessary to build the periodic structure composed of two layers, as the GB translate the lattice by 1/3 of the lattice period along the armchair direction ($\mathbf{a}_{AC}$ vector defined in Chapter 2).

5.4.1 Electronic Structure

The modifications induced in the electronic properties of graphene bilayers by the introduction of the GBs are now discussed. The BZ that corresponds to our super-cells has a rectangular form, as presented in Fig. 5.7. The four high-symmetry $\vec{k}$-points are the same as those considered in Ref. [31]: $\Gamma(0{,}0)$, $X(\pi/a_x,\ 0)$, $L(\pi/a_x,\ \pi/a_y)$ and $Y(0,\ \pi/a_y)$, where a_x and a_y ($= |\mathbf{T_{GB}}|$) in Fig. 5.5 are the modulus of the lattice vectors of the bilayer super-cells perpendicular and parallel to the defect line, respectively. From this definition, the lines Γ-Y and X-L are parallel to the defect line.

A general result for all models is that the introduction of the extended one-dimensional defects disrupts the Bernal stacking of the two layers. As a consequence, the character of AB' stacked graphene bilayer is lost, giving rise to an electronic structure formed by the combination of the uncoupled states of the defective and pristine sheets.

In Figs. 5.13, 5.14, 5.16, 5.9, 5.18 and 5.19 are shown the calculated electronic band structures for the defective monolayers and bilayers. In the middle and lower panels, results for the supercell with the two different distances between adjacent GBs are presented. For the sake of comparison, we include the computed bands and DOS for the defective monolayers, in the upper panel. For both monolayer and bilayer models, the direction of the line defects in the super-cell were chosen as the ŷ direction, as shown in Fig.5.7, in a way that the symmetry lines in the BZ are the same for both models and can be compared directly.

GB(5,0)|(3,3): We start by discussing the GB(5,0)|(3,3) model, for which electronic bands and DOS analysis are presented in Fig. 5.13. The super-cells sizes are defined by

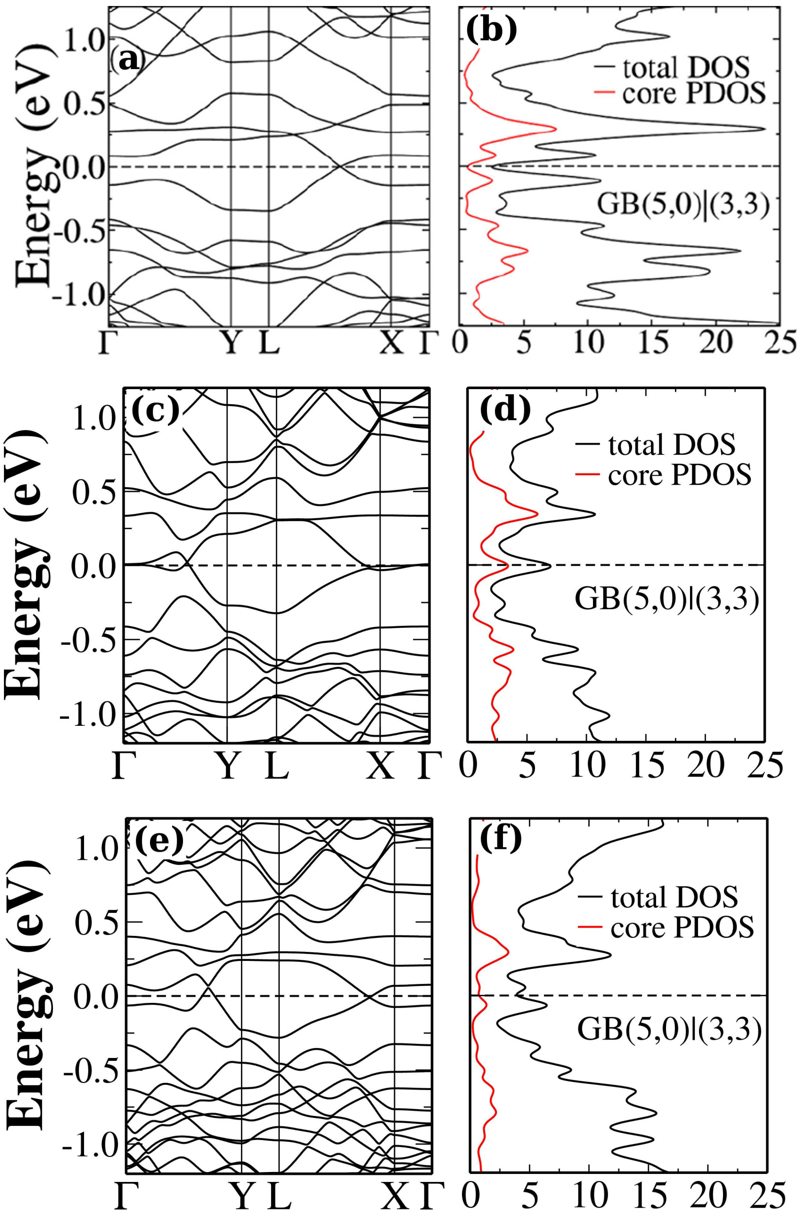

FIGURE 5.13: Electronic structure for monolayer (upper panel) and bilayer graphene with supercells of two different sizes (middle and lower panels) with GB(5,0)|(3,3). A very similar electronic dispersion is observed for the three systems, with the main differences observed at the FL region.

distances between line defects of d = 13.2 Å and 19.4 Å for the bilayers and d =13.4 Å for the monolayer. Calculations indicate a very similar electronic dispersion when comparing monolayer and bilayer systems, with some differences showing up at the FL region. For the monolayer (Fig. 5.13-a), a Dirac cone is observed along the L-X line, which is parallel to the line defect. Introduction of the bottom pristine monolayer produces the electronic bands in Fig. 5.13-c and e. An appreciable interaction between line defects occurs for the bilayer with the smaller supper-cell size (Fig. 5.13-c). The main differences between this model and the one with a larger distance between the two GB appear along the Γ-Y and L-X lines, both parallel to the line defects. The Dirac cone observed in the monolayer along L-X takes the form of almost flat bands crossing the FL, but it is recovered when we increase the supper-cell size, as seen in Fig. 5.13-e. At the Γ-Y line, we do not observe introduction of bands crossing the FL for the defective monolayer, which appear with the inclusion of the second layer, with Dirac cones being now observed for both sizes of the defect bilayers models.

The analysis of the total DOS and partial DOS (PDOS), shown in Figs. 5.13-b, d and f, indicates a high degree of hybridization of the electronic states of the core atoms with the bulk states, both for the defective monolayer and also for the two supper-cells sizes of the bilayer models, as indicated by the rather moderate contribution of the orbitals centered on the core atoms to the DOS peaks introduced by the defects.

From the general results we see that the null-gap semiconductor character observed for the graphene monolayer with the GB(5,0)|(3,3) is lost when we introduce the pristine layer. Instead, a metallic behavior is observed for the defective bilayers of both supercell sizes due to the raising of the bands crossing the FL, which defines a finite DOS at this energy.

GB(1,2)|(2,1): We know examine the characteristics of the system when we consider the introduction of the GB(1,2)|(2,1) in monolayer and bilayer graphene. The calculated electronic structures for these systems are shown in Fig. 5.14. We analyzed bilayers with supercells of two different sizes, formed by 120 and 168 carbon atoms, for which the distances between the line defects are d = 12.3 Å (middle panel) and 17.2 Å (lower panel), respectively. For the monolayer, the results are for a supper-cell with d = 17.2Å. As already commented, the electronic structure for monolayer has been discussed in Refs.[31, 63]. It shows the generation of an anisotropic Dirac cone along the Γ-Y line in the BZ, parallel to the line defect. This Dirac cone, has, therefore, a Fermi velocity that depends on the direction from the Dirac point in **k** space.

By changing our focus to the bilayer model with GB(1,2)|(2,1), remarkable modifications are observed in the electronic bands. An even more pronounced interaction between adjacent line defects is observed for the smaller supercell, if compared to the GB(5,0)|(3,3). As shown in Fig. 5.14-c, a very small energy gap of ∼50 meV is also observed in this case. The bands along the X-L line present a marked curvature if compared to the defective monolayer, where the corresponding bands presents smoother variations. The linear character of the bands defining the anisotropic Dirac cone in the monolayer is also lost for this model and, instead, two curved bands lifted away from the FL appear. Because of our choice to impose an AB' stacking with respect to the pristine bottom layer, the bilayer containing the GB(1,2)|(2,1) lacks the mirror symmetry with respect to the geometric center of the GB that was found to be connected to the Dirac cone along the Γ-Y line in the monolayer case. Hence, the gap we observe along this line in Fig. 5.14-c is due to the mirror-symmetry breaking. The total DOS presents a sharp peak at ∼0.25 eV above the Fermi level, as shown in Fig. 5.14-d. This peak has just a small contribution from the states of the core atoms (∼21.6%), as shown by the PDOS curve, projected onto the core-atom orbitals in red color, indicating a high degree of hybridization of these states with bulk states.

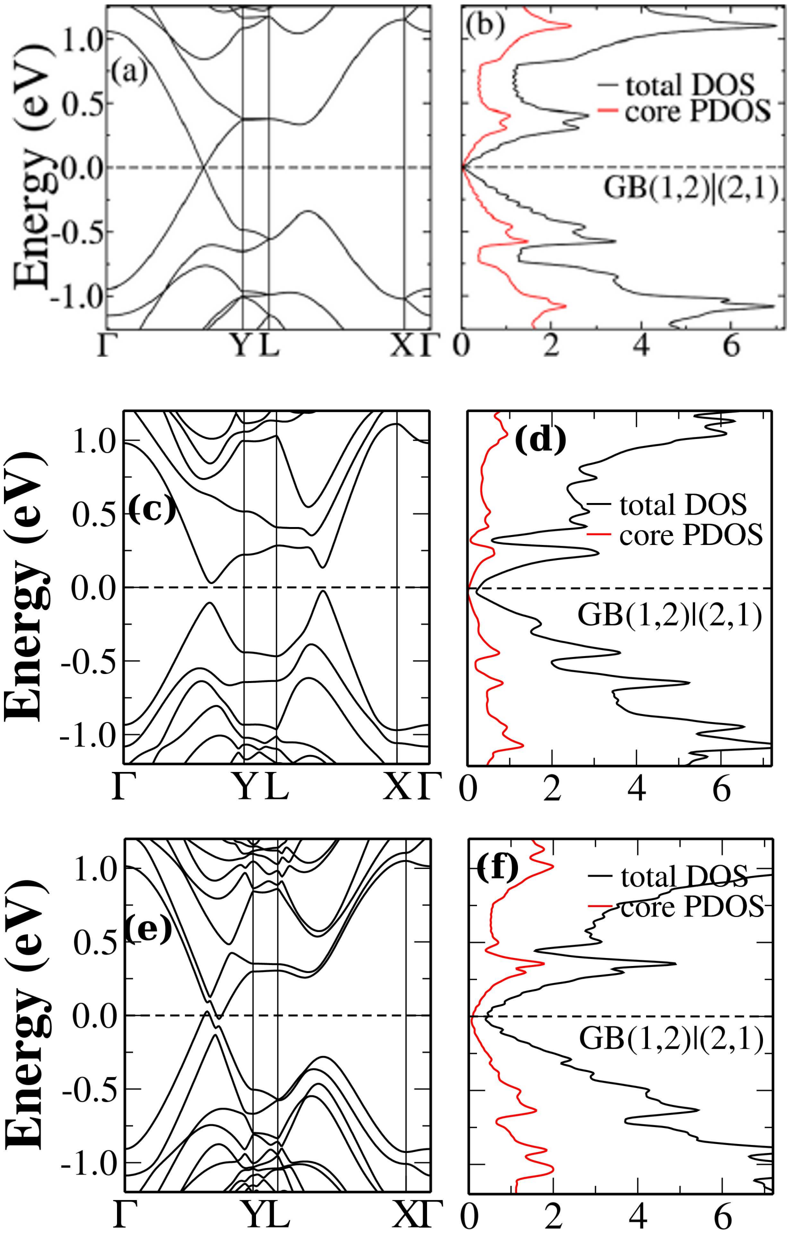

FIGURE 5.14: Electronic structure for monolayer (top panel) and graphene bilayers (middle and lower panels) for systems with GB(1,2)|(2,1). The distances between defect lines are $d = 17.2$ Å for the defective monolayer and $d = 12.3$ Å and $d = 17.2$ Å for the defective bilayers.

By increasing the distance between adjacent line defects, the calculated electronic bands and DOS are shown in Figs. 5.14-e and f. The smoother variation of the bands along the X-L direction is recovered, if compared to the monolayer, and doubled bands along all symmetry lines in the BZ are also observed, due to the introduction of the second graphene layer. An interesting result is the semimetalic behavior observed for the bands along the Γ-X line.

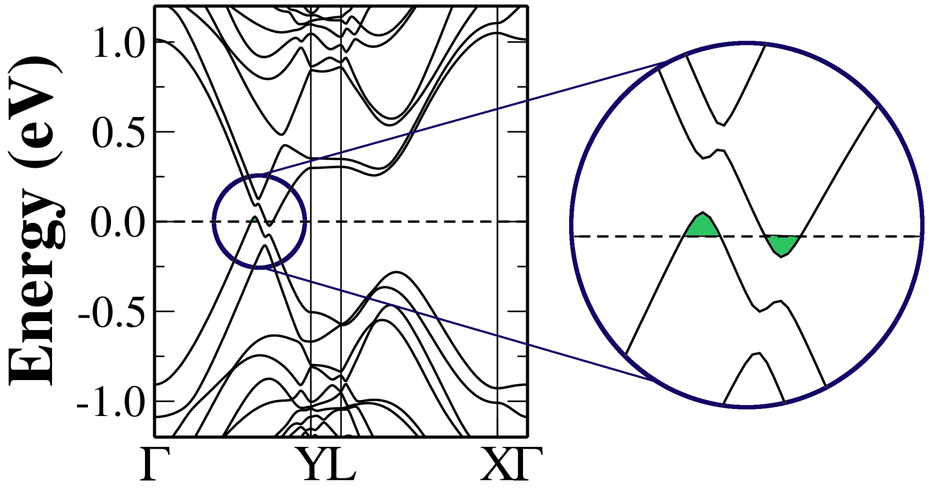

FIGURE 5.15: Electronic structure for defective bilayer graphene with GB(1,2)|(2,1) and d = 17.2 Å. A semimetalic behavior is observed when a second pristine graphene layer in introduced in this system.

A semimetal material is characterized by a small overlap between the bottom of the conduction band and the top of the valence band over a small range of energies. It differs from a typical semiconductor (or even an insulator) in the sense that a semimetal has always non-zero conductivity. Even at zero temperatures, electrons in a semimetal can move to the small portion of the conduction bands that are infinitesimally close in energy to the valence states. On the other hand, a semiconductor becomes an insulator at very low temperatures due to the presence of a finite gap between valence and conduction bands. In this way, a semimetal has no band gap, though just a small density of states is observed at the FL, which is in contrast also with metals, where a characteristic partially filled conduction band introduces an appreciable density of states at the FL.

From this, the GB(1,2)|(2,1) introduced in a graphene monolayer preserves the null-gap semiconducting behavior of pristine graphene, with the difference that in this case the Dirac cone becomes anisotropic and is dislocated out of the **K** point in the BZ. Introduction of the second layer for a sufficiently large distance between line defects gives a semimetal character to the system. For our model, an overlap between bands of ∼30 meV is calculated, as shown in Fig. 5.15, and a small DOS peak is observed at the FL in Fig. 5.14-f.

Regarding localization of defect states, the analysis of the total and partial DOS reveals a very similar behavior as that of the single-layer with this periodic defect. The two peaks above and below the FL calculated for the monolayer model also appear in the presence of the second layer at ∼0.26 eV and ∼ -0.6 eV. Also for this suppercell size, states of defect core hybridize with bulk states, and contribute with just ∼38% to the total DOS of the most pronounced peak above the FL.

GB(5,3)|(7,0): For single layer graphene with the GB(5,3)|(7,0) defect, the presence of the small gap for the monolayer model was already discussed in Ref.[31] and commented here as being a supercell size effect. In the limit of sufficiently large cells the vanishing gap must be recovered. In this calculation, a cell with a distance between the two GB of d = 13.1 Å was used. As for the others tilt GBs considered here, for the GB(5,3)|(7,0) a high degree of hybridization between states from defect-core atoms and bulk states is also observed. From the DOS and PDOS analysis of these states, shown in Fig. 5.16-b, the maximum contribution of the core atoms (red line in PDOS analysis) to the total density of states is of just around 55%.

The calculated band structure and the DOS for the GB(5,3)|(7,0) bilayer models, are presented in Fig. 5.16-c and d for the supercell with d = 13.0 Å and in Fig. 5.16-e and f for a larger supercell, for which d = 14.3 Å. As expected, inclusion of the second graphene layer gives rise to a higher number of bands in all range of energies in the electronic structure, but the main differences are observed around the FL, along the Γ-Y and Y-L symmetry lines. The valence band maximum (VBM) and conduction band minimum (CBM), now touch the FL, and even for the smaller cell size, there is no energy gap, as observed before for monolayer with the same distance between defects. The VBM is observed along the Γ-Y direction for the defective bilayer, instead of along the Y-L line, as calculated for monolayer. However, the CBM preserves its general appearance, being localized near the Y point, along the Y-L line.

By considering the larger supercell for bilayer GB(5,3)|(7,0), the main effect of increasing the distance between line defects (from 13.0 Å to 14.3 Å, as shown in the example in Fig. 5.11), is to modify the positions of the CBM and VBM to the L point and along the L-X line, respectively. Also for this supercell size, states from the defect atoms are mixed with bulk states, indicating their weak localization on the defect core.

GB(2,0)|(2,0): We discuss now the modifications induced in the electronic properties of the monolayer and bilayer graphene by the introduction of the translational GB(2,0)|(2,0). Starting with the monolayer model, the band structure and DOS for the translational GB(2,0)|(2,0) calculated in Ref.[31] are shown in the Fig. 5.17. The occurrence of two sharp resonances at ∼ ± 0.1 eV from de FL is observed as a consequence of the flat bands that appear in the band structure along the Γ-Y and L-X lines in this energy range. The DOS peak just above the FL differs from the tilt grain boundaries

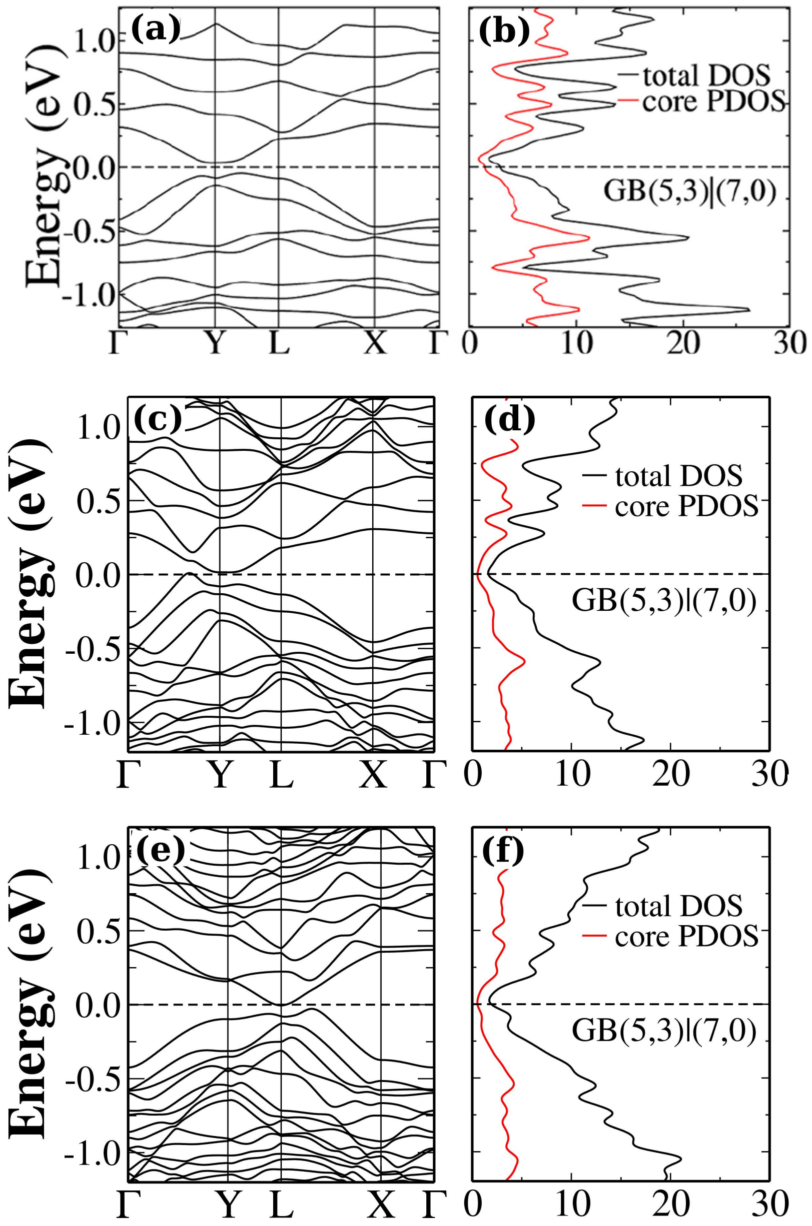

FIGURE 5.16: Electronic structure for monolayer (upper panel) and bilayer graphene (middle and lower panels) with GB(5,3)|(7,0). For the three models, electronic states due to the defect are mixed with bulk states indicating a high degree of hybridization between such states.

by the degree of localization of the corresponding states on the defect core, which adds up to for ∼96% if we consider the contribution of atomic-basis orbitals from the carbon atoms at the first and second zigzag lines, in addition to those from the carbon dimers at the center of the defect core. For the defect in its neutral charge state, the states that form this peak are empty, hence no spin polarization is induced.

By doping the layer with extra charge, the FL is raised by about ∼0.07 eV, and a spin-polarized calculation reveals a stable ferromagnetic state, with a magnetic moment of 0.52 μ_B and with a formation energy that is lower by ∼40 meV (per defect unit) when

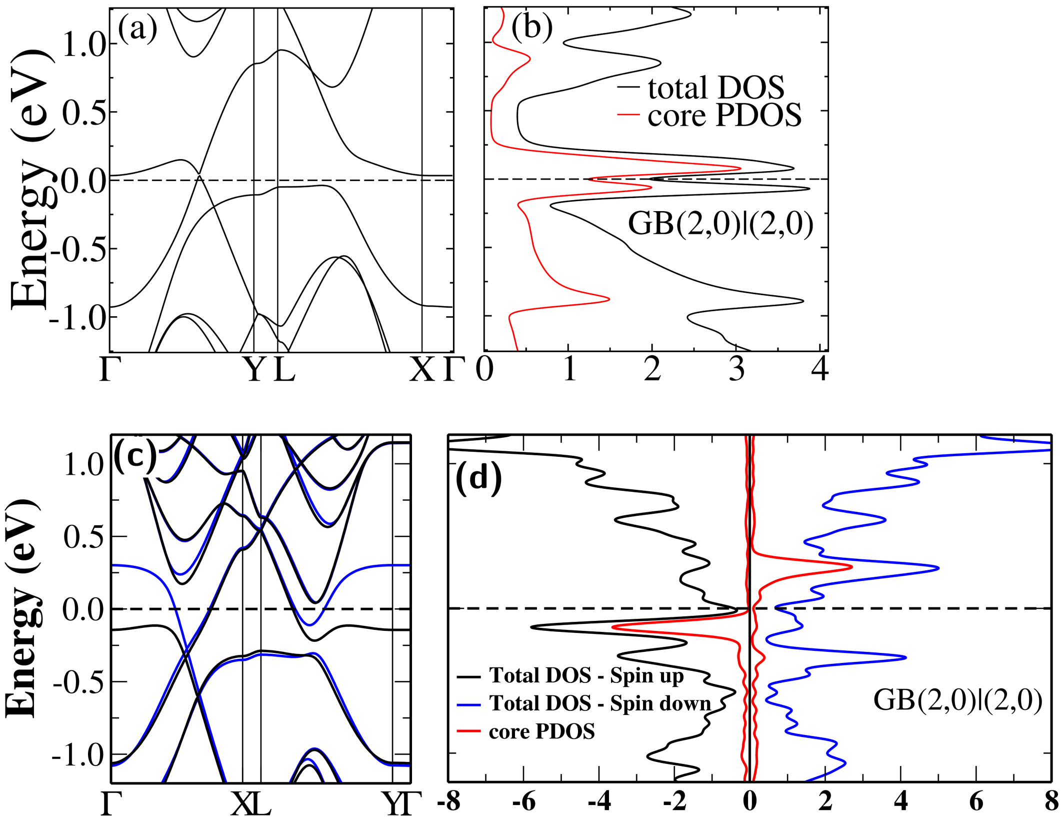

FIGURE 5.17: Band structure and DOS of the translational GB(2,0)|(2,0) in monolayer graphene. In the neutral charge state, there is no occurrence of magnetism in this system and electronic states are as shown in (a-b). By doping the system with extra charge, a spin-polarized calculation reveals a stable magnetic state, for which electronic bands are presented in (c-d).

compared to the unpolarized spin state. The electronic bands for this case are shown in Fig. 5.17, where the difference between states of majority and minority spins can be easily identified by the black and blue curves, and the contribution from the core atoms by the red color .

Turning our attention to the defective bilayer graphene, the introduction of a bottom pristine layer together with the defective GB(2,0)|(2,0) monolayer produces the two supercells shown in Fig. 5.12, that were used in our calculations. For these models the distances between the defect lines are d=14.4 Å and 23.0 Å and the supercells are composed by 158 and 254 carbon atoms, respectively.

For the supercell of smaller distance between adjacent line defects (d = 14.4Å), band structure calculations reveals a high localized peak at the FL in the DOS, as shown by the black curve in Fig. 5.18-b. The contribution of states from the carbon atoms that form the defect core (red curve) indicates a great contribution of these states to the total DOS, which reaches ~73%. A magnetic state with magnetic moment of 0.35 μ_B per defect unit is obtained, even for the neutral system. Analysis of the calculated electronic

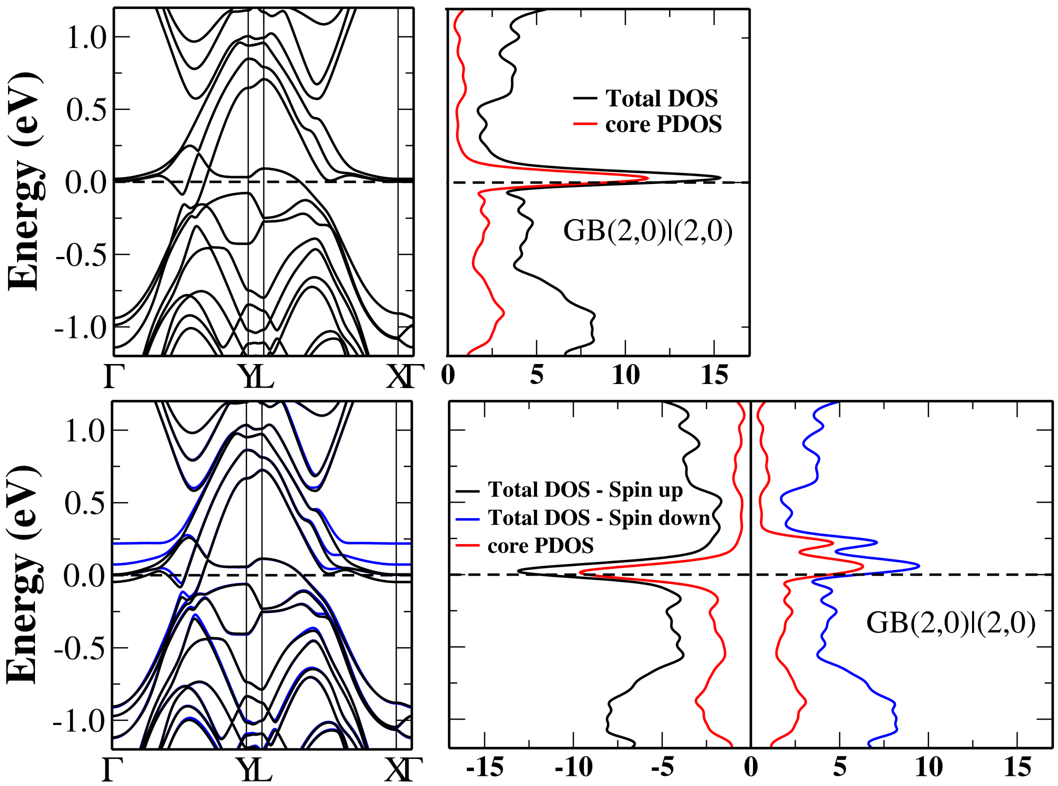

FIGURE 5.18: Electronic bands and DOS for the bilayer graphene with distance between translational GB(2,0)|(2,0) d = 14Å. (a) Calculation with no spin polarization shows a highly-localized peak at the FL, with a contribution of states from atoms that form the core of ∼73%. (b) Spin polarization calculation stabilizes a magnetic state with magnetic moment $0.12\mu_B$ (per defect unit). The main differences between total DOS of majority (black curve) and minority (blue curve) spin show up between -0.1 and 0.3 eV.

structure for majority and minority spins for this model are presented Fig. 5.18-d. The total DOS for both spin channels, in black and blue colors, present narrow peaks that have a large contribution from states of carbon atoms that form the GB core, as shown by the PDOS projected onto the core atoms, in red color. For minority spin (total DOS in blue), the two narrow peaks above the FL, at 0.06 eV and 0.2 eV, have contributions of ∼65% from states of the core atoms. A third narrow peak appears at the Fermi level for the majority spin states (total DOS in black). The contribution from the core atoms to this peak is of 73%. Flat bands crossing the FL are connected with this DOS peak, which is responsible for the occurrence of magnetism in this neutral system.

Calculations with a larger supercell, where we increase the distance between defect lines to d = 23 Å, enable us to investigate the influence of concentration of the GBs in the electronic structure of this system. By including four extra zigzag lines of carbon atoms, we increase the bulk region in the supercell, as shown in Fig. 5.12. The calculated band structure and DOS for this model are shown in Fig. 5.19. For this larger supercell we recover the situation observed in the defective monolayer with GB(2,0)|(2,0): a sharp peak above the Fermi level (at 0.05 eV) is mainly formed by states from the core atoms, which contributes with ∼74% of the total DOS in this energy value. For this neutral charge state, there is no occurrence of magnetism. Similar to the GB(2,0)|(2,0) monolayer, the localized nature of the states associated with this peak is indicative of the possible occurrence of a magnetic instability. A second less pronounced peak is also observed below the FL, at -0.16 eV. This peak is less localized on the core atoms, as just ∼48% originate from the orbitals centered on these atoms.

By doping the system with extra charge, the Fermi level is raised by ∼0.03 eV and we observe a stable magnetic state with magnetic moment 0.30 μ_B per defect unit. This state presents a formation energy 2 meV (per defect unit) lower than the neutral system.

From analysis of DOS and PDOS for this structure, shown in Fig. 5.19-e and f, we can see the two narrow peaks introduced at the FL region; one of then, due to states with majority spin, is observed at ∼0.22 eV above the FL (blue curve in Fig. 5.19-f), while the second peak is partially occupied, and can be seen to be localized exactly at the Fermi level (black curve in Fig. 5.19-f). From PDOS projected onto the core-defect atoms, shown by the red curve in Fig. 5.19-f, we observe that ∼70% of these localized states for both spins come from the defective atoms.

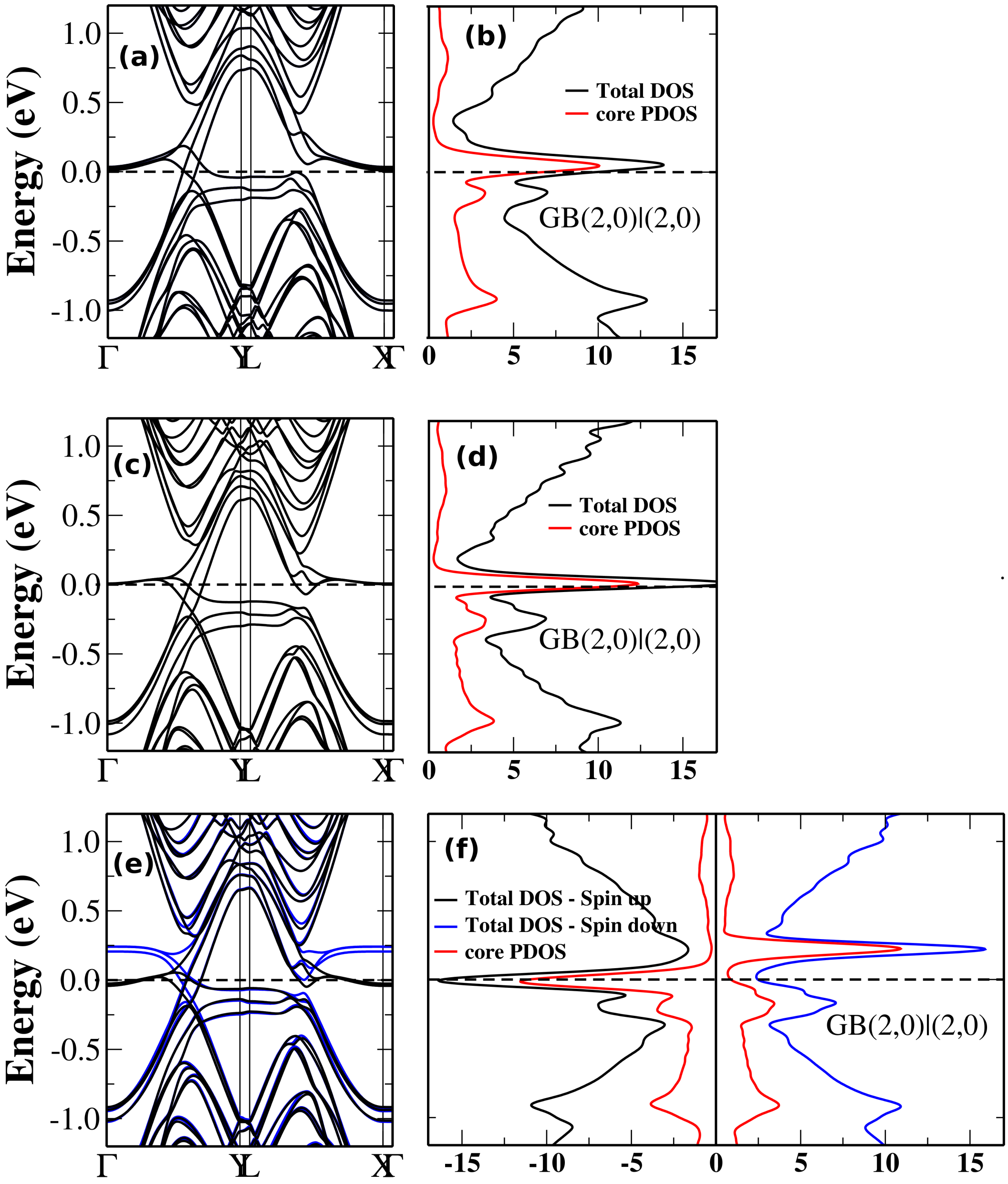

FIGURE 5.19: Electronic structure for GB(2,0)|(2,0) graphene bilayer, for the 254-atoms supercell (d=23.0 Å). The neutral system in (a-b) does not present magnetic moment. (c-d) By adding an extra charge, the FL is raised by 0.03 eV and a spin polarization calculation reveals a magnetic state with total DOS for majority and minority spins as represented black and blue colors, respectively in (e-f).

5.4.2 Conclusions

In this work we use first principles calculations to investigate the modifications induced in the electronic properties of bilayer graphene by introduction of three tilt grain boundaries, named GB(1,2)|(2,1), GB(5,0)|(3,3), and GB(5,3)|(7,0), and the translational grain boundary GB(2,0)|(2,0).

The theoretical work in Ref. [31] addresses the issue of the degree of hybridization between the electronic states associated with the extended line defects with those of the bulk of graphene. Ab initio calculations indicate that the translational GB introduces states near the FL that are strongly confined to the core of the defect and a ferromagnetic instability is observed. On the other hand, states introduced by the tilt GBs are just partially confined to the defect core, and no magnetic states are observed for systems with such defects.

Addition of a second pristine graphene layer to the systems formed by the defective monolayers induces some interesting modifications in the electronic properties of the defective bilayers obtained.

For the GB(5,0)|(3,3) bilayer graphene a metallic behavior is observed for two supercell sizes, differing by the distance between two line defects. This is a different result observed from that of the monolayer with this defect, where a null-gap semiconductor character is observed.

The GB(1,2)|(2,1) introduced in a graphene monolayer also presents a semiconducting behavior, which is changed to a semi-metal character when we consider the defective bilayer with this GB with a sufficiently large distance between the GBs. For this model, interaction between adjacent line defects is observed for the smaller supercell investigated, where a small energy gap (∼50 meV) shows up in the DOS.

In the case of the third tilt GB, the GB(5,3)|(7,0), the main modifications in the electronic structure concern in a shift of the VBM and CBM to different positions in the BZ. Furthermore, the small gap observed in the monolayer, indicative of a antiresonance introduced in the electronic spectrum by this defect, is not observed in any of the two supercell sizes for the defective bilayers.

Regarding the translational GB(2,0)|(2,0), the strongly confined defect states observed in the defective monolayer persist in the bilayer systems. For the two defective-bilayer supercell sizes investigated, magnetic states are observed due to localized states at the one dimensional defect. For the larger supercell, such magnetic state is stabilized by introduction of extra charge, while for the smaller model spin-polarization calculations reveal a magnetic behavior for the neutral system induced by the interaction between adjacent defect lines.

Chapter 6

Electronic Transmission in Graphene: Monolayer–Bilayer interfaces.

6.1 Introduction

Carbon based electronics has been a subject of intensive research since graphene became one of the most promising two-dimensional materials for the new generation of electronic devices. Since then, an intense activity in the study of the electronic properties of this material has emerged. Much progress has been made, but it is still a challenge to obtain a total control of the properties of any material in the nanoscale.

As already discussed in many works, it is very common that the synthesis process of graphene results in polycristalline samples with abundant topological defects, which strongly influence its electronic, chemical and mechanical properties[40, 64–66]. In special, a large volume of both theoretical and experimental works addressing the effect of one-dimensional line defects in transport properties of this material has been accumulated in the last years[28, 30, 31, 67]. Going beyond the common grain boundaries (GBs) commonly found in graphene, boundaries in general can have an important influence on transport properties of materials in nanoscale. Electronic transport, for example, has been investigated for different structural domain boundaries, such as grain boundaries in polycristalline graphene[68] and sheared and tensile bilayer graphene[69, 70].

As discussed in the the previous chapter, graphene bilayers have been a subject of intense study in the recent years, as the interlayer registry between two graphene layers, can alter drastically its electronic properties, opening up many possibilities of different physics. It is well known today that a perpendicular electric-field can open a gap in an AB'-stacked graphene bilayer[52, 53], which happens due to the symmetry breaking introduced by the shift between the graphene layers. This shift can occur in many different ways and may give rise to multiple stacking domains in a unique sample.

Many works have reported [71–73] that transitions between two different domains in graphene bilayer, can occur by means of distortions in the graphene lattice, defining the so called soliton boundaries. In Ref. [71], for example, San-Jose and collaborators discuss the controversial question about the energy gap in pristine bilayer graphene: while some experimental groups have found a metallic behavior for this material[74–76], others find a finite gap even at zero magnetic field[77, 78]. This dichotomy has been interpreted as an electronic instability that can be induced by many-body correlations[74], but in Ref. [71], an alternative explanation is proposed, which is based on the formation of solitons. Regions of tensile and strained graphene layers, induce smooth boundaries between AB'- and BA'-stacked bilayer regions, which is shown to result in an insulating-like behavior, rather than the metallic character observed by the hyperbolic dispersion at low energies.

An alternative interpretation for the structure of stacking boundaries has also been investigated in Ref. [79]. The authors demonstrate by dark-field image on TEM and STEM complemented by theoretical results with DFT calculations and classical potential molecular dynamics, that the stacking boundaries are not atomically sharp as suggested by the formation of solitons and grain boundaries. Instead, they would be formed by ripples in graphene layers, which result in smooth transitions between AB' and BA' stackings.

The possibility of formation of stacking boundaries by rippling of graphene layers, motivated the study of transport on this type of system, which will be discussed in this chapter. A simplified model can be adopted if we observe that the rippled regions can obey the physics of monolayer graphene, as the distance between stacked layers in these regions (~ 7 Å, according to Ref.[79] is large enough to uncouple the layers. In this way, such layers do not interact with each other anymore, and the usual electronic properties of a bilayer graphene are not observed, but instead, a region with two independent monolayers of graphene is established.

With these considerations, we investigate transport in graphene through boundaries defined by transitions between regions of two coupled layers, where we consider the physics of an AB stacking arrangement, and regions of two uncoupled layers, which obeys the physics of monolayer graphene.

We consider basically three situations: electrons emerging from a semi-infinite region of uncoupled layers, that we define here as a k-region, being scattered to a semi-infinite region of two coupled layers, that is, a region of graphene bilayer, which we call q-region throughout this chapter. We also consider the opposite situation: emergent electrons from a region of bilayer graphene crossing an interface with a region of two uncoupled layers. A third case consider a barrier problem, where a region of uncoupled graphene layers of width d is placed between two semi-infinite regions of bilayer graphene, defining two interfaces.

6.2 Linear and Parabolic dispersion of single and double layer graphene: a continuum approach.

Our starting point is the definition of the Hamiltonian for massless Dirac electrons in graphene, which, around the **K** point in the Brillouin zone, is given by:

$$H = \upsilon_F \sigma \cdot \mathbf{p} \tag{6.1}$$

where $\upsilon_F = 3ta/(2\hbar)$ is the Fermi velocity, with t the nearest-neighbor hopping matrix in graphene and a the carbon-carbon bond length in this material ($a = 1.42$Å); $\sigma = (\sigma_x, \sigma_y)$ are the Pauli Matrices and $\mathbf{p} = -i\hbar\nabla$, the momentum operator.

For all different cases we are considering in this work, it is more convenient to use a 4x4 matrix Hamiltonian to describe our regions of graphene monolayers, instead of the usual 2x2 representation. Our 4x4 Hamiltonian is built in a way that the 2x2 blocks of the main diagonal represent the hamiltonian for each monolayer, arbitrarily defined as layers a and b through this chapter. The 2x2 off-diagonal blocks can introduce terms of interaction between layers. For notational convenience we use natural units ($\hbar = 1 = \upsilon_F$), and the matrix representation for Hamiltonian 6.1 for uncoupled layers, is:

$$H = \begin{pmatrix} \sigma \cdot \mathbf{k} & \mathbf{0} \\ \mathbf{0} & \sigma^* \cdot \mathbf{k} \end{pmatrix} = \begin{pmatrix} 0 & k_x + ik_y & 0 & 0 \\ k_x - ik_y & 0 & 0 & 0 \\ 0 & 0 & 0 & k_x - ik_y \\ 0 & 0 & k_x + ik_y & 0 \end{pmatrix} \tag{6.2}$$

Solving for the energy eigenvalues gives $\varepsilon_\pm(k) = \pm\sqrt{k_x^2 + k_y^2} = \pm k$, with k the absolute value of momentum eigenvalue. The corresponding eigenstates are $\varphi_a^\pm(\mathbf{k}, \mathbf{r}) = e^{i\mathbf{k}\cdot\mathbf{r}}\phi_a^\pm(\mathbf{k})$

and $\varphi_b^{\pm}(\mathbf{k},\mathbf{r}) = e^{i\mathbf{k}\cdot\mathbf{r}}\phi_b^{\pm}(\mathbf{k})$ for layers a and b, respectively, for which the spinors $\phi_a^{\pm}(\mathbf{k})$ and $\phi_b^{\pm}(\mathbf{k})$ have the form:

$$\phi_a^{\pm}(\mathbf{k}) = \frac{1}{\sqrt{2}}\begin{pmatrix} \pm e^{i\theta_k} \\ 1 \\ 0 \\ 0 \end{pmatrix} \tag{6.3}$$

$$\phi_b^{\pm}(\mathbf{k}) = \frac{1}{\sqrt{2}}\begin{pmatrix} 0 \\ 0 \\ \pm e^{-i\theta_k} \\ 1 \end{pmatrix} \tag{6.4}$$

with θ_k=arctan(k_y/k_x), the propagation angle of waves in the region of uncoupled layers.

Although it is well established that electrons in graphene can be treated as massless Dirac particles at low energies, it is important to determine the limit of this approach. By investigation of absorption spectrum of graphene in high magnetic fields, Plochocka *et. al*[80] shows that in the low energy part of the energy spectrum, electrons in graphene are well described by a linear dispersion relation. However, for energies higher than 500 meV a deviation from the ideal behavior of Dirac particles is observed. At an energy of 1.25 eV, for example, deviation from the linearity is around 40 meV.

In order to be consistent with experimental results, we consider a range of energies where the linearity of Dirac cones is valid, extrapolating for slight higher values.

The regions of bilayer graphene are governed by a low-energy effective bilayer hamiltonian. This hamiltonian describes a Bernal (or AB') stacked honeycomb lattice, where atoms of lattice A, in the top layer, are placed directly above the atoms of lattice B' in the bottom layer. The interlayer hopping energy term γ ($\approx$0.35 eV) couples the matrices of the previous non interacting system, and the general form of $H_{AB'}$, in an AB'BA' basis is:

$$H_{AB} = \begin{pmatrix} 0 & q_x + iq_y & \gamma & 0 \\ q_x - iq_y & 0 & 0 & 0 \\ \gamma & 0 & 0 & q_x - iq_y \\ 0 & 0 & q_x + iq_y & 0 \end{pmatrix} \tag{6.5}$$

with $\mathbf{q}$=(q_x,q_y) the momentum operator. For free electrons in a bilayer graphene, the solution of the eigenvalue problem for 6.5, gives the well know parabolic relation between low energy states and total momentum $q = \sqrt{{q_x}^2 + {q_y}^2}$, as

$$\varepsilon_c^{\pm}(\vec{q}) = \frac{\pm\gamma + \sqrt{4q^2 + \gamma^2}}{2} \tag{6.6}$$

and

$$\varepsilon_v^{\pm}(\vec{q}) = \frac{\pm\gamma - \sqrt{4q^2 + \gamma^2}}{2} \tag{6.7}$$

where ε_c and ε_v stands for eigenvalues of conduction and valence bands respectively, represented in Fig. 6.1. The associated eigenvectors $\Psi_\nu^{\pm}(\Psi_A, \Psi_B, \Psi_{B'}, \Psi_{A'})$ are given by $\Psi_c^{\pm}(\mathbf{q}, \mathbf{r}) = e^{i\mathbf{q}\cdot\mathbf{r}}\omega_c^{\pm}(\mathbf{q})$ and $\Psi_v^{\pm}(\mathbf{q}, \mathbf{r}) = e^{i\mathbf{q}\cdot\mathbf{r}}\omega_v^{\pm}(\mathbf{q})$, with corresponding spinors:

$$\omega_c^{\pm}(\mathbf{q}) = N_c^{\pm}(\mathbf{q})\frac{|q|}{q_x + iq_y}\begin{pmatrix} \pm\epsilon_c^{\pm} \\ \pm(q_x - iq_y) \\ \epsilon_c^{\pm} \\ q_x + iq_y \end{pmatrix} \tag{6.8}$$

$$\omega_v^{\pm}(\mathbf{q}) = N_v^{\pm}(\mathbf{q})\frac{|q|}{q_x + iq_y}\begin{pmatrix} \pm\epsilon_v^{\pm} \\ \pm(q_x - iq_y) \\ \epsilon_v^{\pm} \\ q_x + iq_y \end{pmatrix} \tag{6.9}$$

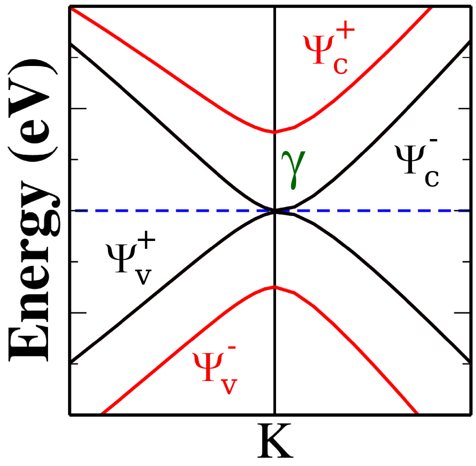

FIGURE 6.1: Band structure of bilayer graphene. Double parabolic bands are observed at low energies with two of them (Ψ_v^+ and Ψ_c^-) touching at zero energies and the other two (Ψ_v^- and Ψ_c^+) showing an energy gap of 2γ ($\gamma \approx 0.35$ eV).

and normalization factors $N^{\pm}_{\nu}(\mathbf{q}) = \left[2\left(|\mathbf{q}|^2 + (\epsilon^{\pm}_{\nu})^2\right)\right]^{-1/2}$, where the subscript ν stands for the conduction (c) and valence (v) bands.

The problems presented here can be considered as the well known 2D step problem, where we consider transmission of electronic waves through the interface between two semi-infinite regions, governed by different Hamiltonians. We also investigate situations similar to the barrier-type problem, where a third region is included, defining a finite region between two interfaces with two semi-infinite regions.

To solve these kind of problems, it is very common to start from determination of the wave-functions corresponding to the different regions, following by invoking their continuity at the interface, to ensure the enforcement of boundary conditions. From this procedure, transmission and reflection coefficients can be obtained. Without lack of generality, we will assume in all cases considered here, that the incidence is always from a state of positive energy (E^{+}_{i}). Also, we consider the interfaces lying along the $\hat{}y$ direction, and so, due to the momentum conservation, electrons will conserve the y-component of the wavevector, and we have always $k_y = q_y$. With these considerations, we will be dealing basically with two situations: electrons crossing an interface between a k- and a q-region from one of the states of positive energy $\varphi^{+}_{a(b)}$ in the $k-$region that can be transmitted to the two states of positive energy in graphene bilayer $\Psi^{\pm}_{c}$ in the q-region and also reflect back to the uncoupled layers. For scattering from the q- to the k-region, electrons emerging from states of positive energy $\Psi^{\pm}_{c}$, can be transmitted to states φ^{+}_{a} and/or φ^{+}_{b}, or reflected back to states $\Psi^{\pm}_{c}$ in the q-region. A schematic example for the case of scattering from the k- to the q-region is shown in Fig.6.2.

In this work, all Hamiltonians are of first order in momentum, and only continuity of the wave function needs to be taken into account, and not their derivatives. However, we must be careful in computing transmission and reflection coefficients. Conservation of probability current $(\mathbf{J})$ normal to the interface will determine the scattering properties of the system. As our interfaces are in the ŷ direction, x̂ component of the current must be conserved. With these considerations, for $k-$ and $q-$regions we must have always

$$J^{k}_{x} = J^{q}_{x}. \tag{6.10}$$

The probability current in each medium can be calculated by taking the mean values of the current operator, defined as equation 6.11, with its corresponding $\Psi^{i}_{I,II}$ states (i = q, k).

$$\vec{J} = e\vec{\sigma} \Rightarrow J^{i}_{I,IIx} = e\langle\Psi^{i}_{I,II}|\sigma_x|\Psi^{i}_{I,II}\rangle \tag{6.11}$$

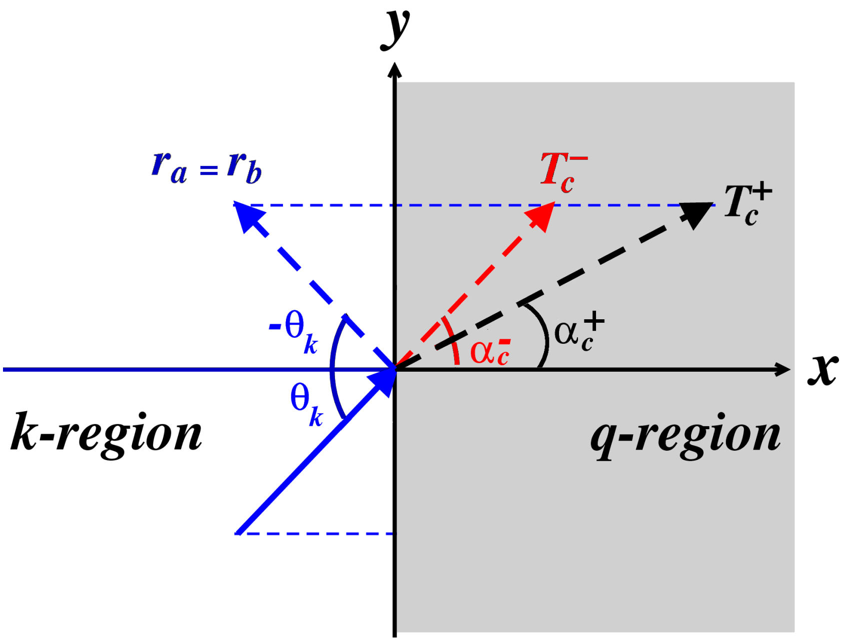

FIGURE 6.2: Example of incidence from the k- to the q-region. Electron emerging from a state of positive energy $\varphi^+_{a(b)}$ with angle of incidence θ_k can be transmitted to the q-region for states $\Psi^\pm_c$ with transmission probabilities $T^\pm_c$ or reflected back to the q-region. Angles $\theta_k (= arctan(k_y/k_x))$, and $\alpha^\pm_c$ are also shown.

6.3 Scattering

6.3.1 Monolayer-Bilayer interface

We start by considering the incidence of an electron from a semi-infinite k-region through an interface with a semi-infinite q-region. The two uncoupled layers in the k-region are completely equivalent, and we can choose the incidence from layer a. Defining r_a and r_b as the reflection coefficients for layers a and b, respectively, the wave-function in the k-region can be written:

$$\Psi^k_I(\mathbf{k},\mathbf{r}) = \varphi^+_a(\mathbf{k},\mathbf{r}) + r_a\varphi^+_a(\mathbf{k},\mathbf{r}) + r_b\varphi^+_b(\mathbf{k},\mathbf{r}), \tag{6.12}$$

By conservation of energy, electrons can be transmitted to both states of positive eigenvalues in the q-region of bilayer graphene $\Psi^\pm_c(\mathbf{q},\mathbf{r})$, with probabilities t^+_c and t^-_c, and the wave function assume the form:

$$\Psi^q_{II}(\mathbf{q},\mathbf{r}) = t^+_c\Psi^+_c(\mathbf{q},\mathbf{r}) + t^-_c\Psi^-_c(\mathbf{q},\mathbf{r}). \tag{6.13}$$

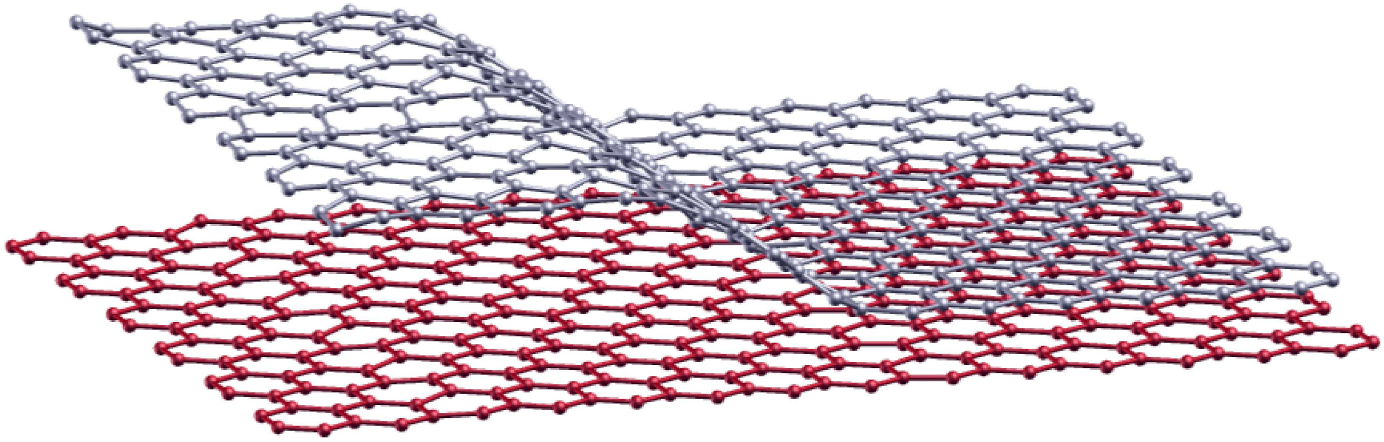

Figure 6.3: Interface between uncoupled layers, that obey the Dirac Hamiltonian of monolayer graphene, and a region of bilayer graphene for which a parabolic dispersion is observed at low energies.

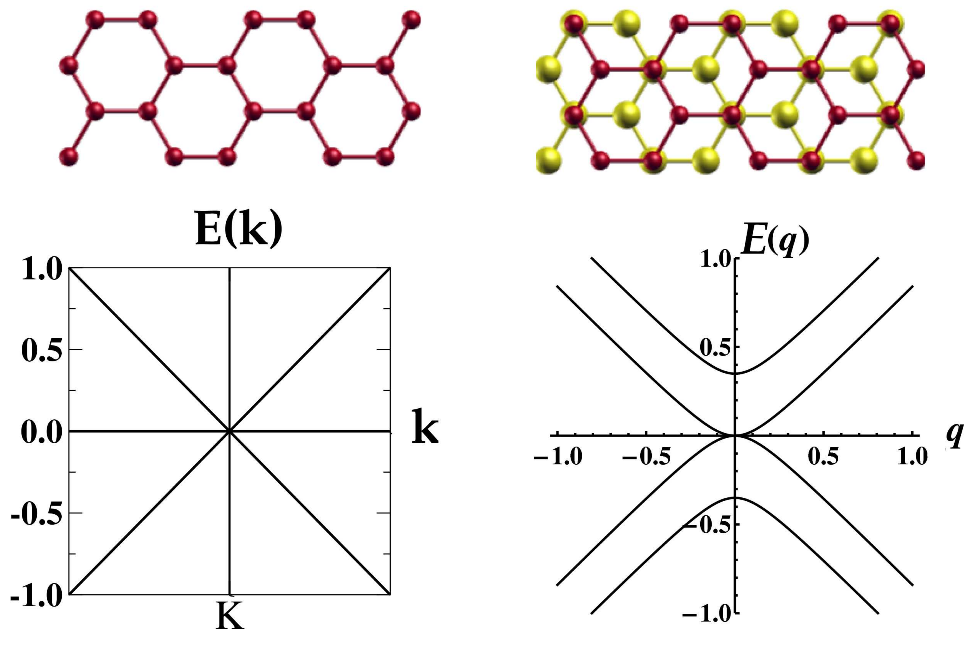

Figure 6.4: Scattering from k- to q-region: electrons initially in a region with linear dispersion (left panel), characteristic of monolayer graphene systems, go through a region of bilayer graphene with parabolic dispersion (right panel).

Computation of coefficients r_a, r_b, t_c^+ and t_c^- can be done by invoking continuity of the wave functions at the interface of the different media. At the interface (x=0) we must have:

$$\Psi_I^k(\mathbf{k}, x = 0, y) = \Psi_{II}^q(\mathbf{q}, x = 0, y), \tag{6.14}$$

and so:

$$\begin{aligned}\varphi_a^+(k_x, k_y, 0, y) + r_a\varphi_a^+(-k_x, k_y, 0, y) + r_b\varphi_b^+(-k_x, k_y, 0, y) = \\ t_c^+\Psi_c^+(q_x, q_y, 0, y) + t_c^-\Psi_c^-(q_x, q_y, 0, y).\end{aligned} \tag{6.15}$$

For the k-region, with uncoupled monolayers, J_x^k for the state $\Psi_I^k(\mathbf{k}, \mathbf{r})$ is:

$$J_{Ix}^k = [1 - |r_a|^2 - |r_b|^2]cos(\theta_k) \tag{6.16}$$

where $\theta_k = arctan(k_y/k_x)$ is the angle of incidence of the particle with respect to the normal to the interface, $\hat{\mathrm{x}}$ direction in our case, as shown in Fig. 6.2.

In the same way, we define the scattering angles for states Ψ_c^+ and Ψ_c^- as α_c^+ and α_c^-, and conservation of momentum give us:

$$k_y = q_{yc}^+ = q_{yc}^- \tag{6.17}$$

and so:

$$ksin(\theta_k) = q_c^+ sin(\alpha_c^+) = q_c^- sin(\alpha_c^-). \tag{6.18}$$

For the q-region, we have to be more careful in calculating the probability current. Conservation of energy requires $\varepsilon_c^\pm = +k$, and enable us to write the momenta amplitudes $q_c^\pm$ as a function of the incident energy $+k$, by doing:

$$\varepsilon_c^+ = \frac{\gamma + \sqrt{4{q_c^+}^2 + \gamma^2}}{2} = k \rightarrow q_c^+ = \sqrt{k(k-\gamma)} \tag{6.19}$$

$$\varepsilon_c^- = \frac{-\gamma + \sqrt{4{q_c^-}^2 + \gamma^2}}{2} = k \rightarrow q_c^- = \sqrt{k(k+\gamma)}. \tag{6.20}$$

The expression for q_c^+ shows the existence of evanescent states in the q-region for bands Ψ_c^+ when the incident energy is less than γ. For such range of energies, q_c^+ becomes imaginary, and electrons cannot propagate in these states.

However, incident energy greater than γ is not the only requirement to observe transmission to states Ψ_c^+. Scattering angles $\alpha_c^\pm$ written as a function of k, (eq. 6.21 and 6.22) shows that the argument of *arcsin* for α_c^- is always real and less than 1. However, this is not true for α_c^+. For values of k less than a critical value k_c, the argument of *arcsin* becomes greater than 1 and we have an imaginary angle.

$$\alpha_c^+ = arcsin\left(\sqrt{\frac{k}{k-\gamma}} sin(\theta_k)\right) \tag{6.21}$$

$$\alpha_c^- = arcsin\left(\sqrt{\frac{k}{k+\gamma}} sin(\theta_k)\right) \tag{6.22}$$

This means that for $k < k_c$ (and not just $k < \gamma$), we must observe total reflection for Ψ_c^+ states. It is easy to see that:

$$k_c = \frac{\gamma}{cos^2(\theta_k)}. \tag{6.23}$$

Hence, for the band of higher energies in bilayer graphene, governed by eigenvectors Ψ_h^+, we have three regimes:

1. $k < \gamma$: total reflection and an exponential decay of the state;
2. $\gamma < k < k_c$: no exponential decay but still total reflection of electrons;
3. $k > k_c$: partial transmission and reflection.

This behavior is a consequence of conservation of ŷ component of momentum. In Fig. 6.5, a vectorial representation of momentum in k- and q-region is shown. For incidence from the degenerate cones of uncoupled monolayers, it is just possible to conserve the ŷ component of $\mathbf{k}$ (k_y) when $\mathbf{k}$ is in the range represented by the yellow area. For incidence with any momentum outside that interval, there is no possible q_c^+ in q-region which conserves k_y, and so, it is not possible to observe transmission to Ψ_c^+ states.

Therefore, states accessible to the scattered particle depends on its incident energy (and momentum) k, and we will deal with each specific case in the following.

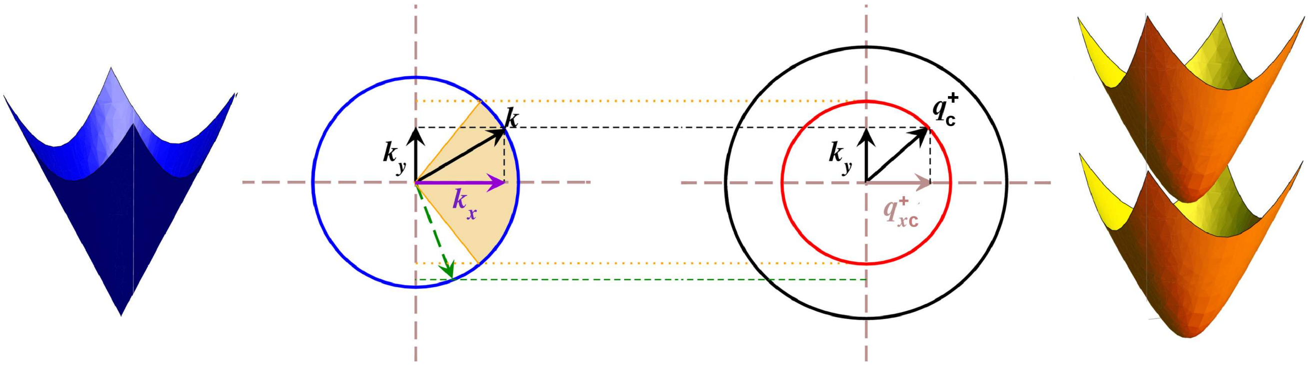

(a)

FIGURE 6.5: Critical energies occurs for initial states when it is not possible to conserve the ŷ component of momentum in the scattering process. The yellow area in the blue circle corresponds to the range of initial momentum **k** in the k-region for which the ŷ component can be conserved in the q-region. For scattering from a k- to a q-region we have $k_c = \frac{\gamma}{cos^2(\theta_k)}$.

Incident energy $k < \gamma$

For electrons with incident energy $k < \gamma$, both momentum q_c^+ and its scattering angle α_c^+ are complex. For this range of energies, q_c^+ and α_c^+ are purely imaginary, and so we can define:

$$q_c^+ = iQ_c^+ \qquad and \qquad \alpha_c^+ = -i\Omega_c^+ \tag{6.24}$$

with $Q_c^+ = \sqrt{k(\gamma - k)}$ and $\Omega_c^+ = arcsinh\left(\sqrt{\frac{k}{\gamma-k}}sin(\theta_k)\right)$ real and positive numbers. As the ŷ component of momentum q_{yc}^+ is always real, an imaginary q_c^+ means that its x̂ component q_{xc}^+ must be imaginary, and we can write it as $q_{xc}^+ = iQ_{xc}^+$. As $q_{xc}^+ = q_c^+cos(\alpha_c^+)$, for $k < \gamma$, we can write $q_{xc}^+ = iQ_c^+cos(-i\Omega_c^+) = iQ_c^+cosh(\Omega_c^+)$, from which $Q_{xc}^+ = Q_c^+cosh(\Omega_c^+)$. With these definitions, eigenstate Ψ_c^+ for $k < \gamma$ is:

$$\Psi_c^+(\mathbf{q}) = e^{-Q_{xc}^+x+iq_{yc}^+y}N_c^+(\mathbf{q})\frac{Q_c^+}{Q_{xc}^+ + q_{yc}^+}\begin{pmatrix} \epsilon_c^+ \\ i(Q_{xc}^+ - q_{yc}^+) \\ \epsilon_c^+ \\ i(Q_{xc}^+ + q_{yc}^+) \end{pmatrix} \tag{6.25}$$

The probability current density can be obtained by:

$$J_x^q = e\langle\Psi_{II}^q|\sigma_x|\Psi_{II}^q\rangle \tag{6.26}$$

and we find:

$$J_x^q = e\frac{2\sqrt{k(k+\gamma)}cos(\Omega_c^+)}{\gamma+2k}|t_c^-|^2 \qquad (k<\gamma) \tag{6.27}$$

with $|t_c^-|$ the coefficient transmission for the band of lower energies in the graphene bilayer, governed by eigenstates Ψ_c^-. To obtain the total transmission coefficient $T = 1-|r_a|^2-|r_b|^2$, we invoke the conservation of $\vec{J}$, which requires $J_x^k = J_x^q$, and we have:

$$T_{k<\gamma} = \frac{2\sqrt{k(k+\gamma)}}{\gamma+2k}\frac{cos(\Omega_c^+)}{cos(\theta_k)}|t_c^-|^2. \tag{6.28}$$

As expected, there is no contribution from states Ψ_h^+ to the transmission probability: particles are transmitted just to states Ψ_c^-.

Incident energy $\gamma < k < k_c$

For incident particles with energy k in the range $\gamma < k < k_c$, momentum q_c^+ is no longer complex, but the scattering angle α_c^+ is still complex, as the argument of *arcsin* in 6.21 is bigger than one. In this case, we consider:

$$sin(\alpha_c^+) \to sin(\xi + i\beta) = \left(\sqrt{\frac{k}{k-\gamma}}sin(\theta_k)\right). \tag{6.29}$$

Eq. 6.29 can be rewritten if we expand the argument of $sin(\xi+i\beta)$ as:

$$sin(\xi+i\beta) = sen(\xi)cosh(\beta) + icos(\xi)sinh(\beta), \tag{6.30}$$

and, for $sin(\xi+i\beta)$ be real and bigger than one, we need to consider $\xi = \pi/2$, which results:

$$sin(\pi/2 + i\beta) = cosh(\beta) \tag{6.31}$$

and we have a coherent result, as the function $cosh(x)$ is always real and has a minimum value of 1 for any $x \in \Re$. By comparing equations 6.29 and 6.31 we find:

$$\beta = arcosh\left(\sqrt{\frac{k}{k-\gamma}}sin(\theta_k)\right). \tag{6.32}$$

The x̂ component of momentum, q_{xc}^+, now takes the form:

$$q_{xc}^+ = q_c^+ cos(\pi/2 + i\beta) = iq_c^+ sinh(\beta) = iQ_{xc}^+ \tag{6.33}$$

where now $Q_{xc}^+ = q_c^+ sinh(\beta)$.

The eigenstate Ψ_c^+ for $\gamma < k < k_c$ has the same structure as for incident energy $k < \gamma$, but now, the spatial component is not evanescent anymore, as the momentum q_c^+ is real.

The probability current is calculated as in Eq. 6.11, and it is found to be given by the same expression as in the case $k < \gamma$:

$$J_x^q = \frac{2\sqrt{k(k+\gamma)}cos(\beta)}{\gamma + 2k}|t_c^-|^2. \tag{6.34}$$

and the total coefficient transmission is:

$$T_{\gamma<k<k_c} = \frac{2\sqrt{k(k+\gamma)}}{\gamma + 2k}\frac{cos(\beta)}{cos(\theta_k)}|t_c^-|^2. \tag{6.35}$$

As for incident energy $k < \gamma$, also for this range of values of k, there is no transmission to the higher-energy band states, but just reflection to the uncoupled layers a and b and partial transmission to states Ψ_c^-.

Incident energy $k > k_c$

For particles with incident energy $k > k_c$, all momentum and scattering angles are real and we can compute transmission and reflection coefficients directly from H_{AB}. By evaluating the current probability, we obtain:

$$J_{xII}^q = 2\sqrt{k}\left[\frac{\sqrt{k+\gamma}}{\gamma + 2k}cos(\alpha_c^-)|t_c^-|^2 + \frac{\sqrt{k-\gamma}}{2k-\gamma}cos(\alpha_c^+)|t_c^+|^2\right] \tag{6.36}$$

and the total transmission coefficient is obtained as:

$$T_{k>k_c} = \frac{2\sqrt{k}}{cos(\theta_k)}\left[\frac{\sqrt{k+\gamma}}{\gamma + 2k}cos(\alpha_c^-)|t_c^-|^2 - \frac{\sqrt{k-\gamma}}{\gamma - 2k}cos(\alpha_c^+)|t_c^+|^2\right] \tag{6.37}$$

As expected, incident particles with energy bigger than $k_c = \gamma/cos^2(\theta_k)$ can be scattered for both states of positive energy in graphene bilayer. There is partial transmission for these bands and partial reflection for states to the k-region.

6.3.2 Transmission and Reflection coefficients

Direct Incidence We start by considering a direct incidence:

$$\theta_k = \alpha_c^+ = \alpha_c^- = 0 \tag{6.38}$$

and our problem can be addressed as an unidimensional problem. In this case we have $cos(\theta_k) = cos(0) = 1$, $k_c = \gamma$ and there are just two regimes to be considered: $k < \gamma$ and $k > \gamma$. We can use the matrix representation for continuity of the wave functions (Eq. 6.16), as:

$$M \cdot \vec{\eta} = \vec{\eta_0} \tag{6.39}$$

where:

$$M = \begin{pmatrix} \frac{1}{\sqrt{2}} & 0 & N_c^+ \epsilon_c^+ & -N_c^- \epsilon_c^- \\ -\frac{1}{\sqrt{2}} & 0 & N_c^+ q_{xc}^+ & N_c^- q_{xc}^- \\ 0 & \frac{1}{\sqrt{2}} & N_c^+ \epsilon_c^+ & -N_c^- \epsilon_c^- \\ 0 & \frac{1}{\sqrt{2}} & N_c^+ q_{xc}^+ & N_c^- q_{xc}^- \end{pmatrix}$$

$$\vec{\eta} = \begin{pmatrix} r_a \\ r_b \\ t_c^+ \\ t_c^- \end{pmatrix}$$

$$\vec{\eta_0} = \begin{pmatrix} \frac{1}{\sqrt{2}} \\ \frac{1}{\sqrt{2}} \\ 0 \\ 0 \end{pmatrix}$$

with solution for coefficients r_a, r_b, t_c^+, t_c^-:

$$\vec{\eta} = M^{-1} \cdot \vec{\eta_0}. \tag{6.40}$$

By solving (6.40), we found the expressions for reflection and transmission coefficients:

$$r_a = -\frac{\gamma + \sqrt{k(k-\gamma)} - \sqrt{k(k+\gamma)}}{\gamma} \tag{6.41}$$

$$r_b = \frac{2k - \sqrt{k(k-\gamma)} - \sqrt{k(k+\gamma)}}{\gamma} \tag{6.42}$$

$$t_c^+ = \frac{\sqrt{k(2k-\gamma)}}{k + \sqrt{k(k-\gamma)}} \tag{6.43}$$

$$t_c^- = \frac{\sqrt{k(2k+\gamma)}}{k + \sqrt{k(k+\gamma)}}. \tag{6.44}$$

which are valid for $k > \gamma$.

For $k < \gamma$, we can make the substitution of imaginary q_c^+ and α_c^+ in the wave functions, impose the boundary conditions to find the coefficients (this is equivalent to make $q_c^+ = \sqrt{k(k-\gamma)} \rightarrow i\sqrt{k(\gamma-k)}$ in equations 6.41-6.44).

Substitution of expressions 6.41-6.44 in Eqs. 6.28 and 6.37 gives us the transmission amplitudes for states $\Psi_c^\pm$ as a function of the incident energy k, for $k < \gamma$ and $k > k_c$, respectively. The resulting plot can be seen in Fig. 6.7. Reflection for layers a and b can also be obtained, and are presented in Fig. 6.6.

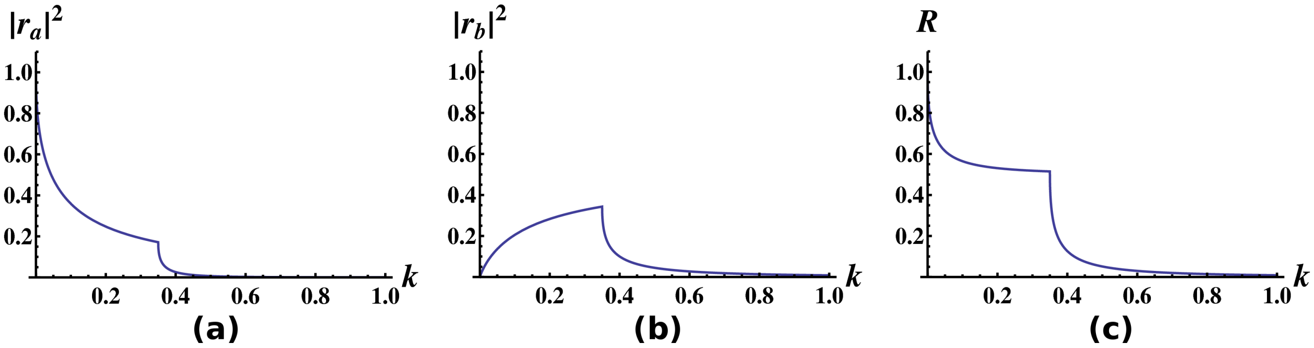

FIGURE 6.6: Reflection coefficients $|r_a|^2$, $|r_b|^2$ and $R = |r_a|^2 + |r_b|^2$ for direct incidence ($\theta_k = 0$) from k- to q-region as a function of the energy of incidence k.

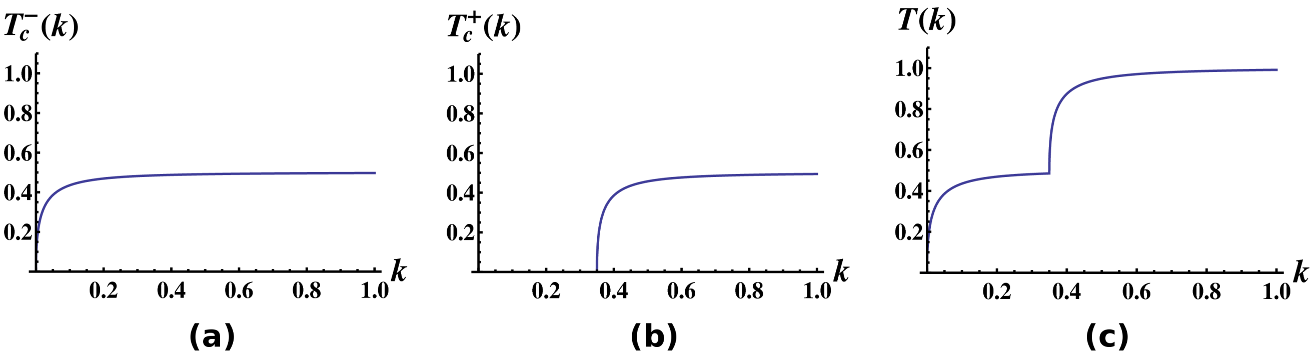

FIGURE 6.7: Transmission coefficients T_c^+ and T_c^- to states of higher and lower energy in bilayer graphene Ψ_c^+ and Ψ_c^-, and total transmission to the q-region $T = T_c^+ + T_c^-$.

We see that for small k, the particle is mainly reflected to the same layer of incidence (layer a). By increasing the incidence energy of electrons, we start to observe reflection to states of layer b and also transmission to Ψ_c^- states of the bilayer, followed by a decreasing of reflection to layer a. As expected, no transmission to states Ψ_c^+ is observed for energy of incidence $k < \gamma$, as can be seen in Fig. 6.7. When the incident particle has energy bigger than the interaction energy between layers in the bilayer (γ), total reflection for layers a and b shows a faster decrease, as can be seen by plots of coefficients R for $k > 0.35$ eV, in Fig. 6.6-c. These remarkable decrease in reflection for uncoupled layers is followed by an increasing of the amplitude transmission to $\Psi_c^\pm$ states. For $k \gtrsim 0.65$ eV, transmission to both states in graphene bilayer are equally possible, and reflection for both uncoupled layers are quite small.

Oblique Incidence For oblique incidence, $\theta_k \neq 0$ in k-region, and the particle propagates with angles $\alpha_c^\pm$ in the graphene bilayer, and we now have to consider a bidimensional problem. Generalization of matrices M and η_0 are then obtained for the angle of incidence $-\frac{\pi}{2} < \theta_k < \frac{\pi}{2}$, as:

$$M = \begin{pmatrix} \frac{e^{-i\theta_k}}{\sqrt{2}} & 0 & N_c^+ \epsilon_c^+ e^{-i\alpha_c^+} & -N_c^- \epsilon_c^- e^{-i\alpha_c^-} \\ -\frac{1}{\sqrt{2}} & 0 & N_c^+ q_c^+ e^{-2i\alpha_c^+} & N_c^- q_c^- e^{-2i\alpha_c^-} \\ 0 & \frac{e^{i\theta_k}}{\sqrt{2}} & N_c^+ \epsilon_c^+ e^{-i\alpha_c^+} & -N_c^- \epsilon_c^- e^{-i\alpha_c^-} \\ 0 & \frac{1}{\sqrt{2}} & N_c^+ q_c^+ & N_c^- q_c^- \end{pmatrix}$$

$$\vec{\eta_0} = \begin{pmatrix} \frac{e^{i\theta_k}}{\sqrt{2}} \\ \frac{1}{\sqrt{2}} \\ 0 \\ 0 \end{pmatrix}$$

By the same process used to obtain the coefficients for direct scattering, we derive their generalization for oblique incidence:

$$r_a = \frac{k^2 - q_c^+ q_c^- cos(\alpha_c^+ - \alpha_c^-)}{q_c^+ q_c^- cos(\alpha_c^+ - \alpha_c^-) + k[k + q_c^+ cos(\alpha_c^+ + \theta_k) + q_c^- cos(\alpha_c^- + \theta_k)]} \tag{6.45}$$

$$r_b = \frac{-kcos(\theta_k)[q_c^+ cos(\alpha_c^+) - q_c^- cos(\alpha_c^-)]}{q_c^+ q_c^- cos(\alpha_c^+ - \alpha_c^-) + k[k + q_c^+ cos(\alpha_c^+ - \theta_k) + q_c^- cos(\alpha_c^- - \theta_k)]} \tag{6.46}$$

$$t_c^+ = \frac{(1 + e^{-2i\theta_k})(k + q_c^- e^{i(\alpha_c^- + \theta_k)} \sqrt{q_c^{+2} + k^2})}{2[q_c^+ q_c^- cos(\alpha_c^+ - \alpha_c^-) + k[k + q_c^+ cos(\alpha_c^+ - \theta_k) + q_c^- cos(\alpha_c^- - \theta_k)]]} \tag{6.47}$$

$$t_c^- = \frac{(1+e^{-2i\theta_k})(k+q_c^+ e^{i(\alpha_c^+ +\theta_k)}\sqrt{{q_c^-}^2+k^2})}{2[q_c^+ q_c^- cos(\alpha_c^+ - \alpha_c^-) + k[k + q_c^+ cos(\alpha_c^+ - \theta_k) + q_c^- cos(\alpha_c^- - \theta_k)]]} \tag{6.48}$$

which are valid in these forms for $k > k_c$, when there are no evanescent states.

Reflection and transmission coefficients as a function of the angle of incidence θ_k, can be seen in Figs. 6.8 and 6.9. In this representation, we can define the critical angle from 6.23 $\theta_c(k) = arcos\left(\sqrt{\frac{\gamma}{k}}\right)$ which depends on the incident energy k. Transmission for states Ψ_c^+ is observed for $-\theta_c(k) < \theta_k < \theta_c(k)$, that corresponds to $k > k_c$, as can be seen in Fig. 6.9-b for different values of k. By increasing the incident energy from $k \gtrsim \gamma$, transmission to such states is observed also to increase, until saturating at ~ 0.5 for $k \gtrsim 0.7$. On the other hand, transmission to states Ψ_c^- is observed for any angle of incidence. For these states, transmission is also constant in ~ 0.5 for intermediate angles, but an abrupt decrease is observed as we increase θ_k for T_c^-, that goes to null values as $\theta_k \Rightarrow \pi/2$, as should be expected.

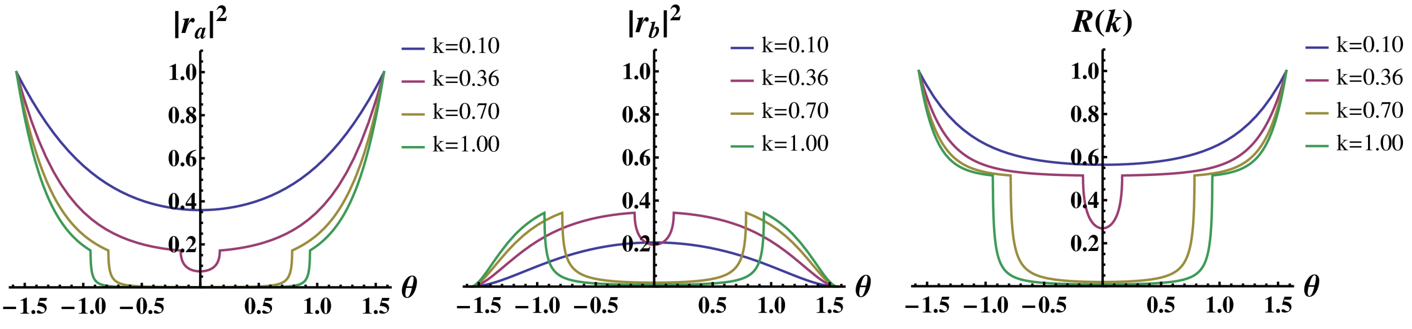

(a) **(b)** **(c)**

FIGURE 6.8: k-to q-region: Reflection coefficients $|r_a|$, $|r_b|$ for layers a and b and total reflection $|R| = |r_a| + |r_b|$ as a function of the angle of incidence θ_k.

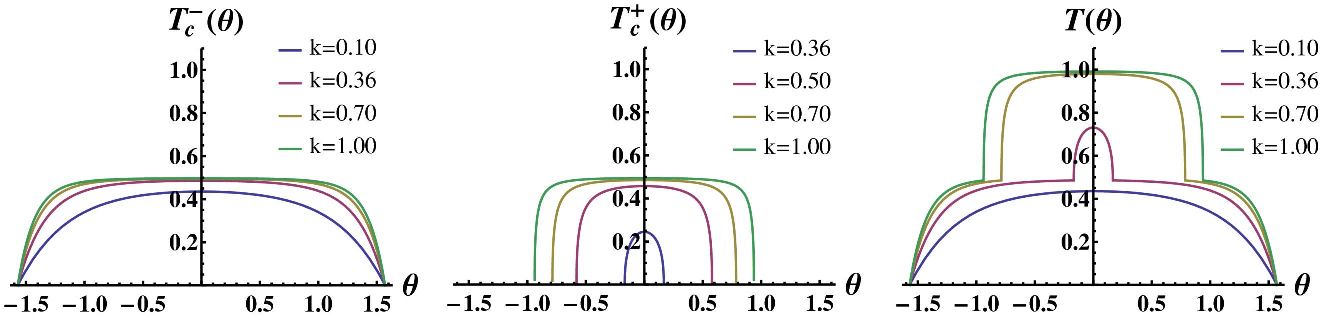

(a) **(b)** **(c)**

FIGURE 6.9: k-to q-region: Transmission coefficients $T_c^{\mp}$ for states $Psi_c^{\mp}$ and total reflection $T = T_c^- + T_c^+$ to the q-region as a function of the angle of incidence θ_k.

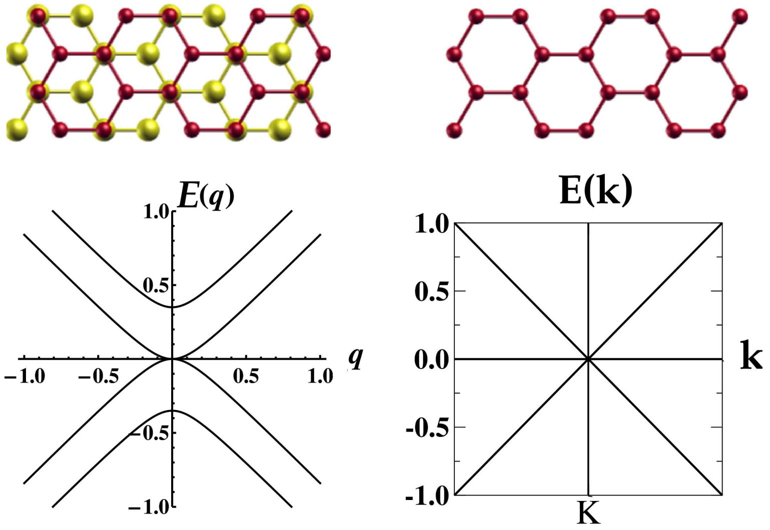

FIGURE 6.10: For scattering from a q- to a k-region electrons at low energies go from a parabolic to a linear dispersion regime.

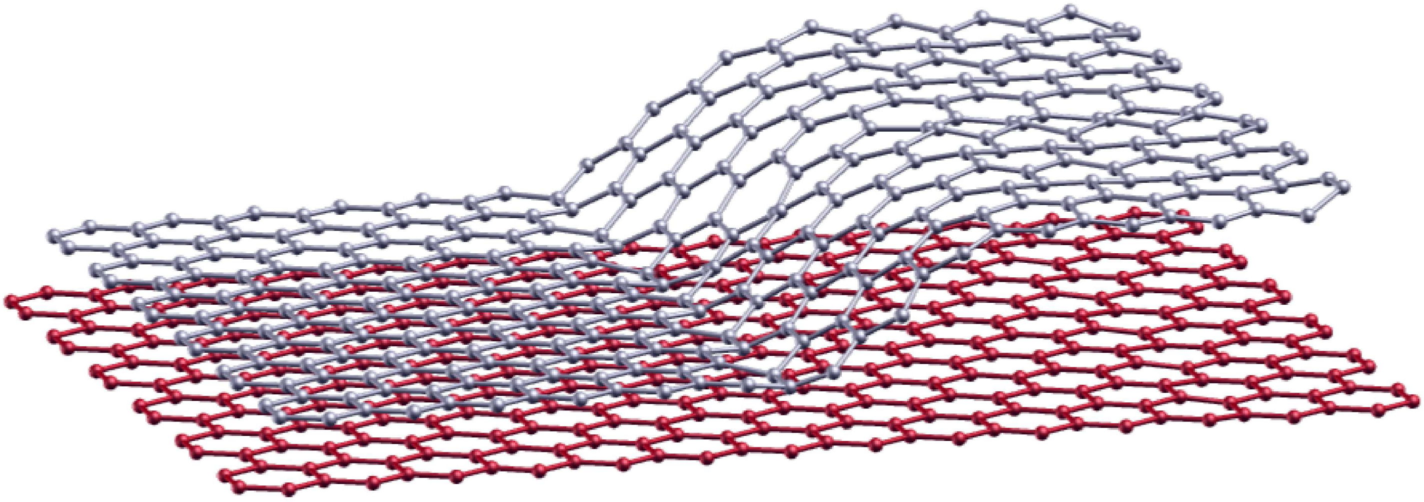

FIGURE 6.11: Interface between bilayer graphene and a second region of uncoupled graphene layers.

6.3.3 Bilayer-Monolayer interface

When we consider a particle coming from the q-region and going through the interface with a k-region, the initial state can be Ψ_c^+ or Ψ_c^-, the two states of positive energies in bilayer graphene. For incidence from the gapped state Ψ_c^+, there will be always a state in the k-region where it is possible to conserve the $\hat{y}$ component of momentum. Therefore, for incidence from these states, there are no critical energies (or critical angles) and we will always observe propagating states in the k-region. On the other hand, incidence from states of lower energy Ψ_c^-, will define the critical energy k_c:

$$k_c = \gamma tg^2(\alpha_c^-) \tag{6.49}$$

obtained by straightforward manipulation of expressions for conservation of momentum (Eq. 6.18). Incidence from states Ψ_c^- will, therefore, be totally reflected to the q-region for $k < \gamma tg^2(\alpha_c^-)$. For this range of energies, the propagation angle in the k-region, θ_k, will be imaginary, and by the same process used for the immaginary angle in the scattering from the k-region to the q-region for $\gamma < k < k_c$, we can make:

$$\theta_k \Rightarrow \pi/2 + i\beta \tag{6.50}$$

with

$$\beta = arcosh\left(\sqrt{\frac{k+\gamma}{k}} sin(\alpha_c^-)\right). \tag{6.51}$$

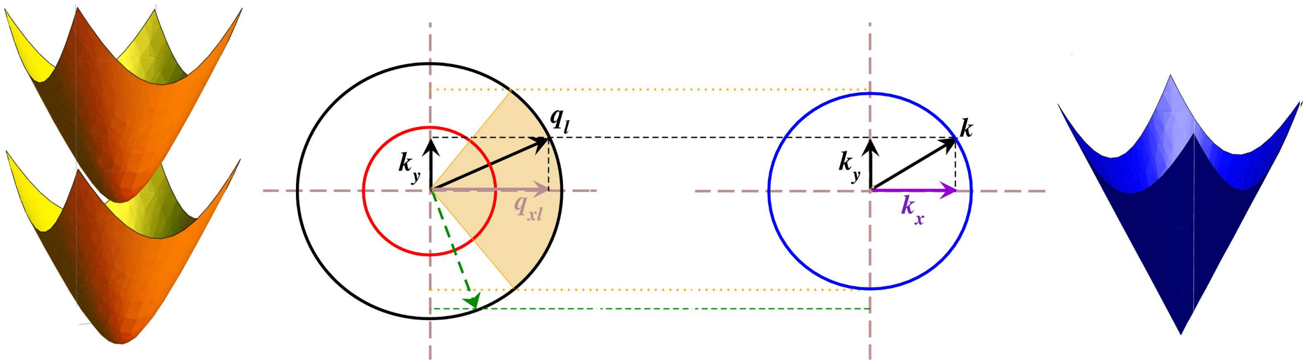

FIGURE 6.12: For electrons crossing an interface between a q- and a k-region the critical angle k_c is defined as $k_c = \gamma tg^2(\alpha_c^-)$ for incidence from Ψ_c^-.

Indeed, computation of probability current for $k < \gamma tg^2(\alpha_c^-)$ gives:

$$J_x^k = 0 \tag{6.52}$$

showing that there is no current in the k-region, as electrons can not be transmitted to any of the uncoupled layers when they are initially in Ψ_c^- with incident energy $k < k_c$.

For propagating states in the k-region, probability currents for the q- and k-regions assume the form:

$$J_x^q = 4k\left[N_c^{i2} q_c^i cos(\alpha_c^i)(1 - |r_c^i|^2) - N_c^{j2} q_c^j cos(\alpha_c^j)|r_c^j|^2\right] \tag{6.53}$$

$$J_x^k = \left[|t_a|^2 + |t_b|^2\right] cos(\theta_k) \tag{6.54}$$

where in expression for J_x^q, i, j stands for $+, -$ states, with i the incident state. By continuity of J_x we have:

$$\frac{cos(\theta_k)}{4k{N_c^i}^2 q_c^i cos(\alpha_c^i)} \left[|t_a|^2 + |t_b|^2\right] = 1 - |r_c^i|^2 - \frac{{N_c^j}^2 q_c^j}{{N_c^i}^2 q_c^i} \frac{cos(\alpha_c^i)}{cos(\alpha_c^j)} |r_c^j|^2 \tag{6.55}$$

Transmission and reflection coefficients can be evaluated by the same process considered in the k- to q-region scattering. Solution for continuity of wave functions at the interface ($x = 0$), for incidence from Ψ_c^+ states, gives:

$$r_c^+ = \frac{e^{-2i\alpha_c^+}[-q_c^+(kcos(\alpha_c^+ - \theta_k) + q_c^- cos(\alpha_c^+ + \alpha_c^-)) + k(k + q_c^- cos(\alpha_c^- + \theta_k))]}{q_c^+[kcos(\alpha_c^+ + \theta_k) + q_c^- cos(\alpha_c^+ - \alpha_c^-)) + k(k + q_c^- cos(\alpha_c^- + \theta_k))]} \tag{6.56}$$

$$r_c^- = \frac{2ie^{i(\alpha_c^- - \alpha_c^+)} cos(\alpha_c^+) N_c^- {q_c^-}^2 [q_c^+ sin(\alpha_c^+) - ksin(\theta_k)]}{N_c^+[{q_c^+}^2(kcos(\alpha_c^+ + \theta_k) + q_c^- cos(\alpha_c^+ - \alpha_c^-)) + kq_c^+(k + q_c^- cos(\alpha_c^- + \theta_k))]} \tag{6.57}$$

$$t_a = \frac{\sqrt{2}ke^{-i\theta_k}(1 + e^{-2i\alpha_c^+})[ke^{i\theta_k} + q_c^- cos(\alpha_c^-) - iq_c^+ sin(\alpha_c^+)]}{N_h[q_h^2(kcos(\alpha_c^+ + \theta_k) + q_c^- cos(\alpha_c^+ - \alpha_c^-)) + kq_c^+(k + q_c^- cos(\alpha_c^- + \theta_k))]} \tag{6.58}$$

$$t_b = \frac{\sqrt{2}ke^{-i\theta_k}(1 + e^{-2i\alpha_c^+})[ke^{-i\theta_k} + q_c^- cos(\alpha_c^-) + iq_c^+ sin(\alpha_c^+)]}{N_c^+[{q_c^+}^2{}_h(kcos(\alpha_c^+ + \theta_k) + q_c^- cos(\alpha_c^+ - \alpha_c^-)) + kq_c^+(k + q_c^- cos(\alpha_c^- + \theta_k))]}. \tag{6.59}$$

For direct incidence, when $\alpha_c^+ = 0 \to \alpha_c^- = \theta_k = 0$, Eqs. 6.56-6.59 take a simpler form:

$$r_c^+ = \frac{2k - \gamma - 2\sqrt{k(k-\gamma)}}{\gamma} \tag{6.60}$$

$$r_c^- = 0 \tag{6.61}$$

$$t_c^+ = t_c^- = \frac{2k\sqrt{|k-\gamma|}}{\sqrt{|k-\gamma|+k}(k+\sqrt{k(k-\gamma)})}. \tag{6.62}$$

For incidence from states of lower energy, Ψ_c^-, a very similar result is obtained. Now, t_a, t_b, r_c^+ and r_c^- are:

$$r_c^- = \frac{e^{2i\alpha_c^-}[k^2 + kq_c^+ cos(\alpha_c^+ + \theta_k) - q_c^-(kcos(\alpha_c^- - \theta_k) + q_c^+ cos(\alpha_c^- + \alpha_c^+)]}{q_c^+[kcos(\alpha_c^+ + \theta_k) + q_c^- cos(\alpha_c^- - \alpha_c^+)) + k(k + q_c^- cos(\alpha_c^- + \theta_k)]} \tag{6.63}$$

$$r_c^+ = \frac{2ie^{i(\alpha_c^- - \alpha_c^+)}cos(\alpha_c^-)N_c^+ {q_c^+}^2[q_c^- sin(\alpha_c^-) - ksin(\theta_k)]}{N_c^-[{q_c^-}^2(q_c^+ cos(\alpha_c^+ - \alpha_c^-) + kcos(\alpha_c^- + \theta_k)) + kq_c^-(k + q_c^+ cos(\alpha_c^+ + \theta_k))]} \tag{6.64}$$

$$t_a = -t_b = \frac{\sqrt{2}ke^{-i\theta_k}(1 + e^{2i\alpha_c^-})[ke^{i\theta_k} + q_c^+ cos(\alpha_c^+) - iq_c^- sin(\alpha_c^-)]}{N_c^-[{q_c^-}^2(q_c^+ cos(\alpha_c^+ - \alpha_c^-) + kcos(\alpha_c^- + \theta_k)) + kq_c^-(k + q_c^+ cos(\alpha_c^+ + \theta_k))]} \tag{6.65}$$

and for direct incidence ($\alpha_c^- = 0 \rightarrow \alpha_c^+ = \theta_k = 0$) 6.63-6.65 reduces to:

$$r_c^- = -\frac{2k + \gamma - 2\sqrt{k(k+\gamma)}}{\gamma} \tag{6.66}$$

$$r_c^+ = 0 \tag{6.67}$$

$$t_c^+ = -t_c^- = \frac{2k\sqrt{k+\gamma}}{\sqrt{2k+\gamma}(k+\sqrt{k(k+\gamma)})} \tag{6.68}$$

The general results for incidence from states Ψ_c^+ and Ψ_c^- are very similar, with a few differences. The first point to notice is that, due to the conservation of the ŷ component of momentum, reflection coefficients r_c^+ and r_c^- are null, when the states of incidence are Ψ_c^- and Ψ_c^+, respectively. This can be checked in expressions 6.57 and 6.64, for which the terms in numerator $q_c^\pm sin(\alpha_c^\pm) - ksin(\theta_k)$ are identically zero.

From this result, we see that reflection in the q-k-interface to the q-region occurs just to the same state of incidence, the other state of positive energy not being accessible, as a requirement of momentum conservation.

For each incident state, transmission to the k-region occurs for both uncoupled layers equally, as should be expected. When the incidence is from the band of higher energy Ψ_c^+, a fast increase of the transmission amplitude is observed for $k \gtrsim \gamma$ (Fig.6.14-a), with a saturation for T_a and $T_b = 0.5$, when reflection to the initial state goes to zero (Fig. 6.13), and the electron is transmitted with the same probability for both uncoupled layers.

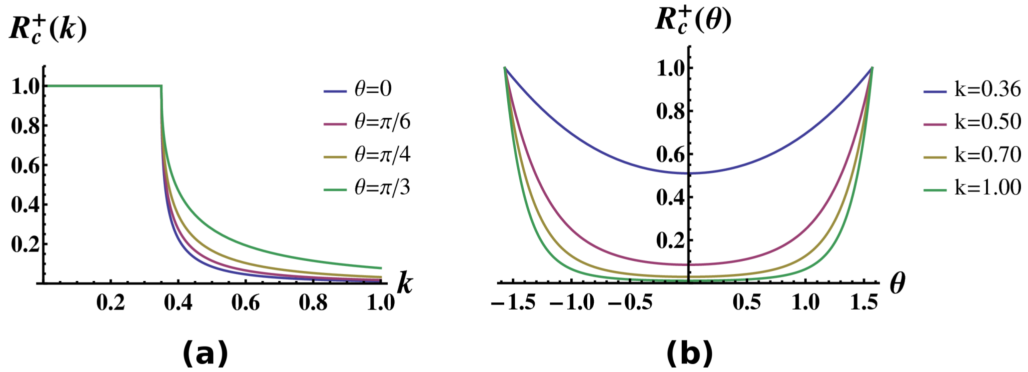

FIGURE 6.13: q- to k-region: Reflection coefficients as a function of the (a) incident energy k and (b) angle of incidence α_c^+ for incidence from states of higher energy Ψ_c^+. Reflection occurs just for the same state of incidence, so that $R = R_c^+$.

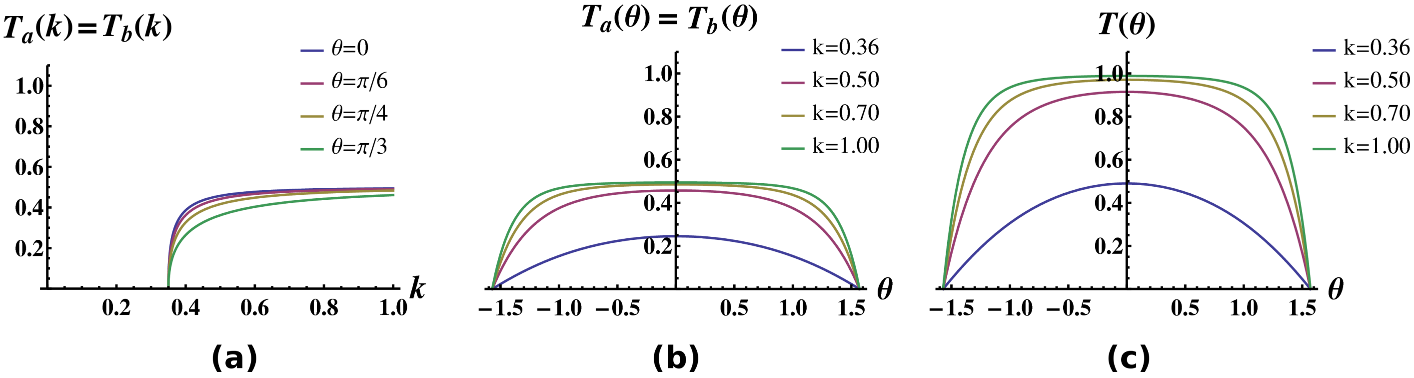

FIGURE 6.14: q- to k-region: Transmission coefficients for incidence from Ψ_c^+ as a function of the (a) incident energy k and (b-c) angle of incidence α_c^+. For incidence from Ψ_c^+ states, electrons are equally transmitted for both uncoupled layers and the total transmission is $T = 2 \times T_{a(b)}$.

For incidence from Ψ_c^-, the state in bilayer graphene of lower energy, transmission to the k-region depends on the critical energy $k_c = \gamma tan^2(\alpha_c^-)$. As shown in Fig. 6.16, different angles of incidence α_c^- will define the energy value for which we start to observe transmission to the layers in the k-region. Also for this case, transmission occurs in the same way for both graphene layers, and a saturation at 0.5 is observed for higher energies.

We can also look at the structure of wave functions in order to interpret the results obtained. By looking at the matrix representation of states Ψ_c^- and Ψ_c^+, we notice a phase difference between the coupled layers of π and 0, respectively. The state of lower energy is formed by an anti-symmetric combination of states of the individual layers,

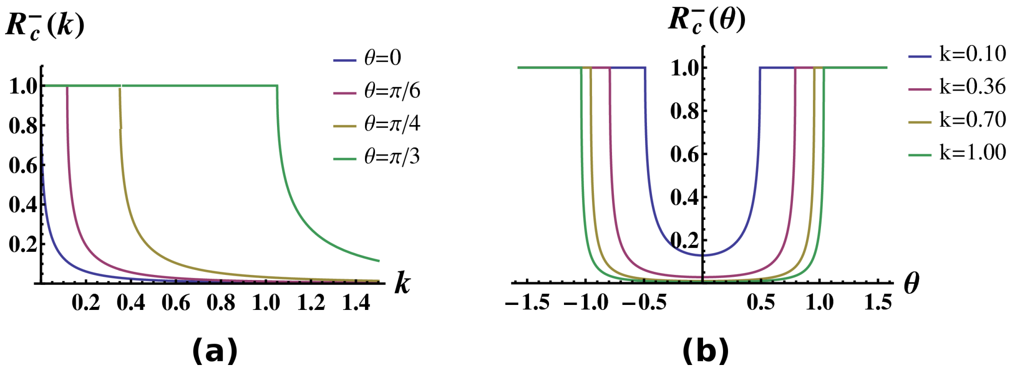

FIGURE 6.15: q- to k-region: Reflection coefficients as a function of the (a) incident energy k and (b) angle of incidence α_c^- for incidence from states of lower energy Ψ_c^-. Reflection occurs just for the same state of incidence, so that $R = R_c^-$. The regions of total reflection (R= 1) are defined by the critical energies $k_c = \gamma tg^2(\alpha_c^-)$.

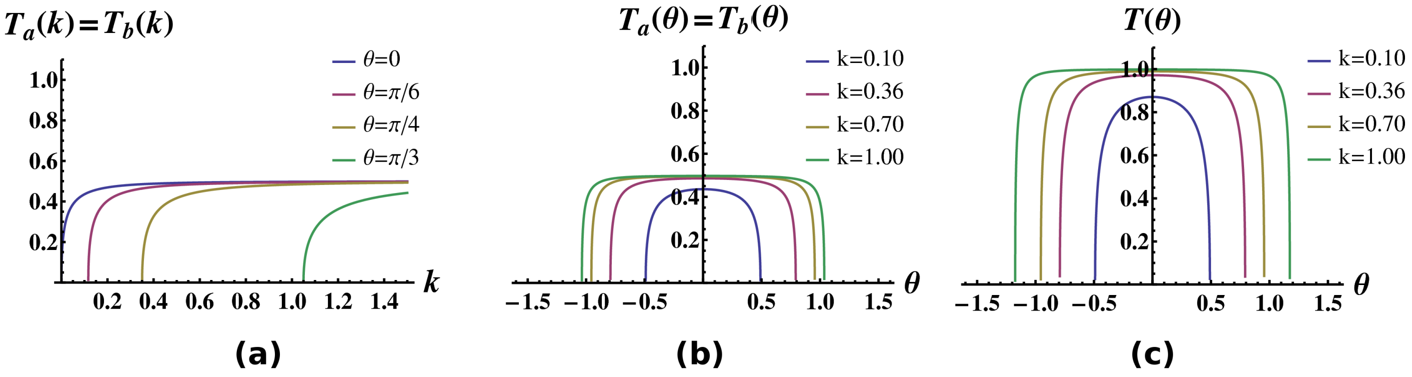

FIGURE 6.16: q- to k-region: Transmission coefficients for incidence from Ψ_c^- as a function of the (a) incident energy k and (b-c) angle of incidence α_c^-. For incidence from Ψ_c^- states, electrons are also equally transmitted for both uncoupled layers, so that the total transmission is $T = 2{\times}T_{a(b)}$. Regions of null transmission ($T = 0$) can be observed for energies $k < k_c = \gamma tg^2(\alpha_c^-)$.

while for state of higher energy, we have a symmetric combination of such states. When the electron is transmitted to the k-region, it will propagate in a state with the form:

$$\Psi_{II}^k(\mathbf{k},\mathbf{r}) = t_a\varphi_a^+(\mathbf{k},\mathbf{r}) + t_b\varphi_b^+(\mathbf{k},\mathbf{r}). \tag{6.69}$$

The transmission coefficients t_a and t_b obtained show that $\Psi_{II}^k(\mathbf{k},\mathbf{r})$ assumes a symmetric or anti-symmetric form in combining states of individual layers, depending on whether the incident state is Ψ_c^+ or Ψ_c^-, respectively. This can be checked by just observing that t_a and t_b have the same signal when the incidence is from Ψ_c^+, while for incidence from Ψ_c^-, t_a = -t_b, producing symmetric and antisymmetric combinations of φ_a^+ and φ_b^+.

6.3.4 Bilayer-Monolayer-Bilayer interfaces: the barrier problem

In the barrier problem, we consider a heterostructure formed by two semi-infinite regions of AB'-stacked graphene bilayer (q-regions) separated by a finite region of two uncoupled graphene monolayers (k-region). The procedure to compute transmission and reflection coefficients is almost the same as in the previous single q-to-k interface problems. The difference now is that we need to match the wave functions from the first q-region and the finite k-region at the first interface at x=0 and at the second interface at x=d, where d is width of the barrier. As in the previous case of scattering at the q-k single interface, the incident state of electron in the graphene bilayer will define the properties of scattering.

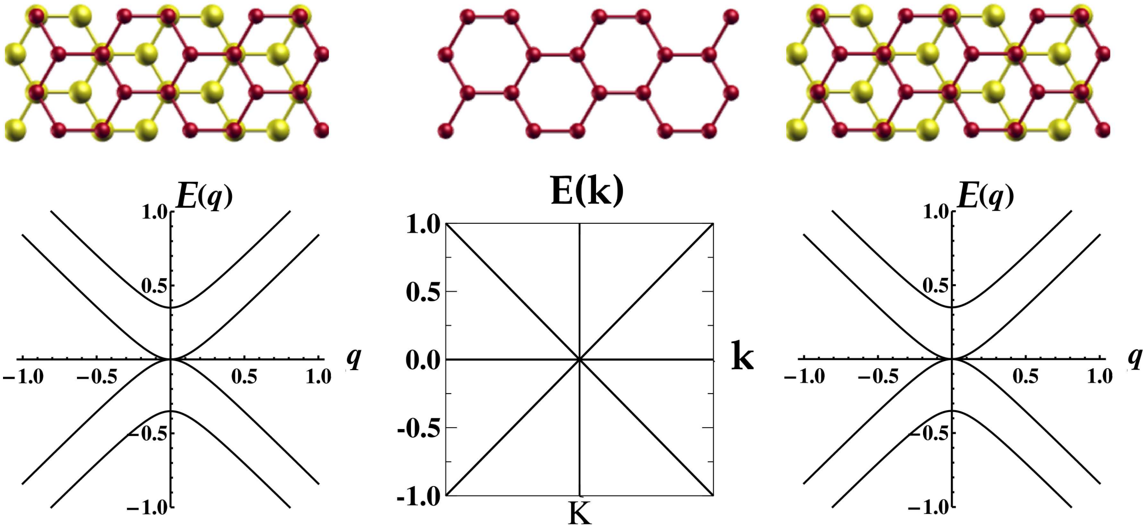

FIGURE 6.17: Dispersion relations for q-k-q regions, that defines the barrier problem of two semi-infinite graphene bilayers separated by a finite region of two uncoupled monolayers.

The general form of the wave functions for the three regions are now:

$$\Psi_I^q(\mathbf{q},\mathbf{r}) = \Psi_c^i(q_{xc},q_{yc},\mathbf{r}) + r_c^i\Psi_c^i(-q_{xc},q_{yc},\mathbf{r}) + r_c^j\Psi_c^j(-q_{xc},q_{yc},\mathbf{r}) \tag{6.70}$$

$$\Psi_{II}^k(\mathbf{k},\mathbf{r}) = \tau_a\varphi_a(k_x,k_y,\mathbf{r}) + \tau_b\varphi_b(k_x,k_y,\mathbf{r}) + \rho_a\varphi_a(-k_x,k_y,\mathbf{r}) + \rho_b\varphi_b(-k_x,k_y,\mathbf{r}) \tag{6.71}$$

$$\Psi_{III}^q(\mathbf{q},\mathbf{r}) = t_c^i\Psi_c^i(q_{xc},q_{yc},\mathbf{r}) + t_c^j\Psi_c^j(q_{xc},q_{yc},\mathbf{r}) \tag{6.72}$$

where the subscript i stands for the initial state (state of incidence) in the graphene bilayer. We notice that in the k-region we have both transmitted waves, coming from medium I, and also reflected waves, due to the presence of the second interface. In order to find the expressions for transmission and reflection terms, we proceed as earlier, and consider the continuity of the wave functions through the interfaces. At $x = 0$ we must have:

$$\Psi^q_I(\mathbf{q}, 0, y) = \Psi^k_{II}(\mathbf{k}, 0, y), \tag{6.73}$$

and at $x = d$:

$$\Psi^k_{II}(\mathbf{q}, d, y) = \Psi^q_{III}(\mathbf{q}, d, y). \tag{6.74}$$

The respective currents for the three regions are now:

$$J^q_{Ix} = 4k\left[\frac{1-|r^i_c|^2}{N^{i2}_c} q^i_c cos(\alpha^i_c) - \frac{|r^j_c|^2}{N^{j2}_c} q^j_c cos(\alpha^j_c)\right] \tag{6.75}$$

$$J^k_{IIx} = (|\tau_a|^2 + |\tau_b|^2 - |\rho_a|^2 - |\rho_b|^2) cos(\theta_k) \tag{6.76}$$

$$J^q_{IIIx} = 4k\left[\frac{|t^i_c|^2}{N^{i2}_c} q^i_c cos(\alpha^i_c) + \frac{|t^j_c|^2}{N^{j2}_c} q^j_c cos(\alpha^j_c)\right]. \tag{6.77}$$

From conservation of probability current:

$$J^q_{Ix} = J^k_{IIx} = J^q_{IIIx} \tag{6.78}$$

and so, the relation between transmission and reflection probability amplitudes in q-regions in media I and III can be written:

$$|r^i_c|^2 + \frac{N^{i2}_c}{N^{j2}_c}\frac{q^j_c cos(\alpha^j_c)}{q^i_c cos(\alpha^i_c)}|r^j_c|^2 + |t^i_c|^2 + \frac{N^{i2}_c}{N^{j2}_c}\frac{q^j_c cos(\alpha^j_c)}{q^i_c cos(\alpha^i_c)}|t^j_c|^2 = 1 \tag{6.79}$$

After solving for 6.73 and 6.74, as in the single q-to-k interface case, for incidence from both initial states, Ψ^+_c and Ψ^-_c, transmission to region III and reflection to region I occurs just to the same state of incidence. The obtained expressions are quite cumbersome, and we just show the ones corresponding to the direct incidence ($\alpha_c^i = 0$). For incidence from state of higher energy Ψ_c^+, transmission and reflection coefficients are:

$$r_c^+ = \frac{\gamma}{2k - \gamma + 2i\sqrt{k(k-\gamma)}cot(kd)} \tag{6.80}$$

$$t_c^+ = \frac{2ie^{-id\sqrt{k(k-\gamma)}}\sqrt{k(k-\gamma)}}{2i\sqrt{k(k-\gamma)}cos(kd) + (2k-\gamma)sin(kd)} \tag{6.81}$$

$$r_c^- = t_c^- = 0 \tag{6.82}$$

while, for incidence from Ψ_c^-, we have:

$$r_c^- = -\frac{\gamma}{2k + \gamma + 2i\sqrt{k(k+\gamma)}cot(kd)} \tag{6.83}$$

$$t_c^- = \frac{2ie^{-id\sqrt{k(k+\gamma)}}\sqrt{k(k+\gamma)}}{2i\sqrt{k(k+\gamma)}cos(kd) + (2k+\gamma)sin(kd)} \tag{6.84}$$

$$r_c^+ = t_c^+ = 0. \tag{6.85}$$

From the above results, the transmission probability to the second q-region $T_c^\pm = |t_c^\pm|^2$, for direct incidence ($\alpha_c^\pm = 0$) for the incident states of positive energy Ψ_c^+ and Ψ_c^-, reduces to:

$$T_c^+ = \frac{8k(k+\gamma)}{8k^2 + 8k\gamma + \gamma^2 - \gamma^2 cos(2kd)} \tag{6.86}$$

$$T_c^- = \frac{8k(k-\gamma)}{8k^2 - 8k\gamma + \gamma^2 - \gamma^2 cos(2kd)}. \tag{6.87}$$

Plots of the calculated T_c^+ and T_c^- as a function of the incident energy k and incident angle $\alpha_c^\pm$ are shown in Figs. 6.18 and 6.19 for T_c^+ and in Figs. 6.20 and 6.21 for T_c^-, respectively.

The oscillatory behavior generated by the self-interference of waves reflected inside the k-region is immediately identified. By varying the barrier width d for fixed incident energies, we see that the oscillations are affected mainly by this parameter.

The resonant points for T_c^+ and T_c^- for direct incidence (blue curves in the plots $T_c^\pm(k)$), can be easily obtained by $\partial T_c^\pm/\partial(kd) = 0$, from which, total transmission probabilities are seen to occur for the incident energies k_n given by:

$$2kd = 2n\pi \Rightarrow k_n = \frac{n\pi}{d}, \tag{6.88}$$

valid for $k_n > 0$ for incidence from Ψ_c^- states and $k_n > \gamma$ for incidence from Ψ_c^+ states.

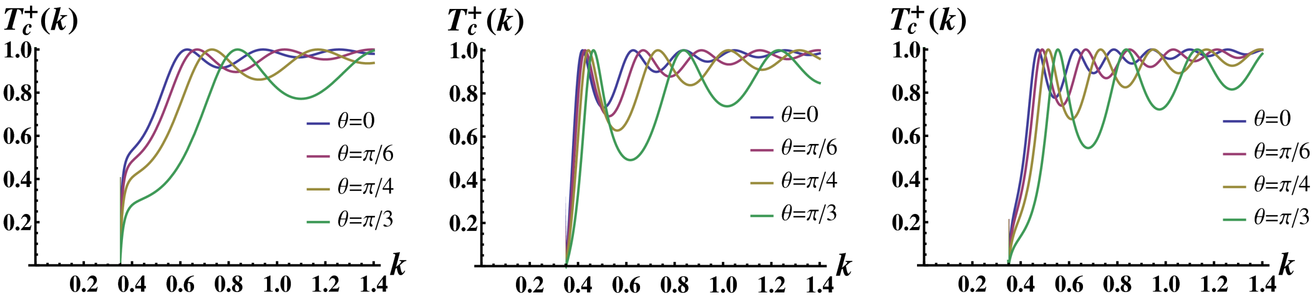

(a) **(b)** **(c)**

FIGURE 6.18: Transmission coefficients T_c^+ for incidence from Ψ_c^+ state as a function of the incident energy k, for the barrier widths (a) d=6 nm, (b) d=10 nm and (a) d=13 nm.

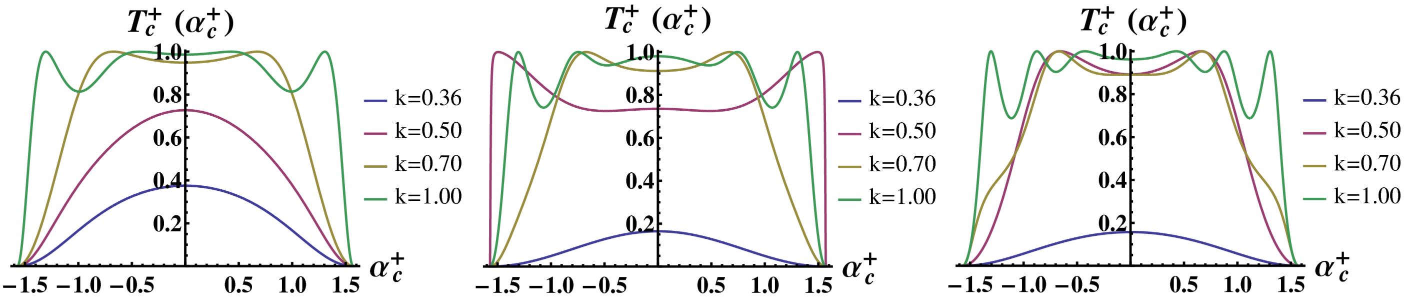

(a) **(b)** **(c)**

FIGURE 6.19: Transmission coefficients T_c^+ for incidence from Ψ_c^+ state as a function of the angle of incidence α_c^+, for the barrier widths (a) d= 6 nm, (b) d= 10 nm and (a) d= 13 nm.

As we have mentioned above, there is no reflection or transmission to states Ψ_c^- in the first and third q-regions when electron emerges from Ψ_c^+ states. As discussed in the previous section, for transmission from q- to k-region, electron will propagate just in a state formed by a symmetric or antisymmetric combination of states of the uncoupled layers, depending on the initial state. This behavior is also observed in the barrier problem. Electrons coming from Ψ_c^+ in the first q-region propagate in states in the media II and III that are formed by symmetric combinations of the uncoupled layers. Indeed, it was checked that the phase difference between layers in region II is null, as the ratio $\frac{\tau_a+\rho_a}{\tau_b+\rho_b}$ is equal to one.

The oscillatory behavior generated due to the self-interference of waves reflected inside the k-region can be seen in Figs. 6.18 and 6.19 for incidence from Ψ_c^+. In Fig. 6.18, the transmission probability T_c^+ as a function of the incident energy k for different values of α_c^+ is plotted for the barrier sizes $d = 10$, 15 and 20, in (a), (b) and (c), respectively. For $k \gtrsim \gamma$, it is observed a low transmission of electrons. However, by slightly increasing the incident energy, transmission starts to occur, reaching the first maximum for direct incidence for $k_2 = 0.62$, for $d = 10$, $k_2 = 0.42$ for $d = 15$ and $k_3 = 0.47$ for $d = 20$. As we we are using natural units, it is important to clarify that the used values for the barriers ($d = 10$, 15, and 20), corresponds to 6 nm, 10 nm and 13 nm, respectively. These values are in the range of those experimentally observed for bilayer graphene with stacking boundaries between regions with an AB' stacking and of uncoupled graphene layers, due to rippling [79], where the widths of most of the observed stacking boundaries are estimated to be $\sim$ 10nm.

The influence of the barrier width d in the results for T_c^+ can be also seen for different incident energies as a function of α_c^+. For a fixed value of k, a higher number of oscillations appears as we increase d, as can be observed by comparing curves of the same color in Figs. 6.19-(a), (b) and (c), which correspond to the same energy of incidence k, for the different barrier sizes. This behavior can be easily checked in Eq. 6.88, where the positions of the maxima varies inversely with d. For each value of d, the oscillatory behavior of T_c^+ appears as the energy increases, more pronounced at the extremes of the incidence angle ($\alpha_c^+ \lesssim \pm\, \pi/2$).

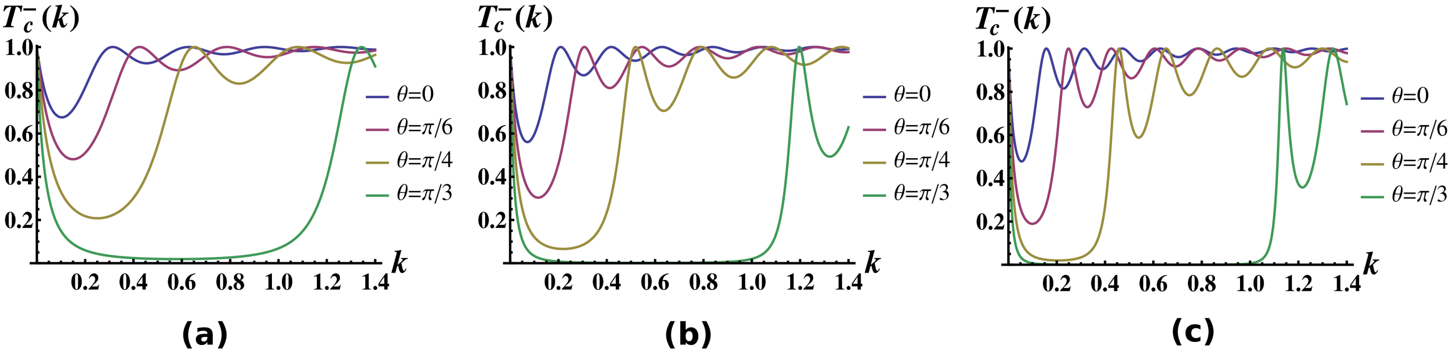

FIGURE 6.20: Transmission coefficients T_c^- for incidence from Ψ_c^- state as a function of the incident energy k, for the barrier widths (a) d=6 nm, (b) d=10 nm and (a) d=13 nm.

The calculated transmission probabilities for incidence from states of lower energy Ψ_c^- are shown in Figs. 6.20 and 6.21. No reflection or transmission to states Ψ_c^+ in regions I and III are observed, and so, the total transmission is purely T_c^-. For the same reasons as the earlier cases, the structure of the wave functions, that are now antisymmetric combinations of states of the uncoupled layers, forbids electrons to access the states of

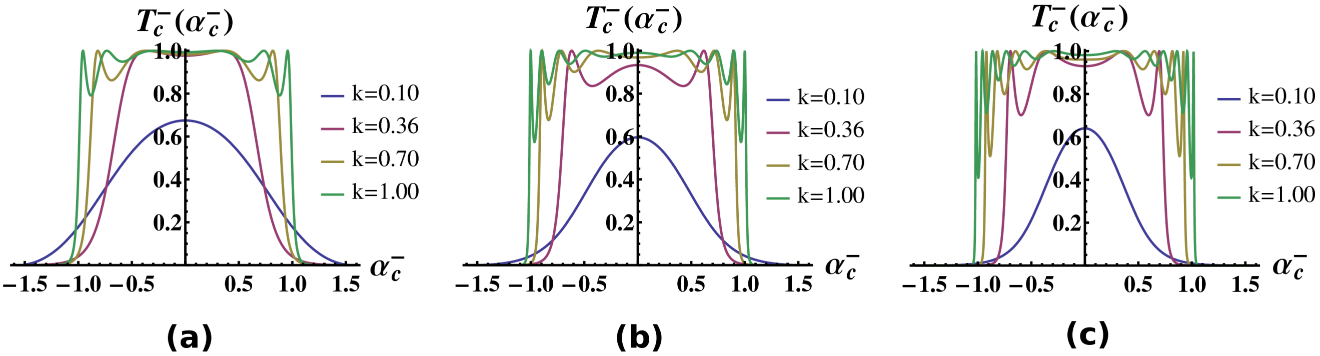

FIGURE 6.21: Transmission coefficients T_c^- for incidence from Ψ_c^- state as a function of the incident angle α_c^-, for the barrier widths (a) d=6 nm, (b) d=10 nm and (a) d=13 nm.

higher energies. In this case, the phase difference between layers in region II is $(\frac{t_1+r_1}{t_2+r_2})$ π.

The calculated transmission probability T_c^- as a function of the incident energy k is shown in Fig. 6.20 for (a) d =10, (b) d =15 and (c) d =20. At very low incident energy, total transmission is observed, an opposite behavior if compared to the incidence from states of higher energy, where we have obtained $T_c^+ = 0$ for $k \gtrsim \gamma$, the minimum allowed energy value in that case. By increasing k, a fast decreasing of transmission is obtained, for all angles of incidence α_c^- and barrier sizes d considered. After this, oscillations in T_c^- are observed, with the maximum values for direct incidence ($\alpha_c^- = 0$) given by 6.88.

The behavior of T_c^- as a function of the incident angle α_c^- is shown in Fig. 6.21 for (a) d =10, (b) d =15 and (c) d =20. Represented in this way, it is easier to see that for values of k from $\gtrsim 0.36$, almost total transmission occurs for small α_c^-. Increasing the barrier size, a higher number of oscillations is observed, more pronounced at the extreme values of α_c^- where some finite transmission occurs.

6.4 Conclusions

The low-energy electronic transport across stacking boundaries in graphene is studied in this work. The electron scattering by interfaces formed between regions of uncoupled and coupled graphene layers is investigated by a continuum approach.

We consider scattering of electrons at interfaces defined between k and q regions, representing regions of single and double graphene layers, respectively. This problem is important in the context of experimentally observed evidences of stacking boundaries formed in bilayer graphene, where regions with uncoupled layers are observed due to the rippling in one of the layers.

From this we investigate transport in graphene for the interfaces formed by k-to-q regions, q-to-k regions and also for the barrier case q-k-q regions.

The critical energies $k_c = \frac{\gamma}{cos^2(\theta_k)}$ for the k-q interface and $k_c = \gamma tan^2(\alpha_c^-)$ for the q-k-q barrier problem define the range of energies for which total reflection is observed for both interfaces types.

For electrons emerging from a graphene bilayer region (q-k and q-k-q interfaces) we observe that reflection to the region of incidence just occurs for the same state of incidence, with the other state of positive energy not being accessible, as a requirement of momentum conservation. For the barrier problem, transmission to the second q-region (after the second interface) also occurs just for the same state of positive energy energy of the incident electron.

Chapter 7

Lattice Relaxation at the Interface of Two Two-Dimensional Crystals: Graphene and Hexagonal Boron-Nitride

7.1 Introduction

Still following the ideas of band gap engineering of graphene, a very recent innovation in this direction has been the creation of hybrid structures of this material and hexagonal boron nitride (h-BN). Heteroepitaxial growth of these two-dimensional (2D) lateral heterostructures has recently attracted attention because of the possibility of generating mixed alloyed phases with tunable electronic properties[41, 81–85].

The very similar structure of graphene and h-BN, both with a honeycomb lattice with a difference in lattice parameters of just ∼2%, provides a good option to produce such hybrid materials, which have shown very interesting physical properties. In special, successful experiments on continuous growth of graphene and h-BN, have demonstrated the controlled production of coherent interfaces between these 2D materials, and modifications in the electronic properties of graphene have already been observed.

In Ref.[86], hybrid films consisting of h-BN and graphene domains, synthesized via chemical vapor deposition (CVD), showed a small bandgap opening of ∼ 18 meV. In other experimental work, Ci et al. demonstrated that the hybrid film with a tunable bandgap can be achieved on Cu foil by simultaneously supplying different proportions of carbon and BN sources. In such one-step growth, the phase-separation leads to randomly-mixed graphene and BN domains[41]. Patterned sequential growth has also been used for the spatially controlled growth of lateral junctions between graphene and BN, to make integrated circuitry or close-loop resonators[83, 84]. Such in-plane G|BN hybrid film with well-defined heterointerfaces has also been theoretically predicted to possess novel magnetic and unique thermal transport properties[48, 87–90].

The possibility of an abrupt heterojunction between BN and G has stimulated a lot of interest owing to the prediction of an abundance of fascinating properties of such 1D interface[48, 86, 91]. Using different microscopy techniques, the successful interfacing of graphene and BN domains has been demonstrated on different metal surfaces, such as Ru(0001)[92], Rh(111)[86] and Cu(100)[82]. There is a great excitement regarding the observation of short-segments of a sharp G-BN interface preferentially linked in the zigzag fashion. Many issues surrounding the formation of continuous and atomically-sharp G|BN heterointerfaces remain unclear. Fault lines and cracks in hybrid films are mainly governed by interfacial strain[93, 94]. However, there is no insight into how strain propagates along the length of such an interface, nor on how the interfacial stress relaxes to avoid the discontinuity of heterointerfaces. In addition, the electronic states are coupled to the underlying metal. Electronic decoupling of the G|BN interface from the metallic substrate is needed to reveal the intrinsic physical properties at the G|BN boundaries.

The work presented in this chapter was developed in collaboration with the experimental group of the Chemistry Department of the Graphene Research Centre (GRC) of the National University of Singapore (NUS). In the experimental work, coherent interfaces between graphene and h-BN were synthesized via CVD, and the structural and electronic properties of the resulting structures were analyzed.

In the growth process of the graphene and h-BN islands that form the heterostructures, the strain due to the lattice mismatch between these materials is observed to accumulate with the increase of the length of the interface, and a breakage of the continuity of the h-BN lattice is observed. In order to keep the continuity of the film along the interface, the occurrence of a misfit dislocation (MD) is proposed, as a strain relief mechanism at atomically abrupt G|BN interfaces. From scanning tunneling images (STM) of the samples, the core dislocation, which is indicated to be formed by 5-7 rings in the hexagonal lattice of BN, is observed at ∼5 lattice constants away from the interface, and a periodicity of these core defects is suggested to occur along the direction parallel to the G|BN interface.

The local electronic states of the G|BN interface was also investigated using scanning tunneling microscopy (STS), in order to probe the interfacial electronic states on the decoupled G|BN interface.

In this chapter we use ab initio calculations, to investigate structural and electronic properties of heterostructures formed by graphene and h-BN. The introduction of a MD formed by 5-7 rings in the BN lattice is considered as a strain relief mechanism, indicated by the experimental results to be necessary to occur in order to form long and sharp interfaces between these materials. Electronic properties are also discussed and the results are compared with that obtained in the experiment.

This work was just published in the journal Nano Letters. Reference: Jiong Lu, Lídia C. Gomes, Ricardo W. Nunes, A. H. Castro Neto, and Kian Ping Loh. **DOI**: 10.1021/nl501900x.

7.2 Experimental Results

Synthesis of hybrid thin films, such as h-BN and graphene, follows a common strategy based on a two-step sequential chemical vapor deposition (CVD). For G|BN heterostructures, a first stage growth of graphene (BN) islands usually occurs. The edges of these islands serve as nucleation sites to seed the growth of BN (G) that will cover the exposed metal surface. Due to the lattice parameter difference between these materials, a strained G-BN interface is obtained. Understanding strain relaxations of such 2D laterally fused interface is useful in fabricating structurally stable heterointerfaces with high degree of atomic coherence. For lattice-mismatched 2D films on 3D substrates, it is widely accepted[95–97] that there exists a critical film width beyond which MDs are introduced in order to release the strain and allow the growth of such structures without breakdown.

In order to study the heterogrowth behavior of in-plane |BN heterojunctions, the experiment was based in BN grown on pre-existing graphene patches on a Ru(0001) substrate. The BN and G domains could be easily distinguished by STM imaging due to the presence of characteristic Moiré blistering of graphene and “nanomesh” patterns of BN. The growth temperature must be carefully controlled during the experiment to suppress interfacial mixing resulting from metal-catalyzed atomic substitution, making possible the formation of a sharp G|BN interface.

By sequentially exposing as-prepared clean Ru to ethylene (C_2H_4) and borazine ($B_3H_6N_3$), the pseudomorphic growth of BN strips on the edge of graphene is observed (Fig. 7.1-a). Short segments of an atomically sharp G|BN interface readily appear at the condition

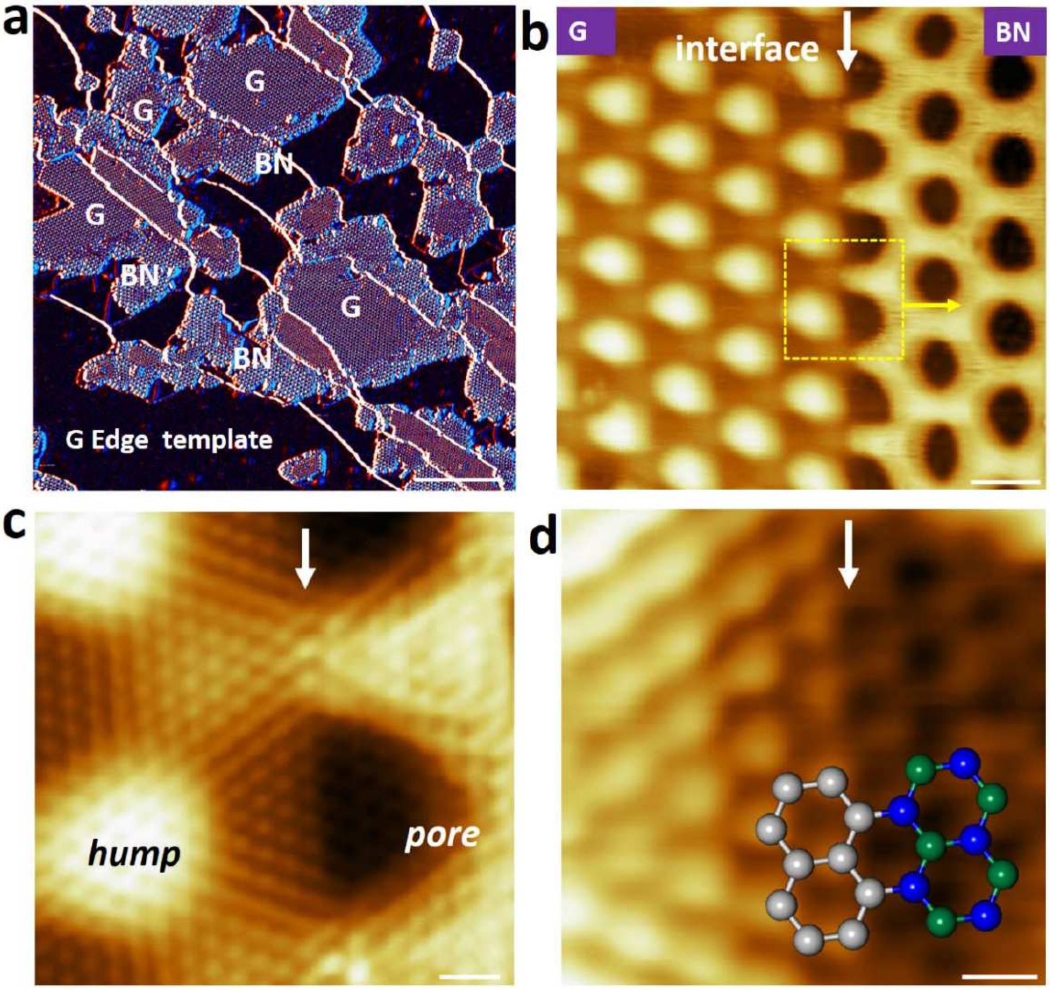

FIGURE 7.1: STM imaging of atomically-sharp G|BN heterointerface. (a) BN nucleates on the edges of graphene on Ru(0001) by a low dosage of borazine (5L) at 800 K. (b) A sharp G|BN interface with length < 21 nm at 800 K. (c) Magnified view in b shows the formation of a seamless G|BN interface at the atomic scale. (d) Magnified view of (c) shows a zigzag edge of graphene bonded to a zigzag edge of BN at the interface. Scale bars in a-d are 50, 2.5, 0.5 and 0.25 nm, respectively.

($\mu_c/\mu_{BN} \lesssim 0.2$), where nanoscale graphene islands are surrounded by BN strips (Fig. 7.1-b). The majority of G|BN boundaries generated in this condition are atomically abrupt and their lengths lie in the range of 10 nm < L < 24 nm (Fig. 7.1-a and b). The seamless bonding between graphene and BN at the interface is revealed in the magnified STM image, where the graphene Moiré hump (bright regions) always faces the nanomesh "pores" (dark regions) at the boundaries (Fig. 7.1-c). As resolved by high-resolution STM imaging (Fig. 7.1-d), graphene and BN connect in a zigzag fashion.

If we assume that the first interfacial C-N(B) bond is well-aligned (vertical to interface), at the 24^{th} interfacial C-N(B) bond within one Moiré unit, the N(B) atoms at the zigzag line linked to the graphene lattice will be dislocated from $\Delta_y = \sim 1.15$ Å (Fig. 7.2). For a seamless bonding between graphene and BN at the interface, BN lattice must adjust

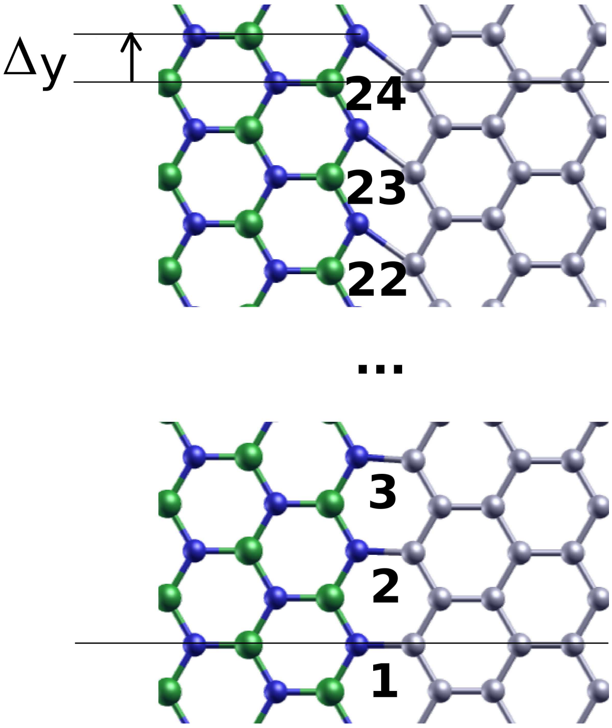

FIGURE 7.2: Stretching in the C-N(B) bonds at the interface between h-BN and graphene due to the mismatching of the lattices.

their bonds in order to adopt values near to that of graphene, which clearly induce strain at the interface region. Such strain must be distributed along the length of the interface or accommodated by the interactions with the Ru substrate, otherwise a discontinuity at the interface is expected to occur.

7.2.1 Interfacial strain relaxation

With the advent of the field of 2D material science and technology, it is important to ask whether the 3D interfacial strain relaxation scenario also applies in 2D mismatched heteroepitaxy, and the length scale at which a defect-free G|BN heterointerface can be formed before dislocations or other defects set in to relieve the strain energy.

As in the case of 3D heteroepitaxy growth, we can also consider that the interfacial strain energy due the lattice mismatching between the G and BN lattices gradually builds up with the increase of the film “thickness”. At a critical thickness, it would become energetically favorable to relieve the strain by having a network of MDs at the interface, beyond which the epitaxial film is apt to return to its stable unstrained bulk structure (Fig. 7.4a)[95, 96].

Indeed, discontinuities are frequently observed at the G|BN interfaces (Fig. 7.3-c) when the interface length exceeds ∼27 nm (∼9 Moiré lattice parameter a_M), presumably due to the accumulation of strain, while interface continuity can be maintained by introducing stretched, irregular Moiré structures close to the G|BN interface (Fig. 7.3-b, d).

As shown in Fig. 7.3-a, an extended G|BN interface can be grown by increasing the coverage of preexisting graphene islands and subsequently filling the entire exposed Ru region by the regrowth of BN. The resulting 1D G|BN interface has a length scale of 100-200 nm. Close examination reveals that a heart-shaped irregular structure in the BN nanomesh is generated at every few Moiré units ($\sim 9\ a_M$). The heart-shaped Moiré structure is introduced where two nanomesh pores overlap and intersect at an angle of 60 (indicated in Fig. 7.3-b). In line with recent theoretical predictions, this irregularity is presumably due to the formation of edge dislocations, which were proposed to consist of heptagon-pentagon pairs[98, 99]. Such a heptagon-pentagon dislocation, as shown in Fig. 7.4-b, can be viewed as a result of inserting a semi-infinite strip of atoms along the armchair direction in the h-BN lattice. Its Burgers vector is oriented along the zigzag direction.

Similar to the strain-relaxation in 3D mismatched heterojunctions, the occurrence of interfacial strain may introduce MDs in the 2D heterogrowth of BN on graphene. To address this issue, the strain profile at the interface was extracted from the atomically resolved STM imaging of bond distances. It is observed that the graphene lattice is not perturbed during the growth of BN, and the strain propagates mainly in the BN side of the interface. Another observation is that misfit dislocations in BN, which are made of non-hexagonal rings, always appear at ~5 lattice constants away from the interface (~ 1.08 nm).

To understand how the strain propagates with the width of the BN strip, a width-dependent strain profile was obtained by measuring the average strain of each BN zigzag line parallel to the G|BN interface (starting from the interface: first line to sixth line as indicated in the inset in Fig. 7.4-c). As shown in Fig. 7.4-c, which describes the strain profile along the perpendicular direction from the interface, the strain in BN rapidly builds up in the first three atomic rows and reaches a maximum value of 5.9% at the sixth row. Since the lattice constant of BN is larger than that of graphene (edge substrate), the BN lattice is compressed at the interface. At a critical width of ~5-6 lines (equal to ~1.08-1.29 nm), the accumulated strain reaches a maximum. The occurrence of maximum strain agrees with the location where the MDs are usually found, which is typically at a distance of 1.08 nm from the interface (Fig. 7.3-e and 7.4-b). As reflected in the strain profile analysis, the strain is relieved at regions where MDs occur: the measured strain decays within the first three rows (from the MD position), and returns to its bulk value at the fourth row.

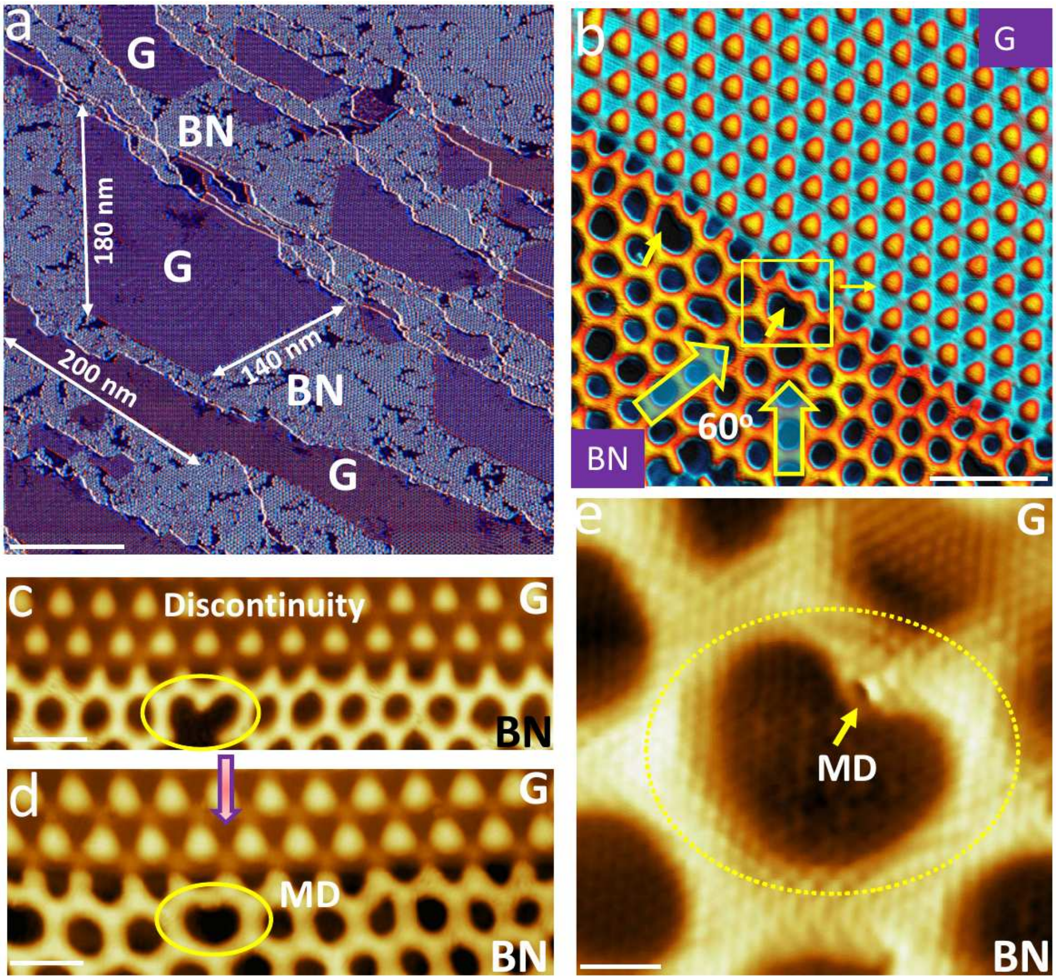

FIGURE 7.3: The formation of MDs at extended G|BN interface (> 100nm). (a) Large-scale STM image of domain-wise G|BN with extended linear sharp interface at 800 K with an increased ratio of μ_C/μ_{BN} (in the range between 0.4-0.6); the growth of G islands (∼0.5 monolayer) followed by a dosage of borazine of: 30 Langmuir (30 L) to cover all the remaining Ru surface. (b) Magnified view shows the formation of MD in BN Moiré pattern close to interface zones. (c) Interface discontinuity occurs when the length of 1D interface extends above ∼24 nm. (d) MD sets in to relieve interface strain and keep the continuity of G|BN boundary. (e) High-resolution imaging of MD reveals the structure of the dislocation core. Scale bars in (a-e) are 100, 10, 5, 5 and 1 nm respectively.

7.3 Ab initio calculations

To gain further understanding on the effect of the introduction of the MD in the h-BN lattice to form the G|BN interface with graphene, strain profiles of these heterostructures were obtained from structure optimization in DFT.

The atomic configuration of the linking edge of graphene and h-BN, has been reported as formed by B-C bonds[86, 94] However, many factors in the synthesis process can influence the interface composition. Most of the works with this kind of hybrid material consider the growth of graphene islands first, followed by injection of some BN source.

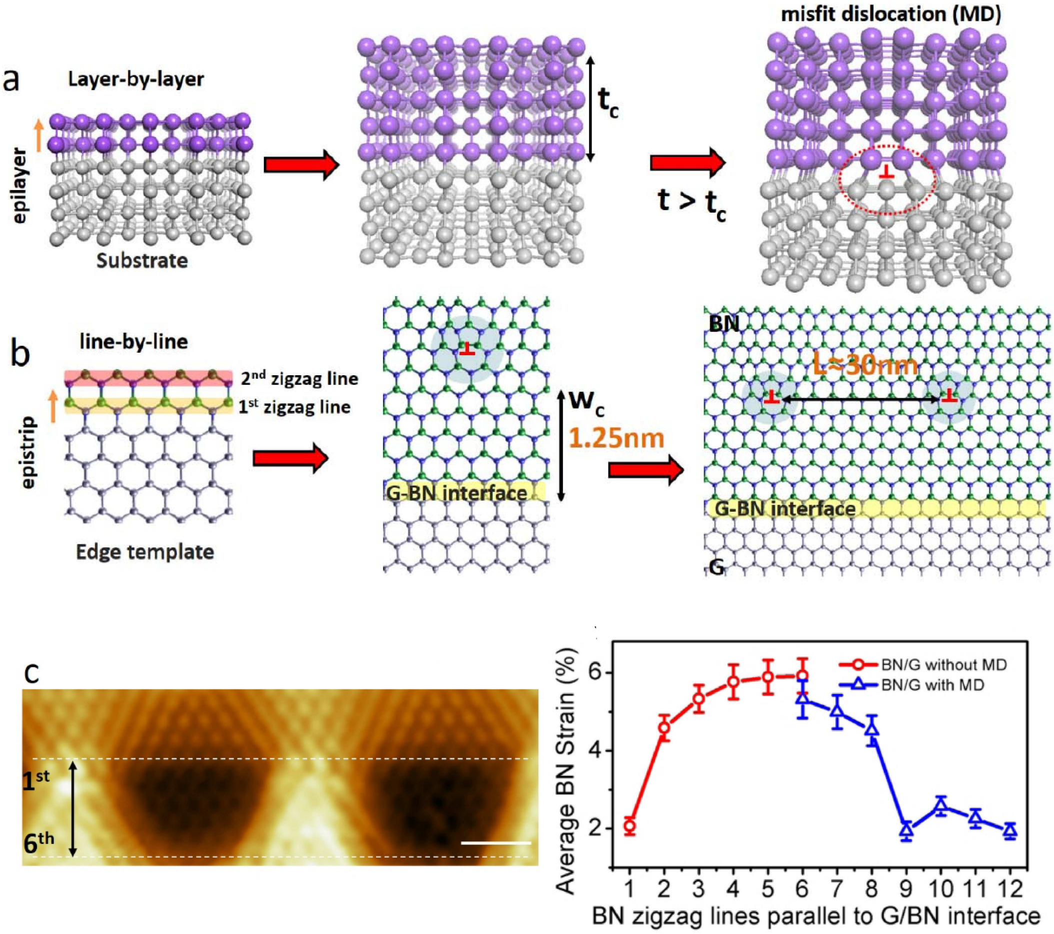

Figure 7.4: Strain profile of BN at G|BN interface with and without MD. (a), Illustrates the formation of MDs in layered heteroepitaxial growth of thin film above a critical thickness (t_c). (b), For the graphene edge templated heterogrowth of BN, a misfit dislocation forms above the critical width (w_c) to relieve strain. (c) Left: atomic resolved coherent lattice at the G|BN interface for strain analysis. Right: Experimental values of strain propagation parallel to the interface before (in red) and after (in blue) introducing MD.

Changing the BN source, or doing the inverse process, where h-BN islands are first growth, followed by graphene, at various temperatures and pressures, could favor the formation of interfaces formed by C-N bonds or even by a mixing of C-B and C-N bonds. In other words, kinetic factors in the synthesis process are of essential importance to define the interface composition, and both possibilities can be considered as possible to occur.

With these considerations, we investigate models with both C-B and C-N interfaces, as shown in Fig. 7.5. To simulate these systems, calculations with graphene-BN ribbons are done. The ribbons are periodic along the direction of the interface and finite in the perpendicular direction. By the same reasons discussed in Chapter 4, considering ribbons to model this problem is necessary due to the lack of inversion symmetry in the BN lattice. If we want to investigate the interfaces individually, we have to use ribbons

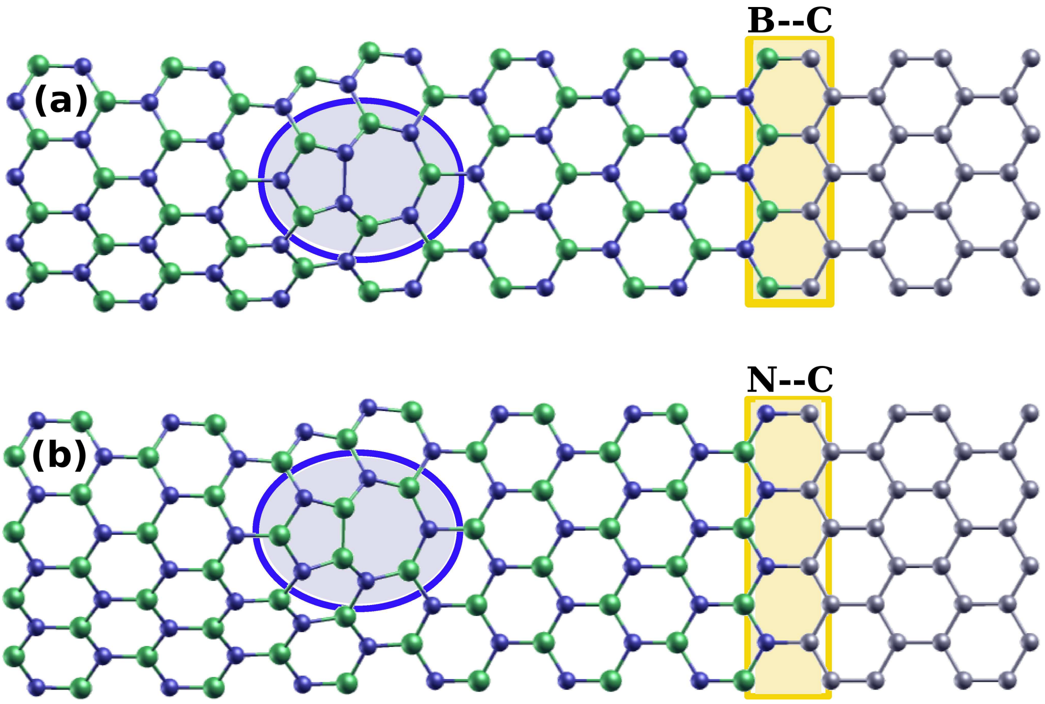

FIGURE 7.5: Interfaces between h-BN and graphene formed by (a) C-B and (b) C-N bonds. Nitrogen and boron atoms in h-BN are respresented in blue and green colors, while carbon atoms are shown in gray. The core MDs in the h-BN lattice formed by the pentagon-heptagon pair for each of these interfaces are also shown.

which contain the desired interface, otherwise, employing periodic boundary conditions in the direction perpendicular to the interface would require to include two types of G|BN interfaces in the same calculation.

For all models, the 5-7 pair is placed at the zigzag line at ∼1.08 nm from the G|BN interface, which corresponds to ∼5 lattice parameters of h-BN. This value was choosen in the range observed in the experiment (∼1.05-1.29 nm).

As the experimental results indicates, the structure of the pre-grown graphene island is not affected by the pos synthesized h-BN lattice, so that it can be considered as a "rigid substract". We take advantage of this fact to build ribbons with a smaller number of carbon atoms to simulate the graphene side of the interface, in order to save computational time. For this, we use 5 zigzag lines of carbon atoms, corresponding to a width of ∼8.5Å, to simulate the graphene side for all models and constrain the positions of the C atoms of the two zigzag lines at the edge of the ribbon to their nominal bulk-monolayer values, as highlighted by the blue box in Fig. 7.6 for a C-N interface, such that we can simulate the effect of the 'bulk' of graphene. The carbon atoms that forms the three zigzag lines nearest to the interface are allowed to relax.

Addressing the issue of the strain in the bonds near the interface is a bit tricky, because of the long-range nature of these distortions. However, by doing calculations with ribbons

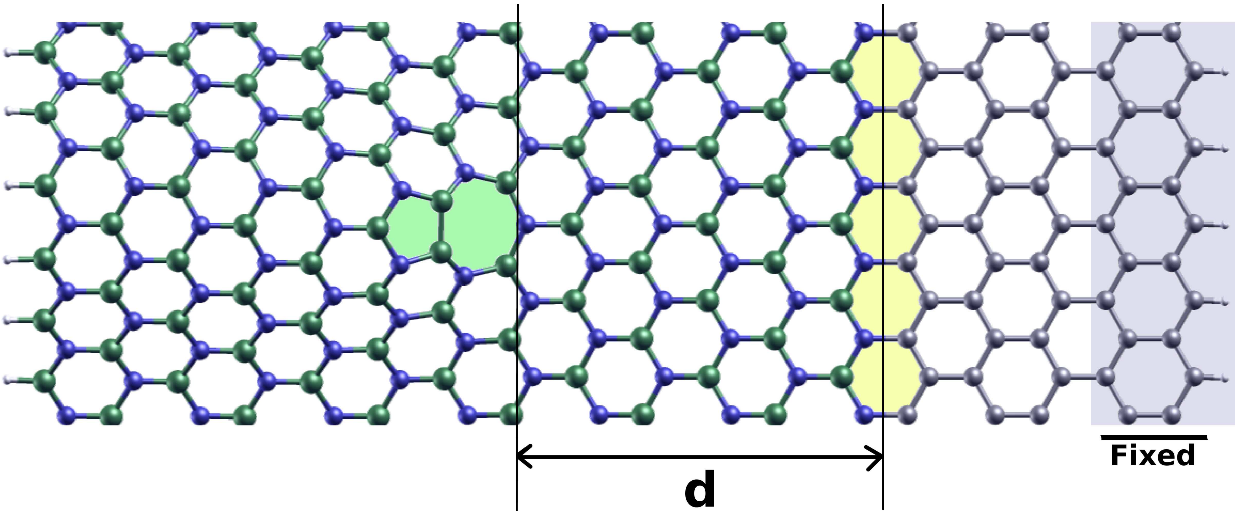

FIGURE 7.6: Example of a super-cell with C-N interface. In order to simulate the graphene substrate, the two zigzag lines of carbon atoms at the edge of graphene side (in light blue box), are fixed during the optimization of the structure. The distance **d** of the 5-7 ring (in light green) from the interface (in light yellow) is chosen as that observed in the experiment, of ∼ 5 lattice parameter.

of increasing lateral sizes (i. e., in the direction perpendicular to the interface) we have a consistent picture of the behavior of the strain in these model structures. For this, three models for C-N interfaces were used, which differ just by the lateral size of the ribbons. As the total number of zigzag lines of carbon atoms is fixed in the optimization process, the widths of the ribbons are defined by the size of the h-BN side. The narrowest ribbon is formed by a total of 18 zigzag lines of atoms, where $n_{BN} = 13$ is the number of BN zigzag lines (∼ 26Å). Two wider ribbons with $n_{BN} = 17$ and $n_{BN} = 19$, corresponding to widths of ∼ 34 Å and 39 Å, respectively, were also used.

For the sake of comparison, we use models for interfaces without the inclusion of the MD. In this case, ribbons of two different lateral sizes were considered, with $n_{BN} = 11$ and 15.

7.3.1 Strain calculations for G|BN interfaces with and without misfit dislocation

After careful optimization of the structures, the average strain for each zigzag BN line parallel to the G-BN interface, was calculated according to:

$$\langle s \rangle = \frac{1}{N_b} \sum_{i=1}^{N_b} \frac{|d_i - d_0|}{d_0} \tag{7.1}$$

where, N_b is the total number of B-N bonds in the zigzag line, d_i is a given bond length between boron and nitrogen atoms, and d_0 is the bulk reference value obtained from a bulk calculation. From our DFT simulations, d_0 = 1.452Å, which matches very well with the experimental value in the literature of ∼1.45 Å Fig. 7.7 shows the calculated average strain in the BN side for nanoribbons of different sizes, with and without MD. The data points presented in the plot refer to each zigzag BN line located after the position of the MD, in the region that can be considered as the 'bulk' part of the BN lattice, as shown in the lower panel in Fig. 7.7.

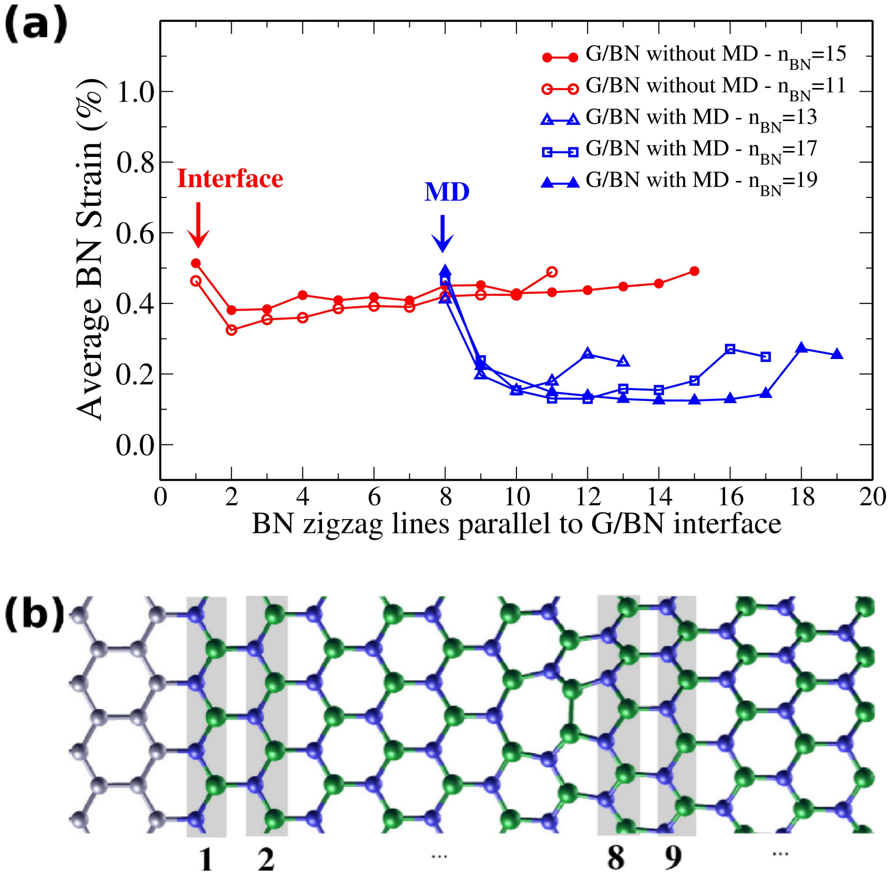

FIGURE 7.7: (a), Average strain profile for interfaces with (in blue color) and without (in red color) MD for different lateral sizes of the nanoribbons. Ribbons with 11 and 15 lines of zigzag BN lines (n_{BN}) where used for the models without MD, while ribbons with n_{BN} = 13, 17 and 19 were used for the interfaces where we have included the MD. (b), A nanoribbon with MD, showing the numbering scheme for the zigzag BN lines [the horizontal axis in (a)] for which the average strain were computed.

For interfaces formed without the MD, the calculated ⟨s⟩ for the two nanoribbons sizes used are indicated by open red circles for n_{BN} =11, and by full red circles for the wider model, with n_{BN} =15. The calculated values indicate that the average strain slight increases as we increase the number of zigzag BN lines for ribbons of both sizes, assuming a value around of 0.43%, indicating a homogeneously strained film. For approximately the last 3 points, an increasing in the average strain is observed due to edge effects.

For all models with the MD, the inclusion of the 5-7 pair causes a decreasing of ⟨s⟩ in the h-BN lattice. Results for models composed by C-N interfaces are represent in blue color for the three different ribbon sizes, with $n_{BN} = 13$ (open blue triangles), 17 (open blue squares), and 19 (filled blue triangles) zigzag BN lines. The average strain abruptly decreases for the first three BN lines from the MD into the h-BN 'bulk'. Starting by the fourth BN line, the strain is observed to decrease saturating at ∼0.12%, except for the last 2-3 points, where an increasing in strain is observed due to edge effects. This value is a well converged result for ⟨s⟩ for the bulk region in h-BN. This can be observed from the data points corresponding to lines 6-9 for the ribbon of intermediated size (for which $n_{BN} = 17$) and further confirmed by the widest ribbon ($n_{BN} = 19$), which shows an almost flat region formed by points corresponding to lines 6-12. These results can be certainly extended for systems of larger regions of BN bulk. The regions affected by edge effects can be easily identified and excluded from the analysis of the average strain.

We can check that the atomic configuration of the interface considered in this work (C-N and C-B) does not affect the strain profile of the h-BN lattice by performing calculations for C-B interfaces. In Fig. 7.8, we show results for both interfaces, with and without the MD. We use the ribbons with lateral sizes corresponding to n_{BN} =17 zigzag BN lines, and exclude the last three points due to the edge effects, which do not affect the converged values of ⟨s⟩ for the others BN lines. There is a very small deviation between values of both interfaces models (less than 0.07%) and, in the context of the strain-release mechanism these results indicate that both atomic configurations of the zigzag linked G|BN boundary (C-B and C-N), and consequently, the atomic configuration of the 5-7 rings, are equally possible to be observed in G|BN lateral heterostructures.

It must be pointed out that for 2D BN layers grown on Ru, the lattice mismatch between the substrate and the overlayer generates an averaged strain of 2.2%. The strain at the G|BN heterointerfaces is certainly modulated by the underlying metal surface. To eliminate the influence of the metal, the delamination of the hybrid film using O_2 intercalation was provided in the experimental work. The hybrid film was decoupled after annealing, as can be observed from the remarkably reduced corrugation in G and BN (inset of Fig. 7.13-b). The maximum strain of BN at decoupled boundaries is slightly reduced (from 5.9% to 4.0%) due to the exclusion of strong substrate interactions but the strain still accumulates as we move away from the interface. From these results, could be concluded that although the metal substrate introduces additional strain at the G|BN interface, it does not change the general trend of strain dependence with the distance from the interface, and the simulations, which do not take substrate effects into account, are apt to describe the experimental results.

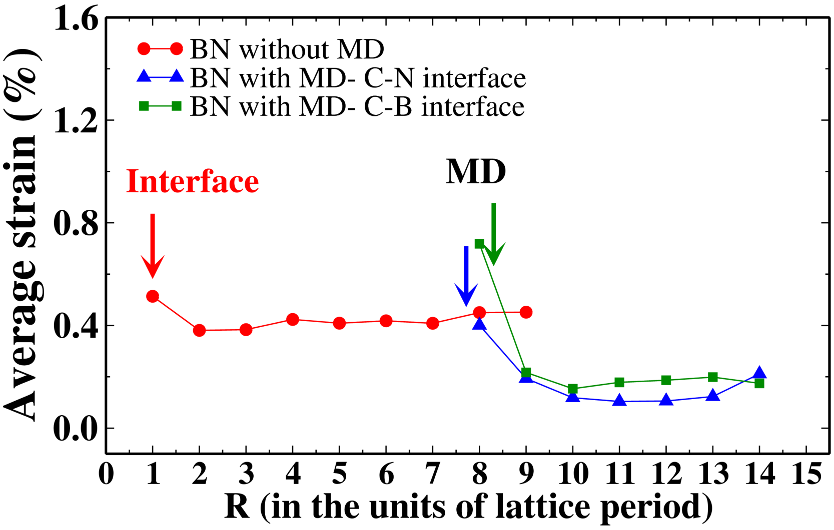

h!

FIGURE 7.8: Average strain profile for C-B (in green color) and C-N (in blue color) zigzag linked interfaces compared to that of defect free interface (in red color). Both atomic configurations of the zigzag linked G|BN boundary (C-B and C-N) with the MD are equally efficient in relief the strain in the BN lattice.

The mechanism of strain release can be explained by the natural occurrence of buckling in the h-BN lattice, induced by the heptagon-pentagon pair. This simple core dislocation structure, formed by five and seven membered rings in a hexagonal lattice, has already been extensively studied in carbon based structures such as carbon nanotubes[100] and graphene[67, 101, 102] in the context of structural deformations.

One isolated 5-7 pair is formed by the insertion of a semi-infinite strip of atoms along the armchair direction in the hexagonal lattice as shown in the right panel in Fig. 7.9. However, when combined with another 5-7 pair, it originates the known Stone-Wales (SW) defect, that can be generated by an in-plane rotation of two atoms in the lattice with respect to the midpoint of the bond. Defined in this way, a SW defect does not introduce 'extra' atoms, as the modification is local and consists of just transformation of four hexagons into two heptagons and two pentagons, as shown in the left panel in Fig. 7.9.

Both these dislocation cores are known to induce buckling in planar sp^2 bonded structures, which is shown by theoretical results to be more energetically favorable to occur than for the structure to remain flat. As discussed in Ref. [103], theoretical results indicate that the bond between the rotated atoms in a SW defect in graphene is compressed by about 7% if compared to the pristine hexagonal lattice. Since in-plane motion of carbon atoms in graphene is stiffer than out of plane motion, the alternative to expand this compressed bond is, for the involved atoms, to displace in the direction perpendicular to the plane of the flat layer. This movement of the atoms affects the neighboring bonds, which are also pulled out of the plane in an attempt to adopt bond lengths as similar as possible to the planar sp^2-bonded network. This explanation is shown to be general and also valid for other planar structures with honeycomb lattices, in special for h-BN [99, 103]. For exactly the same reasons, isolated heptagon-pentagon pairs also induce buckling in planar sp^2 bonded structures as a consequence of the strain in the compressed bonds that occur between atoms in the odd-coordinated rings, as shown in the right panel in Fig. 7.9.

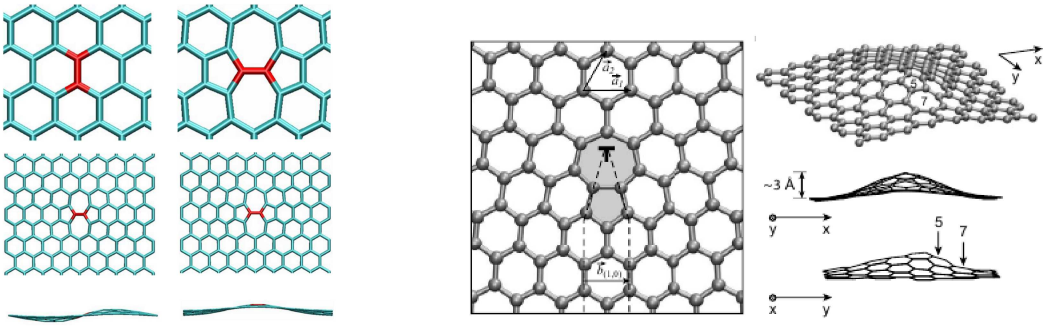

Figure 7.9: Stone-Wales (left) and isolated pentagon-heptagon pair (right) introduced in a hexagonal lattice. Both defects induce buckling in the planar sp^2 bonded structure as a mechanism of strain relief due to the compressed bonds.

With these considerations, we propose the idea of introducing 5-7 rings in the hexagonal lattice of h-BN as a mechanism of strain relief: the initially planar structure comes out of the plane, enabling the bonds to adjust their lengths to the bulk values, due to this additional spatial degree of freedom. Accordingly, $\langle s \rangle$ is reduced, avoiding the breakdown of the h-BN lattice. Initial and optimized structures for the C-N model can be seen in Fig. 7.10. This optimized structure is very similar to that obtained for a C-B interface, where the introduction of the MD also induces the buckling of the BN lattice.

It is interesting to notice that, commonly, MDs occur in heterostructures as a mechanism to 'correct' the mismatch between the materials by introducing additional lines (in 2D structures) or planes of atoms (in 3D materials) in the lattice with smaller lattice parameter, in order to correct the difference with the larger lattice of the second material and relieve the accumulated strain. So, at first we could expect that additional lines of atoms would be introduced in graphene, not in h-BN, which has the larger lattice. However our results indicates that in the growth process, it is more efficient for the h-BN to come out of the plane to release the strain, which can be achieved by the introduction of the 5-7 ring with the orientation that we have considered.

In Fig. 7.11, hight profiles for two valleys in the BN lattice are shown with and without the MD, extracted from the experiment. The width of a valley of the Moiré Pattern without the MD is ~1.75 nm, while for a valley with a dislocation core, it is ~4 nm. From this difference, it seems that the effect of the introduction of the defect is to merge two valleys. The profile of the BN lattice in these regions (valleys with and without the

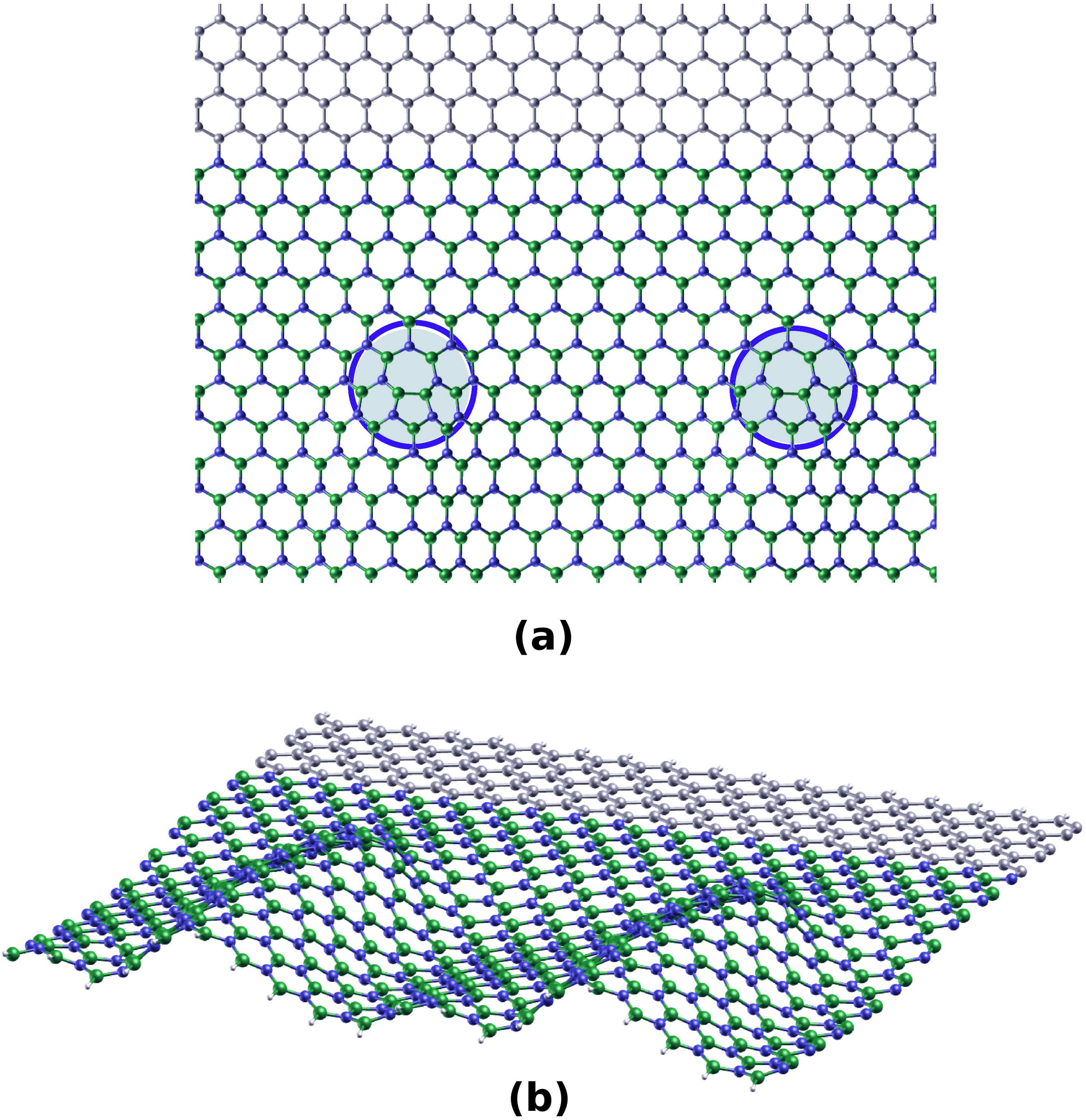

Figure 7.10: Initial supercell with MD and the optimized structure: the pentagon-heptagon pair induces the buckling of the heterostructure, and a reduction of the strain is observed.

core defect) shows that the MD may cause a slight buckling of the BN lattice. While the absolute value of the vertical displacement of atoms due to buckling is not accurate, since STM only gives apparent heights, the qualitative behavior agrees with what we obtained with the introduction of the 5-7 ring in our calculations.

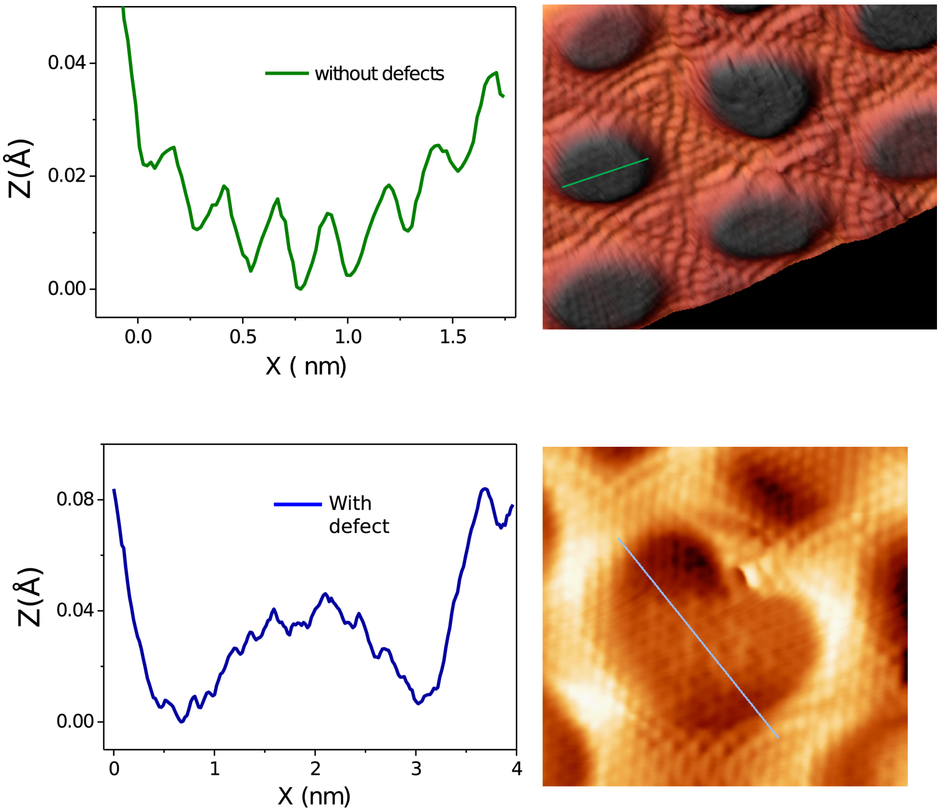

Figure 7.11: High profiles in valleys with and without the dislocation core in BN-lattice.

7.4 Energetics

Total energy of the optimized structures were used to understand the energetics of the interfaces. Stoichiometry of the defect-core will be determinant to identify the stability of the interfaces, as the chemical potentials of boron and nitrogen depend on the sources of these atoms in the growth process. In our calculations, the h-BN lattice with the misfit dislocation is not stoichiometric, as the inclusion of the odd-coordinated heptagon-pentagon pair introduces an extra B or N atom, depending on the interface type. In order to compare the relative stability of the 1D interfaces between graphene and h - BN, the formation energies E$_f^{int}$ for both interfaces (C-B and C-N) were calculated for different environments, from:

$$E_f^{C-N(B)} = \frac{E_{tot}^{rib} - N_N\mu_N - N_B\mu_B - N_C\mu_C - N_H\mu_H - n_{B(N)}^{edge}\lambda_{B(N)}^{edge} - n_C^{edge}\lambda_C^{edge}}{l} \tag{7.2}$$

where E$_{tot}^{rib}$ is the total energy of the ribbons obtained from the DFT calculations, l is the length of the supercell along the interface direction, N_B, N_N, N_C, and N_H are the numbers of boron, nitrogen, carbon, and hydrogen atoms in the ribbon, with respective chemical potentials μ_B, μ_N, μ_C, and μ_H. We also have n_C^{edge} and $n_{B(N)}^{edge}$ as the number of edge units in the supercell, which is formed by C-H pairs in the graphene side and by B-H (N-H) pairs for C-N (C-B) interfaces, in the BN lattice side. The terms $\lambda_{B(N)}^{edge}$ and λ_C^{edge} are the edge energy per edge units $n_{B(N)}^{edge}$ and n_C^{edge}. Results for supercells with MD at two different distances from the interface $d_1 = 0.65$ nm and $d_2 = 1.08$ nm are also considered.

If we assume that the growth process for the formation of the interface occurs in equilibrium with a 'bulk' BN monolayer, we impose the constraint $\mu_{BN} = \mu_B + \mu_N$[39]. From our calculations, μ_{BN} is assumed as the total energy per BN pair for a pristine h-BN monolayer. By considering two chemical potential environments (an B-rich and an N-rich), we consider different sources of boron and nitrogen atoms to define limiting values for the chemical potentials. The extreme N-rich case is defined by the gas-phase of the N_2 molecule as the nitrogen source. For the opposite limit, we choose the BH_3 gas as the boron source for the B-rich scenario. For intermediate chemical potentials, the gas-phase of diborane molecule B_2H_6 and the bulk α-B crystal were used as B sources, while other two values for μ_N were obtained from the gas-phase of the ammonia molecule NH_3 and the N_2 crystalline phase of this atom.

The same interval for the limiting values of the chemical potentials for boron and nitrogen were considered in the theoretical work in Chapter 4 and Ref.[104], where a detailed discussion about these limits as a physically acceptable range for μ_B and μ_N was presented.

The formation energy of the interfaces defined in Eq. 7.2 is defined such that the contribution of the edges in both graphene and h-BN sides is discounted. This can be done by considering the formation energy per edge unit (that is, per C-H pair at the graphene edge and per B(N)-H pair at the h-BN edge) given by $\lambda_{B(N)}^{edge}$ and $\lambda_{C)}^{edge}$, which were also obtained from Chapter 4 and Ref.[104] for the same values of chemical potentials considered here.

The results for $E_f^{C-N(B)}$ for the two interface type models with MDs, as a function of the chemical potential of nitrogen μ_N, are shown in Tab. 7.1 and also in Fig. 7.12.

Analysis of the calculated formation energies according to Eq. 7.2 reveals that both C-N and C-B interfaces can be energetically favorable, depending, besides all the kinetics involved in the synthesis process, on the boron and nitrogen chemical potentials.

As expected, the C-B and C-N interfaces are more energetically favorable under B-rich and N-rich environments, respectively. For the N-rich region both interface types can coexist for synthesis with values of μ_N around that of the ammonia molecule.

C-B + C-N (supercell)	0.59					
	B-rich			N-rich		
	BH_3	B-bulk	B_2H_6	NH_3	N-bulk	N_2-gas
C-B - Defect free	-0.01	0.14	0.14	0.33	0.52	0.54
C-N - Defect free	0.62	0.48	0.48	0.28	0.10	0.09
C-B + C-N	0.61	0.62	0.62	0.61	0.62	0.63
C-B with MD at d_1	0.57	0.67	0.68	0.82	0.95	0.96
C-B with MD at d_2	0.50	0.59	0.61	0.75	0.86	0.87
C-N with MD at d_1	1.01	0.91	0.91	0.77	0.64	0.63
C-N with MD at d_2	0.95	0.84	0.85	0.71	0.58	0.57

TABLE 7.1: Formation energy per unit length (eV/Å) for C-B and C-N interfaces with and without the MD for different values of N-rich and B-rich chemical potentials. Calculations of individual interfaces were obtained using ribbons. Results for two positions for the 5-7 ring from the interface ($d_1 = 0.65$ nm and $d_2 = 1.08$ nm) are also included.

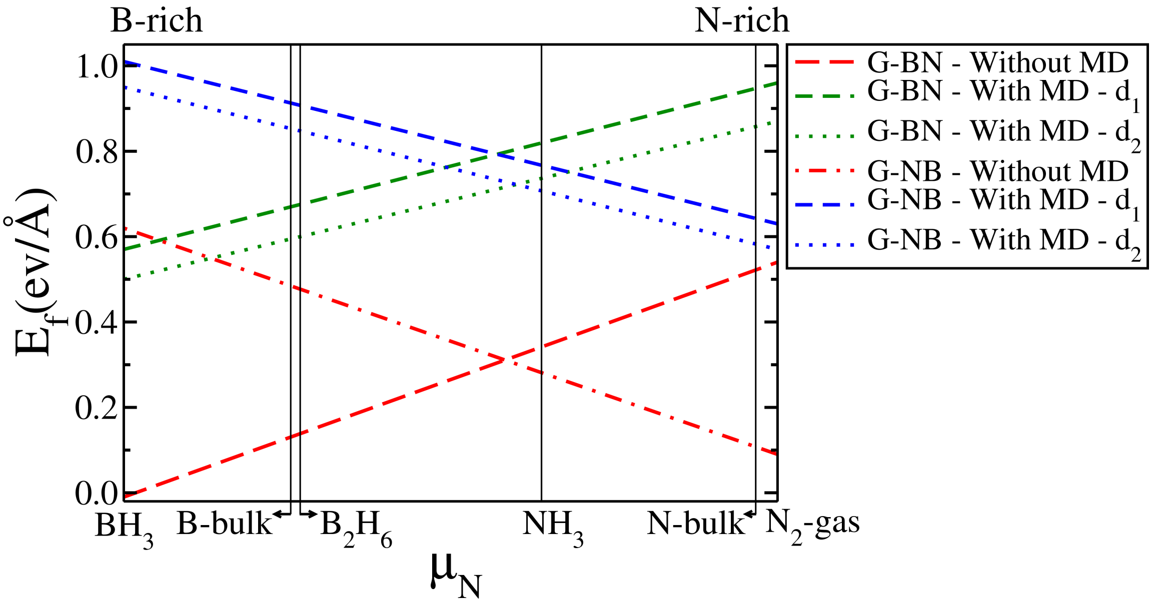

FIGURE 7.12

Regarding the distance of the MD to the interface, we calculated $E_f^{C-N(B)}$ for structures considering the inclusion of the defect core at 3 and 5 lattice units from the interface, which gives us the distances (according to the Fig. 7.6) $d_1 = 0.65$ nm and $d_2 = 1.08$ nm, respectively. The choice of the 5-7 ring nearest to the interface than the experimentally observed value of 1.08 nm can give us insight on a favorable position for the defect core from an energetic point of view. Indeed, we observe that the formation energy of the system is increased when we consider the distance $d_1 = 0.65$ nm for both C-B and C-N configurations and for the different chemical environments. The differences are ~ 0.8 eV/Å for the C-B interface and ~ 0.6 eV/Å for the C-N interface.

The lower values obtained for the interfaces without the MD (shown by the red curves) are expected. Due to the limitation on the system size imposed by computational limitation involved in treating the system using an ab initio approach, the supercells used in the calculations are usually much smaller than the real systems. This precludes us from simulating a G|BN lateral heterostructure large enough for the cost to introduce the MD to be lower than that of a defect-free interface. In this way our results are, in fact, on a length scale where the system can form seamless interfaces between graphene and h-BN without the breakdown of the h-BN lattice.

For large enough systems, it is expected that $E_f^{C-N(B)}$ will assume higher values for the defect-free case, due to the strain accumulation, and a system with the MD should be energetically more favorable.

7.5 Electronic Properties

7.5.1 Interfacial electronic states probed by STS

Zigzag type G|BN heterointerfaces have been predicted to possess interesting properties such as half-metallicity, antiferromagnetism and other transport properties[87, 91, 105–107]. The ability to resolve the zigzag type coherent G|BN interface allows the investigation of its local electronic states using scanning tunneling spectroscopy (STS).

For freestanding graphene, localized states at zigzag edges produce flat bands and sharp density of states (DOS) at the Fermi Level (E_F)[108, 109]. However, such zigzag states are quenched when graphene is attached to Ru, because the orbital hybridization between carbon and Ru depletes the DOS near E_F. Upon the bonding of the graphene edge to BN, such localized edge states remain absent due to the coupling with the metal, as evident from the STS study as shown in Fig. 7.13-c.

In contrast, a great enhancement of the differential conductance (dI/dV) is observed at the decoupled G|BN interface (Fig. 7.13-e), which results in the appearance of distinct bright spots (due to enhanced local DOS) when imaged by STM (Fig. 7.13-b and d). In contrast, such bright spots are absent in as-grown G|BN interfaces as well as in interfaces where only BN or G is decoupled (Fig. 7.13-c). The STS collected at the decoupled BN sites (C point marked in the inset of Fig. 7.13-d) is relatively featureless with a low tunneling conductance owing to its insulating nature, while the decoupled graphene close to the interface displays p-doping as reflected by the presence of a dip at ∼0.15 eV (Dirac point) in the STS curve (collected at A point in the inset of Fig. 7.13-d)[110].

At a zigzag-type G|BN interface, the bonding between the atoms at the interface gives rise to a high-energy antibonding orbital, which shifts the conduction band right above E_F . In addition, the strong mixing of π orbitals between the C and N (or B) atoms at

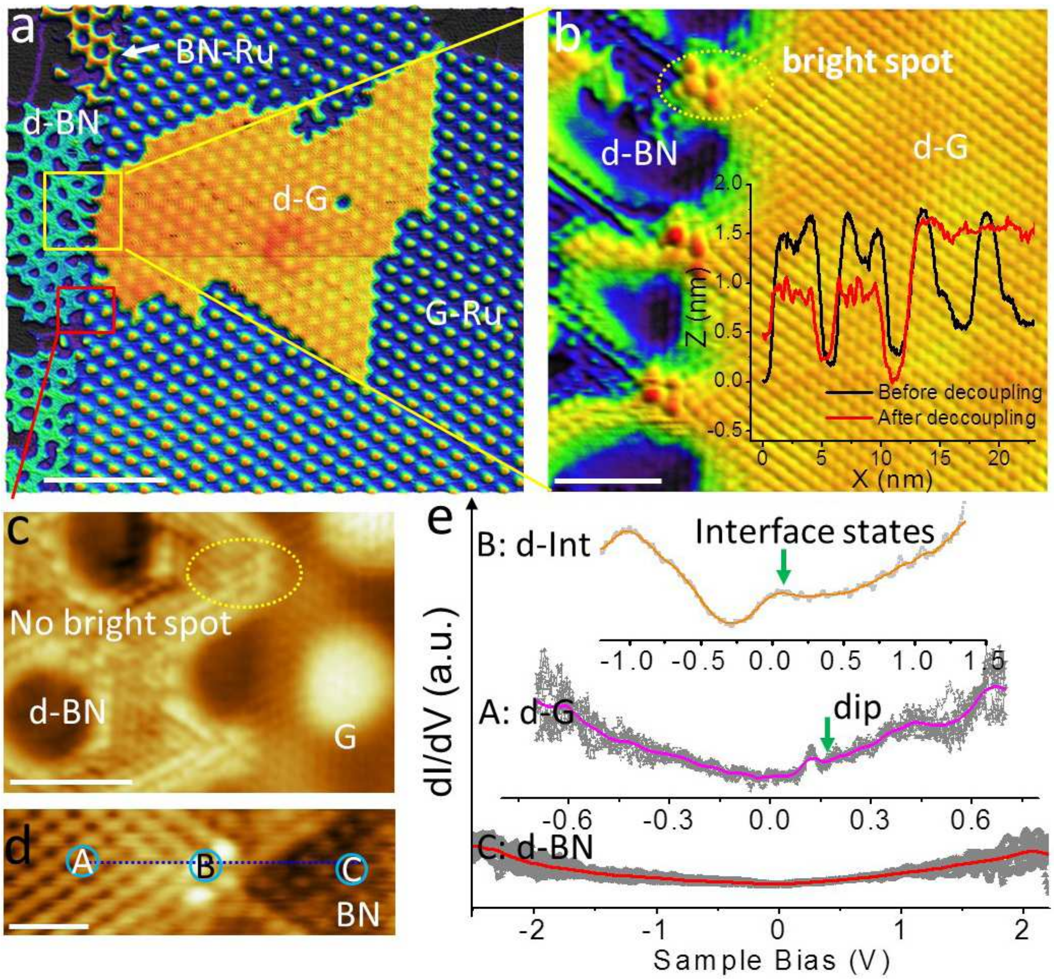

FIGURE 7.13: Probing the intrinsic electronic states at the G|BN interface after O_2 intercalation. (a) Large-scale STM image to show the co-existence of decoupled G|BN interface and coupled interface. (b) The presence of interface states generates bright spots at the interface of G|BN after decoupling. Inset: height profile along the direction perpendicular to the interface of G|BN, before and after decoupling. (c) No bright spots are observed at the boundary between decoupled BN and coupled graphene. (d) STS spectra collected along the line perpendicular to the G|BN interface. (e) STS spectra collected along the line perpendicular to the G|BN interface as marked in d. Scale bars in a-d are 20, 2, 2 and 0.5 nm respectively.

the interface also increases the DOS around E_F, leading to an increase of the tunneling conductance (Fig. 7.13-d). A feature peaked at ∼80 meV above E_F is present in the dI/dV spectrum collected at the bright spots (point B in Fig. 7.13-d).

7.5.2 Interfacial electronic states - Ab initio calculations.

In order to provide further insight into these experimental observations, we carried out ab initio calculations of the electronic structure of G|BN heterolayers with coherent interfaces with a periodic array (17.5 Å) of 5-7 dislocation cores located at a distance of 1.15 nm away from the interface. We employ the same methodology as in the strain-profile calculations.

The calculated electronic density of states (DOS) for both monolayer models, with N-C and B-C coherent interfaces, are shown in Fig. 7.14. An analysis of the degree of localization of these electronic states on different atoms can be done by the partial DOS (PDOS) projected onto such atoms.

We start by examining the PDOS summed over the interface atoms. The added contributions of the orbitals of the B, N, and C atoms on the two zigzag lines at the interface is represented by the red curve, while the individual contributions are shown by the green (C), blue (N), and orange (B) curves. The total DOS, represented by the black curve, shows two sharp peaks around the Fermi level (FL) for both interface types.

For the C-N interface, the first peak, at the FL, is only partially localized on the interface atoms, with ∼40% of the total DOS deriving from these atoms. A different scenario is observed for the second peak, located at ∼0.1 eV above FL: the PDOS curves show that this peak is associated with states that are strongly localized at the interface, with a contribution of ∼90% from the orbitals of the interface atoms. The individual PDOS curves for each species of interface atoms show that the B atoms at the interface have a negligible contribution, and that the localized peak is essentially due to 1D states along the interface derived from the interfacial C-N bonds.

For the C-B interface model, similar results are observed, when compared to the C-N interface. Two sharp peaks are present around the FL, the one at ∼0.03 eV above the FL is only partially localized on the states of the interface atoms, also with a contribution of just ∼40% to the total DOS. A strong contribution from the interface states of ∼90% is now observe for the DOS peak below the FL, at ∼ -0.15 eV, with the smaller contribution given now by the nitrogen atoms.

In Fig. 7.13-e, we can see a peak at 0.08 eV above E_F in the dI/dV spectrum collected at the point B (Fig.7.13-d), which represents the interface states of G|BN. Even though just one peak is observed in the experimental results, we see that this peak is broad, with a width of ∼0.4 eV, and probably represents the overlap of the two peaks observed in the DFT calculation that could not be distinguished from each other due to the resolution of the experiment.

In Fig. 7.15 it is shown a representative isosurface of states obtained from the calculation of the local density of states (LDOS) in the energy range of 0.05 to 0.15 eV for the C-N interface, and -0.2 to 0.06 for C-B interface, which comprises the sharp localized peak in the DOS due to the interface atoms for both interface types. In each case, the states in the corresponding range of energies are strongly concentrated at the interface, specifically

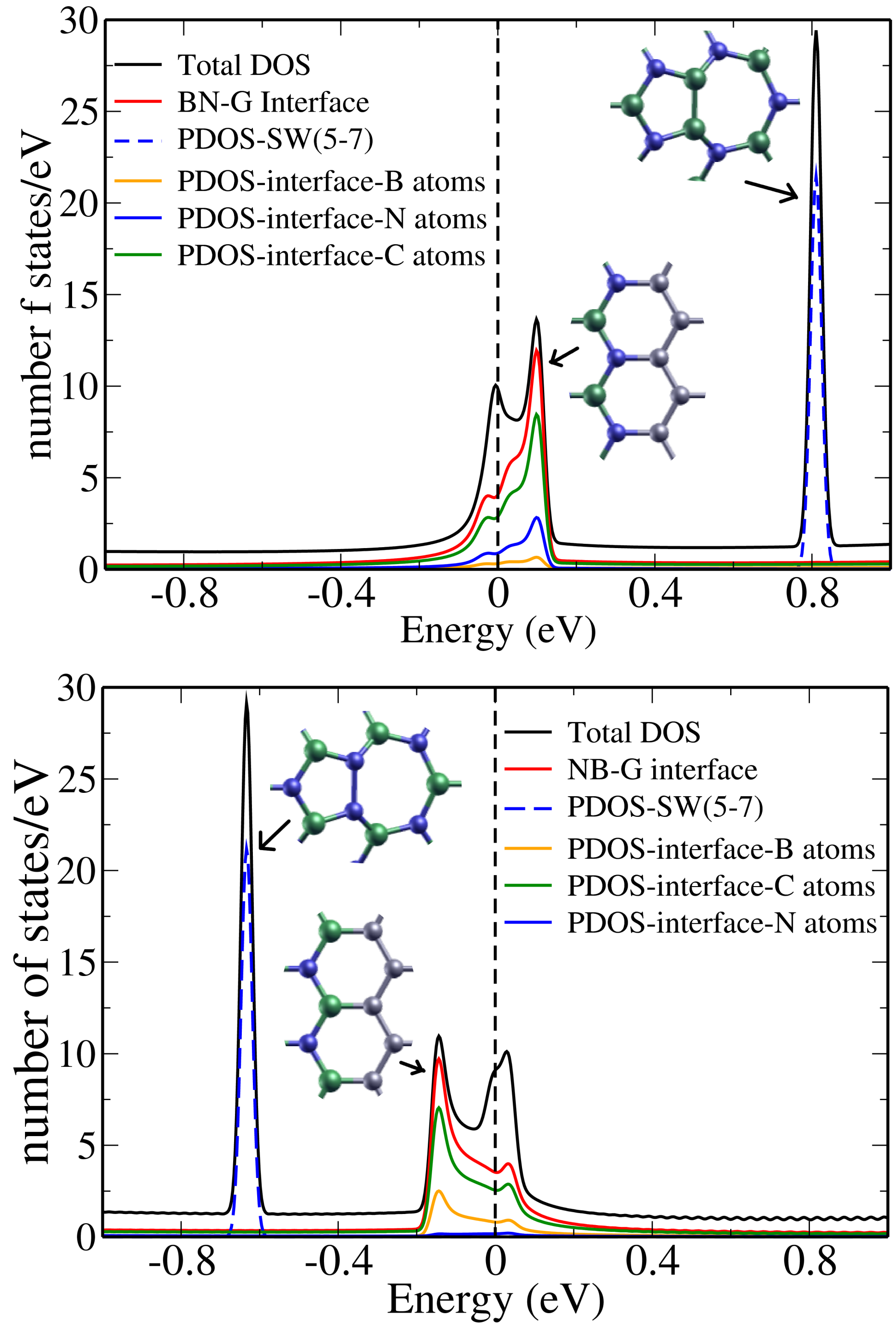

FIGURE 7.14: Calculated electronic properties of G|BN heterostructures with linked C - N (higher panel) and C - B (lower panel) zigzag interfaces. Total density of states (DOS) and partial DOS (PDOS) analysis shows the introduction of interface states near the FL at ∼ 0.08 eV for C-N and ∼ -0.15 eV for C-B interfaces. States due to the 5-7 pair introduce a sharp peak at 0.8 eV and -0.63 eV, for C-N and C-B, respectively.

on the C-N and C-B bonds for the different interfaces, with negligible contribution from other atoms. Even the second line of carbon atoms in the graphene side, and the boron or nitrogen atoms (depending on the interface type) bonded to the interface atoms in the BN lattice, do not contribute to the charge density, again demonstrating the high degree of localization of the states due to the hybridization of the C and N (or C and B) orbitals.

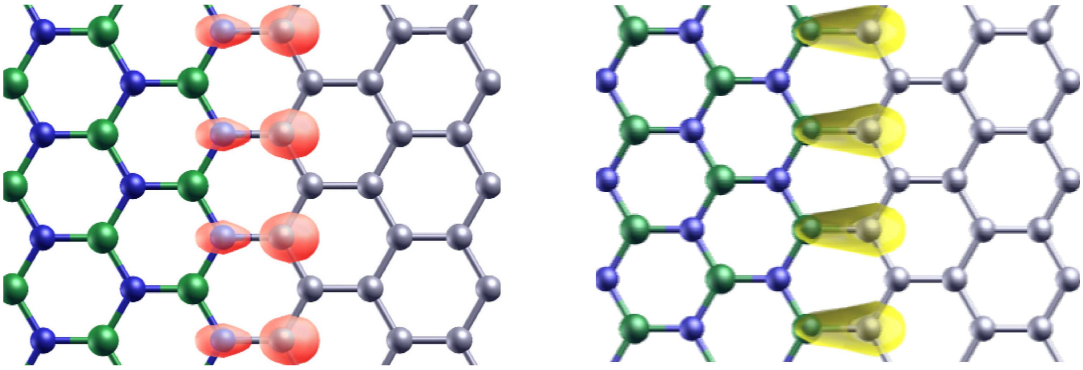

Figure 7.15: Local density of states (LDOS) for G|BN heterostructures with C-N (left) and C-B (right) bonds at the interface. For each interface the LDOS is plotted for states in the energy range corresponding to the peaks in the DOS with major contribution from the atoms of the interface (0.05 to 0.15 eV for the C-N interface and -0.2 to 0.06 eV for the C-B interface).

Another important point is the contribution of the MD core atoms to the DOS. The projected DOS (PDOS) onto the orbitals of the boron and nitrogen atoms that form the 5-7 rings indicate the introduction of a sharp peak at ∼ 0.8 eV for the structure with a C-N interface, as shown by the blue dashed line in Fig. 7.14 (upper panel). This result is consistent with the observation of bright spots at the bias voltage of 1V for the decoupled layers in the experimental work, which could be an indication of the formation of this interface configuration in the experiment.

For the model with the C-B interface, a similar peak due to the heptagon-pentagon pair is observed below the FL level, at ∼ -0.63 eV (blue dashed line in the lower panel in Fig. 7.14). The high localization of the states from the MD atoms clearly show that they do not introduce states at the FL in both interface types. These results strongly suggest that scattering of the interfacial states by the MD core should be negligible, and the dislocations should not have a detrimental effect on the 1D electronic transport at the interface.

It is also important to comment about the edge states introduced in the electronic structure analysis. As we are dealing with nanoribbons to address our problem, it is important to check if such edges states can affect our results, as they are just an artificial element introduced into the problem to make the calculations feasible. In Fig. 7.14, the total density of states excluding the states due to the edge atoms is presented. A more complete analysis of such states can be done, in order support the assumption that they do not affect the main results.

In Fig. 7.16, the total DOS including edge states is presented in cyan color for both C-N and C-B interfaces. By a PDOS analysis of the edge states, we can see that they are strongly localized on the edge atoms and do not contribute to the localized peak due to the interface states.

The strong localization of the edge states means that the edge atoms do not contribute to the localized peak due to the interface states. The states due to the C-H-saturated edge, represented by the sharp peak in green color, is at the FL (0 eV) and do not hybridize with the interface or with the MD states. States due to the N-H and B-H-saturated edges, shown in yellow, are observed far from the FL (at $\sim$ -1.3eV and $\sim$ 1.5 eV, for N-H and B-H edges, respectively), and clearly do not contribute to the physics of the interface. These results confirms that the interface states are not affected by the edge states, which can be easily eliminated from the analysis of the DOS.

7.6 Conclusions and Perspectives

In conclusion, we use DFT calculations to characterize structural and electronic properties of atomically sharp G|BN heterointerfaces. As reported by the experimental group with which we collaborate to develop this work, long and sharp G|BN interfaces can only be formed in the presence of some strain relief mechanism, due to the mismatch between the graphene and boron nitride lattices.

Our calculations indicate a reduction of the strain in the h-BN lattice when MDs formed by 5-7 rings are introduced in the hexagonal lattice of BN. This result can be explained by the natural occurrence of buckling in the h-BN, induced by the core dislocation. The atoms in the initially planar structure come out of the plane enabling the bonds to adjust their lengths to the bulk values, due to this additional degree of freedom. Consequently, the strain $\langle s \rangle$ is reduced, avoiding the breakdown of the h-BN lattice.

The electronic properties of the interfaces are also discussed. The experimental results indicate that the electronic states associated with the formation of the coherent G|BN boundaries are characterized by a strong 1D confinement at the interface region, and an enhancement of the DOS near the FL is observed. Indeed, our first principles calculations indicate the formation of highly-localized states formed mainly by orbitals from the atoms at the interface, with energies near the FL. Among the two types of boundaries investigated, formed by linked C-N and C-B zigzag interfaces, the C-N interface presents a highly-localized peak which agrees with experimental results for the collected dI/dV spectrum, being an indicative that the interfaces in the experiments should be composed of bonds between C and N atoms.

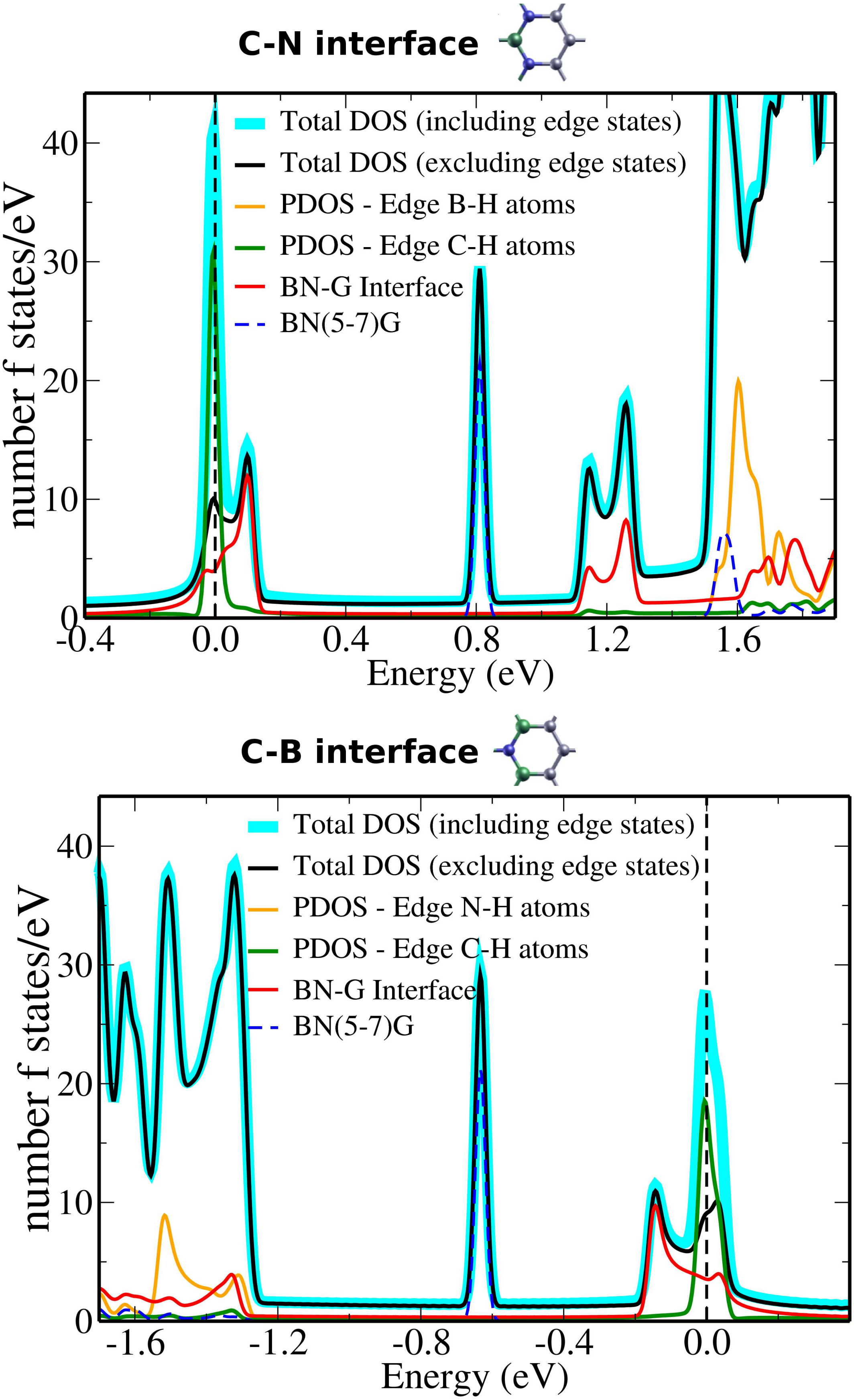

FIGURE 7.16: Calculated electronic properties of G-BN heterostructures with linked C-N (higher panel) and C-B (lower panel) zigzag interfaces including the edge states of both graphene and h-BN lattice. Edge states (in green and yellow) are strongly localized at the edges and can be discerned from the interface states.

Finally, this work will be extended by calculations including the Ru substrate, in order to obtain a better quantitative agreement with experimental results. Magnetic properties of the C-N and C-B interfaces will also be considered.

Chapter 8

Beyond Graphene: Electronic and Structural Properties of Bulk and Few-layers Semiconductors Monochalcogenides.

8.1 Introduction

As discussed in the previous chaperts, the special properties of two-dimensional materials, in special graphene and hexagonal BN, have attracted significant attention of the research community in the last years. A great part of the special properties of materials in this lower-dimensional world have been already explored, both theoretically and experimentally, and it is clear that manipulation and control of materials properties in such size scale is an arduous task. Great advances have already been achieved, but industrial-scale applications remain a challenge. The search for well controlled methods to tune the graphene band gap is one of the main topics in the study of this material. Introduction of defects [111], application of strain [69, 112], doping [113, 114], construction of heterostructures [112] are just a few examples of the many attempts that have shown promising results in this direction.

In this scenario, black phosphorus (BP) is part of the group of materials attracting attention in two-dimensional materials research. Discovered in 1914 by Bridgman [115], who measured some properties like density (2.69 gm/cm^3), compressibility [116] and electrical resistivity as a function of pressure over the range of temperatures of ~ 273 K to 348 K [115, 117], BP is the thermodynamically stable form of phosphorus (P) at room temperature and pressure [118, 119].

Black phosphorus adopts an orthorhombic structure with eight atoms per unit cell and its lattice parameters have been determined in experimental and theoretical [119–121] works. The P atoms are arranged in puckered layers, and inside a single layer each atom is covalently bonded to three neighbors. The bulk is formed by these layers stacked together by van der Waals forces.

BP shares with graphene properties like high mobility and a van der Waals monoatomic crystal character [120]. The presence of a direct band gap makes black phosphorus a new promise of a two-dimensional gapped material. Many works have predicted the band gap of BP to increase with decreasing the number of layers. For the bulk, a gap of 0.3 eV has been observed [119, 122–125], while a value of 2 eV is predicted [121] for monolayer BP, which is also termed ‘phosphorene’.

The hexagonal structure of phosphorene, which makes it conceptually similar to graphene in defining some of its interesting properties, opens up the question of whether other materials with such structure can also be considered as potentially important, as part of the two-dimensional group of materials for the future applications in nanoelectronic devices.

The monochalcogenides GeS, GeSe, SnS and SnSe form structures that can be considered derivatives of the orthorhombic black phosphorus [126]. At determined pressure and temperature, each of these compounds can adopt an orthorhombic crystal structure with space group Pnma-D_{2h}^{16} (α phase) (for BP the space group is D_{2h}^{18} [127]).

The α phase of SnS has been investigated as an absorber material for production of thin film photovoltaic (PV) cells, a technology of increasing importance in the demand for energy conversion. Although PV cells based on CdTe and $\mathrm{CuInGaSe_2}$ compounds have also shown promising results due to their high efficiencies [128–130], many factors make their usage difficult such as the high cost and toxicity of Cd [27, 130, 131]. From this, SnS, which is made of abundant and nontoxic elements, has attracted attention as an alternative absorber material for thin PV cells. In addition, the layered structure of α-SnS, combined with its semiconductor behavior with an optical band gap of ~ 1.3 eV, in the range of the optimal values for solar cells (1.1 to 1.5 eV), makes SnS an attractive alternative in this group of promising materials for PV application.

The optoelectronic properties are of essential importance in the construction of this type of nanodevice, and so many theoretical works have been done in an attempt to determine electronic and optical properties of SnS for its bulk form as well for few-layer and single-layer structures, which remain still poorly explored.

In this chaper, we present preliminary results of a study of two-dimensional semiconductors monochacogenides. This work is still in progress and focuses on the electronic and optical properties of these materials. It will be further developed in collaboration with the theoretical group of the GRC/NUS.

We use first-principles calculations to investigate electronic and structural properties of the four aforementioned metal monochalcogenides MX, with M=(Sn, Ge) and X=(S, Se), forming the following group of compounds: SnS, SnSe, GeS and GeSe. We investigate single-layer, double-layer and bulk structures for each of these materials, in an initial attempt to determine their structural stability in the α-phase, as well as to obtain information about basic important electronic properties, such as band gap characteristics. Preliminary results are presented and discussed.

8.2 Structural and Electronic Properties

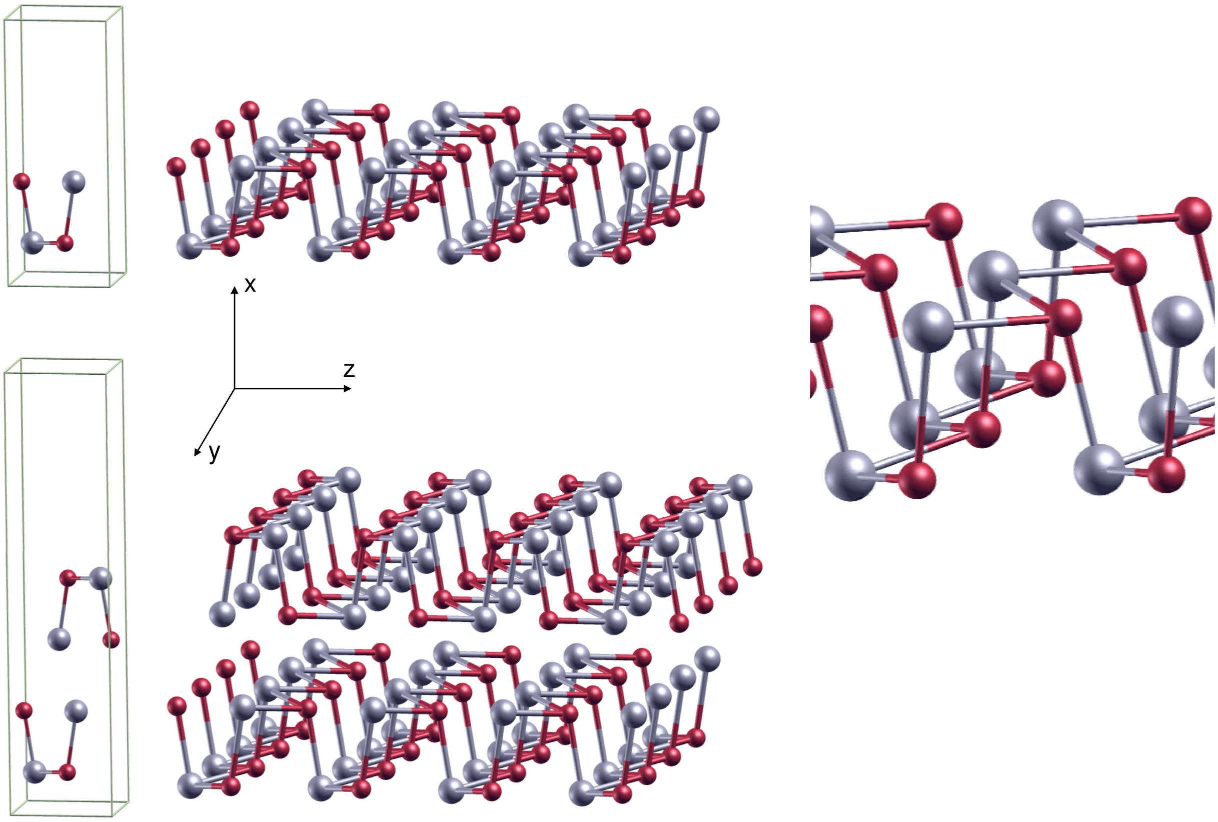

FIGURE 8.1: Structural model for the orthorhombic cell of the α-phase. We show the unitcells for single and double layers, which are repeated along the $\hat{x}$ direction. A zoom in the structure shows one atomic species and its three first neighbors of the second atomic species that compounds the system.

8.2.1 Crystal Structure of the α phase.

The α phase is defined by an orthorhombic structure with eight atoms per unit cell. For the materials considered here, we have four atoms of each species. These atoms are arranged in two puckered layers and each atomic species is covalently bonded to three neighbors of the other atomic species, as shown by the enlarged picture in Fig.8.1.

At high temperatures (> 800 K), SnS and SnSe adopt a more symmetric structure (β phase) with space group Cmcm-D_{2h}^{17} [132, 133]. In this phase, the unit cell is also formed by double puckered layers[126], but now each atom is bonded to four atoms of the second atomic species. A phase transformation from α to β phase has been also theoretically predicted for SnS at high pressures[133]. In our initial calculations, we consider just the α phase of the four different compounds. The β phase will also be investigated in the next steps of this work. Optimization calculations were performed for single and double layers and also for the bulk, in order to investigate the stability of these systems.

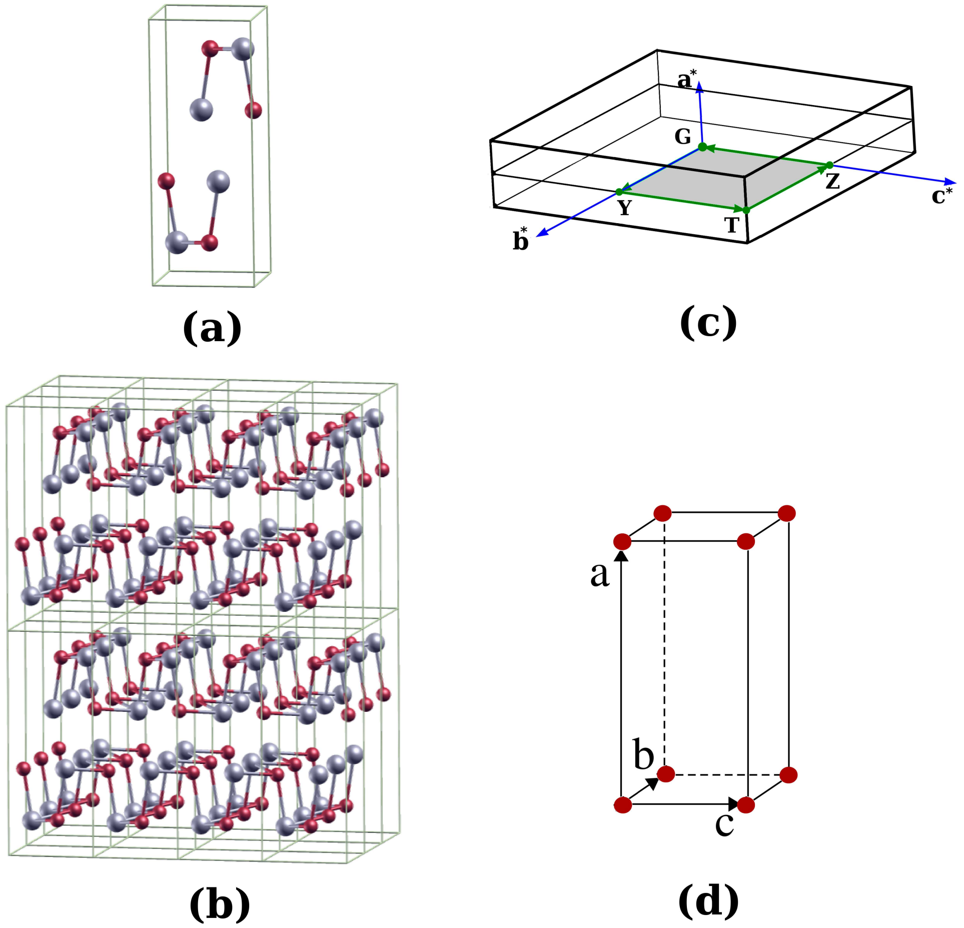

(a) **(c)**

(b) **(d)**

FIGURE 8.2: (a) Unitcell and (b) the repeated structure of the bulk in the α phase. The respective BZ is shown in (c) with the special points Γ, Y, T, Z, localized at the $\mathbf{b}*$-$\mathbf{c}*$, plane, corresponding to the plane of the puckered layers in the reals space. The orthorhombic lattice is shown in (d)

The orthorhombic unit cell of the α phase, contains 8 atoms, being 4 of each atomic species for bilayer and bulk models. For the monolayer, 4 atoms (2 of each atomic species) compose the unit cell. By following Ref.[132–134], layers are chosen to sit on the y-z plane, and so, interlayer forces are in the x-direction. Considering the axes of the primitive orthorhombic unit cell $\mathbf{a_0}$, $\mathbf{b_0}$ and $\mathbf{c_0}$, the atomic positions in the crystal vector units are: $\pm(x,\frac{1}{4},z;\ \frac{1}{2}+x,\frac{1}{4},\frac{1}{2}-z)$. For SnS at 295 K[132, 135] we have: $\mathbf{a_0}$=11.20 Å, $\mathbf{b_0}$=3.99 Å, and $\mathbf{c_0}$=4.33 Å with atomic coordinates x(Sn)=z(Sn)=0.12, x(S)=0.85 and z(S)=0.48.

For monolayer and bilayer models, vacuum regions of 8 and 9 Å, respectively, were used between adjacent images in direction perpendicular to the layers for each structure. Convergence tests with greater vacumm regions were done, and the values used are enough to avoid interaction between neighboring images.

	Single-Layer		Double-Layer		Bulk		
	b	**c**	**b**	**c**	**a**	**b**	**c**
GeS	3.68	4.40	3.67	4.42	10.81	3.68	4.40
GeSe	3.99	4.26	3.97	4.31	11.31	3.91	4.45
SnS	4.07	4.24	4.05	4.28	11.37	4.02	4.35
SnSe	4.30	4.36	4.25	4.42	11.81	4.22	4.47

TABLE 8.1: Optimized lattice vectors for α phase of SnS, SnSe, Ges, GeSe.

Starting with the SnS compound, optimization of the bulk structure gives the equilibrium unit cell lattice vectors in good agreement with experimental results in Ref. [126, 132, 136] (a= 11.20 Å, b=3.98Å and c=4.33Å) and also with calculated values from others theoretical works [130, 131, 133]. Our calculated vectors for bulk of SnSe, are also very close to that obtained in a previous experimental work [137] of **a**=11.50 Å, **b**=4.15 Å, and **c**=4.44.

By comparing the calculated values for SnS and SnSe and also for GeS and GeSe, shown in Tab.8.1, we observe that the most compact structure is that of GeS, which presents the smallest lattice vectors for single-layer, double-layers and also for bulk, while SnSe presents the largest lattice parameters for all models.

The optimized bond lengths are shown in Tab. 8.2. The different types of interatomic distances, represented in Fig. 8.3, are given as in Ref. [126], where the refinement of atomic distances was done by X-ray diffraction. Our values agree very well for most of the bonds considered, the major deviations observed are for C1, C2 and E, defined as the interlayer bonds.

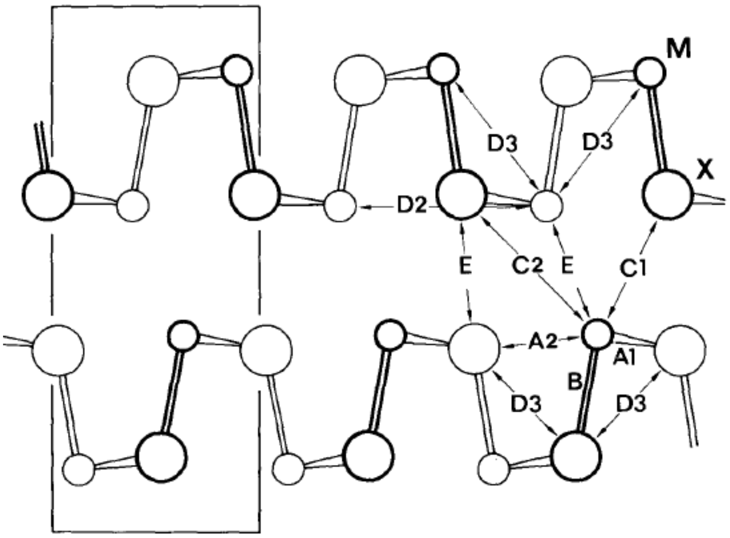

FIGURE 8.3: Different types of interatomic distances for the α phase of SnS, SnSe, GeS, GeSe. The small circles (M) stands for Sn and Ge, while the large circles (X) stands for Se and S atomic species. Figure taken from Ref. [126].

A(1)-A(2)	Type	SnS	SnSe	GeS	GeSe
A_1–A_2	A1 in	2.69 (2.66)	2.84 (2.79)	2.47 (2.44)	2.62 (2.57)
A_1–A_2	B in	2.65 (2.63)	2.78 (2.74)	2.46 (2.45)	2.59 (2.56)
A_1–A_2	A2 in	3.30 (3.29)	3.35 (3.34)	3.33 (3.28)	3.37 (3.32)
A_1–A_2	C1 ex	3.44 (3.39)	3.55 (3.47)	3.37 (3.28)	3.47 (3.37)
A_1–A_2	C2 ex	4.16 (4.09)	4.24 (4.10)	4.06 (3.92)	4.17 (3.94)
A_1–A_1	D2 in	4.36 (4.33)	4.47 (4.44)	4.40 (4.30)	4.45 (4.39)
A_1–A_1	D3 in	4.17 (4.15)	4.31 (4.29)	3.92 (3.89)	4.03 (4.03)
A_1–A_1	E ex	3.57 (3.49)	3.70 (3.55)	3.50 (3.33)	3.69 (3.39)
A_2–A_2	D2 in	4.36 (4.33)	4.47 (4.44)	4.40 (4.30)	4.45 (4.39)
A_2–A_2	D3 in	3.75 (3.71)	3.96 (3.88)	3.55 (3.51)	3.78 (3.67)
A_2–A_2	E ex	3.95 (3.90)	4.02 (3.94)	3.78 (3.64)	3.84 (3.71)

TABLE 8.2: Ab initio interatomic distances according to Fig. 8.3. A_1 stands for atomic species Sn and Ge while A_2 represents S and Se. With the interatomic distances type we denote in and ex as the distances valid for intra and inter puckered layers, respectively. The experimental values obtained in Ref. [126] are shown in parenthesis.

8.2.2 Electronic Properties of single-layer, double-layer and bulk models.

The calculated electronic band structures are presented in this section. For the simple orthorhombic lattice adopted by these systems, the brillouin zone (BZ) is defined as in Fig. 8.2-c, where the high symmetry points Γ-Y-T-Z-Γ are defined to sit in the plane x=0. A general trend is observed for all compounds, where the energy gap E_g decreases as we increase the number of layers, a result that agrees with previous works that also investigate SnS electronic structures by first principles [130], and it seems to extends for the others IV-VI compounds considered in this chapter.

Except for single and double-layers GeSe, bulk GeS and single-layer SnSe, which shows direct band gaps, indirect gaps are observed for all the other materials. The calculated values for E_g are summarized in Tab. 8.3 and discussed in the following.

	Monolayer		Bilayer		Bulk	
	E_T(eV)	Gap (eV)	E_T(eV)	Gap (eV)	E_T(eV)	Gap (eV)
SnS	-749.17	1.40	-1498.53	1.13	-1498.73	0.83
SnSe	-706.72	1.01 *	-1412.63	0.79	-1413.62	0.55
GeS	-771.99	1.69	-1544.12	1.55	-1544.26	1.24 *
GeSe	-729.50	1.14 *	-1459.08	1.02 *	-1459.17	0.59

Table 8.3: Total energies (E_T) and gap energies(E_g) for monolayer, bilayer and bulk of SnS, SnSe, GeS, GeSe. The star (*) indicates the direct band gaps.

SnS: Starting with SnS, Fig. 8.4 shows the electronic structure for the single-layer, double-layer and bulk, calculated along the high symmetry lines Z-Γ-Y-T-Z of the Brillouin zone (BZ). For all models, indirect energy gaps are obtained, with the valence band maximum (VBM) and conduction band minimum (CBM), located along the Z-Γ and Γ-Y lines, respectively. For better visualization, these points will be highlighted by the green and red small circles for the results of all compounds, discussed in this section.

The calculated values for E_g of 1.40, 1.13 and 0.82 eV are lower than those obtained in Ref. [130] using the GW method [138, 139] for the band structure calculation, which gives E_g = 2.57, 1.57 and 1.07 eV for single-layer, double-layer and bulk SnS, respectively. This difference was expected, because the GW approximation to the electronic self-energy has shown reliable results of electronic and optical properties for a wide range of materials [125, 140], opposite to the known underestimation of electronic gaps observed for GGA/DFT methods. Despite these differences in the calculated energy gaps, we notice that the shape of the bands is preserved, and the positions of VBM and CBM are obtained along the same directions in the BZ.

With these considerations, our calculations, although not as accurate as demanded for the study of the optical properties of these systems, already show some coherent results for the α phase of SnS, a behavior that we believe to extend to the other compounds, due to their similar chemical characteristics. Furthermore, the present preliminary results will be used in addition to those obtained in the next steps of this work with more accurate methods, as a mean of comparison to investigate the main characteristics affected by the different approaches.

For all compounds in our calculations, other k-points show energy eigenvalues very close to the conduction band maximum (CBM) and valence band minimum (VBM). Due to this small difference in energy, such points can be considered as “competing” points, for which energy gaps defining direct transitions must also be considered.

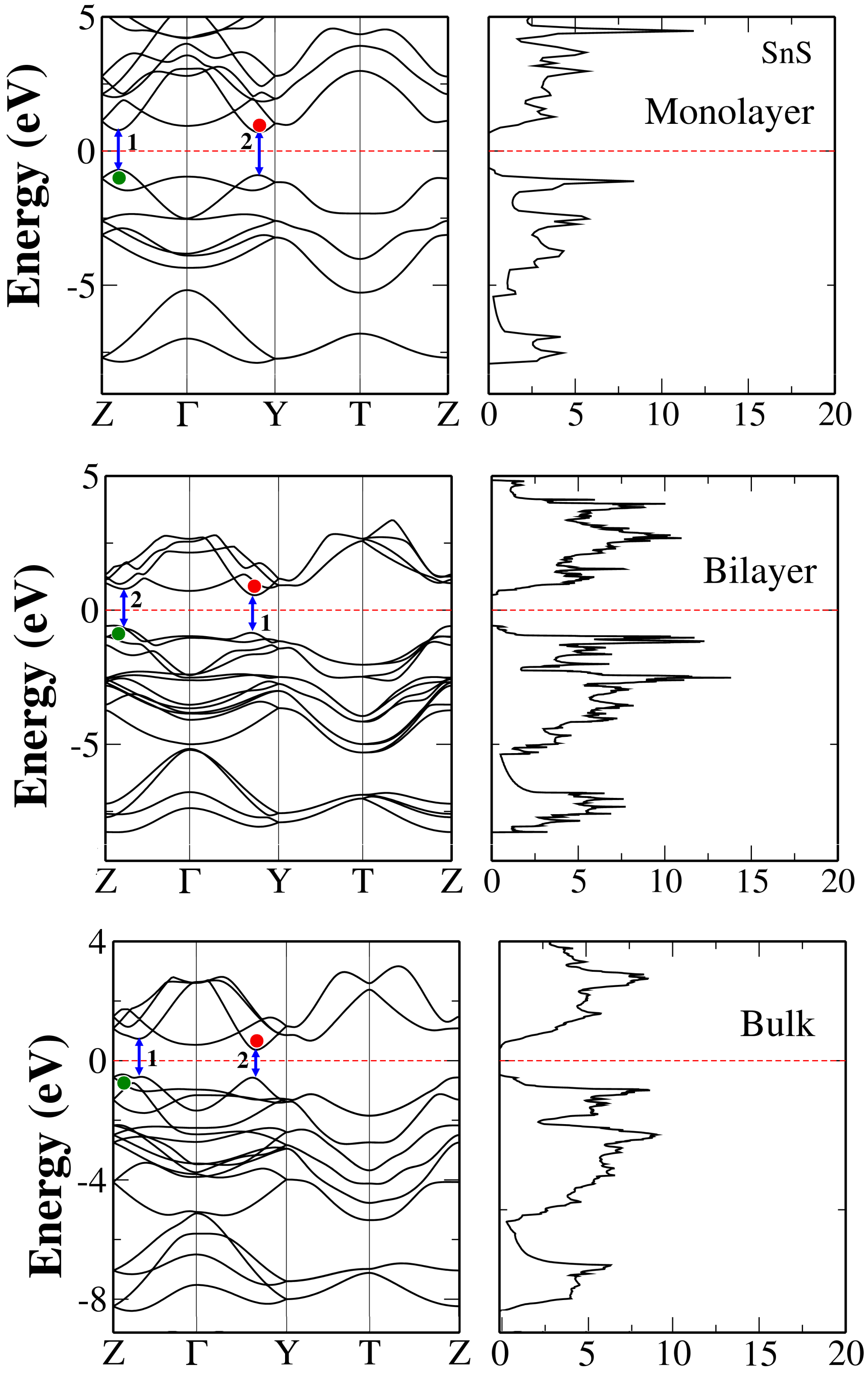

FIGURE 8.4: Electronic band structures for single-layer, double-layer and bulk for α phase of SnS. Indirect band gaps are calculated for all models, and direct band gaps higher in energy by a few meV define the possible direct transitions 1 and 2. The red and green points mark positions of CBM and VBM respectively.

Continuing the analysis of electronic structure of α-SnS, in addition to the indirect band gap observed for the single-layer, two direct gaps higher in energy by 0.17 eV (represented by transition 1 in Fig. 8.4-a), and 0.20 eV (transition 2) are also identified along Z-Γ and Γ-Y lines, respectively.

For double-layer and bulk models, the same trend is observed, and two direct gaps along the same high symmetry lines as in the single-layer are observed. For the double-layer, the two points closest in energy to the CBM and VBM, are higher and lower in energy by 0.23 eV (transition 1 in Fig. 8.4-b) and 0.27 eV (transition 2 in Fig. 8.4-b), respectively. For the bulk, the direct gaps differs in energy by 0.11 eV and 0.45 eV, as seen for transitions 1 and 2 in Fig. 8.4-c, respectively.

SnSe: For single-layer SnSe, the CB has two degenerate minima along the Z-Γ and Γ-Y lines, and a direct gap of 1.12 eV is calculated with the VBM along Z-Γ. A second maxima at 0.12 eV below the VBM is obtained in the Γ-Y direction, for which an additional direct transition is obtained.

By adding one more layer to form the double-layer model, some modifications are observed. The CBM is now in the Γ-Y direction, and the material is characterized by an indirect gap of 0.79 eV, with the VBM still located on the Z-Γ direction. These CBM and VBM also define direct transitions higher in energy if compared to the indirect one, by 0.18 eV and 0.25 eV, respectively. For the bulk model, a well defined CBM is observed in the Γ-Y direction, and an indirect gap of 0.55 eV is defined with the VBM in the Z-Γ direction. In this case, the second point nearest in energy to the VBM, lower in energy by 0.17 eV, is located along the Γ-Y direction, and defines a direct gap of 0.72 eV. In the same way, a k-point along Z-Γ is very close in energy to the CBM and defines a direct gap of 0.85 eV.

	Single-layer		Double-layer		Bulk	
Transition	1	2	1	2	1	2
SnS	1.47	1.60	1.36	1.40	0.93	1.27
SnSe	1.12	1.55	0.98	1.05	0.85	0.72
GeS	1.91	1.98	1.63	-	-	-
GeSe	1.68	-	-	-	0.85	0.93

Table 8.4: Direct transitions energies observed from band structure calculations for all compounds, indicated by blue arrows in Figs. 8.4, 8.5, 8.6 and 8.7. These transitions are higher in energy by a few eV than the energy gaps.

GeS: Electronic structure calculations indicate that an indirect gap of 1.67 eV is obtained for the single-layer model, which is defined by the CMB and VBM along the Γ-Y and Z-Γ lines, respectively. There are indications of occurrence of direct transitions

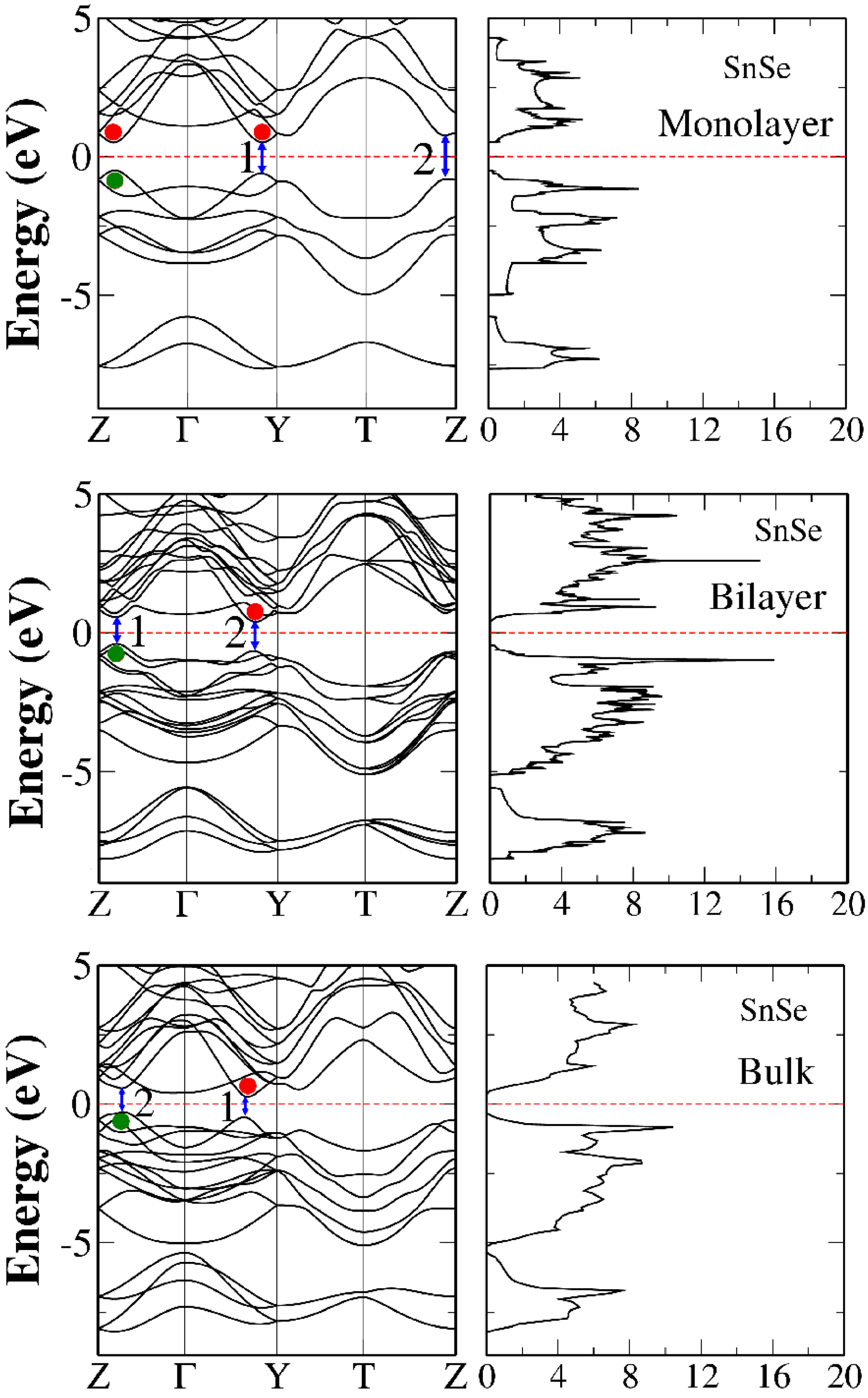

FIGURE 8.5: Electronic band structures for single-layer, double-layer and bulk for α phase of SnSe. A direct gap is predicted for single-layer, while indirect gaps are calculated for double-layer and bulk. The red and green points mark positions of CBM and VBM respectively.

at the Γ point, and near the Z point, along the Z-Γ line, as represented by transitions 1 and 2 in Fig. 8.6-a.

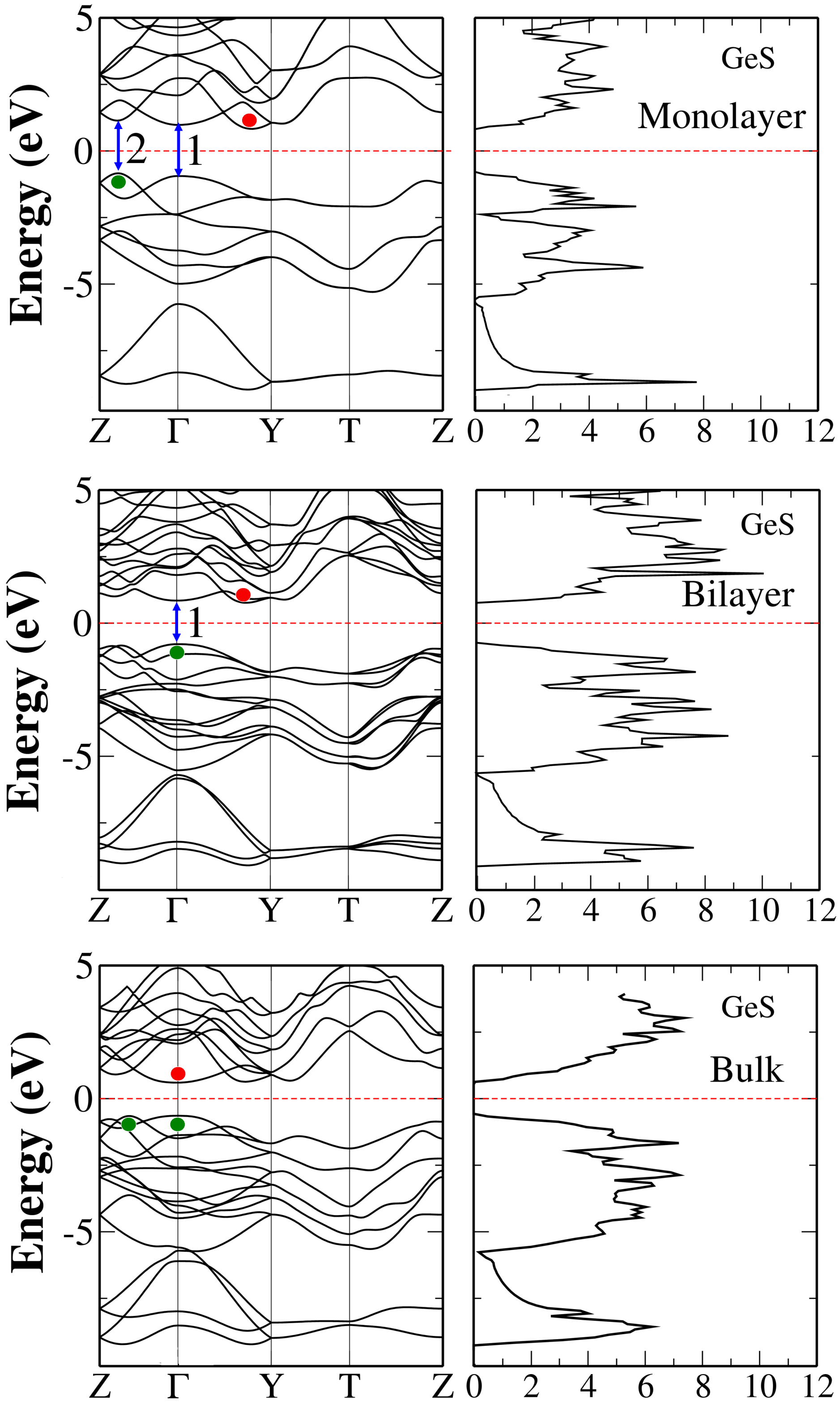

FIGURE 8.6: Electronic band structures for single-layer, double-layer and bulk for α phase of GeS. Indirect gaps are predicted for single-layer and double-layer, while a direct gap is calculated for the bulk. The red and green points mark positions of CBM and VBM respectively.

In double-layer GeS, the gap is indirect and lower in energy by 0.12 eV than that of single-layer. The CBM is calculated to remain along Γ-Y, while the VBM is observed at the Γ point. A second minimum of the CB is calculated at the Γ point, higher in energy by 0.08 eV, with a direct gap of 1.63 eV.

For the bulk, two degenerate k-points define the VBM, the first one near to Z point, along the Z-Γ line, and the second one at the Γ point, defining a direct gap of 1.24 eV.

GeSe: For the single-layer of GeSe, our calculations produce a direct gap E_g=1.14 eV along the Z-Γ line. A second direct gap is also indicated to occur near the Y point, as represented by transition 1 in Fig.8.7-a. This latter gap is higher in energy by 0.54 eV. For the double-layer structure, a direct gap of 1.07 eV is calculated in the Z-Γ direction, near the Z point.

Similar to the single- and double-layer models for GeSe, the electronic structure for the bulk also shows the VBM in the Z-Γ direction. The calculated indirect energy gap is 0.6 eV, and the CMB is also in the Z-Γ direction, but closer to the Γ point. Two possible direct gaps one on the Z-Γ line and another at the Γ point are also suggested by our first calculations. These are higher in energy by ∼0.33 and 0.25 eV than the indirect gap, respectively.

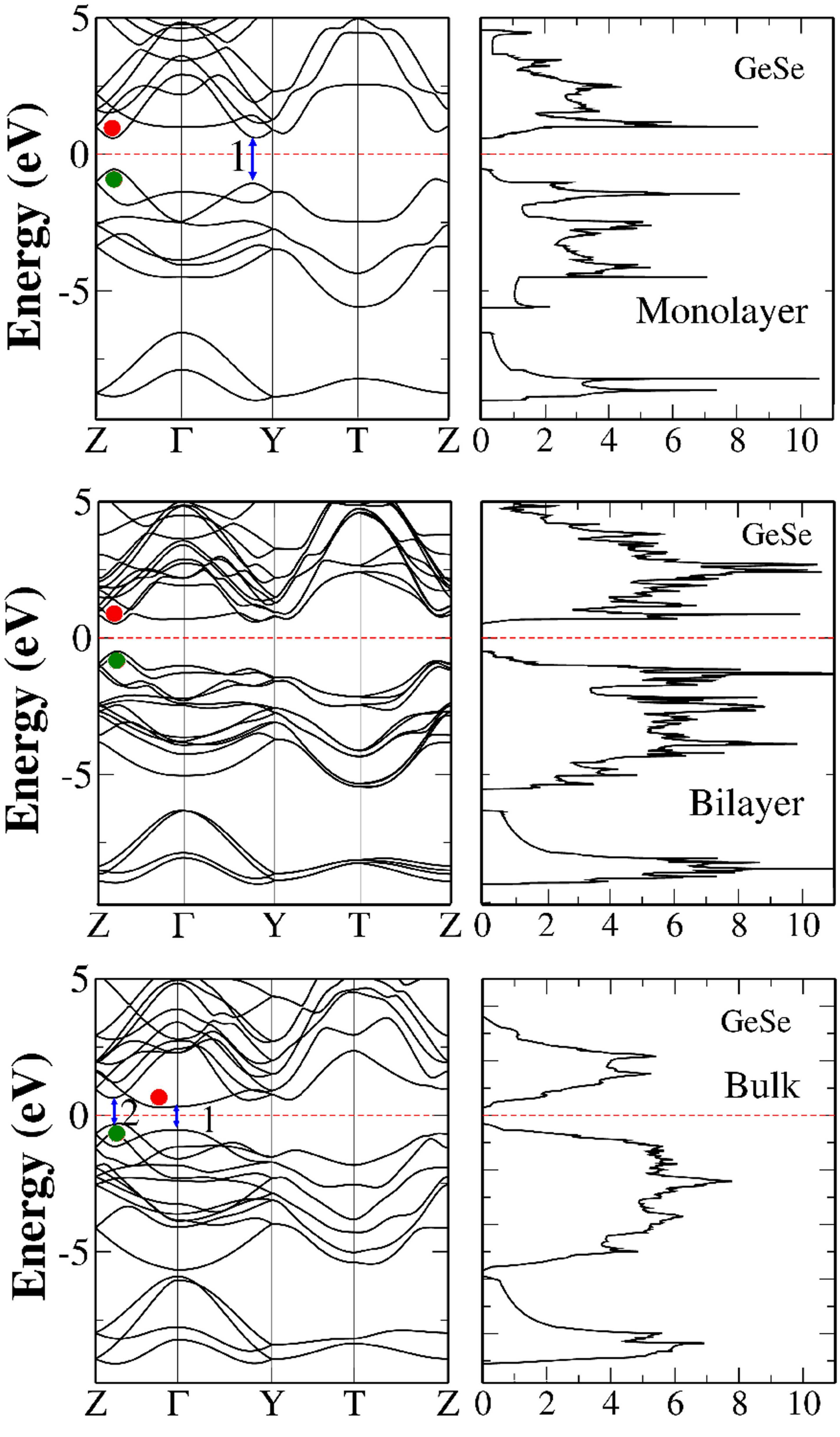

FIGURE 8.7: Electronic band structures for single-layer, double-layer and bulk for α phase of GeSe. A direct gap is observed for single-layer and double-layer systems, while an indirect gap is calculated for the bulk. The red and green points mark positions of CBM and VBM respectively.

8.3 Conclusion and Final Comments

The preliminary results presented in this chapter discuss the electronic properties of the α phase of single and double layers and also the bulk of metal monochalcogenides forming the group of compounds: SnS, SnSe, GeS, GeSe.

A clear dependence of the gap energy E_g on the number of layers of these semiconductors is observed, where E_g decreases as we increase the number of layers. By comparing our calculated results with those of the more accurate GW approach for the SnS compound investigated in a previous theoretical work, we see that despite the underestimated gaps calculated by our DFT-GGA approximation, the shape of the electronic bands are preserved, as well the positions of the VBM and CBM. This can give us a first qualitative insight on the electronic and optical properties of these materials.

In the next steps of this work we will investigate the optical properties of the systems by calculation of important properties such as the dielectric function $\epsilon(\omega)$ and conductivity $\sigma(\omega)$, that describe most of the macroscopic optical properties of solids. Structural properties will also be studied in more details, where Van der Waals forces will be considered in our calculations.

Bibliography

[1] K. S. Novoselov, A. K. Geim, S. V. Morozov, D. Jiang, Y. Zhang, S. V. Dubonos, I. V. Grigorieva, and A. A. Firsov. Electric field effect in atomically thin carbon films. *Science*, 306(5696):666–669, 2004. doi: 10.1126/science.1102896. URL `http://www.sciencemag.org/content/306/5696/666.abstract`.

[2] Sheneve Z. Butler, Shawna M. Hollen, Linyou Cao, Yi Cui, Jay A. Gupta, Humberto R. Gutiérrez, Tony F. Heinz, Seung Sae Hong, Jiaxing Huang, Ariel F. Ismach, Ezekiel Johnston-Halperin, Masaru Kuno, Vladimir V. Plashnitsa, Richard D. Robinson, Rodney S. Ruoff, Sayeef Salahuddin, Jie Shan, Li Shi, Michael G. Spencer, Mauricio Terrones, Wolfgang Windl, and Joshua E. Goldberger. Progress, challenges, and opportunities in two-dimensional materials beyond graphene. *ACS Nano*, 7(4):2898–2926, 2013. doi: 10.1021/nn400280c. URL `http://dx.doi.org/10.1021/nn400280c`. PMID: 23464873.

[3] Lifeng Wang, Bin Wu, Jisi Chen, Hongtao Liu, Pingan Hu, and Yunqi Liu. Monolayer hexagonal boron nitride films with large domain size and clean interface for enhancing the mobility of graphene-based field-effect transistors. *Advanced Materials*, 26(10):1559–1564, 2014. ISSN 1521-4095. doi: 10.1002/adma.201304937. URL `http://dx.doi.org/10.1002/adma.201304937`.

[4] Qing Hua Wang, Kourosh Kalantar-Zadeh, Andras Kis, and Michael S. Coleman, Jonathan N. Strano. Electronics and optoelectronics of two-dimensional transition metal dichalcogenides. *Nat Nano*, 7(11):699–712, 2012. doi: 10.1038/nnano.2012.193. URL `http://dx.doi.org/10.1038/nnano.2012.193`.

[5] et. al Hernandez, Yenny. High-yield production of graphene by liquid-phase exfoliation of graphite. *Nat Nano*, 3(9):563–568, 2008. doi: 10.1038/nnano.2008.215. URL `http://dx.doi.org/10.1038/nnano.2008.215`.

[6] Li Song, Lijie Ci, Hao Lu, Pavel B. Sorokin, Chuanhong Jin, Jie Ni, Alexander G. Kvashnin, Dmitry G. Kvashnin, Jun Lou, Boris I. Yakobson, and Pulickel M.

Ajayan. Large scale growth and characterization of atomic hexagonal boron nitride layers. *Nano Letters*, 10(8):3209–3215, 2010. doi: 10.1021/nl1022139. URL `http://dx.doi.org/10.1021/nl1022139`. PMID: 20698639.

[7] A. H. Castro Neto, F. Guinea, N. M. R. Peres, K. S. Novoselov, and A. K. Geim. The electronic properties of graphene. *Rev. Mod. Phys.*, 81:109–162, Jan 2009. doi: 10.1103/RevModPhys.81.109. URL `http://link.aps.org/doi/10.1103/RevModPhys.81.109`.

[8] P. R. Wallace. The band theory of graphite. *Phys. Rev.*, 71:622–634, May 1947. doi: 10.1103/PhysRev.71.622. URL `http://link.aps.org/doi/10.1103/PhysRev.71.622`.

[9] R. M. Ribeiro and N. M. R. Peres. Stability of boron nitride bilayers: Ground-state energies, interlayer distances, and tight-binding description. *Phys. Rev. B*, 83:235312, Jun 2011. doi: 10.1103/PhysRevB.83.235312. URL `http://link.aps.org/doi/10.1103/PhysRevB.83.235312`.

[10] Kenji Watanabe, Takashi Taniguchi, and Hisao Kanda. Direct-bandgap properties and evidence for ultraviolet lasing of hexagonal boron nitride single crystal. *Nat Mater*, 3(6):404–409, Jun 2004. ISSN 1476-1122. doi: 10.1038/nmat1134. URL `http://dx.doi.org/10.1038/nmat1134`.

[11] Klaus Capelle. A bird's-eye view of density-functional theory. *Brazilian Journal of Physics*, 36:1318–1343, 12 2006. ISSN 0103-9733. URL `http://www.scielo.br/scielo.php?script=sci_arttext&pid=S0103-97332006000700035&n`

[12] P. Hohenberg and W. Kohn. Inhomogeneous electron gas. *Phys. Rev.*, 136:B864–B871, Nov 1964. doi: 10.1103/PhysRev.136.B864. URL `http://link.aps.org/doi/10.1103/PhysRev.136.B864`.

[13] W. Kohn and L. J. Sham. Self-consistent equations including exchange and correlation effects. *Phys. Rev.*, 140:A1133–A1138, Nov 1965. doi: 10.1103/PhysRev.140.A1133. URL `http://link.aps.org/doi/10.1103/PhysRev.140.A1133`.

[14] R. M. Dreizler and E. K. U. Gross. *Density Functional Theory*. Springer, Berlin, 1990.

[15] Robert G. Parr and Weitao Yang. *Density-Functional Theory of Atoms and Molecules (International Series of Monographs on Chemistry)*. Oxford University Press, USA, 1994. ISBN 0195092767.

[16] D. M. Ceperley and B. J. Alder. Ground state of the electron gas by a stochastic method. *Phys. Rev. Lett.*, 45:566–569, Aug 1980. doi: 10.1103/PhysRevLett.45.566. URL `http://link.aps.org/doi/10.1103/PhysRevLett.45.566`.

[17] John P. Perdew and Wang Yue. Accurate and simple density functional for the electronic exchange energy: Generalized gradient approximation. *Phys. Rev. B*, 33:8800–8802, Jun 1986. doi: 10.1103/PhysRevB.33.8800. URL `http://link.aps.org/doi/10.1103/PhysRevB.33.8800`.

[18] John P. Perdew, Kieron Burke, and Matthias Ernzerhof. Generalized gradient approximation made simple. *Phys. Rev. Lett.*, 77: 3865–3868, Oct 1996. doi: 10.1103/PhysRevLett.77.3865. URL `http://link.aps.org/doi/10.1103/PhysRevLett.77.3865`.

[19] A. D. Becke. Density-functional exchange-energy approximation with correct asymptotic behavior. *Phys. Rev. A*, 38: 3098–3100, Sep 1988. doi: 10.1103/PhysRevA.38.3098. URL `http://link.aps.org/doi/10.1103/PhysRevA.38.3098`.

[20] Chengteh Lee, Weitao Yang, and Robert G. Parr. Development of the colle-salvetti correlation-energy formula into a functional of the electron density. *Phys. Rev. B*, 37:785–789, Jan 1988. doi: 10.1103/PhysRevB.37.785. URL `http://link.aps.org/doi/10.1103/PhysRevB.37.785`.

[21] L. J. Sham and M. Schlüter. Density-functional theory of the energy gap. *Phys. Rev. Lett.*, 51:1888–1891, Nov 1983. doi: 10.1103/PhysRevLett.51.1888. URL `http://link.aps.org/doi/10.1103/PhysRevLett.51.1888`.

[22] Gale J. D. Garcia A. Junqueira J. Ordejon P. Sanchez-Portal D Soler J. M., Artacho E. The siesta method for ab initio order-n materials simulation. *J. Phys. Cond. Matt.*, 14:2745–2779, 2002. doi: 10.1088/0953-8984/14/11/302. URL `http://iopscience.iop.org/0953-8984/14/11/302`.

[23] et. al Giannozzi P. Quantum espresso: a modular and open-source software project for quantum simulations of materials. *J. Phys. Cond. Matt.*, 21:395502, 2009. doi: 10.1088/0953-8984/21/39/395502. URL `http://iopscience.iop.org/0953-8984/21/39/395502`.

[24] N. Troullier and José Luriaas Martins. Efficient pseudopotentials for plane-wave calculations. *Phys. Rev. B*, 43:1993–2006, Jan 1991. doi: 10.1103/PhysRevB.43.1993. URL `http://link.aps.org/doi/10.1103/PhysRevB.43.1993`.

[25] A. Zunger J. Ihm and M. L. Cohen. Momentum-space formalism for the total energy of solids. *J. Phys. C: Solid State Phys*, 12:4409, 1979. doi: 10.1088/0022-3719/12/21/009. URL `http://iopscience.iop.org/0022-3719/12/21/009`.

[26] M. L. Cohen. Pseudopotentials and total energy calculations. *Phys Scr*, 5, 1982. doi: 10.1088/0031-8949/1982/T1/001. URL `http://iopscience.iop.org/1402-4896/1982/T1/001`.

[27] Brad D. Malone and Efthimios Kaxiras. Quasiparticle band structures and interface physics of sns and ges. *Phys. Rev. B*, 87: 245312, Jun 2013. doi: 10.1103/PhysRevB.87.245312. URL `http://link.aps.org/doi/10.1103/PhysRevB.87.245312`.

[28] Florian Banhart, Jani Kotakoski, and Arkady V. Krasheninnikov. Structural defects in graphene. *ACS Nano*, 5(1):26–41, 2011. doi: 10.1021/nn102598m. URL `http://dx.doi.org/10.1021/nn102598m`. PMID: 21090760.

[29] Mousumi Upadhyay Kahaly, Satinder P. Singh, and Umesh V. Waghmare. Carbon nanotubes with an extended line defect. *Small*, 4(12): 2209–2213, 2008. ISSN 1613-6829. doi: 10.1002/smll.200701039. URL `http://dx.doi.org/10.1002/smll.200701039`.

[30] Bozkurt P. Oleynik I. I. Lahiri J., Lin Y. and Batzill M. An extended defect in graphene as a metallic wire. *Nat Nano*, 5(5):326–329, 2010. doi: 10.1038/nnano.2010.53. URL `http://dx.doi.org/10.1038/nnano.2010.53`.

[31] Simone S. Alexandre, A. D. Lúcio, A. H. Castro Neto, and R. W. Nunes. Correlated magnetic states in extended one-dimensional defects in graphene. *Nano Letters*, 12(10):5097–5102, 2012. doi: 10.1021/nl3017434. URL `http://dx.doi.org/10.1021/nl3017434`. PMID: 22950362.

[32] Xiuling Li, Xiaojun Wu, Xiao Cheng Zeng, and Jinlong Yang. Band-gap engineering via tailored line defects in boron-nitride nanoribbons, sheets, and nanotubes. *ACS Nano*, 6(5):4104–4112, 2012. doi: 10.1021/nn300495t. URL `http://dx.doi.org/10.1021/nn300495t`. PMID: 22482995.

[33] Eduardo Machado-Charry, Paul Boulanger, Luigi Genovese, Normand Mousseau, and Pascal Pochet. Tunable magnetic states in hexagonal boron nitride sheets. *Applied Physics Letters*, 101(13): 132405, 2012. doi: http://dx.doi.org/10.1063/1.4754143. URL `http://scitation.aip.org/content/aip/journal/apl/101/13/10.1063/1.4754143`.

[34] W. Auwärter, M. Muntwiler, J. Osterwalder, and T. Greber. Defect lines and two-domain structure of hexagonal boron nitride films on ni(111). *Surface Science*, 545(1–2):L735–L740, 2003. ISSN 0039-6028. doi: http://dx.doi.org/10.1016/j.susc.2003.08.046. URL `http://www.sciencedirect.com/science/article/pii/S0039602803010902`.

[35] Alexandre S. S.; Gomes L. C.; Chacham H.; Nunes R. W. Stoichiometric antiphase boundaries in monolayer boron-nitride. *Bulletin of the American Physical Society*, 2012. URL `http://meetings.aps.org/link/BAPS.2012.MAR.B7.14`.

[36] J. Kotakoski, A. V. Krasheninnikov, U. Kaiser, and J. C. Meyer. From point defects in graphene to two-dimensional amorphous carbon. *Phys. Rev. Lett.*, 106:105505, Mar 2011. doi: 10.1103/PhysRevLett.106.105505. URL `http://link.aps.org/doi/10.1103/PhysRevLett.106.105505`.

[37] Ovidiu Cretu, Yung-Chang Lin, and Kazutomo Suenaga. Evidence for active atomic defects in monolayer hexagonal boron nitride: A new mechanism of plasticity in two-dimensional materials. *Nano Letters*, 14(2):1064–1068, 2014. doi: 10.1021/nl404735w. URL `http://dx.doi.org/10.1021/nl404735w`. PMID: 24467438.

[38]

[39] Richard M. Martin. Interatomic forces and ionicity in covalent crystals. *Solid State Communications*, 8(10):799–802, 1970. ISSN 0038-1098. doi: http://dx.doi.org/10.1016/0038-1098(70)90435-7. URL `http://www.sciencedirect.com/science/article/pii/0038109870904357`.

[40] Ki Kang Kim, Allen Hsu, Xiaoting Jia, Soo Min Kim, Yumeng Shi, Mario Hofmann, Daniel Nezich, Joaquin F. Rodriguez-Nieva, Mildred Dresselhaus, Tomas Palacios, and Jing Kong. Synthesis of monolayer hexagonal boron nitride on cu foil using chemical vapor deposition. *Nano Letters*, 12(1):161–166, 2012. doi: 10.1021/nl203249a. URL `http://dx.doi.org/10.1021/nl203249a`. PMID: 22111957.

[41] et. al Ci L. Atomic layers of hybridized boron nitride and graphene domains. *Nat Mater*, 9(5):430–435, 2010. doi: 10.1038/nmat2711. URL `http://dx.doi.org/10.1038/nmat2711`.

[42] Zheng Liu, Li Song, Shizhen Zhao, Jiaqi Huang, Lulu Ma, Jiangnan Zhang, Jun Lou, and Pulickel M. Ajayan. Direct growth of graphene/hexagonal boron nitride stacked layers. *Nano Letters*, 11(5):2032–2037, 2011. doi: 10.1021/nl200464j. URL `http://dx.doi.org/10.1021/nl200464j`. PMID: 21488689.

[43] Walter Orellana and H. Chacham. Stability of native defects in hexagonal and cubic boron nitride. *Phys. Rev. B*, 63:125205, Mar 2001. doi: 10.1103/PhysRevB.63.125205. URL `http://link.aps.org/doi/10.1103/PhysRevB.63.125205`.

[44] Mário S. C. Mazzoni, R. W. Nunes, Sérgio Azevedo, and H. Chacham. Electronic structure and energetics of $\mathrm{b}_x\mathrm{c}_y\mathrm{n}_z$ layered structures. *Phys.*

Rev. B, 73:073108, Feb 2006. doi: 10.1103/PhysRevB.73.073108. URL `http://link.aps.org/doi/10.1103/PhysRevB.73.073108`.

[45] Simone S. Alexandre, Hélio Chacham, and R. W. Nunes. Structure and energetics of boron nitride fullerenes: The role of stoichiometry. *Phys. Rev. B*, 63:045402, Jan 2001. doi: 10.1103/PhysRevB.63.045402. URL `http://link.aps.org/doi/10.1103/PhysRevB.63.045402`.

[46] Simone S. Alexandre, R. W. Nunes, and H. Chacham. Energetics of the formation of dimers and solids of boron nitride fullerenes. *Phys. Rev. B*, 66:085406, Aug 2002. doi: 10.1103/PhysRevB.66.085406. URL `http://link.aps.org/doi/10.1103/PhysRevB.66.085406`.

[47] Sérgio Azevedo, Mário S. C. Mazzoni, R. W. Nunes, and H. Chacham. Stability of antiphase line defects in nanometer-sized boron nitride cones. *Phys. Rev. B*, 70:205412, Nov 2004. doi: 10.1103/PhysRevB.70.205412. URL `http://link.aps.org/doi/10.1103/PhysRevB.70.205412`.

[48] Yuanyue Liu, Somnath Bhowmick, and Boris I. Yakobson. Bn white graphene with colorful edges: The energies and morphology. *Nano Letters*, 11(8):3113–3116, 2011. doi: 10.1021/nl2011142. URL `http://dx.doi.org/10.1021/nl2011142`. PMID: 21732643.

[49] Chuanhong Jin, Fang Lin, Kazu Suenaga, and Sumio Iijima. Fabrication of a freestanding boron nitride single layer and its defect assignments. *Phys. Rev. Lett.*, 102:195505, May 2009. doi: 10.1103/PhysRevLett.102.195505. URL `http://link.aps.org/doi/10.1103/PhysRevLett.102.195505`.

[50] Jannik C. Meyer, Andrey Chuvilin, Gerardo Algara-Siller, Johannes Biskupek, and Ute Kaiser. Selective sputtering and atomic resolution imaging of atomically thin boron nitride membranes. *Nano Letters*, 9(7):2683–2689, 2009. doi: 10.1021/nl9011497. URL `http://dx.doi.org/10.1021/nl9011497`. PMID: 19480400.

[51] Kwiseon Kim, Walter R. L. Lambrecht, and Benjamin Segall. Elastic constants and related properties of tetrahedrally bonded bn, aln, gan, and inn. *Phys. Rev. B*, 53:16310–16326, Jun 1996. doi: 10.1103/PhysRevB.53.16310. URL `http://link.aps.org/doi/10.1103/PhysRevB.53.16310`.

[52] Edward McCann. Asymmetry gap in the electronic band structure of bilayer graphene. *Phys. Rev. B*, 74:161403, Oct 2006. doi: 10.1103/PhysRevB.74.161403. URL `http://link.aps.org/doi/10.1103/PhysRevB.74.161403`.

[53] Eduardo V. Castro, K. S. Novoselov, S. V. Morozov, N. M. R. Peres, J. M. B. Lopes dos Santos, Johan Nilsson, F. Guinea, A. K. Geim, and A. H. Castro Neto. Biased

bilayer graphene: Semiconductor with a gap tunable by the electric field effect. *Phys. Rev. Lett.*, 99:216802, Nov 2007. doi: 10.1103/PhysRevLett.99.216802. URL `http://link.aps.org/doi/10.1103/PhysRevLett.99.216802`.

[54] J. M. B. Lopes dos Santos, N. M. R. Peres, and A. H. Castro Neto. Graphene bilayer with a twist: Electronic structure. *Phys. Rev. Lett.*, 99:256802, Dec 2007. doi: 10.1103/PhysRevLett.99.256802. URL `http://link.aps.org/doi/10.1103/PhysRevLett.99.256802`.

[55] J. M. B. Lopes dos Santos, N. M. R. Peres, and A. H. Castro Neto. Continuum model of the twisted graphene bilayer. *Phys. Rev. B*, 86:155449, Oct 2012. doi: 10.1103/PhysRevB.86.155449. URL `http://link.aps.org/doi/10.1103/PhysRevB.86.155449`.

[56] Pong W. T. and Durkan C. A review and outlook for an anomaly of scanning tunnelling microscopy (stm): superlattices on graphite. *J. Phys. D*, 38:R329–R355, Oct 2005. doi: 10.1088/0022-3727/38/21/R01. URL `http://iopscience.iop.org/0022-3727/38/21/R01`.

[57] Zhao Y. Rong and Pieter Kuiper. Electronic effects in scanning tunneling microscopy: Moiré pattern on a graphite surface. *Phys. Rev. B*, 48:17427–17431, Dec 1993. doi: 10.1103/PhysRevB.48.17427. URL `http://link.aps.org/doi/10.1103/PhysRevB.48.17427`.

[58] Matos M. J. S. Coelho P. M. Paniago R. M. Mendes-de Sa T. G., Goncalves A. M. B. and Lacerda R. G. Correlation between (in)commensurate domains of multilayer epitaxial graphene grown on sic(0001) and single layer electronic behavior. *Nanotech*, 23:1–9, Oct 2012. doi: 10.1088/0957-4484/23/47/475602. URL `http://iopscience.iop.org/0957-4484/23/47/475602`.

[59] E. Cisternas and J. D. Correa. Ab-initio analysis of superstructures revealed by stm on bilayer graphene. *ArXiv e-prints*, 2012. doi: 10.1016/j.chemphys.2012.09.021. URL `http://arxiv.org/abs/1202.2612`.

[60] J. M. Campanera, G. Savini, I. Suarez-Martinez, and M. I. Heggie. Density functional calculations on the intricacies of moiré patterns on graphite. *Phys. Rev. B*, 75:235449, Jun 2007. doi: 10.1103/PhysRevB.75.235449. URL `http://link.aps.org/doi/10.1103/PhysRevB.75.235449`.

[61] Guohong Li, A. Luican, J. M. B. Lopes dos Santos, A. H. Castro Neto, A. Reina, J. Kong, and E. Y. Andrei. Observation of van hove singularities in twisted graphene layers. *Nat Phys*, 6(2):109–113, Feb 2010. ISSN 1745-2473. doi: 10.1038/nphys1463. URL `http://dx.doi.org/10.1038/nphys1463`.

[62] P Simonis, C Goffaux, P.A Thiry, L.P Biro, Ph Lambin, and V Meunier. {STM} study of a grain boundary in graphite. *Surface Science*, 511(1–3):319–322, 2002. ISSN 0039-6028. doi: http://dx.doi.org/10.1016/S0039-6028(02)01511-X. URL `http://www.sciencedirect.com/science/article/pii/S003960280201511X`.

[63] Joice da Silva Araújo and R. W. Nunes. Complex evolution of the electronic structure from polycrystalline to monocrystalline graphene: Generation of a new dirac point. *Phys. Rev. B*, 81:073408, Feb 2010. doi: 10.1103/PhysRevB.81.073408. URL `http://link.aps.org/doi/10.1103/PhysRevB.81.073408`.

[64] Aurélien Lherbier, Simon M.-M. Dubois, Xavier Declerck, Yann-Michel Niquet, Stephan Roche, and Jean-Christophe Charlier. Transport properties of graphene containing structural defects. *Phys. Rev. B*, 86:075402, Aug 2012. doi: 10.1103/PhysRevB.86.075402. URL `http://link.aps.org/doi/10.1103/PhysRevB.86.075402`.

[65] Jiong Lu, Yang Bao, Chen Liang Su, and Kian Ping Loh. Properties of strained structures and topological defects in graphene. *ACS Nano*, 7(10):8350–8357, 2013. doi: 10.1021/nn4051248. URL `http://dx.doi.org/10.1021/nn4051248`.

[66] Feng Hao, Daining Fang, and Zhiping Xu. Mechanical and thermal transport properties of graphene with defects. *Applied Physics Letters*, 99(4):041901, 2011. doi: http://dx.doi.org/10.1063/1.3615290. URL `http://scitation.aip.org/content/aip/journal/apl/99/4/10.1063/1.3615290`.

[67] Oleg V. Yazyev and Steven G. Louie. Topological defects in graphene: Dislocations and grain boundaries. *Phys. Rev. B*, 81: 195420, May 2010. doi: 10.1103/PhysRevB.81.195420. URL `http://link.aps.org/doi/10.1103/PhysRevB.81.195420`.

[68] J. N. B. Rodrigues, N. M. R. Peres, and J. M. B. Lopes dos Santos. Scattering by linear defects in graphene: A continuum approach. *Phys. Rev. B*, 86:214206, Dec 2012. doi: 10.1103/PhysRevB.86.214206. URL `http://link.aps.org/doi/10.1103/PhysRevB.86.214206`.

[69] Giulio Cocco, Emiliano Cadelano, and Luciano Colombo. Gap opening in graphene by shear strain. *Phys. Rev. B*, 81:241412, Jun 2010. doi: 10.1103/PhysRevB.81.241412. URL `http://link.aps.org/doi/10.1103/PhysRevB.81.241412`.

[70] F. Guinea, M. I. Katsnelson, and A. K. Geim. Energy gaps and a zero-field quantum hall effect in graphene by strain engineering. *Nat Phys*, 6 (1):30–33, Jan 2010. ISSN 1745-2473. doi: 10.1038/nphys1420. URL `http://dx.doi.org/10.1038/nphys1420`.

[71] P. San-Jose, R. V. Gorbachev, A. K. Geim, K. S. Novoselov, and F. Guinea. Stacking boundaries and transport in bilayer graphene. *Nano Letters*, 14(4):2052–2057, 2014. doi: 10.1021/nl500230a. URL `http://dx.doi.org/10.1021/nl500230a`. PMID: 24605877.

[72] Mikito Koshino. Electronic transmission through *ab*-*ba* domain boundary in bilayer graphene. *Phys. Rev. B*, 88:115409, Sep 2013. doi: 10.1103/PhysRevB.88.115409. URL `http://link.aps.org/doi/10.1103/PhysRevB.88.115409`.

[73] Jonathan S. Alden, Adam W. Tsen, Pinshane Y. Huang, Robert Hovden, Lola Brown, Jiwoong Park, David A. Muller, and Paul L. McEuen. Strain solitons and topological defects in bilayer graphene. *Proceedings of the National Academy of Sciences*, 110(28):11256–11260, 2013. doi: 10.1073/pnas.1309394110. URL `http://www.pnas.org/content/110/28/11256.abstract`.

[74] Wenzhong Bao, Jairo Velasco, Fan Zhang, Lei Jing, Brian Standley, Dmitry Smirnov, Marc Bockrath, Allan H. MacDonald, and Chun Ning Lau. Evidence for a spontaneous gapped state in ultraclean bilayer graphene. *Proceedings of the National Academy of Sciences*, 109(27):10802–10805, 2012. doi: 10.1073/pnas.1205978109. URL `http://www.pnas.org/content/109/27/10802.abstract`.

[75] Velasco J. et. al. Transport spectroscopy of symmetry-broken insulating states in bilayer graphene. *Nat Nano*, 7(3):156–160, Mar 2012. ISSN 1748-3387. doi: 10.1038/nnano.2011.251. URL `http://dx.doi.org/10.1038/nnano.2011.251`.

[76] F. Freitag, J. Trbovic, M. Weiss, and C. Schönenberger. Spontaneously gapped ground state in suspended bilayer graphene. *Phys. Rev. Lett.*, 108:076602, Feb 2012. doi: 10.1103/PhysRevLett.108.076602. URL `http://link.aps.org/doi/10.1103/PhysRevLett.108.076602`.

[77] Frank Freitag, Markus Weiss, Romain Maurand, Jelena Trbovic, and Christian Schönenberger. Homogeneity of bilayer graphene. *Solid State Communications*, 152(22):2053–2057, 2012. ISSN 0038-1098. doi: http://dx.doi.org/10.1016/j.ssc.2012.09.001. URL `http://www.sciencedirect.com/science/article/pii/S0038109812005066`.

[78] Frank Freitag, Markus Weiss, Romain Maurand, Jelena Trbovic, and Christian Schönenberger. Spin symmetry of the bilayer graphene ground state. *Phys. Rev. B*, 87:161402, Apr 2013. doi: 10.1103/PhysRevB.87.161402. URL `http://link.aps.org/doi/10.1103/PhysRevB.87.161402`.

[79] Junhao Lin, Wenjing Fang, Wu Zhou, Andrew R. Lupini, Juan Carlos Idrobo, Jing Kong, Stephen J. Pennycook, and Sokrates T. Pantelides. Ac/ab stacking boundaries in bilayer graphene. *Nano Letters*, 13(7):3262–3268, 2013. doi: 10.1021/nl4013979. URL `http://dx.doi.org/10.1021/nl4013979`. PMID: 23772750.

[80] P. Plochocka, C. Faugeras, M. Orlita, M. L. Sadowski, G. Martinez, M. Potemski, M. O. Goerbig, J.-N. Fuchs, C. Berger, and W. A. de Heer. High-energy limit of massless dirac fermions in multilayer graphene using magneto-optical transmission spectroscopy. *Phys. Rev. Lett.*, 100:087401, Feb 2008. doi: 10.1103/PhysRevLett.100.087401. URL `http://link.aps.org/doi/10.1103/PhysRevLett.100.087401`.

[81] Marco Bernardi, Maurizia Palummo, and Jeffrey C. Grossman. Optoelectronic properties in monolayers of hybridized graphene and hexagonal boron nitride. *Phys. Rev. Lett.*, 108:226805, Jun 2012. doi: 10.1103/PhysRevLett.108.226805. URL `http://link.aps.org/doi/10.1103/PhysRevLett.108.226805`.

[82] Lei Liu, Jewook Park, David A. Siegel, Kevin F. McCarty, Kendal W. Clark, Wan Deng, Leonardo Basile, Juan Carlos Idrobo, An-Ping Li, and Gong Gu. Heteroepitaxial growth of two-dimensional hexagonal boron nitride templated by graphene edges. *Science*, 343(6167):163–167, 2014. doi: 10.1126/science.1246137. URL `http://www.sciencemag.org/content/343/6167/163.abstract`.

[83] et. al Zheng L. In-plane heterostructures of graphene and hexagonal boron nitride with controlled domain sizes. *Nat Nano*, 8(2):119–124, Feb 2013. ISSN 1748-3387. doi: 10.1038/nnano.2012.256. URL `http://dx.doi.org/10.1038/nnano.2012.256`.

[84] Mark P. Levendorf, Cheol-Joo Kim, Lola Brown, Pinshane Y. Huang, Robin W. Havener, David A. Muller, and Jiwoong Park. Graphene and boron nitride lateral heterostructures for atomically thin circuitry. *Nature*, 488(7413): 627–632, Aug 2012. ISSN 0028-0836. doi: 10.1038/nature11408. URL `http://dx.doi.org/10.1038/nature11408`.

[85] Jiong Lu, Kai Zhang, Xin Feng Liu, Han Zhang, Tze Chien Sum, Antonio H. Castro Neto, and Kian Ping Loh. Order-disorder transition in a two-dimensional boron-carbon-nitride alloy. *Nat Commun*, 4, Oct 2013. URL `http://dx.doi.org/10.1038/ncomms3681`. Article.

[86] Yabo Gao, Yanfeng Zhang, Pengcheng Chen, Yuanchang Li, Mengxi Liu, Teng Gao, Donglin Ma, Yubin Chen, Zhihai Cheng, Xiaohui Qiu, Wenhui Duan, and Zhongfan Liu. Toward single-layer uniform hexagonal boron nitride–graphene

patchworks with zigzag linking edges. *Nano Letters*, 13(7):3439–3443, 2013. doi: 10.1021/nl4021123. URL `http://dx.doi.org/10.1021/nl4021123`. PMID: 23758663.

[87] Ashwin Ramasubramaniam, Doron Naveh, and Elias Towe. Tunable band gaps in bilayer transition-metal dichalcogenides. *Phys. Rev. B*, 84:205325, Nov 2011. doi: 10.1103/PhysRevB.84.205325. URL `http://link.aps.org/doi/10.1103/PhysRevB.84.205325`.

[88] Jin-Wu Jiang, Jian-Sheng Wang, and Bing-Shen Wang. Minimum thermal conductance in graphene and boron nitride superlattice. *Applied Physics Letters*, 99(4):043109, 2011. doi: http://dx.doi.org/10.1063/1.3619832. URL `http://scitation.aip.org/content/aip/journal/apl/99/4/10.1063/1.3619832`.

[89] Alper Kınac ı, Justin B. Haskins, Cem Sevik, and Tahir Çağ ın. Thermal conductivity of bn-c nanostructures. *Phys. Rev. B*, 86: 115410, Sep 2012. doi: 10.1103/PhysRevB.86.115410. URL `http://link.aps.org/doi/10.1103/PhysRevB.86.115410`.

[90] Yungang Zhou, Zhiguo Wang, Ping Yang, and Fei Gao. Novel electronic and magnetic properties of graphene nanoflakes in a boron nitride layer. *The Journal of Physical Chemistry C*, 116(13):7581–7586, 2012. doi: 10.1021/jp300593q. URL `http://dx.doi.org/10.1021/jp300593q`.

[91] Zhizhou Yu, M. L. Hu, C. X. Zhang, C. Y. He, L. Z. Sun, and Jianxin Zhong. Transport properties of hybrid zigzag graphene and boron nitride nanoribbons. *The Journal of Physical Chemistry C*, 115(21):10836–10841, 2011. doi: 10.1021/jp200870t. URL `http://dx.doi.org/10.1021/jp200870t`.

[92] P. Sutter, R. Cortes, J. Lahiri, and E. Sutter. Interface formation in monolayer graphene-boron nitride heterostructures. *Nano Letters*, 12(9):4869–4874, 2012. doi: 10.1021/nl302398m. URL `http://dx.doi.org/10.1021/nl302398m`. PMID: 22871166.

[93] Shijun Zhao and Jianming Xue. Mechanical properties of hybrid graphene and hexagonal boron nitride sheets as revealed by molecular dynamic simulations. *Journal of Physics D: Applied Physics*, 46(13):135303, 2013. URL `http://stacks.iop.org/0022-3727/46/i=13/a=135303`.

[94] Gang Hee Han, Julio A. Rodríguez-Manzo, Chan-Woo Lee, Nicholas J. Kybert, Mitchell B. Lerner, Zhengqing John Qi, Eric N. Dattoli, Andrew M. Rappe, Marija Drndic, and A. T. Charlie Johnson. Continuous growth of hexagonal graphene and boron nitride in-plane heterostructures by atmospheric pressure chemical vapor

deposition. *ACS Nano*, 7(11):10129–10138, 2013. doi: 10.1021/nn404331f. URL `http://dx.doi.org/10.1021/nn404331f`. PMID: 24182310.

[95] E.A. Fitzgerald. Dislocations in strained-layer epitaxy: theory, experiment, and applications. *Materials Science Reports*, 7(3):87–142, 1991. ISSN 0920-2307. doi: http://dx.doi.org/10.1016/0920-2307(91)90006-9. URL `http://www.sciencedirect.com/science/article/pii/0920230791900069`.

[96] R. Hull and J. C. Bean. Nucleation of misfit dislocations in strained-layer epitaxy in the ge$_x$si$_{1-x}$/si system. *Journal of Vacuum Science & Technology A*, 7(4):2580–2585, 1989. doi: http://dx.doi.org/10.1116/1.575800. URL `http://scitation.aip.org/content/avs/journal/jvsta/7/4/10.1116/1.575800`.

[97] S. C. Jain, A. H. Harker, and R. A. Cowley. Misfit strain and misfit dislocations in lattice mismatched epitaxial layers and other systems. *Philosophical Magazine A*, 75(6):1461–1515, 1997. doi: 10.1080/01418619708223740. URL `http://dx.doi.org/10.1080/01418619708223740`.

[98] Ashley L. Gibb, Nasim Alem, Jian-Hao Chen, Kristopher J. Erickson, Jim Ciston, Abhay Gautam, Martin Linck, and Alex Zettl. Atomic resolution imaging of grain boundary defects in monolayer chemical vapor deposition-grown hexagonal boron nitride. *Journal of the American Chemical Society*, 135(18):6758–6761, 2013. doi: 10.1021/ja400637n. URL `http://dx.doi.org/10.1021/ja400637n`. PMID: 23550733.

[99] Yuanyue Liu, Xiaolong Zou, and Boris I. Yakobson. Dislocations and grain boundaries in two-dimensional boron nitride. *ACS Nano*, 6(8):7053–7058, 2012. doi: 10.1021/nn302099q. URL `http://dx.doi.org/10.1021/nn302099q`. PMID: 22780217.

[100] Marco Buongiorno Nardelli, B. I. Yakobson, and J. Bernholc. Brittle and ductile behavior in carbon nanotubes. *Phys. Rev. Lett.*, 81: 4656–4659, Nov 1998. doi: 10.1103/PhysRevLett.81.4656. URL `http://link.aps.org/doi/10.1103/PhysRevLett.81.4656`.

[101] C.P Ewels, M.I Heggie, and P.R Briddon. Adatoms and nanoengineering of carbon. *Chemical Physics Letters*, 351(3–4):178–182, 2002. ISSN 0009-2614. doi: http://dx.doi.org/10.1016/S0009-2614(01)01371-9. URL `http://www.sciencedirect.com/science/article/pii/S0009261401013719`.

[102] F. de Juan A. Carpio, L. L. Bonilla and M. A. H. Vozmediano. Dislocations in graphene. *New Journal of Physics*, 10.

[103] Jie Ma, Dario Alfè, Angelos Michaelides, and Enge Wang. Stone-wales defects in graphene and other planar sp^2-bonded materials. *Phys. Rev. B*, 80:033407, Jul 2009. doi: 10.1103/PhysRevB.80.033407. URL `http://link.aps.org/doi/10.1103/PhysRevB.80.033407`.

[104] L. C. Gomes, S. S. Alexandre, H. Chacham, and R. W. Nunes. Stability of edges and extended defects on boron nitride and graphene monolayers: The role of chemical environment. *The Journal of Physical Chemistry C*, 117(22):11770–11779, 2013. doi: 10.1021/jp400420m. URL `http://dx.doi.org/10.1021/jp400420m`.

[105] Jeil Jung, Zhenhua Qiao, Qian Niu, and Allan H. MacDonald. Transport properties of graphene nanoroads in boron nitride sheets. *Nano Letters*, 12(6):2936–2940, 2012. doi: 10.1021/nl300610w. URL `http://dx.doi.org/10.1021/nl300610w`. PMID: 22524401.

[106] Z. M. Liu, Y. Zhu, and Z. Q. Yang. Half metallicity and electronic structures in armchair bcn-hybrid nanoribbons. *The Journal of Chemical Physics*, 134(7):074708, 2011. doi: http://dx.doi.org/10.1063/1.3553257. URL `http://scitation.aip.org/content/aip/journal/jcp/134/7/10.1063/1.3553257`.

[107] Er-Jun Kan, Xiaojun Wu, Zhenyu Li, X. C. Zeng, Jinlong Yang, and J. G. Hou. Half-metallicity in hybrid bcn nanoribbons. *The Journal of Chemical Physics*, 129(8):084712, 2008. doi: http://dx.doi.org/10.1063/1.2971187. URL `http://scitation.aip.org/content/aip/journal/jcp/129/8/10.1063/1.2971187`.

[108] Kyoko Nakada, Mitsutaka Fujita, Gene Dresselhaus, and Mildred S. Dresselhaus. Edge state in graphene ribbons: Nanometer size effect and edge shape dependence. *Phys. Rev. B*, 54:17954–17961, Dec 1996. doi: 10.1103/PhysRevB.54.17954. URL `http://link.aps.org/doi/10.1103/PhysRevB.54.17954`.

[109] Chenggang Tao, Liying Jiao, Oleg V. Yazyev, Yen-Chia Chen, Juanjuan Feng, Xiaowei Zhang, Rodrigo B. Capaz, James M. Tour, Alex Zettl, Steven G. Louie, Hongjie Dai, and Michael F. Crommie. Spatially resolving edge states of chiral graphene nanoribbons. *Nat Phys*, 7(8):616–620, Aug 2011. ISSN 1745-2473. doi: 10.1038/nphys1991. URL `http://dx.doi.org/10.1038/nphys1991`.

[110] Yuanbo Zhang, Victor W. Brar, Feng Wang, Caglar Girit, Yossi Yayon, Melissa Panlasigui, Alex Zettl, and Michael F. Crommie. Giant phonon-induced conductance in scanning tunnelling spectroscopy of gate-tunable graphene. *Nat Phys*, 4(8):627–630, Aug 2008. ISSN 1745-2473. doi: 10.1038/nphys1022. URL `http://dx.doi.org/10.1038/nphys1022`.

[111] W. Oswald M. Dvorak and Z. Wu. Bandgap opening by patterning graphene, July 2013.

[112] Harihar Behera and Gautam Mukhopadhyay. Strain-tunable band gap in graphene/h-bn hetero-bilayer. *Journal of Physics and Chemistry of Solids*, 73(7):818–821, 2012. ISSN 0022-3697. doi: http://dx.doi.org/10.1016/j.jpcs.2012.02.010. URL `http://www.sciencedirect.com/science/article/pii/S0022369712000753`.

[113] Ovidiu Cretu, Arkady V. Krasheninnikov, Julio A. Rodriguez-Manzo, Litao Sun, Risto M. Nieminen, and Florian Banhart. Migration and localization of metal atoms on strained graphene. *Phys. Rev. Lett.*, 105:196102, Nov 2010. doi: 10.1103/PhysRevLett.105.196102. URL `http://link.aps.org/doi/10.1103/PhysRevLett.105.196102`.

[114] Prashant P. Shinde and Vijay Kumar. Direct band gap opening in graphene by bn doping: Ab initio calculations. *Phys. Rev. B*, 84:125401, Sep 2011. doi: 10.1103/PhysRevB.84.125401. URL `http://link.aps.org/doi/10.1103/PhysRevB.84.125401`.

[115] P. W. Bridgman. Two new modifications of phosphorus. *Journal of the American Chemical Society*, 36(7):1344–1363, 1914. doi: 10.1021/ja02184a002. URL `http://dx.doi.org/10.1021/ja02184a002`.

[116] P. W. Bridgman. The compressibility and pressure coefficient of resistance of ten elements. *Proc. Am. Acad. Arts Sci.*, 62(8):207–226, 1927. doi: 10.2307/25130122. URL `http://www.jstor.org/stable/i25130120`.

[117] P. W. Bridgman. Measurements of certain electrical resistances, compressibilities and thermal expansions to 20000 kg/cm^3. *Proc. Am. Acad. Arts Sci.*, 70(3):71–101, 1935. doi: 10.2307/20023122.

[118] Robert B. Jacobs. Phosphorus at high temperatures and pressures. *The Journal of Chemical Physics*, 5(12), 1937.

[119] Robert W. Keyes. The electrical properties of black phosphorus. *Phys. Rev.*, 92:580–584, Nov 1953. doi: 10.1103/PhysRev.92.580. URL `http://link.aps.org/doi/10.1103/PhysRev.92.580`.

[120] Steven P. Koenig, Rostislav A. Doganov, Hennrik Schmidt, A. H. Castro Neto, and Barbaros Özyilmaz. Electric field effect in ultrathin black phosphorus. *Applied Physics Letters*, 104(10): 103106, 2014. doi: http://dx.doi.org/10.1063/1.4868132. URL `http://scitation.aip.org/content/aip/journal/apl/104/10/10.1063/1.4868132`.

[121] Yukihiro Takao and Akira Morita. Electronic structure of black phosphorus: Tight binding approach. *Physica B+C*, 105(1–3):93–98, 1981. ISSN 0378-4363. doi: http://dx.doi.org/10.1016/0378-4363(81)90222-9. URL `http://www.sciencedirect.com/science/article/pii/0378436381902229`.

[122] Y. Maruyama, S. Suzuki, K. Kobayashi, and S. Tanuma. Synthesis and some properties of black phosphorus single crystals. *Physica B+C*, 105(1–3):99–102, 1981. ISSN 0378-4363. doi: http://dx.doi.org/10.1016/0378-4363(81)90223-0. URL `http://www.sciencedirect.com/science/article/pii/0378436381902230`.

[123] A. S. Rodin, A. Carvalho, and A. H. Castro Neto. Strain-induced gap modification in black phosphorus. *Phys. Rev. Lett.*, 112: 176801, May 2014. doi: 10.1103/PhysRevLett.112.176801. URL `http://link.aps.org/doi/10.1103/PhysRevLett.112.176801`.

[124] Douglas Warschauer. Electrical and optical properties of crystalline black phosphorus. *Journal of Applied Physics*, 34(7), 1963.

[125] Yuichi Akahama, Shoichi Endo, and Shin ichiro Narita. Electrical properties of black phosphorus single crystals. *Journal of the Physical Society of Japan*, 52(6):2148–2155, 1983. doi: 10.1143/JPSJ.52.2148. URL `http://dx.doi.org/10.1143/JPSJ.52.2148`.

[126] Hans Georg von Schnering and Heribert Wiedemeier. The high temperature structure of β-sns and β-snse and the b16-to-b33 type λ-transition path. 156:143, 2014 1981. ISSN 00442968. doi: 10.1524/zkri.1981.156.1-2.143. URL `http://www.degruyter.com/view/j/zkri.1981.156.issue-1-2/zkri.1981.156.1-2.143/zk` 1-2.

[127] A. Morita. Semiconducting black phosphorus. *Applied Physics A*, 39 (4):227–242, 1986. ISSN 0947-8396. doi: 10.1007/BF00617267. URL `http://dx.doi.org/10.1007/BF00617267`.

[128] Martin A. Green, Keith Emery, Yoshihiro Hishikawa, Wilhelm Warta, and Ewan D. Dunlop. Solar cell efficiency tables (version 39). *Progress in Photovoltaics: Research and Applications*, 20(1):12–20, 2012. ISSN 1099-159X. doi: 10.1002/pip.2163. URL `http://dx.doi.org/10.1002/pip.2163`.

[129] Ingrid Repins, Miguel A. Contreras, Brian Egaas, Clay DeHart, John Scharf, Craig L. Perkins, Bobby To, and Rommel Noufi. 199%-efficient zno/cds/cuingase2 solar cell with 812% fill factor. *Progress in Photovoltaics: Research and Applications*, 16(3):235–239, 2008. ISSN 1099-159X. doi: 10.1002/pip.822. URL `http://dx.doi.org/10.1002/pip.822`.

[130] Georgios A. Tritsaris, Brad D. Malone, and Efthimios Kaxiras. Optoelectronic properties of single-layer, double-layer, and bulk tin sulfide: A theoretical study. *Journal of Applied Physics*, 113:233507, 2013.

[131] Julien Vidal, Stephan Lany, Mayeul d'Avezac, Alex Zunger, Andriy Zakutayev, Jason Francis, and Janet Tate. Band-structure, optical properties, and defect physics of the photovoltaic semiconductor sns. *Applied Physics Letters*, 100(3):032104, 2012. doi: http://dx.doi.org/10.1063/1.3675880. URL `http://scitation.aip.org/content/aip/journal/apl/100/3/10.1063/1.3675880`.

[132] A. R. H. F. Ettema, R. A. de Groot, C. Haas, and T. S. Turner. Electronic structure of sns deduced from photoelectron spectra and band-structure calculations. *Phys. Rev. B*, 46:7363–7373, Sep 1992. doi: 10.1103/PhysRevB.46.7363. URL `http://link.aps.org/doi/10.1103/PhysRevB.46.7363`.

[133] Sebahaddin Alptekin and Murat Durandurdu. Formation of a cmcm phase in sns at high pressure; an ab initio constant pressure study. *Solid State Communications*, 150(17–18):870–874, 2010. ISSN 0038-1098. doi: http://dx.doi.org/10.1016/j.ssc.2010.02.002. URL `http://www.sciencedirect.com/science/article/pii/S0038109810000876`.

[134] Georgios A. Tritsaris, Brad D. Malone, and Efthimios Kaxiras. Optoelectronic properties of single-layer, double-layer, and bulk tin sulfide: A theoretical study. *Journal of Applied Physics*, 113:233507, 2013.

[135] N. Koteeswara Reddy and K.T. Ramakrishna Reddy. Sns films for photovoltaic applications: Physical investigations on sprayed snxsy films. *Physica B: Condensed Matter*, 368(1–4):25–31, 2005. ISSN 0921-4526. doi: http://dx.doi.org/10.1016/j.physb.2005.06.032. URL `http://www.sciencedirect.com/science/article/pii/S0921452605008495`.

[136] P. Dera A. Krimmel P. Bouvier L. Ehm, K. Knorr and M. Mezouar. Pressure-induced structural phase transition in the iv-vi semiconductor sns. *J. Phys. Cond. Matt.*, 16:3545–355, 2004. doi: 10.1088/0953-8984/16/21/004. URL `http://iopscience.iop.org/0953-8984/16/21/004`.

[137] I. Lefebvre, M. A. Szymanski, J. Olivier-Fourcade, and J. C. Jumas. Electronic structure of tin monochalcogenides from sno to snte. *Phys. Rev. B*, 58:1896–1906, Jul 1998. doi: 10.1103/PhysRevB.58.1896. URL `http://link.aps.org/doi/10.1103/PhysRevB.58.1896`.

[138] Falco Hüser, Thomas Olsen, and Kristian S. Thygesen. Quasiparticle gw calculations for solids, molecules, and two-dimensional materials. *Phys.*

Rev. B, 87:235132, Jun 2013. doi: 10.1103/PhysRevB.87.235132. URL `http://link.aps.org/doi/10.1103/PhysRevB.87.235132`.

[139] Lars Hedin. New method for calculating the one-particle green's function with application to the electron-gas problem. *Phys. Rev.*, 139:A796–A823, Aug 1965. doi: 10.1103/PhysRev.139.A796. URL `http://link.aps.org/doi/10.1103/PhysRev.139.A796`.

[140] Mark S. Hybertsen and Steven G. Louie. Electron correlation in semiconductors and insulators: Band gaps and quasiparticle energies. *Phys. Rev. B*, 34:5390–5413, Oct 1986. doi: 10.1103/PhysRevB.34.5390. URL `http://link.aps.org/doi/10.1103/PhysRevB.34.5390`.